Pericardial adiposity and cardiac arrhythmia vulnerability

Simon Philip Wells

Bachelor of Medical Science (Honours), Master of Research

ORCID Identifier: 0000-0002-8071-2563

Submitted in total fulfilment of the requirements

for the degree of Doctor of Philosophy

at both the

University of Melbourne and the University of Birmingham

(as a Universitas 21 Joint PhD award)

August 2020

Department of Physiology
Faculty of Medicine, Dentistry and Health Sciences
University of Melbourne
Australia

Institute of Cardiovascular Sciences
College of Medical and Dental Sciences
University of Birmingham
United Kingdom

Summary of Contents

Note, Chapters 3 and 6 (data chapters) are presented in the form of constructed manuscripts for submission. Chapter 4 (data chapter) is adapted from a manuscript published prior to thesis submission. Chapter 5 (data chapter) is also presented in the form of a constructed manuscript for submission and contains data from an accepted manuscript.

Abstract

Background: The cellular mechanisms that predispose to arrhythmia include heterogeneic conduction slowing and/or changes in repolarisation time (e.g. regional alterations in transmural electrophysiology). Augmented pericardial adiposity is an independent risk factor for atrial and ventricular fibrillation, but the cellular mechanisms are unknown. Very limited data indicate pericardial adipose tissue exhibits paracrine characteristics, secreting factors which modulate cardiac electrophysiology. Recent evidence demonstrates pericardial adipose tissue can synthesise oestrogens which are known to affect cardiomyocyte function. It is hypothesised that augmented pericardial adiposity promotes epicardial conduction slowing and/or repolarisation prolongation through paracrine mechanisms to predispose to arrhythmia.

Research aims: (*relevant chapters in brackets*)

1. Establish that transmural electrophysiology is modulated in the context of elevated cardiac adiposity. (*3*)
2. Compare electrophysiology of cardiomyocyte cultures from different origins as prelude to examining the paracrine influences of pericardial adipose tissue. (*4*)
3. Ascertain that obesity and epicardial adiposity associate with cardiac electrophysiological remodelling which may increase arrhythmia vulnerability. (*5*)
4. Identify that sex steroids can modulate atrial electrophysiology, indicating their potential as paracrine regulators of arrhythmia vulnerability. (*6*)

Methods: Cardiac electrophysiology was assessed in both atrial and ventricular tissues utilising multiple *in vitro* methodologies. To establish the effects of adiposity on transmural electrophysiology, male rats were fed a high fat diet, then tangential left

ventricular slices were electrophysiologically mapped. To optimise cardiomyocyte culture conditions, neonatal rat ventricular myocyte (NRVM) and human induced pluripotent stem cell-derived cardiomyocyte (hiPSC-CM) electrophysiology was compared. Fragments of epicardial adipose tissue were co-cultured with hiPSC-CMs to assess the paracrine influence on cardiomyocyte electrophysiology. The effects of obesity on left atrial electrophysiology were determined using male mice fed a Western diet. Left atrial electrophysiology was also assessed in male and female chow-fed mice in the absence/presence of sex steroids.

Results: Some of the overall findings of this investigation include:

1. Augmented pericardial adiposity likely disrupts ventricular transmural conduction gradients through putative local actions on the epicardium.
2. hiPSC-CM and NRVM cultures display similar electrophysiology and exhibit good capacity to detect changes in repolarisation via experimental intervention.
3. Obesity associates with prolonged epicardial atrial action potential duration. This is caused by a paracrine influence of pericardial adipose tissue on cardiomyocytes.
4. Oestrogen and testosterone prolong repolarisation and slow conduction in the left atrium, indicating their potential as paracrine regulators of arrhythmia vulnerability.

Conclusions: Pericardial adipose tissue has capacity to selectively prolong epicardial activation and repolarisation. This is at least in part, mediated through a paracrine mechanism. Prolonged repolarisation and slowed conduction predispose to triggered and reentrant arrhythmias, respectively. Together, these data indicate that augmented cardiac adiposity has a causative effect on cardiomyocyte electrophysiology to increase arrhythmia likelihood.

Declaration

This is to certify that:

I. The thesis comprises only my original work towards the PhD, except where otherwise stated.

II. Due acknowledgement has been made in the text to all other material used.

III. The thesis is fewer than 50,000 words in length, exclusive of tables, bibliographies, and appendices.

IV. The thesis is fewer than 100,000 in entirety.

Simon P Wells

August 2020

Acknowledgements

I have had the great fortune of pursuing a prestigious Universitas 21 joint PhD over the past 3.5 years. This opportunity as been an immense privilege, affording me opportunity to work alongside several amazing people across the two hemispheres and I am hugely grateful to all those who have supported me along this journey. Firstly, to my lead supervisors at the University of Melbourne, Dr Jim Bell and Prof Lea Delbridge, thank you for your continued guidance and mentorship. Lea, although I am yet to correctly fill out a progress meeting form, I am hugely appreciative of the time you have invested in me through our weekly meetings and all the continual pushes you have given along the way. Your work ethic and intellectual scientific capacity is hugely inspiring. Jim, from the start you have been my first port of call for guidance on study designs, troubleshooting, data interpretation, etc. I am hugely grateful for your patience, relentless optimism, and detailed thoughtful feedback – in particular, your method of drafting a presentation story out of confusing datasets is remarkable and has been resolutely encouraging.

I would also like to acknowledge Dr Claire Curl. I must especially thank you for your assistance and time (and weekends!) with the rat high fat diet experiments. It has been excellent and insightful working in the lab with you.

Dr Davor Pavlovic, your input from Birmingham has been brilliant. Your daily support and friendly open-door policy during my Birmingham stint was invaluable. In addition, your professional advice and ongoing support through our monthly meetings and your Melbourne visits has been truly excellent. This has been instrumental in me securing my next career step prior to PhD completion, so thank you.

More directly, I acknowledge the contributions of several lab members for their input to work in this thesis. A detailed breakdown of contributions is indicated on Pages xxvi to xxix, but I would like to make special mention to Ms Helen Waddell, Dr Christopher O'Shea and Dr Evangelyn Sim. Helen, optimising the microelectrode array was a challenge in my first year, but when you came on board it became an extremely fun challenge. I will cherish the MEA playlists! Chris, I really appreciate your assistance with the optical mapping experiments, especially your efforts explaining the analysis module. Evangelyn, your knowledge and technical expertise with human iPS cultures has been invaluable.

To all the past/present members of the Cardiac Phenomics Laboratory and Prof Paulus Kirchhof and the Heart Failure and Arrhythmia Cluster, I extend a great note of gratitude for your feedback and collaborative efforts along the way. A special mention goes out to Johannes Janssens, Helen Waddell, Parisa Koutsifeli and Eleia Chan who have been with me from the start, providing excellent support and friendship. Among many things, I will miss the spontaneous trips to PA's (which unwaveringly led to nights at the Toff). You guys have provided a strong support network, which I am very appreciative of.

Finally, to all my friends and family who have provided resolute support throughout, thank you very much. To my parents, none of this would have been possible without your continued love and dedication to our family and my learnings. I am thankful for the sacrifices you have made for me during my education (I promise this is the last degree!).

Table of contents

List of Figures

Chapter 1

Chapter 3

Chapter 4

Chapter 5

Chapter 6

List of Tables

Chapter 6

List of abbreviations

+Adip	epicardial adipose tissue co-culture conditions
AF	atrial fibrillation
APD	action potential duration
APD_x	action potential duration at x% repolarisation
BPM	beats per minute
Ca^{2+}	calcium ion
CACNA1C	calcium voltage-gated channel subunit alpha1 C gene
$Ca_V1.2$	voltage-gated calcium channel 1.2 (carries $I_{Ca,L}$)
Ctrl	control
DMEM	Dulbecco's modified eagle medium
FGF	fibroblast growth factor
FP_{amp}	field potential amplitude
FP_{dur}	field potential duration
FP_{min}	field potential minimum
FP_{pre}	field potential upstroke maximum
HFD	high fat diet
hiPSC-CMs	human induced pluripotent stem cell-derived cardiomyocytes
$I_{Ca,L}$	L-type calcium current
I_K	delayed rectifier currents
$I_{K,ATP}$	adenosine triphosphate-sensitive potassium current
I_{K1}	inward rectifying potassium current
I_{kr}	rapid component of the delayed rectifier current
I_{ks}	slow component of the delayed rectifier current
I_{NCX}	sodium-calcium ion exchanger current
I_{to}	transient outward potassium currents
$I_{to,f}$	fast transient outward potassium current
$I_{to,s}$	slow transient outward potassium current
I_{kur}	ultra-rapid component of the delayed rectifier current
I_{Na}	voltage-gated sodium current
IsoP	isoproterenol
K^+	potassium ion
KCNA4	potassium voltage-gated channel subfamily A member 4 gene
KCND2	potassium voltage-gated channel subfamily D member 2 gene
KCND3	potassium voltage-gated channel subfamily D member 3 gene
KCNH2	potassium voltage-gated channel subfamily H member 2 gene

KCNJ2	potassium inwardly rectifying channel subfamily J member 2 gene
KCNJ11	potassium inwardly rectifying channel subfamily J member 11 gene
KCNQ1	potassium voltage-gated channel subfamily Q member 1 gene
Kir2.x	inward rectifying potassium channel 2.x (carriers I_{K1})
Kir6.2	inward rectifying potassium channel 6.1 (carriers $I_{K,ATP}$)
$K_V1.4$	voltage-gated potassium channel 1.4 (carries $I_{to,s}$)
$K_V4.2$	voltage-gated potassium channel 4.2 (carries $I_{to,f}$)
$K_V4.3$	voltage-gated potassium channel 4.3 (carries $I_{to,f}$)
$K_V7.1$	voltage-gated potassium channel 11.1 (carries I_{Ks})
$K_V11.1$	voltage-gated potassium channel 11.1 (carries I_{Kr})
MEA	microelectrode array
Na^+	sodium ion
$Na_V1.5$	voltage-gated sodium channel 1.5 (carries I_{Na})
NCX1	sodium/calcium exchanger (carries I_{NCX})
NRVMs	neonatal rat ventricular myocytes
SCN5A	sodium voltage-gated channel alpha subunit 5 gene
SLC8A1	sodium/calcium exchanger gene
SEM	standard error of the mean
TGF-β1	tissue growth factor beta one
TNF-α	tissue necrosis factor alpha

Relevant publications

Comprising thesis content:

Wells SP, Curl CL, …, Kirchhof P, Pavlovic D, Delbridge LMD and Bell JR. Prolonged activation of ventricular epicardium disrupts a transmural conduction gradient in context of high cardiac adiposity. **Manuscript in preparation (Chapter 3)**

Wells SP[*], Waddell HM[*], Sim CB, Lim SY, Bernasochi GB, Pavlovic D, Kirchhof P, Porrello ER, Delbridge LMD, Bell JR. Cardiomyocyte functional screening - interrogating comparative electrophysiology of high-throughput model cell systems. *Am J Physiol Cell Physiol*, 2019; 317: (6), C1256-C1267. **(Chapter 4 adapted)**

Wells SP, O'Shea C, Sim CB, …, Porrello ER, Kirchhof P, Pavlovic D, Delbridge LMD and Bell JR. Obesity and epicardial adipose tissue associate with prolonged repolarisation in murine atria and human cardiomyocytes. **Manuscript in preparation (Chapter 5, Figures: 5.1-5.5, 5.6A & F, 5.7 and 5.8)**

Nalliah CJ[*], Bell JR[*], Raaijmakers AJA, Waddell HW, **Wells SP**, Bernasochi GB, Montgomery MK, Binny S, Watts TM, Joshi S, Lui E, Sim CB, Larobina M, O'Keefe M, Goldblatt J, Royse A, Lee G, Porrello ER, Watt MJ, Kistler PM, Sanders P, Delbridge LMD[#], Kalman JM[#]. Epicardial Adipose Tissue Accumulation Confers Atrial Conduction Abnormality *J Am Coll Cardiol*, 2020; 76: (10), 1197-1211 **(Chapter 5, Figures: 5.6B-E)**

Wells SP, O'Shea C, …, Kirchhof P, Pavlovic D, Delbridge LMD and Bell JR. Oestrogen and testosterone mediate non-transcriptional regulation of left atrial electrophysiology in a sexually dimorphic manner. **Manuscript in preparation (Chapter 6)**

Collaborative papers (during candidature):

O'Shea C, Holmes AP, Yu TY, Winter J, **Wells SP**, Correia J, Boukens BJ, De Groot JR, Chu GS, Li X, Ng GA, Kirchhof P, Fabritz L, Rajpoot K, Pavlovic D. ElectroMap: High-throughput open-source software for analysis and mapping of cardiac electrophysiology. *Sci Rep*, 2019; 9: (1), 1389

O'Shea C, Holmes AP, Yu TY, Winter J, **Wells SP**, Parker BA, Fobian D, Johnson DM, Correia J, Kirchhof P, Fabritz L, Rajpoot K, Pavlovic D. High-Throughput Analysis of Optical Mapping Data Using ElectroMap. *J Vis Exp*, 2019; 4: (148), DOI: 10.3791/59663

Bernasochi GB, **Wells SP**, Rupasinghe TWT, …, Sim CB, Nalliah CJ, Kalman JM, Porrello ER, Pavlovic D, Roessner U, Boon WC, Bell JR, Delbridge LMD. Local modulation of cardiac sex steroids: evidence from the aromatase knockout mouse. **Manuscript in preparation**

Abstracts:

Wells SP, Waddell HM, Delbridge, LMD, Bell JR. Differential effect of electrical stimulation and β-adrenergic stimulation on neonatal rat ventricular myocyte monolayer conduction properties. *Proceedings from the Australian Physiological Society Meeting*, Melbourne, 2017.

Waddell HM, **Wells SP**, Delbridge LMD, Bell JR. Establishing reference conditions for electrophysiological recordings of spontaneously beating neonatal rat cardiomyocytes on a multi-electrode array. *Proceedings from the Australian Physiological Society Meeting*, Melbourne, 2017.

Wells SP, Waddell HM, Delbridge, LMD, Bell JR. Optimising and validating culture conditions for high-spatial electrophysiological mapping of primary cardiomyocyte monolayers using the microelectrode array. *Proceedings from the Physiological Society's "Future Physiology" Meeting,* Leeds, 2017.

Wells SP, Waddell HM, Delbridge, LMD, Bell JR. Optimising cardiomyocyte monolayer culture methodology for high-spatial resolution electrophysiological mapping. *Proceedings from the British Pharmacological Society Meeting,* London, December 2017

O'Shea C, **Wells SP,** Holmes AP, Winter J, Correia J, Kirchhof P, Pavlovic D. Development and validation of high-throughput processing and analysis software platform for cardiac optical mapping. *Heart*, 104(Suppl 6): A98 LP-A98, 2018.

Hepburn C, Syeda F, Yu T, Holmes AP, Roth VC, Wright T, Kabir SN, Menon P, **Wells SP**, Vloumidi E, Apicella C, Lutz S, Fortmueller L, Isaacs A, Stoll M, Gkoutos G, Pavlovic D, Kirchhof P, Fabritz L. Desmosomal instability increases atrial arrhythmia susceptibility after endurance training. *Heart*, 104:A95-A96, 2018.

Waddell HM, **Wells SP**, Delbridge LMD, Bell JR. Assessing Sex and Sex Steroid Influence on Cardiac Electrophysiology in Cultured Monolayers. *Heart, Lung and Circulation*, 27 (S148), Brisbane, 2018.

Wells SP, Waddell HM, O'Shea C, Kirchhof P, Pavlovic D, Delbridge, LMD, Bell JR. Acute oestradiol slows conduction and prolongs action potential duration in the left atrium, but not in cardiomyocyte cultures. *Proceedings from the Australian Physiological Society Meeting*, Sydney, 2018.

Waddell HM, **Wells SP**, Sim CB, Porrello ER, Delbridge LMD, Bell JR. Microelectrode Array Screening of Different Cardiomyocyte Cultures Reveals Inherent Disparities in Cardiac Cell Electrophysiology. *Heart, Lung and Circulation*, 28 (S147), Adelaide, 2019.

Wells SP, O'Shea C, Waddell HM, Kirchhof P, Pavlovic D, Delbridge LMD, Bell JR. Acute Oestradiol Slows Conduction in Male, but not Female, Murine Left Atria. *Heart, Lung and Circulation*, 28 (S200), Adelaide, 2019.

Cao LL, Kabir SN, **Wells SP**, Holmes AP, Fabritz L, Brain KL. A new, fluorescence-based technique to label and monitor sympathetic nerve function in the murine heart and mesenteric artery. *Midlands Cardiovascular Research Network 2nd Open Scientific Meeting*, 2019.

Author contribution Chapter 3

"Prolonged activation of ventricular epicardium disrupts a transmural conduction gradient in the context of high cardiac adiposity"

Chapter presented in the style of a manuscript for submission to *Heart Rhythm*.

Wells SP, Curl CL, …, Kirchhof P, Pavlovic D, Delbridge LMD, Bell JR. "Prolonged activation of ventricular epicardium disrupts a transmural conduction gradient in context of high cardiac adiposity". **In preparation**

Details of final authorship are indicative and pending, as the final version for submission is still under development.

Contribution of candidate: SPW 85%	
	– Setup & optimisation of cardiac slice-MEA technique – Experimental design – Animal husbandry & cohort management – Histology – Data analysis – Figure preparation – Chapter draft and finalisation
Contribution of others: 15%	
	– Histology: *SPW*, *Histopathology Dept* (*University of Melbourne*) – Mapping analysis scripts: *SPW, CMT, COS, DP* – Final chapter development and review: *SPW, CLC, DP, PK, LMD, JRB*

Author contribution Chapter 4

"High-throughput examination of the electrophysiological properties of cardiomyocyte cultures from different origins"

Chapter adapted from published manuscript:

Wells SP[*], Waddell HM[*], Sim CB, Lim, SY, Bernasochi GB, Pavlovic D, Kirchhof P, Porrello ER, Delbridge LMD[#], Bell JR[#] "Cardiomyocyte functional screening: interrogating comparative electrophysiology of high-throughput model cell systems", *Am J Physiol Cell Physiol*, 2019 317 (6): C1256-C1267

[*/#] contributed equally to this publication

Contribution of candidate: SPW 70%	
	– Setup of MEA system – Development and optimisation of culture conditions and seeding approaches for NRVMs and hiPSC-CMs onto MEAs – Development and optimisation of experimental MEA recording and analysis protocols for NRVMs and hiPSC-CMs – Cardiomyocyte isolation and culture – Data analysis – Figure preparation – Chapter (and published manuscript) draft and finalisation
Contribution of others: 30%	
	– Performing optimised NRVM-MEA experiments: *SPW, HMW* – Development of optimal seeding approach for hiPSC-CMs: *SPW, CBS* – Differentiation induction of hiPSC-CMs: *CBS, ERP* – NRVM data analysis: *SPW, HMW* – Final chapter development and review: *SPW, DP, PK, LMD, JRB*

Author contribution Chapter 5

"Obesity and epicardial adipose tissue associate with prolonged repolarisation in murine atria and human cardiomyocytes"

This chapter contains data from two proposed manuscripts under finalisation

Wells SP, O'Shea C, Sim CB, …, Porrello ER, Kirchhof P, Pavlovic D, Delbridge LMD, Bell JR. "Obesity and epicardial adipose tissue associate with prolonged repolarisation in murine atria and human cardiomyocytes". **In preparation**. (Figures: 4.1-4.5 and 4.8).

Nalliah CJ[*], Bell JR[*], Raaijmakers AJA, Waddell HW, **Wells SP**, Bernasochi GB, Montgomery MK, Binny S, Watts TM, Joshi S, Lui E, Sim CB, Larobina M, O'Keefe M, Goldblatt J, Royse A, Lee G, Porrello ER, Watt MJ, Kistler PM, Sanders P, Delbridge LMD[#], Kalman JM[#]. Epicardial Adipose Tissue Accumulation Confers Atrial Conduction Abnormality *J Am Coll Cardiol*, 2020; 76: (10), 1197-1211 (Figures: 5.6B-E).

[*/#] contributed equally to this publication

Contribution of candidate: SPW 75%	
	– Setup of MEA system – MEA protocol design, optimisation, and implementation – Tissue collection, preparation, and cell culture – Optical mapping experiments – Data analysis – Figure preparation – Chapter draft and finalisation
Contribution of others: 25%	
	– Provision of sheep tissue: *SPW, CNM* – hiPSC-CM differentiation and culture management: *SPW, CBS, ERP* – Animal cohort management: *SPW, COS, DP, PK* – Optical mapping experiments: *SPW, COS* – Optical mapping data analysis: *SPW, COS* – Final chapter development and review: *SPW, DP, PK, LMD, JRB*

Author contribution Chapter 6

"Male and female atria exhibit distinct acute electrophysiological responses to sex steroids"

Chapter presented in the style of a manuscript for submission to *Biology of Sex Differences.*

Wells SP, O'Shea C, …, Kirchhof P, Pavlovic D, Delbridge LMD and Bell JR. "Oestrogen and testosterone mediate non-transcriptional regulation of left atrial electrophysiology in a sexually dimorphic manner". **In preparation**.

Details of final authorship are indicative and pending, as the final version for submission is still under development.

Contribution of candidate: SPW 70%	
	– Protocol design, optimisation, and implementation – Optical mapping experiments – Data analysis – Figure preparation – Chapter draft and finalisation
Contribution of others: 30%	
	– Optical mapping experiments: *SPW, COS* – Optical mapping data analysis: *SPW, COS* – Final chapter development and review: *SPW, DP, PK, LMD, JRB*

Chapter 1

Literature review:

Cardiac adiposity, local sex steroids and arrhythmia

1.1 Introduction

Cardiac arrhythmias pose a significant and growing global healthcare burden. Heterogeneic conduction slowing and/or changes in repolarisation time are the key cellular mechanisms underpinning arrhythmogenesis (1,2). Recent evidence implicates augmented pericardial adiposity as a prominent independent risk factor for atrial and ventricular fibrillation (3-7), but the cellular mechanisms are largely unexplored. Non-cardiac adipose tissue serves as an endocrine organ with substantial secretory capacity. Investigations in the literature are limited, but indicate pericardial adipose tissue similarly possesses secretory capacity, locally releasing factors which promote myocardial structural and electrical remodelling which may be proarrhythmic (8,9). More recent data indicate a potential role for sex steroid-mediated modulation of myocardial arrhythmia vulnerability (10). Pericardial adipose tissue is a site of androgen-oestrogen conversion and experimentally, oestradiol increases atrial arrhythmia risk (10). These findings highlight a potential role for sex steroids in atrial fibrillation pathology. With the involvement of sex steroids in arrhythmia vulnerability, this review also explores sex differences in cardiac electrophysiology and arrhythmia pathophysiology. Discussion of this collection of themes highlights key knowledge deficits to form the justification for investigations into the underlying mechanisms linking pericardial adiposity and arrhythmia vulnerability.

1.2 Cardiac electrophysiology overview

1.2.1 The cardiac conduction system

The ability of the heart to continually pump blood at a regular dynamic rhythm ensures adequate oxygen supply to all organs. Cardiac contraction is a highly organised process to maximise blood ejection efficiency. Electrical impulses, termed action potentials, propagate through the myocardium in an ordered fashion to define the contraction routine via the process of excitation-contraction coupling. An action potential is initiated by pacemaker cells at the sinoatrial node in the wall of the right atrium. This impulse propagates across the atria initiating depolarisation and contraction, then transits to the atrioventricular node where there is a delay to ensure maximal ejection of blood from the atria into the ventricles. The action potential then travels along Purkinje fibres in the ventricular septum to the apex of the heart, around the ventricular free walls back towards the base. Depolarisation and contraction from apex to base is essential to ensure blood is efficiently pumped out of the ventricles into the aorta and pulmonary artery (11).

Viewing the heart as a 3-dimensional structure adds another layer of complexity to the conduction system organisation. Impulses must propagate across the heart wall itself, not just from apex to base in a single layer. In the ventricle, Purkinje fibres run along and predominantly terminate in the endocardium/sub-endocardium. Action potentials then travel transmurally to depolarise the epicardium (12).

1.2.2 The cardiac action potential

Formation of the cardiac action potential

Regional depolarisation and repolarisation in the cardiac conduction system can be detected as distinct waveforms on the surface electrocardiogram. A cardiac cycle begins with atrial depolarisation (P-wave), followed by ventricular depolarisation (QRS complex) terminating in ventricular repolarisation (T-wave)(11,13). In atrial and ventricular cardiomyocytes, a five-phase action potential (numbered 0-4; **Figure 1.1**) drives this sequence of depolarisation and repolarisation, conducting from cell-to-cell via gap junctions to facilitate contraction. The cycle begins at Phase 4, where cardiomyocytes are at resting membrane potential (approximately -90 mV). When action potentials from the sinoatrial node arrive at cardiomyocytes, the membrane potential is depolarised to a threshold (approximately -70mV) triggering the opening of voltage-gated sodium channels (namely, $Na_V1.5$) and rapid influx of Na^+ (I_{Na}) to generate the action potential upstroke (Phase 0). $Na_V1.5$ quickly inactivates (1-2ms) at positive membrane potentials and then slower voltage-gated Ca^+ and K^+ open to begin repolarisation. Phase 1 encompasses transient outward K^+ currents comprised of a fast component ($I_{to,f}$; mediated via $K_V4.2/4.3$) and a slow component ($I_{to,s}$; mediated via $K_V1.4$). I_{to} generates the action potential notch characteristic of early repolarisation. $K_V4.2/4.3$ then close, shortly followed by $K_V1.4$ and I_{to} ceases. During the next Phase (2), voltage-gated L-type Ca^{2+} channels open ($Ca_V1.2$), resulting in Ca^{2+} influx ($I_{Ca,L}$) which initiates Ca^{2+}-induced Ca^{2+} release from the sarcoplasmic reticulum and contractile processes. This Ca^{2+} influx is balanced by the rapid (I_{Kr}) and slow (I_{ks}) delayed rectifier K^+ currents carried through $K_V11.1$ and $K_V7.1$, respectively. This generates the action

potential plateau which ceases when $Ca_V1.2$ inactivates and Phase 3 begins, with continued I_K through $K_V11.1$ and $K_V7.1$ driving the cell back to resting membrane potential, coinciding with relaxation/diastole (1,2). Calcium is extruded from the cell via the sodium-calcium exchanger, NCX1 (I_{NCX}; exchanging one calcium ion for 3 sodium ions), and is also sequestered back into the sarcoplasmic reticulum. The inward rectifying potassium current IK_1 (carried through Kir2.x) stabilises the resting membrane potential (Phase 4) and initially helps shape Phase 0. ATP-sensitive K^+ channels (Kir6.2) are typically blocked by intracellular ATP under physiological conditions, hence contribute only a small amount to repolarisation. In a pathological setting (e.g. hypoxia), they become important mediators of action potential morphology (1,2).

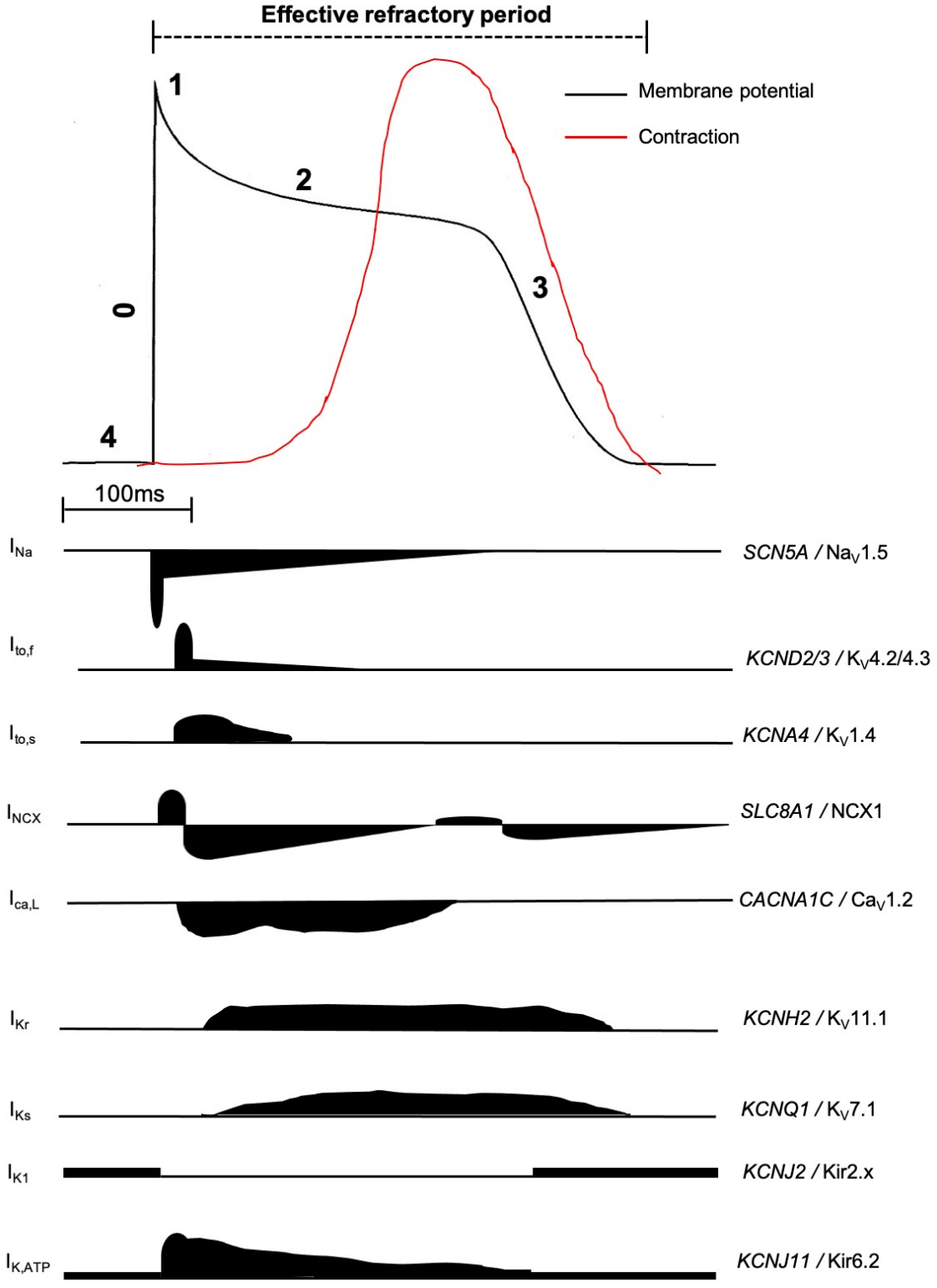

Figure 1.1 The cardiac action potential, underlying ionic currents and contraction cycle. Five phases (numbered 0-4) characterise the cardiac action potential (black). Ca^{2+} influx during Phase 2 drives Ca^{2+}-induced Ca^{2+} release and contraction (red). Currents are listed down the left hand side and are defined as follows: I_{Na}, voltage-gated Na^+; $I_{to,f/s}$ fast and slow transient outward K^+; I_{NCX}, Na^+/Ca^{2+} exchanger; $I_{Ca,L}$, L-type Ca^{2+}; $I_{Kr/s}$ rapid and slow delayed rectifier K^+; I_{K1}, inward rectifier K^+; $I_{K,\ ATP}$, ATP-sensitive K^+. The right-hand side denotes the *gene* / primary channel protein which carries the current.

Regional differences in action potential morphology

An important feature of the cardiac action potential is the long repolarisation time, termed refractory period. During this, further stimulation is not able to excite cells due to $Na_V1.5$ voltage and time dependent inactivation. Other excitable tissues do not have such a prolonged refractory period. In the heart, a long refractory period is essential to avoid tetanic contraction, maintaining ability to fill with and pump blood efficiently. Repolarisation time is not uniform throughout the heart. Atrial cardiomyocyte action potential duration is shorter than ventricular due to the unique presence of the ultrarapid outward current (I_{Kur}) and greater density of $I_{to,f}$ (14). This results in a more pronounced notch (Phase 1) and shorter plateau (Phase 2) that occurs at a lower membrane potential (**Figure 1.2**).

Transmural differences in repolarisation also exist. Atrial and ventricular epicardial cardiomyocytes exhibit an action potential duration significantly shorter than endocardial cardiomyocytes due to regional differences in voltage-gated K^+ channel expression (15-21). In the ventricle, this is thought to be important to offset the transmural delay in depolarisation (i.e. propagation from endocardium to epicardium), ensuring that the heart wall repolarises homogenously (16)(**Figure 1.3**). The interval between the electrocardiogram T-wave peak and the end of the T-wave represents transmural dispersion of repolarisation across the ventricle (22-24). Epicardial repolarisation coincides with the T-wave peak and midmyocardial cell repolarisation coincides with the end of the T-wave (22-24). This interpretation is somewhat controversial, with several studies not able to corroborate presence of midmyocardial cells (16,25-28), and more recent evidence from left ventricular wedge preparations

indicating that transmural repolarisation is synchronised (16). Others indicate that this dispersion index may be a result of left-right ventricular asynchronous repolarisation (29,30).

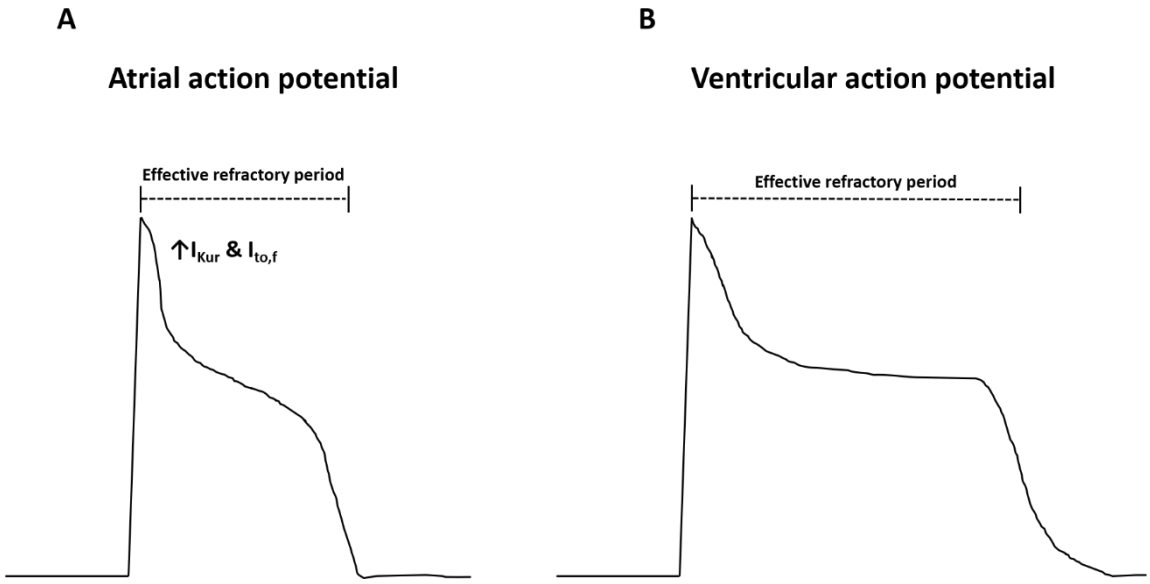

Figure 1.2 Atrial *vs* ventricular epicardial action potential morphology. Atrial epicardial action potentials **(A)** exhibit a more pronounced notch and shorter Phase 2 plateau, hence refractory period, compared to ventricular action potentials **(B)**.

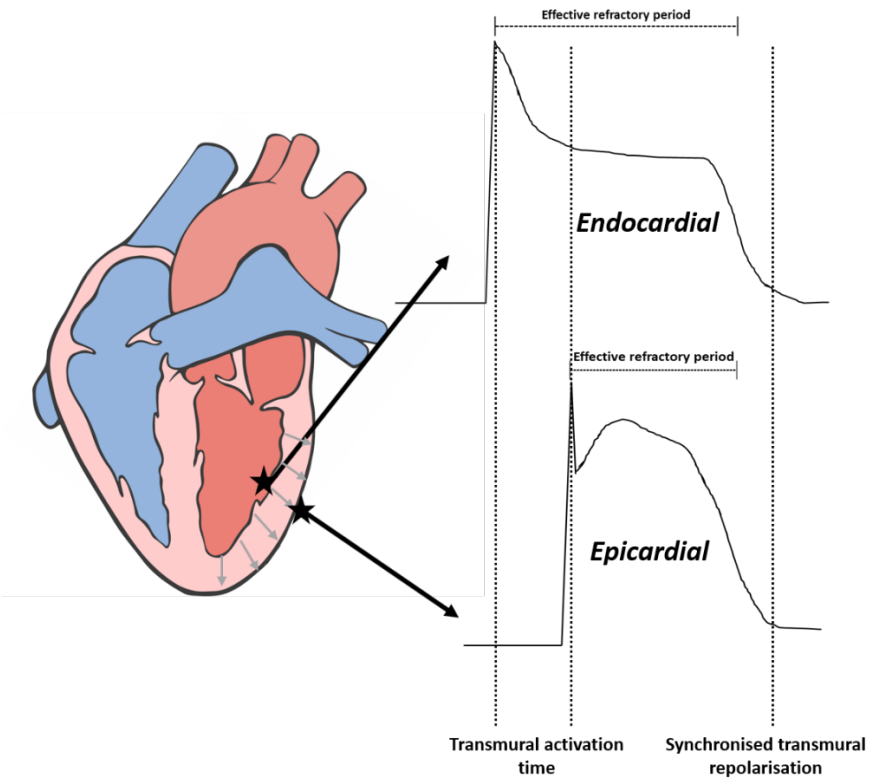

Figure 1.3 Endocardial *vs* epicardial ventricular action potential morphology. Action potentials transit from endocardium to epicardium. This results in a transmural activation delay. Endocardial action potential duration/refractory period is longer than epicardial, resulting in synchronised transmural repolarisation.

Species differences in action potential morphology

The cardiac action potential is not uniform between species. Mice and rats have a similar resting membrane potential and Phase 0 upstroke; however, Phase 1 is significantly more pronounced, resulting in a rapid early repolarisation wave (J wave) on the electrocardiogram compared to humans. Mice and rats also lack a definitive Phase 2 plateau. These species differences are a result of greater I_{to} density and reduced I_{Kr} and I_{Ks} in rodents compared to humans (31)(**Figure 1.4**). These differences in ion conductance are themselves a result of greater expression of $K_V4.3/4.3$ and reduced $K_V11.1$ and $K_V7.1$ in rodent myocardium compared to humans and larger animals (31).

This rapid repolarisation in rodents is consistent with their heart rates being 6-10-fold greater than humans.

Common features between humans and rodents are the transmural repolarisation gradient and repolarisation-rate dependency of the cardiac action potential (16,20,21). Action potential duration and effective refractory period shorten as heart rate is increased. In humans, this is more pronounced as heart rate can increase by 140-170% (32), whereas in rats and mice this increase is 40-50% and 30-40%, respectively (33-36). Humans also possess a positive force-frequency relationship, allowing for greater pumping efficiency during stress/exercise (37-39). In rats, this is response is less pronounced (40), and in mice often no relationship between rate and force production is observed (41). As such, humans have much greater reserve to increase cardiac output in response to exercise/stressors (33).

The mechanisms underlying repolarisation-rate dependency are complex and split across two main phases. An initial rapid shortening in action potential duration develops within milliseconds and then a further gradual shortening that happens over the following seconds-minutes (42). The initial shortening is caused by changes in gating characteristics of specific currents. Incomplete recovery of inward currents (fast I_{Na} and $I_{Ca,L}$) contributes to the initial shortening in repolarisation time (42-44). I_{Ks} plays a major role in mediating the second phase. During rapid pacing/heart rates, the slow deactivation kinetics of $K_V7.1$ are thought to favour the channel in the open state, allowing biophysical accumulation of I_{Ks}, shortening repolarisation time/action potential duration (45). Sympathetic/β-adrenergic stimulation (typically associated with increases in heart rates *in vivo*) promotes $K_V7.1$ phosphorylation, causing a hyperpolarising shift,

meaning enhanced activation and delayed deactivation kinetics, abbreviating repolarisation (46). In small rodents, the role of I_{Ks} biophysical accumulation is thought to be less important in mediating repolarisation-rate dependency. $I_{to,f}$ accumulation at higher pacing rates is thought to account for repolarisation-rate dependency seen in rodents (47).

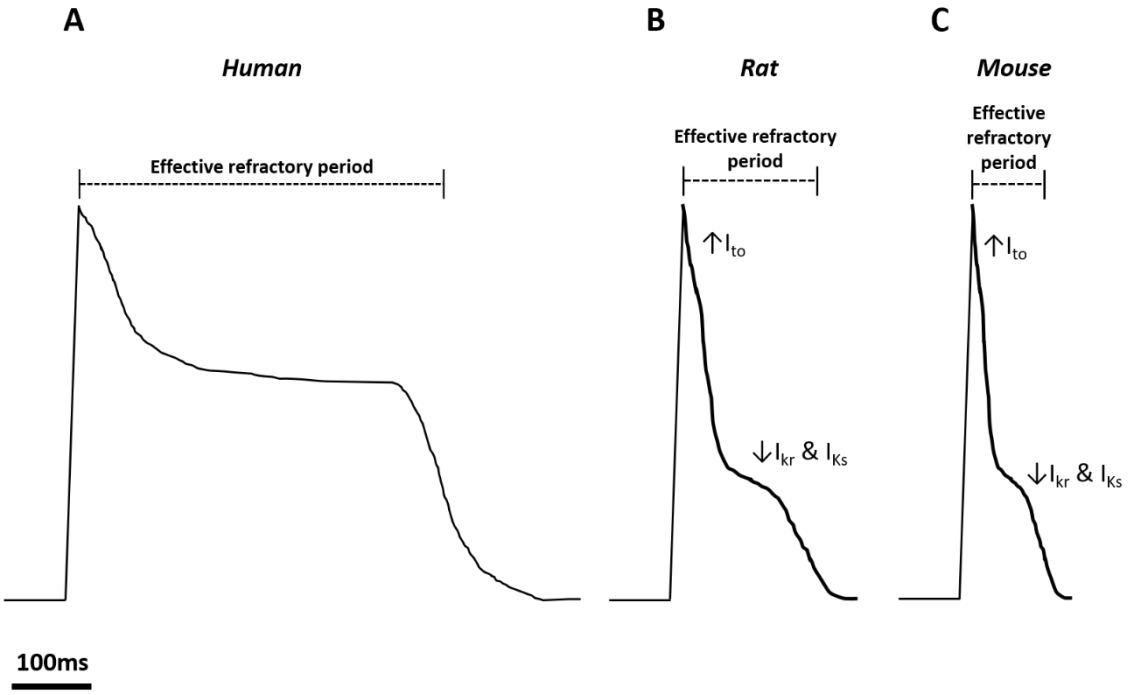

Figure 1.4 Species differences in ventricular epicardial action potential morphology. The human action potential **(A)** has a similar Phase 0 upstroke, but longer refractory period in comparison to rat **(B)** and **(C)** mouse. The mouse action potential duration is also shorter than the rat. These species differences are due to greater early repolarisation, facilitated by increased I_{to} density, and the absence of a clear plateau phase in rodents.

1.3 Cardiac arrhythmogenesis: pathophysiology and mechanisms

Heterogeneic (i.e. regional) changes in the refractory period and cell-cell conduction of action potentials are key mechanisms which predispose to arrhythmias, hence are important measures in preclinical investigations (1,2). Arrhythmias are defined as a heart rate/rhythm that is too slow, fast, or irregular. There are several different types, each characterised by the chamber affected and result in different pathologies. This review focuses on two prominent arrhythmia types, atrial fibrillation (the most common arrhythmia) and ventricular fibrillation (the most life-threatening arrhythmia).

1.3.1 Atrial fibrillation pathophysiology

Atrial fibrillation is the most common arrhythmia affecting up to 4% of the population (48). It is characterised by rapid disorderly excitation of the atria. Although itself not lethal, atrial fibrillation has significant impact on life quality (hypotension, exercise intolerance, etc.) and associates with a greater risk of stroke and heart failure (49-52). Atrial fibrillation is an emerging epidemic, with 25% of current 40-year olds predicted to develop the disease in their lifetime (53,54). The onset of atrial fibrillation is progressive, beginning with paroxysmal symptoms which develop into persistent then permanent atrial fibrillation.

1.3.2 Ventricular fibrillation pathophysiology

Ventricular fibrillation refers to the irregular, rapid, disorganised contraction of the ventricles which severely impedes ejection of blood from the ventricles. Ventricular fibrillation results in cardiac arrest and sudden cardiac death without immediate

cardiopulmonary resuscitation and defibrillatory intervention. 15-20% of deaths worldwide are a result of sudden cardiac death (55-57). Myocardial infarctions account for 75% of sudden cardiac deaths (56,58), and estimates indicate 3-12% of infarct patients develop ventricular fibrillation resulting in sudden cardiac death (59-63). In non-infarct individuals who die of sudden cardiac death, ventricular tachyarrhythmias are estimated to account for 75-80% of incidences (58,64-67).

1.3.3 Mechanisms of arrhythmogenesis

On a cellular level, the electrical mechanisms predisposing to atrial and ventricular fibrillation are thought to be similar. There are two primary mechanisms which drive arrhythmias, disorders associated with action potential formation (termed triggered activity) and disorders associated with action potential conduction (**Figure 1.5**).

Triggered activity

Triggered activity denotes the ectopic action potential generation that is usually a result of afterdepolarisations. Ectopic activity has been shown to occur in the pulmonary veins and posterior wall of the left atrium to predispose to atrial fibrillation (68-71). In the ventricle, the outflow tracts and sinuses of Valsalva are common sites of ectopy (72).

Afterdepolarisations arise in two forms from distinct mechanisms - early afterdepolarisations and delayed afterdepolarisations (73,74). These can be isolated events or can recur continually inducing fibrillation. Early afterdepolarisations are primarily a result of changes in the time and voltage-dependent recovery of L-type Ca^{2+} channels, but also $Na_V1.5$ inactivation (75,76)(**Figure 1.5A**). Action potential/refractory period prolongation results in L-type Ca^{2+} channels regaining opening capacity. This

leads to transient Ca^{2+} influxes/depolarisations during Phase 2 or 3 of the action potential, driving irregular contractions (73,76,77). Increases in the persistent late sodium current can also increase vulnerability to early afterdepolarisations. This is the mechanism thought to underpin long QT syndrome arrhythmias (74,75).

Delayed afterdepolarisations occur due to Ca^{2+} leak from the sarcoplasmic reticulum during diastole (i.e. Phase 4 of the action potential). This leak via ryanodine receptors can be induced by ischaemia-reperfusion injury, Ca^{2+} channelopathies and chronic catecholamine exposure. The resultant increase in cytosolic Ca^{2+} activates the sodium-calcium ion antiporter (3 Na^{+} imported: 1 Ca^{+} extruded), resulting in a net depolarising current (73,78). If the membrane potential reaches threshold, action potentials can be generated (79)(**Figure 1.5B**). Unstable/depolarised resting membrane potentials are markers of such ectopic activity (80-84).

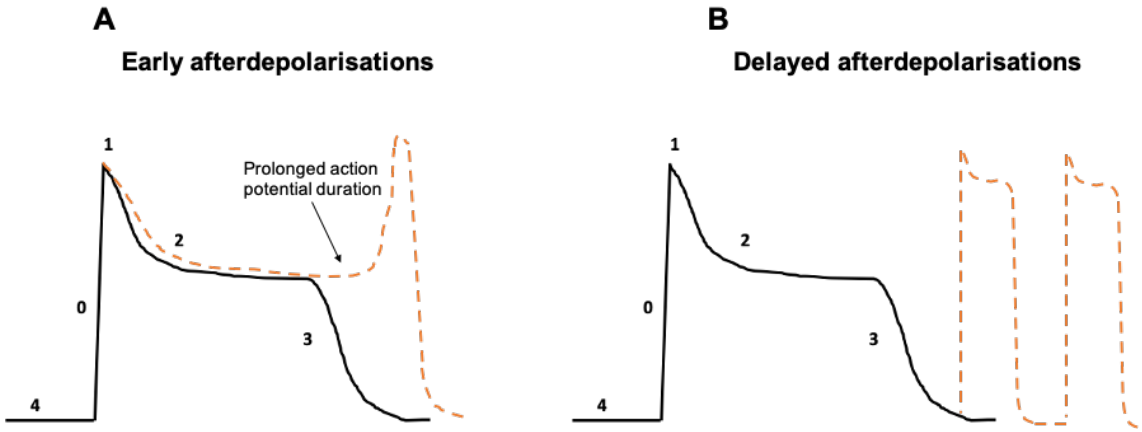

Figure 1.5 Cellular mechanisms of triggered arrhythmias. **(A)** early afterdepolarisations occur during Phase 2 or 3 of the action potential, resulting from re-opening of L-type Ca^{2+} channels. **(B)** delayed afterdepolarisations occur during Phase 4 of the action potential, arising from elevated cytosolic Ca^{2+} concentrations.

Disorders of action potential conduction

Triggered activity underpins the onset of paroxysmal atrial fibrillation in >95% of cases (85). Over time, further electrical and structural remodelling occurs, developing into persistent and permanent arrhythmia (73). The mechanisms that drive this later stage are conduction disorders. Ventricular fibrillation has a sudden onset, with the first symptom often being a life-threatening arrhythmia or sudden death (86,87). It is generally considered that such arrhythmias are a result of impulse conduction disorders rather than triggered activity (88).

Conduction block and reentry pathway formation

Disorders of action potential conduction include conduction block and action potential reentry (**Figure 1.6**). Under physiological conditions action potentials propagate through the heart, split at branch points, and cancel each other out at distal regions or continue to propagate in an orderly fashion (**Figure 1.6A**). A total conduction block is a region of tissue unable to be depolarised by an action potential from the sinoatrial node in the normal routine (**Figure 1.6B**). Unexcitable tissue might, for example be refractory cardiomyocytes or fibrotic scar tissue (74,89). This means this myocardial branch/region will not depolarise, hence contract.

Action potential reentry occurs is the presence of a unidirectional conduction block at a branch point. This means an action potential cannot propagate anterogradely along a particular branch point, hence it will not cancel out in distal tissue, meaning the action potential can travel retrogradely through the unidirectional conduction block and “re-enter” the myocardium. Reentry may not be so problematic if conduction is not slowed in the retrograde unidirectional block pathway, as it will arrive back at a refractory area

of tissue (**Figure 1.6C**). If conduction is sufficiently slowed in the retrograde direction along the unidirectional block branch, then the region of tissue at the initial branch point will have recovered excitability (**Figure 1.6D**). The re-entering action potential will therefore not dissipate, but depolarise tissue at this initial branch point, facilitating functional reentry and rotor formation (73,90,91). Reentry is successful at maintaining arrhythmias because it can result in a self-sustaining circuit of action potential generation, acting as a local (or potentially whole heart) pacemaker (88,92-94). Formation of multiple stable or moving rotors increases vulnerability to arrhythmia/abhorrent contraction (95-97).

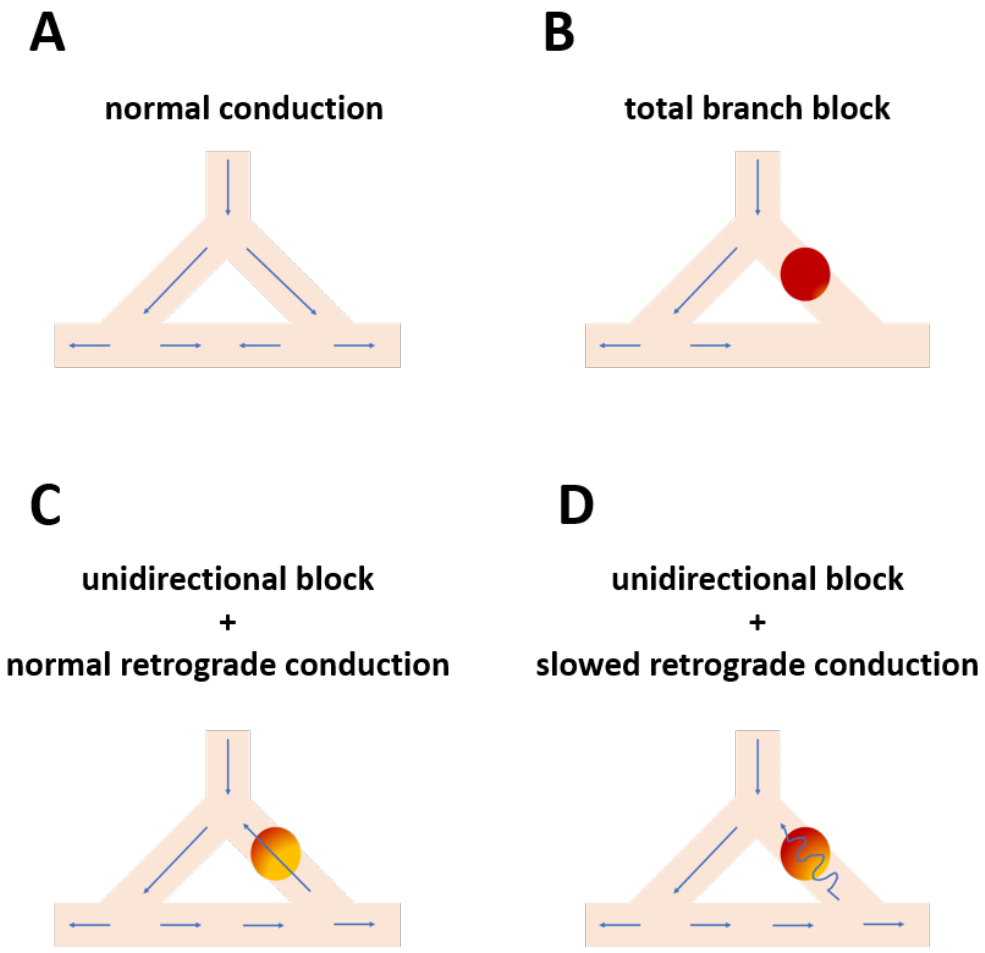

Figure 1.6 Conduction block and reentry pathway formation. **(A)** normal action potential propagation throughout two myocardial branchpoints and its dissipation in a connecting distal branch. **(B)** action potentials do not propagate along a branch with a conduction block, hence do not distally dissipate. **(C)** unidirectional conduction block in a single branch, where conduction is not slowed in the retrograde pathway. **(D)** unidirectional conduction block in a single branch, where conduction is slowed in the retrograde pathway, facilitating rotor formation.

Cellular mechanisms of reentry

For reentry to occur, the wavelength (i.e. how far the action potential can travel) must be less than the path length (i.e. the distance the action potential is required to travel during normal activation)(98). Wavelength is a product of the effective refractory period duration and the action potential conduction velocity, and so any reduction in these two parameters increases the vulnerability to reentry and arrhythmia (74,90,96,99).

The effective refractory period is dependent on $Na_V1.5$ inactivation recovery time. This occurs faster at negative membrane potentials, and so shorter action potential durations and hyperpolarised resting membrane potentials will shorten the effective refractory period, hence wavelength and increase reentry vulnerability (100,101).

Conduction velocity is determined by two key factors (1) cation transit between cells and (2) the size of the depolarising current (I_{Na}). Current flows between cells via gap junctions situated in the intercalated disks, themselves primarily located at the longitudinal ends of the cardiomyocyte. A single gap junction is composed of two connexons (pores connecting adjacent cells), themselves each comprised of six connexin proteins. In the atria, connexin 40 is the dominant form, whilst in the ventricle, connexin 43 expression is more prominent (102,103). Disruption in gap junction coupling, through mutations and scar tissue replacement are seen in atrial/ventricular fibrillation pathology (103).

The size of the depolarising current (I_{Na}) is determined by $Na_V1.5$ expression/function. $Na_V1.5$ typically localises to the intercalated disc, likely to aid in coupling rapid transmembrane conductance to intercellular conductance (103,104). I_{Na} can be

measured experimentally as the action potential amplitude/upstroke velocity. Hence, mutations in *SCN5A* and/or changes in $Na_V1.5$ expression, function and membrane capacitance can reduce this, slowing conduction velocity and wavelength to increase reentry likelihood (73,88,103).

Heterogeneity and reentry vulnerability

As described earlier, regional differences in action potential characteristics can be physiologically beneficial, for example transmural differences in action potential duration offset the transmural activation delay to synchronise ventricular repolarisation (16). Conversely, abhorrent heterogeneity in action potential duration can facilitate rotor formation if a region is refractory when it should be excitable. In the ventricle, transmural and intramural re-entry are key mechanisms of ventricular fibrillation arrhythmogenesis, arising from disrupted regional differences in refractoriness (105-107). Elevated transmural dispersion of ventricular repolarisation (i.e. repolarisation heterogeneity) is a marker for arrhythmia risk (108,109). QRS fragmentation is a clinical measure of heterogeneic ventricular depolarisation and is increased in ventricular arrhythmia patients (110,111). Electrophysiological heterogeneity is prevalent in atrial fibrillation patients but not as readily detectable since repolarisation is masked by the QRS complex (73,112,113).

Spatiotemporal heterogeneities (e.g. alternans) can also predispose to reentry. Repeated beat-to-beat variation in action potential duration and/or calcium transients (e.g. long-short), where adjacent regions of tissue are out of phase (e.g. short-long) with one another, can create areas of conduction block (114). Steeper electrical restitution

(i.e. action potential duration *vs* diastolic interval) has been implicated as a driver for alternans-based arrhythmias (115,116).

1.3.4 Antiarrhythmia treatment strategies

Atrial fibrillation treatment strategies

Atrial fibrillation is managed through a combination of two strategies: anticoagulation medication to prevent stroke and controlling rate and/or rhythm. Tachycardia is controlled through pharmacological interventions, whilst rhythm is more challenging to control, with medications, catheter ablation and cardioversion all options. Antiarrhythmic drugs are spread across four classes based on their mechanism of action. Class I are sodium channel blockers (e.g. flecainide), Class II are β-blockers (e.g. propranolol), Class III are potassium channel blockers (e.g. amiodarone) and Class IV are calcium channel blockers (e.g. nifedipine). There are some additional miscellaneous drugs which do not fit into these four categories (e.g. cardiac glycosides, muscarinic antagonists etc.). Class III antiarrhythmics are interesting as they aim to prolong repolarisation, which, as discussed, can increase the risk of triggered activity. The arrhythmogenic potential of action potential duration prolongation is therefore context specific. In the setting of slowed conduction velocity/shortened refractory period, it may be beneficial to prolong repolarisation to increase the wavelength and reduce reentry vulnerability. Although all these drugs are available and target different aspects of the cardiac action potential they often lack efficacy, as annual arrhythmia recurrence is 40-70% (117). Significant side effects are also of concern with long-term use (118). Catheter ablation typically requires repeated procedures, with recurrence in 20-40% of patients

(118,119). There is a clear need for new alternative treatment strategies which are more targeted to limit poorly tolerated side effects.

Ventricular fibrillation treatment strategies

Ventricular fibrillation is only detected and diagnosed in an emergency requiring immediate cardiopulmonary resuscitation and defibrillation. If successful, then measures are typically put in place to minimise risk of recurrence. These include drug therapy (e.g. β-adrenoceptor blockers), cardioverter defibrillator implantation, surgical ablation of ectopic sources, stent implantation or coronary bypass surgery to improve cardiac blood flow (120).

1.3.5 Arrhythmia risk factors

Pertinent atrial fibrillation risk factors include genetic predispositions, hypertension, aging and obesity. Atrial fibrillation is prevalent in 4% of the general population (48), but 10% of the population over the age of 80 (121). For every unit increase in body mass index, there is a parallel 3-3.5% increase in atrial fibrillation risk (122). Most recently, an independent association between pericardial adipose tissue deposition and atrial fibrillation risk has been established. This link was first established through computed tomography scans in a small cohort of 273 individuals; 218 referred for atrial fibrillation ablation and a sinus rhythm control group (undergoing scans for evaluation of potential cardiac symptoms). Pericardial adipose tissue volume, estimated from these scans, was 34% greater in the atrial fibrillation group. Furthermore, the degree of atrial fibrillation progression also associated with pericardial adipose tissue volume, with persistent atrial fibrillation patients having great deposition than paroxysmal patients. Using a

multivariate model, correcting for various atrial fibrillation comorbidities/risk factors (e.g. age, sex, hypertension, diabetes etc.) revealed an independent association with pericardial adipose tissue volume and atrial fibrillation risk, with Odds ratios of 1.1 and 1.2 for paroxysmal and persistent atrial fibrillation, respectively (123).

Just a few months after the publication from Al Chekakie *et al*., a larger dataset from the Framingham Heart Study solidified this association as specific to pericardial adipose tissue deposition, not other adipose depots. In the study by Thanassoulis *et al*., 3217 individuals (mean age 51 years, 48% women, 54 with atrial fibrillation) underwent multi-detector computed tomography thoracic and abdominal scans between 2002-2005. Intrathoracic, pericardial and abdominal adipose tissue volumes were estimated from these scans. Using a multivariate analysis model adjusting for common atrial fibrillation risk factors (e.g. obesity, sex, systolic blood pressure, PR interval, heart failure etc.), revealed a specific association of pericardial adipose tissue volume and atrial fibrillation risk (Odds ratio, 1.28). This association was not present for other adipose tissue depots (5).

Pericardial adipose tissue comprises the three visceral adipose tissue depots surrounding the heart: epicardial (situated between the outer epicardium and the visceral layer of pericardium), paracardial (situated between the visceral and parietal pericardium) and intra-thoracic (124). Further studies have demonstrated left atrial-specific adiposity is linked with increased atrial fibrillation risk (123,125) and the underlying myocardial regions demonstrate electrical instability that may predispose to atrial fibrillation (126). Interestingly, Kusayama and colleagues have shown in a small cohort study that it is specifically pericardial, and not visceral, adipose tissue deposition

that links with atrial fibrillation risk (127). More recently, cardiac adiposity has been correlated with atrial fibrillation recurrence post-ablation therapy (6).

Pericardial adipose tissue accumulation has also been identified as a potential risk factor for ventricular fibrillation. The links between elevated pericardial adiposity and ventricular fibrillation are not as well solidified as with atrial fibrillation – likely a consequence of the sudden severe onset of ventricular fibrillation, compared with gradual development of symptoms in atrial fibrillation patients, permissible of clinical investigation. Epicardial adipose thickness is an independent risk factor for diastolic heart failure (3,128-131) – of which >30% of mortalities are a result of ventricular fibrillation/sudden cardiac death (132). In systolic heart failure patients, elevated pericardial adiposity associates with a 1.5-fold increase in ventricular tachycardia/fibrillation risk (7). Patients undergoing ventricular ablation surgery with an epicardial adipose thickness >15.5mm have greater arrhythmia recurrence (4).

1.4 Pericardial adiposity and arrhythmia vulnerability

1.4.1 Physiological role of pericardial adipose tissue

White adipose tissues are endocrine organs, possessing great secretory capacity to release various factors, including cytokines, growth factors, inflammatory mediators, and hormones (e.g. oestrogen) which modulate function of a wide variety of other tissues (133). Epicardial and paracardial adipose tissue are white adipose tissue depots arising from distinct embryonic origins (134,135). In adults, pericardial adipose tissue acts as a source for triglycerides and free fatty acid production/secretion utilised for

cardiac metabolism. This bypasses the need for high free fatty acid levels in the coronary circulation, preventing potentially toxic cardiomyocyte exposure (136-138).

Pericardial adiposity is equal between men and women when correcting for age and body mass index (139,140). Clinical and rodent experimental evidence indicates a significant rise in pericardial adipose tissue deposition with both aging and obesity in men and postmenopausal women – a timepoint where cardiac disease risk increases significantly (10,141,142).

1.4.2 Mechanisms linking pericardial adiposity and arrhythmia vulnerability

The exact mechanisms of how pericardial adiposity increases arrhythmia risk are largely unexplored. Adipose infiltration into the epicardial muscle layers and an adipose-mediated paracrine effect on the myocardium are two mechanisms likely involved. There is limited clinical and experimental evidence exploring these mechanisms, and available data primarily focuses on the association in the atria.

Pericardial adipose tissue infiltration into the epicardium

Adipose infiltration into the myocardium presents a physical conduction barrier, facilitating action potential reentry. Biopsies from atrial cardiomyopathy and atrial fibrillation patients indeed demonstrate fibro-fatty infiltrates, but there have been no studies directly associating this with conduction abnormalities (143-145). In post-infarct sheep hearts, adipose tissue infiltration at the border zone has been detected and the extent of infiltration correlates with vulnerability to ventricular tachycardia (146). *In*

silico models of the ventricular myocardium also indicate adipose infiltration results in augmented arrhythmia vulnerability (147).

The paracrine influence of pericardial adipose tissue on the myocardium

The paracrine effects of pericardial adipose tissue on the myocardium is likely complex, with potential capacity to promote structural and electrical remodelling. As an endocrine organ, pericardial adipose tissue has substantial secretory potential. The proximity between pericardial adipose tissue (especially epicardial adipose tissue) and the myocardium indicates that the concentration of locally released factors may be much higher than those delivered systemically. Interestingly, since pericardial adipose tissue is situated near the epicardial surface, augmentation of its effects locally may disrupt transmural differences in electrophysiology, facilitating arrhythmia vulnerability.

Lin *et al.,* (2012) demonstrate that epicardial adipocytes can modulate cardiomyocyte electrophysiology through a paracrine effect. Co-incubating rabbit left atrial cardiomyocytes with epicardial adipocytes resulted in a prolonged action potential duration and a depolarised diastolic potential (8). These changes were driven by larger $I_{Ca,L}$, late I_{Na}, and I_{to}, and reduced I_K. Co-culturing cardiomyocytes with adipocytes from a different visceral depot did not recapitulate all these effects, indicating the properties of epicardial adipose tissue are distinct. As discussed earlier, prolongation in action potential duration is proarrhythmic, predisposing to early afterdepolarisations. Indeed, under β-adrenoceptor stress, epicardial adipose tissue-incubated cardiomyocytes exhibited a greater incidence of triggered ectopic beats (8). The adipose secreted factors involved were not explored, nor were the subcellular signalling mechanisms. Others have implicated a role for Ca^{2+}/calmodulin-dependent protein kinase II. In

apolipoprotein E deficient mice, pericardial adipose tissue content correlated with action potential duration prolongation – an effect reversible by Ca^{2+}/calmodulin-dependent protein kinase II inhibition (148).

Atrial structural remodelling can be mediated through the release of pro-fibrotic adipokines, with various compounds (including activin A, TGF-β1, metalloproteinases and connective tissue growth factor) being detected with potential for promoting fibrosis (9,149-151). Secretome from human epicardial adipose tissue has been shown to directly stimulate fibrosis of rat atrial tissue in organo-culture conditions via activin A (9). Others have implicated pericardial adipose tissue as a mediator of ventricular fibrosis in high fat-fed pigs (152) and a driver for fibrotic infiltration post myocardial infarction in mice (153). Similar to adipose infiltration, regional fibrosis would elevate reentry risk, but whether this electrical remodelling occurs in this context has not yet been established.

There is also evidence of pro-inflammatory and pro-oxidative stress roles of pericardial adipose tissue. Release of TNF-α, monocyte chemoattractant protein-1, and interleukins 1 and 6 have been demonstrated (154). Inflammation is highly associated with arrhythmia pathologies (155). Pericardial adipose tissue has capability to synthesise and release reactive oxygen species. Altered redox balance, has been linked to atrial fibrillation, particularly in the context of obstructive sleep apnoea patients (156).

Recent evidence implicates reciprocal paracrine effects between the atrial epicardium and epicardial adipose tissue. The epicardium contains a resident population of progenitors which can undergo differentiation into adipocytes or fibroblasts when

stimulated by atrial natriuretic peptide or angiotensin II, respectively (145,157). Following acute cardiac injury, the epicardium can be "reactivated", meaning epicardial progenitors undergo differentiation, mediated by atrial release of atrial natriuretic peptide or elevated systemic angiotensin II (145). These data indicate a local self-sustaining source of adipose/fibrosis, that is exacerbated with cardiac disease, promoting the formation of an unstable substrate.

Visceral white adipose tissue depots are themselves major sites of oestrogen synthesis and secretion (158). Very recently, it has been reported that human and rodent pericardial adipose tissue expresses aromatase - the enzyme that converts androgens to oestrogens (10). This indicates a local capacity to synthesise oestrogens, which may exert important autocrine/paracrine actions on myocardial structure and function that contribute to arrhythmia risk. Clinical and experimental data indicate that sex steroids can modulate electrophysiology, although there are several inconsistencies between datasets. To understand how sex steroids modulate cardiac electrophysiology, an appreciation of sex differences in cardiovascular electrophysiology is first required.

1.5 Sex and sex steroid influence on myocardial function

1.5.1 Sex differences in cardiac electrophysiology

Clinical findings consistently indicate women have faster heart rates, longer rate-corrected Q-T intervals and steeper ventricular electrical restitution than men (159,160). On a cellular level, sex steroids are thought to mediate such differences through acute/genomic actions on their respective receptors expressed on both the ventricular and atrial myocardium (161). Myocardial sex steroid receptor expression is comparable between sexes; however, men have approximately 10-fold higher circulating androgens and 10-fold lower circulating oestrogens than pre-menopausal women – indicating sex steroid balance is an important factor mediating myocardial sex differences (162,163).

Pre-clinical investigations for cardiomyocyte electrophysiological sexual dimorphism are distinctly lacking in the atrium and ventricular data has failed to yield consensus (164). Female rabbit left ventricular cardiomyocytes display a longer action potential duration than males at long, non-physiological cycle lengths (2000ms). This difference is abolished when rate is increased through β-adrenoceptor stimulation (165). Female mouse ventricular cardiomyocytes display longer action potential durations than males, at long cycle lengths (250-1000ms), but whether this is apparent at physiological rates remains to be determined (166,167). Female and male dog epicardial and endocardial ventricular cardiomyocytes demonstrate similar action potential durations, but female midmyocardial cells display longer action potential durations than males (168). Oestrogens have been shown to shorten (169,170) prolong (170,171) or not affect (172) ventricular action potential duration - in part, this may be a result of a biphasic concentration dependent effect (170), but also inconsistencies between studies, with

varying treatment durations/concentrations, paced cycle lengths, and historically poor reporting on experimental preparation sex. Androgen effect on ventricular repolarisation has also been inconclusive (170,171,173,174).

There is considerably less literature assessing sex differences/sex steroid influence in the atrium. Wen-Chin *et al*., first demonstrated no sex difference in action potential duration between male and female isolated rabbit left atrial cardiomyocytes paced at long cycle lengths (175); however, pacing intact left atria at more physiological rates revealed a male action potential duration longer than female (176). There is no data available as to how oestrogens modulate atrial electrophysiology, and a single study demonstrating castration associates with left atrial conduction velocity slowing (177).

1.5.2 Sex differences in arrhythmia epidemiology and pathogenesis

The importance of sex differences in arrhythmia pathogenesis are increasingly recognised, although sex-specific treatment strategies are not yet implemented (178). The lifetime risk of sudden cardiac death is almost 4-fold greater in men than women, with the predominant underlying cause being a ventricular arrhythmia (179). Male risk is still greater when accounting for predisposing risk factors such as coronary artery disease (179). Women are at greatest risk of acquired long Q-T syndrome-induced arrhythmias (180).

Atrial fibrillation onset occurs earlier in men and even with age adjustment, the incidence is still higher than in women (181,182). The comorbidities associated with atrial fibrillation are also different between sexes. Men with atrial fibrillation typically have greater incidence of coronary heart disease, whilst women have higher

hypertension and heart failure with preserved ejection fraction prevalence (54). Atrial fibrillation symptom severity is greater in women than men (183,184). Some evidence indicates the primary source of ectopic activity differs between sexes. Men typically undergo catheter ablation of the pulmonary vein/posterior left atrium region, whereas women are more likely to undergo atrioventricular nodal ablation than men. This is likely a consequence of atrioventricular node reentry tachycardia incidence being two-fold greater in women than men (185,186). Use of rhythm control therapy is equal between sexes; however, women have a greater risk of serious adverse drug-induced events than men (187).

The incidence of atrial fibrillation increases drastically post-menopause (a timepoint where systemic oestrogen levels decline) from 0.1% to 9.1% (188). Incidence of arrhythmias is also greater during the luteal phase of the menstrual cycle – a time point of low systemic oestrogen (189). These data have led to the classical view that oestrogens are cardioprotective. Contrarily, the Women's Health Initiative trial demonstrated oestradiol hormone replacement therapy increased atrial fibrillation risk in (post)menopausal women, indicating that the role of sex steroids in mediating arrhythmia risk is complex, potentially involving changes in local oestrogen synthesis capacity with age (190). Acute 17 β-oestradiol has been shown to slow right atrial conduction (191). Experimentally, mouse hearts perfused with 17 β-oestradiol exhibit increased arrhythmia vulnerability (10).

1.5.3 Pericardial adipose tissue, aromatase, and arrhythmia vulnerability

Endogenously, oestrogens are synthesised from androgens via the catalytic actions of aromatase (192). Extragonadal aromatase expression has been identified in brain (193), bone (194), peripheral adipose (195,196), and human and rodent pericardial adipose tissue and myocardium (10,197). Cardiac aromatase expression increases significantly with aging and is greater in females than males throughout all life stages (10). It is not understood how greater potential oestrogenic influence in aged hearts affects cardiac signalling, or indeed whether it plays a role in cardiovascular pathology.

It may be that pericardial adipose tissue-derived oestrogens serve as paracrine mediators of cardiac arrhythmias. Indeed, in isolated Langendorff-perfused mouse hearts, the incidence and duration of atrial arrhythmias strongly correlated with both the amount of pericardial adipose tissue and total aromatase content of the pericardial adipose tissue (10).

The exact mechanisms linking pericardial adipose tissue accumulation, local oestrogenic production/actions and atrial arrhythmia vulnerability remain to be elucidated. With aging and obesity, adipose depots accumulate around the heart and with time these depots may regionally infiltrate into the heart (143-145). Regional infiltrates may provide areas of high oestrogenic capacity, which may be secreted to exert paracrine effects on the epicardium/sub-epicardium to modulate cardiac electrophysiology and predispose to atrial fibrillation – but this has not been explored.

1.6 Experimental approaches to map cardiac electrophysiology

As discussed, the key cellular mechanisms predisposing to arrhythmia are changes in action potential morphology and conduction. Historically, it was only possible to study these electrophysiological parameters at a low spatial resolution using sharp glass electrodes that pierce cells (e.g. patch clamp or microelectrode techniques) or single surface contact electrodes (e.g. the electrocardiogram or monophasic action potential recordings). Although these techniques provide valuable electrophysiological data, they do not allow detection and tracking of impulse propagation through a larger tissue/cell mass.

There are two experimental techniques – the microelectrode array and optical mapping – which can be used for mapping action potential propagation in a high spatial resolution manner, both with their relative merits and drawbacks.

1.6.1 Microelectrode array mapping

Substrate-integrated microelectrode arrays in their simplest form are devices embedded with multiple low-impedance electrodes arranged in a grid formation designed for non-invasive, synchronous, multifocal recordings across excitable tissues/cells. For cardiac applications, microelectrode arrays come in two primary forms. The first is devised to record from intact hearts (either Langendorff-perfused or *in vivo* preparations) and the second to record from isolated tissue (e.g. sectioned ventricle or isolated mouse atria) or cardiomyocyte cultures. Depending on the application and experimental needs, commercially available or custom-made microelectrode arrays come in a variety of layout configurations (32-120 electrodes), substrate surfaces (glass,

plastic, flexible polyimide foil); and electrode: dimensions (10-100µm), spacing (200µm-700µm) and composition (silver chloride, titanium nitride or gold or electrodes)(198-200).

Extracellular field potentials are what the literature denotes as the unipolar electrograms recorded by microelectrode arrays (201). Simultaneous recordings of field potentials at multiple sites allows impulse propagation can be tracked. A single field potential has various key parameters, including amplitude, duration, rise time etc… which correlate with intracellular action potential recordings (202-205). The major caveats of recording non-invasively are difficulty in maintaining sufficient contact with the recording electrodes and signal interpretation (201). Nevertheless, their commercial availability, relative user-friendly interfaces and high throughput capabilities make them attractive tools for mapping cardiac conduction (200).

Cardiomyocytes cultured on microelectrode arrays offer a high-throughput screening platform for compounds with anti-arrhythmic/cardiac electrophysiology-modifying potential, enabling the evaluation of conduction properties (206). Cardiomyocyte studies have traditionally relied on isolated neonatal rodent ventricular myocytes or a limited number of immortalised cell lines (207,208). Recently, human inducible pluripotent stem cell-derived cardiomyocytes (hiPSC-CMs) have become more widely utilised (209). Comparative benchmarking of the electrophysiological properties of these cells has not been extensively examined in a direct approach. Similarly, comparison of electrophysiological sex differences between cultured cardiomyocytes has not been examined, with neonatal rat ventricular cardiomyocytes typically sourced

from mixed male and female litters, without concern for potential sex-specific cardiac electrophysiological differences which are apparent in the adult myocardium.

1.6.2 Optical mapping

Optical mapping records intracellular "optical action potentials" (or calcium transients) from isolated cardiac tissue, whole hearts or cell monolayers using fluorescent potentiometric dyes. Spatiotemporal resolution is determined by camera sensitivity, not electrode density, hence is typically greater than that of microelectrode array technology (69,210,211). Interpretation of optical action potentials is simpler than field potentials and the issue of maintaining sturdy sample-electrode contact is absent.

Cardiac tissue is loaded with a voltage-sensitive potentiometric dye (e.g. Di-4-ANEPPS, Di-8-ANEPPS or RH237) which readily incorporates into plasma membranes. Changes in dye emission wavelength occur in response to changes in transmembrane voltage. This change in fluorescence emission can be optically detected and equated to cellular electrical activity using a rapid-sampling camera (typically either a charge-coupled device or a complementary metal-oxide semiconductor).

Optical mapping has some drawbacks, firstly excitation-contraction uncoupling (typically with blebbistatin and 2,3-Butanedione monoxime) is typically required to minimise motion artefacts (212). This is often not necessary with microelectrode arrays, where tissue/cells are held in position by weights or adherent extracellular matrix protein mixtures. Potentiometric dyes can also slow conduction velocity (213).

Despite the relative merits and caveats of microelectrode arrays and optical mapping, both high spatiotemporal resolution mapping methodologies prove useful tools to study cardiac conduction at a scale no other technique allows.

1.7 Summary: pericardial adipose tissue – a local driver of arrhythmia?

It is well established that with aging and obesity the risk of cardiac diseases, including arrhythmias, increases. However, it is largely underappreciated that this occurs at a time coinciding with increased cardiac adiposity. Over the past decade, pericardial adipose tissue accumulation has been consistently linked with arrhythmia risk, particularly in the context of the atrial fibrillation (3-7,123,125-132). Limited available experimental evidence indicates the causative impact of pericardial adipose tissue on the myocardium is multidimensional. Structural remodelling through adipose tissue infiltration and paracrine-mediated promotion of fibrosis are likely key factors. There is, however, no literature directly assessing how such structural remodelling in the presence of elevated pericardial adiposity modulates cardiac electrophysiology to predispose to arrhythmias. Current antiarrhythmic strategies aim to target the electrophysiological defects with limited success. These treatment options do not address the underlying causative factors, which are likely to involve local influences from pericardial adipose tissue in addition to systemic influences. Further exploration of the direct effects of pericardial adipose tissue on cardiomyocyte electrophysiology is warranted to identify novel efficacious therapeutic strategies.

1.8 Research aims

This body of work aimed to investigate the mechanisms linking pericardial adipose tissue accumulation and cardiac arrhythmia vulnerability.

Four experimental aims were derived from this, each constructed as an individual chapter presented as a manuscript:

1. Establish whether transmural electrophysiology is modulated in the context of elevated cardiac adiposity. (*3*)

2. Compare electrophysiology of cardiomyocyte cultures from different origins as prelude to examining the paracrine influences of pericardial adipose tissue. (*4*)

3. Ascertain whether obesity and epicardial adiposity associate with cardiac electrophysiological remodelling which may increase arrhythmia vulnerability. (*5*)

4. Examine whether sex steroids can modulate atrial electrophysiology, indicating their potential as paracrine regulators of arrhythmia vulnerability. (*6*)

1.9 References

1. Nerbonne JM, Kass RS. Molecular Physiology of Cardiac Repolarization. Physiol Rev 2005;85:1205-1253.

2. Grant AO. Cardiac Ion Channels. Circ Arrhythm Electrophysiol 2009;2:185-194.

3. Nerlekar N, Muthalaly RG, Wong N et al. Association of Volumetric Epicardial Adipose Tissue Quantification and Cardiac Structure and Function. J Am Heart Assoc 2018;7:e009975.

4. Sepehri Shamloo A, Schoene K, Stauber A et al. Epicardial adipose tissue thickness as an independent predictor of ventricular tachycardia recurrence following ablation. Heart Rhythm 2019;16:1492-1498.

5. Thanassoulis G, Massaro JM, O'Donnell CJ et al. Pericardial fat is associated with prevalent atrial fibrillation: the Framingham Heart Study. Circ Arrhythm Electrophysiol 2010;3:345-50.

6. Wong CX, Abed HS, Molaee P et al. Pericardial fat is associated with atrial fibrillation severity and ablation outcome. J Am Coll Cardiol 2011;57:1745-51.

7. Wu CK, Tsai HY, Su MY et al. Pericardial fat is associated with ventricular tachyarrhythmia and mortality in patients with systolic heart failure. Atherosclerosis 2015;241:607-14.

8. Lin YK, Chen YC, Chen JH, Chen SA, Chen YJ. Adipocytes modulate the electrophysiology of atrial myocytes: implications in obesity-induced atrial fibrillation. Basic research in cardiology 2012;107:293.

9. Venteclef N, Guglielmi V, Balse E et al. Human epicardial adipose tissue induces fibrosis of the atrial myocardium through the secretion of adipo-fibrokines. Eur Heart J 2015;36:795-805.

10. Bernasochi GB, Boon WC, Curl CL et al. Pericardial adipose and aromatase: A new translational target for aging, obesity and arrhythmogenesis? J Mol Cell Cardiol 2017;111:96-101.

11. Klabunde RE. Cardiovascular physiology concepts. 2nd ed.

12. Durrer D, Dam RTV, Freud GE, Janse MJ, Meijler FL, Arzbaecher RC. Total Excitation of the Isolated Human Heart. Circulation 1970;41:899-912.

13. Einthoven W. Uber die From des menschlichen Elektrokadiogramms. Pflugers Arch fd ges des Physiol 1895;60:101.

14. Pandit SV. Ionic Mechanisms of Atrial Action Potentials. In: Zipes DP, Jalife J, Stevenson WG, editors. Cardiac Electrophysiology: From Cell to Bedside (Seventh Edition). 7 ed: Elsevier, 2018:293-303.

15. Bányász T, Fülöp L, Magyar J, Szentandrássy N, Varró A, Nánási PP. Endocardial versus epicardial differences in L-type calcium current in canine ventricular myocytes studied by action potential voltage clamp. Cardiovasc Res 2003;58:66-75.

16. Boukens BJ, Sulkin MS, Gloschat CR, Ng FS, Vigmond EJ, Efimov IR. Transmural APD gradient synchronizes repolarization in the human left ventricular wall. Cardiovasc Res 2015;108:188-96.

17. Brunet S, Aimond F, Li H et al. Heterogeneous expression of repolarizing, voltage-gated K+ currents in adult mouse ventricles. J Physiol 2004;559:103-120.

18. Glukhov AV, Fedorov VV, Lou Q et al. Transmural dispersion of repolarization in failing and nonfailing human ventricle. Circ Res 2010;106:981-991.

19. Sicouri S, Antzelevitch C. A subpopulation of cells with unique electrophysiological properties in the deep subepicardium of the canine ventricle. The M cell. Circ Res 1991;68:1729-41.

20. Volk T, Nguyen TH, Schultz JH, Ehmke H. Relationship between transient outward K+ current and Ca2+ influx in rat cardiac myocytes of endo- and epicardial origin. J Physiol 1999;519 Pt 3:841-850.

21. Wen Q, Gandhi K, Capel RA et al. Transverse cardiac slicing and optical imaging for analysis of transmural gradients in membrane potential and Ca(2+) transients in murine heart. J Physiol 2018;596:3951-3965.

22. Antzelevitch C. Transmural dispersion of repolarization and the T wave. Cardiovasc Res 2001;50:426-431.

23. Yan GX, Antzelevitch C. Cellular basis for the normal T wave and the electrocardiographic manifestations of the long-QT syndrome. Circulation 1998;98:1928-36.

24. Lubinski A, Lewicka-Nowak E, Kempa M, Baczynska AM, Romanowska I, Swiatecka G. New insight into repolarization abnormalities in patients with congenital long QT syndrome: the increased transmural dispersion of repolarization. Pacing and clinical electrophysiology : PACE 1998;21:172-5.

25. Malik M, Huikuri HV, Lombardi F, Schmidt G, Verrier RL, Zabel M. Is the T(peak)-T(end) interval as a measure of repolarization heterogeneity dead or just seriously wounded? Heart Rhythm 2019;16:952-953.

26. Bryant SM, Wan X, Shipsey SJ, Hart G. Regional differences in the delayed rectifier current (IKr and IKs) contribute to the differences in action potential

duration in basal left ventricular myocytes in guinea-pig. Cardiovasc Res 1998;40:322-31.

27. Shipsey SJ, Bryant SM, Hart G. Effects of hypertrophy on regional action potential characteristics in the rat left ventricle: a cellular basis for T-wave inversion? Circulation 1997;96:2061-8.

28. Rodríguez-Sinovas A, Cinca J, Tapias A, Armadans L, Tresànchez M, Soler-Soler J. Lack of evidence of M-cells in porcine left ventricular myocardium. Cardiovasc Res 1997;33:307-13.

29. Opthof T, Coronel R, Janse MJ. Is there a significant transmural gradient in repolarization time in the intact heart?: Repolarization Gradients in the Intact Heart. Circ Arrhythm Electrophysiol 2009;2:89-96.

30. Opthof T, Coronel R, Wilms-Schopman FJ et al. Dispersion of repolarization in canine ventricle and the electrocardiographic T wave: Tp-e interval does not reflect transmural dispersion. Heart Rhythm 2007;4:341-8.

31. Boukens BJ, Rivaud MR, Rentschler S, Coronel R. Misinterpretation of the mouse ECG: 'musing the waves of Mus musculus'. J Physiol 2014;592:4613-4626.

32. Stratton JR, Levy WC, Cerqueira MD, Schwartz RS, Abrass IB. Cardiovascular responses to exercise. Effects of aging and exercise training in healthy men. Circulation 1994;89:1648-55.

33. Milani-Nejad N, Janssen PM. Small and large animal models in cardiac contraction research: advantages and disadvantages. Pharmacol Ther 2014;141:235-49.

34. Lujan HL, Janbaih H, Feng HZ, Jin JP, DiCarlo SE. Ventricular function during exercise in mice and rats. Am J Physiol Regul Integr Comp Physiol 2012;302:R68-74.

35. Fewell JG, Osinska H, Klevitsky R et al. A treadmill exercise regimen for identifying cardiovascular phenotypes in transgenic mice. Am J Physiol 1997;273:H1595-605.

36. Desai KH, Sato R, Schauble E, Barsh GS, Kobilka BK, Bernstein D. Cardiovascular indexes in the mouse at rest and with exercise: new tools to study models of cardiac disease. Am J Physiol 1997;272:H1053-61.

37. Rossman EI, Petre RE, Chaudhary KW et al. Abnormal frequency-dependent responses represent the pathophysiologic signature of contractile failure in human myocardium. J Mol Cell Cardiol 2004;36:33-42.

38. Pieske B, Sütterlin M, Schmidt-Schweda S et al. Diminished post-rest potentiation of contractile force in human dilated cardiomyopathy. Functional

evidence for alterations in intracellular Ca2+ handling. J Clin Invest 1996;98:764-76.

39. Chaudhary KW, Rossman EI, Piacentino V, 3rd et al. Altered myocardial Ca2+ cycling after left ventricular assist device support in the failing human heart. J Am Coll Cardiol 2004;44:837-45.

40. Monasky MM, Varian KD, Janssen PM. Gender comparison of contractile performance and beta-adrenergic response in isolated rat cardiac trabeculae. J Comp Physiol B 2008;178:307-13.

41. Stull LB, Hiranandani N, Kelley MA, Leppo MK, Marbán E, Janssen PM. Murine strain differences in contractile function are temperature- and frequency-dependent. Pflugers Arch 2006;452:140-5.

42. Carmeliet E. Action Potential Duration, Rate of Stimulation, and Intracellular Sodium. J Cardiovasc Electrophys 2006;17:S2-S7.

43. Shattock MJ, Bers DM. Rat vs. rabbit ventricle: Ca flux and intracellular Na assessed by ion-selective microelectrodes. Am J Physiol 1989;256:C813-22.

44. Carmeliet E. Intracellular Ca2+ concentration and rate adaptation of the cardiac action potential. Cell Calcium 2004;35:557-573.

45. Stengl M, Ramakers C, Donker DW et al. Temporal patterns of electrical remodeling in canine ventricular hypertrophy: focus on IKs downregulation and blunted beta-adrenergic activation. Cardiovasc Res 2006;72:90-100.

46. Terrenoire C, Clancy CE, Cormier JW, Sampson KJ, Kass RS. Autonomic control of cardiac action potentials: role of potassium channel kinetics in response to sympathetic stimulation. Circ Res 2005;96:e25-34.

47. Knollmann BC, Schober T, Petersen AO, Sirenko SG, Franz MR. Action potential characterization in intact mouse heart: steady-state cycle length dependence and electrical restitution. American Journal of Physiology-Heart and Circulatory Physiology 2007;292:H614-H621.

48. Chugh SS, Havmoeller R, Narayanan K et al. Worldwide epidemiology of atrial fibrillation: a Global Burden of Disease 2010 Study. Circulation 2014;129:837-47.

49. Wong CX, Brooks AG, Leong DP, Roberts-Thomson KC, Sanders P. The Increasing Burden of Atrial Fibrillation Compared With Heart Failure and Myocardial Infarction: A 15-Year Study of All Hospitalizations in Australia. Arch Intern Med 2012;172:739-741.

50. Chen LY, Sotoodehnia N, Buzkova P et al. Atrial fibrillation and the risk of sudden cardiac death: the atherosclerosis risk in communities study and cardiovascular health study. JAMA Intern Med 2013;173:29-35.

51. Miyasaka Y, Barnes ME, Gersh BJ et al. Secular Trends in Incidence of Atrial Fibrillation in Olmsted County, Minnesota, 1980 to 2000, and Implications on the Projections for Future Prevalence. Circulation 2006;114:119-125.

52. Patel NJ, Deshmukh A, Pant S et al. Contemporary Trends of Hospitalization for Atrial Fibrillation in the United States, 2000 Through 2010. Circulation 2014;129:2371-2379.

53. Lloyd-Jones DM, Wang TJ, Leip EP et al. Lifetime Risk for Development of Atrial Fibrillation. Circulation 2004;110:1042-1046.

54. Schnabel RB, Yin X, Gona P et al. 50 year trends in atrial fibrillation prevalence, incidence, risk factors, and mortality in the Framingham Heart Study: a cohort study. Lancet 2015;386:154-62.

55. Gillum RF. Geographic variation in sudden coronary death. Am Heart J 1990;119:380-389.

56. Hayashi M, Shimizu W, Albert CM. The Spectrum of Epidemiology Underlying Sudden Cardiac Death. Circ Res 2015;116:1887-1906.

57. Myerburg R, Castellanos A. Cardiac electrophysiology: from cell to bedside, vol. 1. Philadelphia: Saunders Elsevier, 2009.

58. Deo R, Albert CM. Epidemiology and genetics of sudden cardiac death. Circulation 2012;125:620-637.

59. Bougouin W, Marijon E, Puymirat E et al. Incidence of sudden cardiac death after ventricular fibrillation complicating acute myocardial infarction: a 5-year cause-of-death analysis of the FAST-MI 2005 registry. Eur Heart J 2014;35:116-22.

60. Henriques JP, Gheeraert PJ, Ottervanger JP et al. Ventricular fibrillation in acute myocardial infarction before and during primary PCI. Int J Cardiol 2005;105:262-6.

61. Mehta RH, Harjai KJ, Grines L et al. Sustained ventricular tachycardia or fibrillation in the cardiac catheterization laboratory among patients receiving primary percutaneous coronary intervention: incidence, predictors, and outcomes. J Am Coll Cardiol 2004;43:1765-72.

62. Jabbari R, Engstrøm T, Glinge C et al. Incidence and risk factors of ventricular fibrillation before primary angioplasty in patients with first ST-elevation myocardial infarction: a nationwide study in Denmark. J Am Heart Assoc 2015;4:e001399-e001399.

63. Mehta RH, Starr AZ, Lopes RD et al. Incidence of and outcomes associated with ventricular tachycardia or fibrillation in patients undergoing primary percutaneous coronary intervention. Jama 2009;301:1779-89.

64. Eisenberg MS, Copass MK, Hallstrom AP et al. Treatment of Out-of-Hospital Cardiac Arrests with Rapid Defibrillation by Emergency Medical Technicians. New Engl J Med 1980;302:1379-1383.

65. Liberthson RR, Nagel EL, Hirschman JC, Nussenfeld SR, Blackbourne BD, Davis JH. Pathophysiologic Observations in Prehospital Ventricular Fibrillation and Sudden Cardiac Death. Circulation 1974;49:790-798.

66. Bayés de Luna A, Coumel P, Leclercq JF. Ambulatory sudden cardiac death: mechanisms of production of fatal arrhythmia on the basis of data from 157 cases. Am Heart J 1989;117:151-9.

67. Gang UJO, Jøns C, Jørgensen RM et al. Heart rhythm at the time of death documented by an implantable loop recorder. EP Europace 2009;12:254-260.

68. Sanders P, Berenfeld O, Hocini M et al. Spectral analysis identifies sites of high-frequency activity maintaining atrial fibrillation in humans. Circulation 2005;112:789-97.

69. Holmes AP, Yu TY, Tull S et al. A Regional Reduction in Ito and IKACh in the Murine Posterior Left Atrial Myocardium Is Associated with Action Potential Prolongation and Increased Ectopic Activity. PLOS ONE 2016;11:e0154077.

70. Ridler M-E, Lee M, McQueen D, Peskin C, Vigmond E. Arrhythmogenic Consequences of Action Potential Duration Gradients in the Atria. Can J Cardiol 2011;27:112-119.

71. Jalife J, Berenfeld O, Mansour M. Mother rotors and fibrillatory conduction: a mechanism of atrial fibrillation. Cardiovasc Res 2002;54:204-16.

72. Stevenson WG. Catheter ablation of monomorphic ventricular tachycardia. Curr Opin Cardiol 2005;20:42-7.

73. Heijman J, Guichard J-B, Dobrev D, Nattel S. Translational Challenges in Atrial Fibrillation. Circ Res 2018;122:752-773.

74. Gaztañaga L, Marchlinski FE, Betensky BP. Mechanisms of cardiac arrhythmias. Rev Esp Cardiol 2012;65:174-85.

75. Maruyama M, Lin SF, Xie Y et al. Genesis of phase 3 early afterdepolarizations and triggered activity in acquired long-QT syndrome. Circ Arrhythm Electrophysiol 2011;4:103-11.

76. Yamada M, Ohta K, Niwa A, Tsujino N, Nakada T, Hirose M. Contribution of L-type Ca2+ channels to early afterdepolarizations induced by I Kr and I Ks channel suppression in guinea pig ventricular myocytes. J Membr Biol 2008;222:151-66.

77. Andrade J, Khairy P, Dobrev D, Nattel S. The clinical profile and pathophysiology of atrial fibrillation: relationships among clinical features, epidemiology, and mechanisms. Circ Res 2014;114:1453-68.

78. Clusin WT. Calcium and cardiac arrhythmias: DADs, EADs, and alternans. Crit Rev Clin Lab Sci 2003;40:337-75.

79. Undrovinas AI, Fleidervish IA, Makielski JC. Inward sodium current at resting potentials in single cardiac myocytes induced by the ischemic metabolite lysophosphatidylcholine. Circ Res 1992;71:1231-41.

80. Hussein AA, Ozaki A, Martin DO et al. Spontaneous dissociated firing from the pulmonary veins during ablation of paroxysmal atrial fibrillation: implications and impact on arrhythmia-free survival. Pacing and clinical electrophysiology : PACE 2013;36:988-93.

81. Patterson E, Jackman WM, Beckman KJ et al. Spontaneous pulmonary vein firing in man: relationship to tachycardia-pause early afterdepolarizations and triggered arrhythmia in canine pulmonary veins in vitro. J Cardiovasc Electrophysiol 2007;18:1067-75.

82. Chen Y-J, Chen S-A, Chen Y-C et al. Effects of Rapid Atrial Pacing on the Arrhythmogenic Activity of Single Cardiomyocytes From Pulmonary Veins. Circulation 2001;104:2849-2854.

83. Chen SA, Hsieh MH, Tai CT et al. Initiation of atrial fibrillation by ectopic beats originating from the pulmonary veins: electrophysiological characteristics, pharmacological responses, and effects of radiofrequency ablation. Circulation 1999;100:1879-86.

84. Haïssaguerre M, Jaïs P, Shah DC et al. Spontaneous initiation of atrial fibrillation by ectopic beats originating in the pulmonary veins. The New England journal of medicine 1998;339:659-66.

85. Vincenti A, Brambilla R, Fumagalli MG, Merola R, Pedretti S. Onset mechanism of paroxysmal atrial fibrillation detected by ambulatory Holter monitoring. Europace 2006;8:204-10.

86. Huikuri HV, Castellanos A, Myerburg RJ. Sudden death due to cardiac arrhythmias. New Engl J Med 2001;345:1473-82.

87. Deedwania P. Global risk assessment in the presymptomatic patient. Am J Cardiol 2001;88:17j-22j.

88. Jalife J. Ventricular fibrillation: mechanisms of initiation and maintenance. Annu Rev Physiol 2000;62:25-50.

89. Harrigan RA, Garg M. An interesting cause of wide complex tachycardia: Ashman's phenomenon in atrial fibrillation. J Emerg Med 2013;45:835-41.

90. Mines GR. On circulating excitations in heart muscles and their possible relation to tachycardia and fibrillation. Transactions of the Royal Society of Canada 4 section 1914;1914:43-52.

91. Antzelevitch C, Burashnikov A. Overview of Basic Mechanisms of Cardiac Arrhythmia. Cardiac electrophysiology clinics 2011;3:23-45.

92. Wang J, Liu L, Feng J, Nattel S. Regional and functional factors determining induction and maintenance of atrial fibrillation in dogs. Am J Physiol 1996;271:H148-58.

93. Moe GK, Rheinboldt WC, Abildskov JA. A computer model of atrial fibrillation. Am Heart J 1964;67:200-20.

94. Feng J, Yue L, Wang Z, Nattel S. Ionic Mechanisms of Regional Action Potential Heterogeneity in the Canine Right Atrium. Circ Res 1998;83:541-551.

95. Mandapati R, Skanes A, Chen J, Berenfeld O, Jalife J. Stable Microreentrant Sources as a Mechanism of Atrial Fibrillation in the Isolated Sheep Heart. Circulation 2000;101:194-199.

96. King JH, Huang CL, Fraser JA. Determinants of myocardial conduction velocity: implications for arrhythmogenesis. Front Physiol 2013;4:154.

97. Zou R, Kneller J, Leon LJ, Nattel S. Substrate size as a determinant of fibrillatory activity maintenance in a mathematical model of canine atrium. Am J Physiol Heart Circ Physiol 2005;289:H1002-12.

98. Smeets JL, Allessie MA, Lammers WJ, Bonke FI, Hollen J. The wavelength of the cardiac impulse and reentrant arrhythmias in isolated rabbit atrium. The role of heart rate, autonomic transmitters, temperature, and potassium. Circ Res 1986;58:96-108.

99. Wiener N, Rosenblueth A. The mathematical formulation of the problem of conduction of impulses in a network of connected excitable elements, specifically in cardiac muscle. Archivos del Instituto de Cardiologia de Mexico 1946;16:205-65.

100. Kanki H, Mitamura H, Takatsuki S et al. Postrepolarization refractoriness as a potential anti-atrial fibrillation mechanism of pilsicainide, a pure sodium channel blocker with slow recovery kinetics. Cardiovascular drugs and therapy 1998;12:475-82.

101. Wang Z, Pagé P, Nattel S. Mechanism of flecainide's antiarrhythmic action in experimental atrial fibrillation. Circ Res 1992;71:271-87.

102. Lo CW. Role of Gap Junctions in Cardiac Conduction and Development. Circ Res 2000;87:346-348.

103. Huang CL. Murine Electrophysiological Models of Cardiac Arrhythmogenesis. Physiol Rev 2017;97:283-409.

104. Westenbroek RE, Bischoff S, Fu Y, Maier SK, Catterall WA, Scheuer T. Localization of sodium channel subtypes in mouse ventricular myocytes using quantitative immunocytochemistry. J Mol Cell Cardiol 2013;64:69-78.

105. Nair K, Umapathy K, Farid T et al. Intramural Activation During Early Human Ventricular Fibrillation. Circ Arrhythm Electrophysiol 2011;4:692-703.

106. Valderrábano M, Lee M-H, Ohara T et al. Dynamics of Intramural and Transmural Reentry During Ventricular Fibrillation in Isolated Swine Ventricles. Circ Res 2001;88:839-848.

107. Zaitsev AV, Berenfeld O, Mironov SF, Jalife J, Pertsov AM. Distribution of Excitation Frequencies on the Epicardial and Endocardial Surfaces of Fibrillating Ventricular Wall of the Sheep Heart. Circ Res 2000;86:408-417.

108. Maury P, Sacher F, Gourraud JB et al. Increased Tpeak-Tend interval is highly and independently related to arrhythmic events in Brugada syndrome. Heart Rhythm 2015;12:2469-76.

109. Panikkath R, Reinier K, Uy-Evanado A et al. Prolonged Tpeak-to-Tend Interval on the Resting ECG Is Associated With Increased Risk of Sudden Cardiac Death. Circ Arrhythm Electrophysiol 2011;4:441-447.

110. Das MK, Saha C, El Masry H et al. Fragmented QRS on a 12-lead ECG: a predictor of mortality and cardiac events in patients with coronary artery disease. Heart Rhythm 2007;4:1385-92.

111. Narayanan K, Zhang L, Kim C et al. QRS Fragmentation and Sudden Cardiac Death in the Obese and Overweight. J Am Heart Assoc 2015;4:e001654.

112. Hsueh CH, Chang PC, Hsieh YC, Reher T, Chen PS, Lin SF. Proarrhythmic effect of blocking the small conductance calcium activated potassium channel in isolated canine left atrium. Heart Rhythm 2013;10:891-8.

113. Avula UMR, Abrams J, Katchman A et al. Heterogeneity of the action potential duration is required for sustained atrial fibrillation. JCI Insight 2019;5.

114. Kanaporis G, Blatter LA. Alternans in atria: Mechanisms and clinical relevance. Medicina (Kaunas) 2017;53:139-149.

115. Shattock MJ, Park KC, Yang H-Y et al. Restitution slope is principally determined by steady-state action potential duration. Cardiovasc Res 2017;113:817-828.

116. Franz MR. The electrical restitution curve revisited: steep or flat slope--which is better? J Cardiovasc Electrophysiol 2003;14:S140-7.

117. Valembois L, Audureau E, Takeda A, Jarzebowski W, Belmin J, Lafuente-Lafuente C. Antiarrhythmics for maintaining sinus rhythm after cardioversion of atrial fibrillation. Cochrane Database Syst Rev 2019.

118. Capucci A, Cipolletta L, Guerra F, Giannini I. Emerging pharmacotherapies for the treatment of atrial fibrillation. Expert Opin Emerg Drugs 2018;23:25-36.

119. Kirchhof P, Calkins H. Catheter ablation in patients with persistent atrial fibrillation. Eur Heart J 2017;38:20-26.

120. Al-Khatib SM, Stevenson WG, Ackerman MJ et al. 2017 AHA/ACC/HRS Guideline for Management of Patients With Ventricular Arrhythmias and the Prevention of Sudden Cardiac Death. Circulation 2018;138:e272-e391.

121. Marijon E, Le Heuzey J-Y, Connolly S et al. Causes of Death and Influencing Factors in Patients With Atrial Fibrillation: A Competing-Risk Analysis From the Randomized Evaluation of Long-Term Anticoagulant Therapy Study. Circulation 2013;128:2192-2201.

122. Wang TJ, Parise H, Levy D et al. Obesity and the risk of new-onset atrial fibrillation. Jama 2004;292:2471-7.

123. Al Chekakie MO, Welles CC, Metoyer R et al. Pericardial fat is independently associated with human atrial fibrillation. J Am Coll Cardiol 2010;56:784-8.

124. Alexopoulos N, Katritsis D, Raggi P. Visceral adipose tissue as a source of inflammation and promoter of atherosclerosis. Atherosclerosis 2014;233:104-12.

125. Batal O, Schoenhagen P, Shao M et al. Left atrial epicardial adiposity and atrial fibrillation. Circ Arrhythm Electrophysiol 2010;3:230-6.

126. Nakatani Y, Kumagai K, Minami K, Nakano M, Inoue H, Oshima S. Location of epicardial adipose tissue affects the efficacy of a combined dominant frequency and complex fractionated atrial electrogram ablation of atrial fibrillation. Heart Rhythm 2015;12:257-65.

127. Kusayama T, Furusho H, Kashiwagi H et al. Inflammation of left atrial epicardial adipose tissue is associated with paroxysmal atrial fibrillation. J Cardiol 2016;68:406-411.

128. Vural M, Talu A, Sahin D et al. Evaluation of the relationship between epicardial fat volume and left ventricular diastolic dysfunction. Jap J Radiol 2014;32:331-339.

129. Konishi M, Sugiyama S, Sugamura K et al. Accumulation of pericardial fat correlates with left ventricular diastolic dysfunction in patients with normal ejection fraction. J Cardiol 2012;59:344-51.

130. Fontes-Carvalho R, Fontes-Oliveira M, Sampaio F et al. Influence of epicardial and visceral fat on left ventricular diastolic and systolic functions in patients after myocardial infarction. Am J Cardiol 2014;114:1663-9.

131. Lai Y-H, Hou CJ-Y, Yun C-H et al. The association among MDCT-derived three-dimensional visceral adiposities on cardiac diastology and dyssynchrony in asymptomatic population. BMC Cardiovascular Disorders 2015;15:142.

132. Lee DS, Gona P, Albano I et al. A systematic assessment of causes of death after heart failure onset in the community: impact of age at death, time period, and left ventricular systolic dysfunction. Circ Heart Fail 2011;4:36-43.

133. Coelho M, Oliveira T, Fernandes R. Biochemistry of adipose tissue: an endocrine organ. Arch Med Sci 2013;9:191-200.

134. Iacobellis G. Epicardial and pericardial fat: close, but very different. Obesity (Silver Spring) 2009;17:625; author reply 626-7.

135. Ojha S, Robinson L, Yazdani M, Symonds ME, Budge H. Brown adipose tissue genes in pericardial adipose tissue of newborn sheep are downregulated by maternal nutrient restriction in late gestation. Pediatric Research 2013;74:246-251.

136. Sacks HS, Fain JN. Human epicardial adipose tissue: a review. Am Heart J 2007;153:907-17.

137. Marchington JM, Pond CM. Site-specific properties of pericardial and epicardial adipose tissue: the effects of insulin and high-fat feeding on lipogenesis and the incorporation of fatty acids in vitro. Int J Obes 1990;14:1013-22.

138. Marchington JM, Mattacks CA, Pond CM. Adipose tissue in the mammalian heart and pericardium: structure, foetal development and biochemical properties. Comp Biochem Physiol B 1989;94:225-32.

139. Mancio J, Pinheiro M, Ferreira W et al. Gender differences in the association of epicardial adipose tissue and coronary artery calcification: EPICHEART study: EAT and coronary calcification by gender. Int J Cardiol 2017;249:419-425.

140. Kim JS, Shin SY, Kang JH et al. Influence of Sex on the Association Between Epicardial Adipose Tissue and Left Atrial Transport Function in Patients With Atrial Fibrillation: A Multislice Computed Tomography Study. J Am Heart Assoc 2017;6.

141. Silaghi A, Piercecchi-Marti MD, Grino M et al. Epicardial adipose tissue extent: relationship with age, body fat distribution, and coronaropathy. Obesity (Silver Spring) 2008;16:2424-30.

142. Talman AH, Psaltis PJ, Cameron JD, Meredith IT, Seneviratne SK, Wong DT. Epicardial adipose tissue: far more than a fat depot. Cardiovasc Diagn Ther 2014;4:416-29.

143. Wong CX, Mahajan R, Pathak R, D JT, Sanders P. The Role of Pericardial and Epicardial Fat in Atrial Fibrillation Pathophysiology and Ablation Outcomes. J Atr Fibrillation 2013;5:790.

144. Haemers P, Hamdi H, Guedj K et al. Atrial fibrillation is associated with the fibrotic remodelling of adipose tissue in the subepicardium of human and sheep atria. Eur Heart J 2015;38:53-61.

145. Suffee N, Moore-Morris T, Jagla B et al. Reactivation of the Epicardium at the Origin of Myocardial Fibro-Fatty Infiltration During the Atrial Cardiomyopathy. Circ Res 2020;126:1330-1342.

146. Pouliopoulos J, Chik WWB, Kanthan A et al. Intramyocardial Adiposity After Myocardial Infarction. Circulation 2013;128:2296-2308.

147. De Coster T, Claus P, Kazbanov IV et al. Arrhythmogenicity of fibro-fatty infiltrations. Sci Rep 2018;8:2050.

148. Zhong P, Quan D, Huang Y, Huang H. CaMKII Activation Promotes Cardiac Electrical Remodeling and Increases the Susceptibility to Arrhythmia Induction in High-fat Diet-Fed Mice With Hyperlipidemia Conditions. Journal of cardiovascular pharmacology 2017;70:245-254.

149. Miksztowicz V, Morales C, Barchuk M et al. Metalloproteinase 2 and 9 Activity Increase in Epicardial Adipose Tissue of Patients with Coronary Artery Disease. Curr Vasc Pharmacol 2017;15:135-143.

150. Zeller J, Kruger C, Lamounier-Zepter V et al. The adipo-fibrokine activin A is associated with metabolic abnormalities and left ventricular diastolic dysfunction in obese patients. ESC Heart Fail 2019;6:362-370.

151. Wang Q, Xi W, Yin L et al. Human Epicardial Adipose Tissue cTGF Expression is an Independent Risk Factor for Atrial Fibrillation and Highly Associated with Atrial Fibrosis. Sci Rep 2018;8:3585.

152. Li SJ, Wu TW, Chien MJ, Mersmann HJ, Chen CY. Involvement of pericardial adipose tissue in cardiac fibrosis of dietary-induced obese minipigs- Role of mitochondrial function. Biochimica et biophysica acta Molecular and cell biology of lipids 2019;1864:957-965.

153. Horckmans M, Bianchini M, Santovito D et al. Pericardial Adipose Tissue Regulates Granulopoiesis, Fibrosis, and Cardiac Function After Myocardial Infarction. Circulation 2018;137:948-960.

154. Mazurek T, Zhang L, Zalewski A et al. Human epicardial adipose tissue is a source of inflammatory mediators. Circulation 2003;108:2460-6.

155. Vonderlin N, Siebermair J, Kaya E, Köhler M, Rassaf T, Wakili R. Critical inflammatory mechanisms underlying arrhythmias. Herz 2019;44:121-129.

156. Chadda KR, Fazmin IT, Ahmad S et al. Arrhythmogenic mechanisms of obstructive sleep apnea in heart failure patients. Sleep 2018;41.

157. Suffee N, Moore-Morris T, Farahmand P et al. Atrial natriuretic peptide regulates adipose tissue accumulation in adult atria. Proc Natl Acad Sci USA 2017;114:E771-E780.

158. Bernasochi GB, Bell JR, Simpson ER, Delbridge LMD, Boon WC. Impact of Estrogens on the Regulation of White, Beige, and Brown Adipose Tissue Depots. Comp Physiol 2019.

159. Rautaharju PM, Zhou SH, Wong S et al. Sex differences in the evolution of the electrocardiographic QT interval with age. Can J Cardiol 1992;8:690-5.

160. Malik M, Hnatkova K, Kowalski D, Keirns JJ, van Gelderen EM. QT/RR curvatures in healthy subjects: sex differences and covariates. Am J Physiol Heart Circ Physiol 2013;305:H1798-806.

161. Menazza S, Murphy E. The Expanding Complexity of Estrogen Receptor Signaling in the Cardiovascular System. Circ Res 2016;118:994-1007.

162. Carmina E, Lobo RA. Evaluation of Hormonal Status. In: Strauss JF, Barbieri RL, editors. Yen & Jaffe's Reproductive Endocrinology (Sixth Edition). Philadelphia: W.B. Saunders, 2009:801-823.

163. Lizotte E, Grandy SA, Tremblay A, Allen BG, Fiset C. Expression, distribution and regulation of sex steroid hormone receptors in mouse heart. Cell Physiol Biochem 2009;23:75-86.

164. Linde C, Bongiorni MG, Birgersdotter-Green U et al. Sex differences in cardiac arrhythmia: a consensus document of the European Heart Rhythm Association, endorsed by the Heart Rhythm Society and Asia Pacific Heart Rhythm Society. EP Europace 2018;20:1565-1565ao.

165. Zhu Y, Ai X, Oster RA, Bers DM, Pogwizd SM. Sex differences in repolarization and slow delayed rectifier potassium current and their regulation by sympathetic stimulation in rabbits. Pflugers Archives 2013;465:805-18.

166. Trépanier-Boulay V, St-Michel C, Tremblay A, Fiset C. Gender-based differences in cardiac repolarization in mouse ventricle. Circ Res 2001;89:437-44.

167. Wu Y, Anderson ME. Reduced repolarization reserve in ventricular myocytes from female mice. Cardiovasc Res 2002;53:763-769.

168. Xiao L, Zhang L, Han W, Wang Z, Nattel S. Sex-based transmural differences in cardiac repolarization and ionic-current properties in canine left ventricles. Am J Physiol Heart Circ Physiol 2006;291:H570-H580.

169. Jiang C, Poole-Wilson PA, Sarrel PM, Mochizuki S, Collins P, MacLeod KT. Effect of 17 beta-oestradiol on contraction, Ca2+ current and intracellular free Ca2+ in guinea-pig isolated cardiac myocytes. Br J Pharmacol 1992;106:739-745.

170. Kurokawa J, Tamagawa M, Harada N et al. Acute effects of oestrogen on the guinea pig and human IKr channels and drug-induced prolongation of cardiac repolarization. J Physiol 2008;586:2961-2973.

171. Zhang Y, Hao YC, Song LL, Guo SM, Gu SZ, Lu SG. Effects of sex hormones on action potential and contraction of guinea pig papillary muscle. Zhongguo Yao Li Xue Bao 1998;19:248-50.

172. Moller RA, Datta S, Strichartz GR. Beta-estradiol acutely potentiates the depression of cardiac excitability by lidocaine and bupivacaine. Journal of cardiovascular pharmacology 1999;34:718-27.

173. Ayaz O, Howlett SE. Testosterone modulates cardiac contraction and calcium homeostasis: cellular and molecular mechanisms. Biol Sex Differ 2015;6:9-9.

174. Liu X-K, Katchman A, Whitfield BH et al. In vivo androgen treatment shortens the QT interval and increases the densities of inward and delayed rectifier potassium currents in orchiectomized male rabbits. Cardiovasc Res 2003;57:28-36.

175. Tsai W-C, Chen Y-C, Lin Y-K, Chen S-A, Chen Y-J. Sex Differences in the Electrophysiological Characteristics of Pulmonary Veins and Left Atrium and Their Clinical Implication in Atrial Fibrillation. Circ Arrhythm Electrophysiol 2011;4:550-559.

176. Tsai W-C, Chen Y-C, Kao Y-H, Lu Y-Y, Chen S-A, Chen Y-J. Distinctive sodium and calcium regulation associated with sex differences in atrial electrophysiology of rabbits. Int J Cardiol 2013;168:4658-4666.

177. Sun YL, Li PH, Shi L et al. Valsartan reduced the vulnerability to atrial fibrillation by preventing action potential prolongation and conduction slowing in castrated male mice. J Cardiovasc Electrophys 2018;29:1436-1443.

178. Andrade JG, Deyell MW, Lee AYK, Macle L. Sex Differences in Atrial Fibrillation. Canadian Journal of Pharmacology 2018;34:429-436.

179. Bogle BM, Ning H, Mehrotra S, Goldberger JJ, Lloyd-Jones DM. Lifetime Risk for Sudden Cardiac Death in the Community. J Am Heart Assoc 2016;5.

180. Lehmann MH, Timothy KW, Frankovich D et al. Age-gender influence on the rate-corrected QT interval and the QT-heart rate relation in families with genotypically characterized long QT syndrome. J Am Coll Cardiol 1997;29:93-9.

181. Murphy NF, Simpson CR, Jhund PS et al. A national survey of the prevalence, incidence, primary care burden and treatment of atrial fibrillation in Scotland. Heart 2007;93:606-612.

182. Benjamin EJ, Levy D, Vaziri SM, D'Agostino RB, Belanger AJ, Wolf PA. Independent risk factors for atrial fibrillation in a population-based cohort. The Framingham Heart Study. JAMA 1994;271:840-4.

183. Benjamin EJ, Wolf PA, D'Agostino RB, Silbershatz H, Kannel WB, Levy D. Impact of Atrial Fibrillation on the Risk of Death. Circulation 1998;98:946-952.

184. Wang TJ, Massaro JM, Levy D et al. A risk score for predicting stroke or death in individuals with new-onset atrial fibrillation in the community: the Framingham Heart Study. JAMA 2003;290:1049-56.

185. Porter MJ, Morton JB, Denman R et al. Influence of age and gender on the mechanism of supraventricular tachycardia. Heart Rhythm 2004;1:393-6.

186. Tadros R, Ton AT, Fiset C, Nattel S. Sex differences in cardiac electrophysiology and clinical arrhythmias: epidemiology, therapeutics, and mechanisms. Can J Cardiol 2014;30:783-92.

187. Rienstra M, Van Veldhuisen DJ, Hagens VE et al. Gender-related differences in rhythm control treatment in persistent atrial fibrillation: data of the Rate Control Versus Electrical Cardioversion (RACE) study. J Am Coll Cardiol 2005;46:1298-306.

188. Go AS, Hylek EM, Phillips KA et al. Prevalence of Diagnosed Atrial Fibrillation in Adults National Implications for Rhythm Management and Stroke Prevention: the AnTicoagulation and Risk Factors In Atrial Fibrillation (ATRIA) Study. JAMA 2001;285:2370-2375.

189. Rodriguez I, Kilborn MJ, Liu XK, Pezzullo JC, Woosley RL. Drug-induced QT prolongation in women during the menstrual cycle. Jama 2001;285:1322-6.

190. Perez MV, Wang PJ, Larson JC et al. Effects of postmenopausal hormone therapy on incident atrial fibrillation: the Women's Health Initiative randomized controlled trials. Circ Arrhythm Electrophysiol 2012;5:1108-16.

191. Rosano GMC, Leonardo F, Dicandia C et al. Acute electrophysiologic effect of estradiol 17β in menopausal women. Am J Cardiol 2000;86:1385-1387.

192. Evan R. Simpson, Colin Clyne, Gary Rubin et al. Aromatase—A Brief Overview. Annu Rev Physiol 2002;64:93-127.

193. Sasano H, Takashashi K, Satoh F, Nagura H, Harada N. Aromatase in the human central nervous system. Clin Endocrinol 1998;48:325-9.

194. Sasano H, Uzuki M, Sawai T et al. Aromatase in human bone tissue. J Bone Miner Res 1997;12:1416-23.

195. Mahendroo MS, Mendelson CR, Simpson ER. Tissue-specific and hormonally controlled alternative promoters regulate aromatase cytochrome P450 gene expression in human adipose tissue. J Biol Chem 1993;268:19463-70.

196. Agarwal VR, Ashanullah CI, Simpson ER, Bulun SE. Alternatively spliced transcripts of the aromatase cytochrome P450 (CYP19) gene in adipose tissue of women. J Clin Endocrinol Metab 1997;82:70-4.

197. Bell JR, Mellor KM, Wollermann AC et al. Aromatase Deficiency Confers Paradoxical Postischemic Cardioprotection. Endocrinology 2011;152:4937-4947.

198. Khudhair D, Nahavandi, S, Garmestani, H, Bhatti, A. Microelectrode Arrays: Architecture, Challenges and Engineering Solutions. BioEngineering 2017.

199. Lau DH, Mackenzie L, Shipp NJ et al. Feasibility of high-density electrophysiological study using multiple-electrode array in isolated small animal atria. Clin Exp Pharmacol Physiol 2010;37:1023-7.

200. MCS. Microelectrode Array Catalogue. https://www.multichannelsystems.com/products/microelectrode-arrays, 2020.

201. Spira ME, Hai A. Multi-electrode array technologies for neuroscience and cardiology. Nat Nanotechnol 2013;8:83.

202. Tertoolen LGJ, Braam SR, van Meer BJ, Passier R, Mummery CL. Interpretation of field potentials measured on a multi electrode array in pharmacological toxicity screening on primary and human pluripotent stem cell-derived cardiomyocytes. Biochem Biophys Res Commun 2017.

203. Meyer T, Boven KH, Gunther E, Fejtl M. Micro-electrode arrays in cardiac safety pharmacology: a novel tool to study QT interval prolongation. Drug Saf 2004;27:763-72.

204. Egert UM, Thomas. Heart on a Chip – Extracellular Multielectrode Recordings from Cardiac Myocytes in Vitro. Practical Methods in Cardiovascular Research, 2005:432-453.

205. Egert U, Banach K, Meyer T. Analysis of Cardiac Myocyte Activity Dynamics with Micro-Electrode Arrays. In: Taketani M, Baudry M, editors. Advances in Network Electrophysiology: Using Multi-Electrode Arrays. Boston, MA: Springer US, 2006:274-290.

206. Braam SR, Tertoolen L, van de Stolpe A, Meyer T, Passier R, Mummery CL. Prediction of drug-induced cardiotoxicity using human embryonic stem cell-derived cardiomyocytes. Stem Cell Res 2010;4:107-16.

207. Meiry G, Reisner Y, Feld Y et al. Evolution of Action Potential Propagation and Repolarization in Cultured Neonatal Rat Ventricular Myocytes. J Cardiovasc Electrophys 2001;12:1269-1277.

208. Boyle PM, Franceschi WH, Constantin M et al. New insights on the cardiac safety factor: Unraveling the relationship between conduction velocity and robustness of propagation. J Mol Cell Cardiol 2019;128:117-128.

209. Sala L, Ward-van Oostwaard D, Tertoolen LGJ, Mummery CL, Bellin M. Electrophysiological Analysis of human Pluripotent Stem Cell-derived Cardiomyocytes (hPSC-CMs) Using Multi-electrode Arrays (MEAs). J Vis Exp 2017:e55587.

210. O'Shea C, Holmes AP, Yu TY et al. ElectroMap: High-throughput open-source software for analysis and mapping of cardiac electrophysiology. Sci Rep 2019;9:1389.

211. Winter J, Bishop MJ, Wilder CDE, O'Shea C, Pavlovic D, Shattock MJ. Sympathetic Nervous Regulation of Calcium and Action Potential Alternans in the Intact Heart. Front Physiol 2018;9.

212. Brack KE, Narang R, Winter J, Ng GA. The mechanical uncoupler blebbistatin is associated with significant electrophysiological effects in the isolated rabbit heart. Exp Physiol 2013;98:1009-1027.

213. Larsen AP, Sciuto KJ, Moreno AP, Poelzing S. The voltage-sensitive dye di-4-ANEPPS slows conduction velocity in isolated guinea pig hearts. Heart Rhythm 2012;9:1493-500.

Chapter 2

Overview of materials and methodologies

2.1 Methodology overview

An overview and comparative description of the two key methodologies used in this thesis (microelectrode array and optical mapping) is provided in Chapter 1 (pages 32-35). Chapters 3-6 individually contain detailed descriptions of these techniques and additional methodologies used, where applicable. Refer to the list below for redirection to appropriate methodological descriptions.

Technique	**Chapter(s)**	**Page(s)**
Animal details	3	68, 92
	4	102
	5	148
	6	238
Rat left ventricular tangential slice preparation	3	68, 102
Rat left ventricular tangential slice microelectrode array mapping	3	68, 93
Rat left ventricular tangential slice histology	3	69, 94
Neonatal rat ventricular cardiomyocyte isolation and culture	4	102
Human induced pluripotent stem cell-derived cardiomyocyte (hiPSC-CM) culture	4	103
	5	150
hiPSC-CM-epicardial adipose tissue fragment co-culture	5	151
Microelectrode array mapping of cardiomyocyte cultures	4	104
	5	151
Isolated left atrial optical mapping	5	148
	6	238
Microelectrode array analyses	3	68, 94
	4	104
	5	151
Optical mapping analyses	5	151
	6	239

2.2 Calculation of conduction velocities

Due to the nature of different electrophysiological mapping methodologies used in this study, several different approaches/software packages were used throughout this thesis. To clarify incidences when different packages were used and how conduction velocity was calculated, a detailed description is provided here.

2.2.1 Conduction velocities for cardiac slices (microelectrode array)

Cardiac slice experiments were performed using the microelectrode array system (see Chapter 3 for detailed description). Electrical pacing introduced a stimulus artefact into the recording preparation, which the commercially available mapping software, Cardio2D (used for calculating conduction in spontaneously beating cells – see below) was unable to distinguish from the field potential signal. As such, different recording and analysis packages were used. MC_Rack (Multichannel Systems) was used for experimental recordings, then the last beat in the stimulus train exported from each electrode by manually excluding the stimulus artefact. These files were the imported into a MATLAB-based script provided by Professor Cesare Terracciano (1,2). The script detects the field potential minimum (i.e. maximum point of depolarisation) on each electrode to determine activation across all electrodes (with the stimulus electrodes being manually adjusted to 0ms).

Local conduction velocity was then calculated between neighbouring electrodes by dividing the interelectrode distance (700μm) by the delay in activation. This was calculated between all electrodes and their neighbouring counterparts, then an overall mean local conduction velocity value computed.

Longitudinal conduction velocity was calculated by dividing the time delay in activation between the stimulus site and the electrode furthest from that site along the longitudinal axis of the slice (slice fibre orientation was readily distinguishable using a light microscope) by the distance (4.9mm; i.e. 700μm interelectrode distance x 7 interelectrode spaces). This was performed for each row along the longitudinal axis, then an average calculated. For transverse conduction velocity, the same process was performed, but perpendicular to the longitudinal fibre direction.

2.2.2 Conduction velocities for spontaneously beating cardiomyocyte cultures (microelectrode array)

Spontaneous field potentials were recorded from cardiomyocyte cultures using Cardio2D (Multichannel Systems). Conduction velocity was calculated, and activation maps generated using Cardio2D+ software. The field potential minimum (i.e. maximum point of depolarisation) on each electrode was used to determine activation at each site. Delay in activation between neighbouring electrodes was used to calculate local propagation time, then a mean calculated automatically from this across all electrodes. This was calculated on a beat-to-beat basis for 10 beats, then these ten values averaged together and are used for data presented here.

This approach was used for neonatal rat ventricular cardiomyocytes (Chapter 4). Conduction velocities were not calculated for human induced pluripotent stem cell-derived cardiomyocytes (hiPSC-CMs) in Chapter 4, as these cells were in clusters across a large recording matrix (8x8 electrodes; 1.4mm^2) – making reliable, comparable mapping of conduction not possible. In Chapter 5, hiPSC-CMs were plated in clusters,

but across a smaller recording matrix (3x3 electrodes; 0.16mm^2), meaning connectivity between clusters was improved and field potential activity synchronised across sites. To maximise reliability of measures here and improve comparability to monolayers, conduction velocity data was only included if a signal was detected on >6/9 of the recording electrodes.

2.2.3 Conduction velocities for isolated mouse left atria (optical mapping)

Optical mapping data were analysed using ElectroMap software (3,4). Image stacks acquired in WinFluor during experiments were imported into ElectroMap and spatially and temporally filtered with a 4x4 Gaussian filter and a 3rd order Savitzky-Golay filter, respectively. The last 10-20 beats of each paced cycle length where ensemble averaged, and non-physiological baseline deviations were corrected for using a Top-Hat filter (100ms). Activation at a single pixel was defined as time of 50% depolarisation (automatically detected in ElectroMap). This was detected at every pixel across the left atrium, then delay in activation between neighbouring pixels automatically calculated to generate local conduction velocities in all directions using a polynomial fit method (by factoring in known pixel size)(5). All individual values were summed together to generate a total conduction velocity for the entire left atrium.

2.3 References

1. Chowdhury RA, Tzortzis KN, Dupont E et al. Concurrent micro- to macro-cardiac electrophysiology in myocyte cultures and human heart slices. Sci Rep 2018;8:6947.

2. Watson SA, Scigliano M, Bardi I, Ascione R, Terracciano CM, Perbellini F. Preparation of viable adult ventricular myocardial slices from large and small mammals. Nature Protocols 2017;12:2623.

3. O'Shea C, Holmes AP, Yu TY et al. ElectroMap: High-throughput open-source software for analysis and mapping of cardiac electrophysiology. Scientific Reports 2019;9:1389.

4. O'Shea C, Holmes AP, Yu TY et al. High-Throughput Analysis of Optical Mapping Data Using ElectroMap. J Vis Exp 2019.

5. Bayly PV, KenKnight BH, Rogers JM, Hillsley RE, Ideker RE, Smith WM. Estimation of conduction velocity vector fields from epicardial mapping data. IEEE Trans Biomed Eng 1998;45:563-71.

Chapter 3

Prolonged activation of ventricular epicardium disrupts a transmural conduction gradient in the context of high cardiac adiposity

Manuscripts generated from this chapter:

Wells SP, Curl CL, …, Kirchhof P, Pavlovic D, Delbridge LMD and Bell JR. Prolonged activation of ventricular epicardium disrupts a transmural conduction gradient in the context of high cardiac adiposity. **In preparation**.

Original article

Prolonged activation of ventricular epicardium disrupts a transmural conduction gradient in the context of high cardiac adiposity

Short title: Transmural conduction gradient and cardiac adiposity

Wells SP[1,2], MRes; Curl CL[1], PhD; …; Kirchhof P[2,3], MD; Pavlovic D[2], DPhil; Delbridge LMD[1,*,#], PhD; Bell JR[1,4,*,#], PhD

[1]Department of Physiology, University of Melbourne, Parkville, Victoria, Australia, 3010

[2]Institute of Cardiovascular Sciences, University of Birmingham, Birmingham, United Kingdom, B15 2TT

[3]Department of Cardiology, University Heart and Vascular Center UKE Hamburg, Hamburg, Germany, 20251

[4]Department of Physiology, Anatomy & Microbiology, La Trobe University, Bundoora, Victoria, Australia, 3086

[*]LMD and JRB contributed equally to this work

[#]Correspondence: Cardiac Phenomics Laboratory, School of Biomedical Sciences
University of Melbourne, Victoria, Australia, 3010

Email address: [redacted](L.M.D. Delbridge)

[redacted](J.R. Bell)

Conflict of interest: Nil

Word count: 4,794

Abstract

Background

Transmural differences in ventricular action potential duration ensure synchronised repolarisation. Similar differences in conduction velocity may exist to help define transmural activation/repolarisation patterns. Conduction slowing is a key mechanism predisposing to arrhythmia. Emerging evidence implicates increased pericardial adiposity with ventricular fibrillation risk. Increased adipose tissue deposition around the epicardium may affect transmural conduction.

Objective

The aim of this investigation was to characterise left ventricular intramural conduction characteristics and examine if they are pathologically modulated in the setting of elevated pericardial adiposity.

Methods

Sprague Dawley rats were fed control/high fat diets. Left ventricular 300µm tangential slices were generated from endocardium to epicardium using a vibratome and conduction mapped using microelectrode arrays. Slices were then histologically processed to assess fibrosis.

Results

Transmural repolarisation gradients were evident in ventricular slices from both control and high fat diet rats. Conduction velocity was significantly greater in epicardial *vs* endocardial slices in control rats. Epicardial conduction velocity was slower in ventricular slices from high fat diet fed rats and a transmural conduction gradient was hence absent.

This was associated with significantly greater pericardial adiposity and epicardial fibrosis. The magnitude of the transmural conduction velocity gradient negatively correlated with the extent of epicardial fibrosis.

Conclusion

A conduction velocity gradient exists in the left ventricle, potentially to help maintain normal activation/repolarisation sequence. High fat feeding caused epicardial conduction slowing, hence loss of the transmural gradient, increasing vulnerability to transmural/intramural reentry. Augmented pericardial adiposity and epicardial fibrosis evident with high fat feeding implicates them as potential electrical remodelling mediators.

Keywords

Endocardium ▪ Epicardium ▪ Fibrosis ▪ Intramural conduction ▪ Pericardial adipose tissue ▪ Transmural conduction ▪ Ventricular arrhythmias

Abbreviations

HFD, high fat diet

3.1 Introduction

An organised electrical propagation pathway drives ventricular contraction from apex to base, ensuring blood is efficiently ejected. Action potentials transit from the atrioventricular node to the ventricular endocardium via Purkinje fibres, then travel transmurally to the epicardium.[1] Endocardial action potential duration is substantially longer than epicardial to offset this transmural delay in activation, synchronising left ventricular repolarisation.[2-5] Homogenous repolarisation prevents transmural reentry and ensures the endocardial-epicardial activation sequence is maintained.[3] Similar intramural endocardial-epicardial conduction velocity differences may exist to further help define transmural activation/repolarisation patterns, but this has not been previously investigated.

Transmural and intramural reentry are both established mechanisms implicated in ventricular fibrillation pathogenesis.[6, 7] The underlying early cellular mechanisms which predispose to a transmural reentrant substrate are poorly understood. Clinical studies have reported a link between epicardial adipose tissue accumulation and atrial fibrillation risk.[8] The association between cardiac adiposity and ventricular fibrillation is not as well solidified. Ventricular fibrillation/sudden death are primary causes of mortality in heart failure patients.[9] Epicardial adipose thickness is a significant risk factor for disease progression, ventricular tachycardia/fibrillation risk and post-ablation arrhythmia recurrence in heart failure patients.[9-12]

The aims of this investigation were to explore the presence of transmural conduction velocity gradients in rat ventricular slices and assess the extent to which these are modulated in a high pericardial adiposity setting.

3.2 Methods

For expanded methodological details, see the Supplementary Methods.

Animal details

Experiments were conducted in accordance with the Guide for the Care and Use of Laboratory Animals, National Health and Medical Research Council/Commonwealth Scientific and Industrial Research Organisation/ACC Australian Code of Practice for the Care and Use of Animals for Scientific Purposes (1997), as approved (University of Melbourne Animal Ethics Committee).

Male Sprague Dawley rats were fed either a control (12% lipid energy intake) or high fat diet (HFD; 43% lipid energy intake) for 15-16 weeks.

Cardiac slice preparation

Rat left ventricular slices were generated using previously published protocols (**Figure 3.1**).[13, 14] At age 23-24 weeks, hearts were isolated, the left ventricular free wall dissected and glued onto a vibratome stage. 300μm tangential slices were generated from endocardium to epicardium.

Microelectrode array recordings and analysis

Extracellular field potentials were recorded from slices secured onto microelectrode arrays, continuously superfused with oxygenated Tyrode's buffer (37^{o}C). Electrodes at the peripheral longitudinal end of the tissue were used for pacing. Analysis of conduction velocity and generation of activation maps was performed using a MATLAB-

based script.[14, 15] Field potential duration was calculated as the interval between the first negative peak on the field potential and the final negative deflection.

Histology

Slices were fixed in 10% formalin, histologically processed, and stained with either Picrosirius red to identify Collagen Type I and III or Oil Red O to identify lipids. Fibrosis analysis was performed as previously described.[16] Oil Red O-stained sections were visualised to detect presence/absence of lipid.

Statistical analysis

Data are presented as mean±standard error. Statistical tests used are indicated in the Figure legends throughout. $P<0.05$ was deemed significant and *n* denotes the number of animals/slices used.

3.3 Results

A transmural conduction gradient exists in the rat left ventricle

Endocardial field potential duration was significantly longer than epicardial field potential duration at all cycle lengths (200ms cycle length: endocardium *vs* epicardium: 80.7±9.5 *vs* 49.1±7.7ms; **Figure 3.2A & B**). Field potential duration lengthened as cycle length was increased in both the endocardium and epicardium (**Figure 3.2B**).

To determine the intramural properties of the left ventricular wall, conduction was mapped across all slices from endocardium to epicardium in control-fed rats. Local conduction velocity increased through the myocardium from endocardium to epicardium (endocardium *vs* epicardium: 18.7±2.4cm/s *vs* 39.3±3.9cm/s, $P<0.05$; **Figure 3.2C & D**), coupled with shorter activation times (22.0±3.2ms *vs* 12.3±0.6ms, $P<0.05$; **Figure 3.2E**). To determine whether these conduction differences were anisotropic-dependent, single vector conduction was analysed along the longitudinal and transverse axes separately. Longitudinal conduction velocity was similar in the endocardium and epicardium (**Figure 3.2F**), whilst transverse conduction velocity (indicative of lateral conduction between cardiomyocytes) was significantly greater in the epicardium (29.93±6.1cm/s *vs* 69.06±11.1cm/s, $P<0.05$; **Figure 3.2G**).

High fat feeding associates with increased pericardial adiposity, lipid accumulation and conserved transmural repolarisation

15 weeks of high fat feeding did not significantly increase body weight (control vs HFD: 651.9±20.8g *vs* 724.4±28.4, $P>0.05$; **Figure 3.3A**) or heart weight (**Figure 3.3B**) but induced a significant increase in pericardial adiposity (370.9±71.9mg *vs* 648.8±77.9mg,

P<0.05; **Figure 3.3C**) and hence pericardial adipose tissue:body weight (0.56±0.09mg/g *vs* 0.87±0.07mg/g, *P*<0.05). Lipid content, assessed by Oil Red O staining, was detected only in HFD animals, and this was to a similar extent in the endocardium and epicardium (**Figure 3.3D & E**).

Control and HFD fed animals demonstrated similar endocardial and epicardial field potential durations – both with clear transmural differences and similar regional repolarisation-rate dependencies (**Figure 3.4A & B**). Steeper electrical restitution is classically viewed as pro-arrhythmic.[17] To determine whether this was uniform throughout the myocardium, the magnitude of repolarisation-rate dependency was calculated by assessing the difference between field potential duration at 1000ms and 200ms cycle lengths. Repolarisation-rate dependency was consistent between the endocardium and epicardium, regardless of diet (**Figure 3.4C**).

High fat feeding abolishes the transmural conduction gradient

Control and HFD rats had similar endocardial conduction velocities (**Figure 3.5A & B**). When progressing transmurally through the left ventricular wall, HFD rats did not demonstrate the increase in conduction velocity seen in control animals (**Figure 3.5B**). This effect was driven by slowed epicardial conduction velocity in HFD rats (**Figure 3.5C & D**), resulting in loss of the transmural conduction velocity gradient (Δendocardial-epicardial conduction velocity, control *vs* HFD: 20.7±3.6cm/s *vs* 3.3±3.5cm/s, *P*<0.05; **Figure 3.5E**).

When assessing the anisotropic effect of this conduction difference exhibited by HFD rats (**Figure 3.5F**), there was no difference in the change from endocardium-epicardium

in longitudinal conduction velocity (2.0±7.3cm/s *vs* 1.3±8.7cm/s, *P*>0.05; **Figure 3.5G**); however, the transmural change in transverse conduction was significantly less in HFD animals (39.1±9.8cm/s *vs* 9.9±6.7cm/s, *P*<0.05; **Figure 3.5H**).

Pericardial adiposity associates with epicardial fibrosis to dictate the magnitude of the transmural conduction gradient

Endocardial and epicardial slices were cryosectioned and stained with Picrosirius red to detect fibrosis (**Figure 3.6A**). In control animals, a regional difference in fibrosis was detected between the endocardium and epicardium (**Figure 3.6B**). Post-hoc analysis revealed endocardial fibrosis was similar between control and HFD, whilst epicardial fibrosis was augmented in HFD *vs* control rats (**Figure 3.6B**). There was no correlation between pericardial adiposity and endocardial fibrosis (**Figure 3.6C**); however, a significant positive relationship was seen between pericardial adiposity and epicardial fibrosis (**Figure 3.6D**). The magnitude of the transmural conduction velocity gradient (i.e. epicardial – endocardial conduction velocity; **Figure 3.6E**) did not correlate with the extent of endocardial fibrosis however, negatively correlated with the degree of epicardial fibrosis (**Figure 3.6F**).

3.4 Discussion

This is the first study to demonstrate a ventricular endocardial-epicardial conduction velocity gradient, where epicardial conduction velocity is significantly faster than endocardial. This gradient might be an important aid in defining normal transmural activation/repolarisation. The transmural conduction gradient was abolished with high fat feeding, due to slowed epicardial conduction velocity. High fat feeding also associated with augmented pericardial adiposity and epicardial fibrosis – the extent of which correlated with each other and the absence of a transmural gradient. Together, these data indicate high fat feeding may be proarrhythmic, promoting transmural/intramural reentry. The HFD-induced electrical remodelling might be driven through an associative effect between pericardial adiposity and epicardial fibrosis.

Implications of transmural differences in conduction velocity

Ventricular slices from control rats demonstrated a clear transmural difference in field potential duration (**Figure 3.2A & B**) – a robust extracellular measure of repolarisation time[15, 18]. This transmural difference has been established in various species/preparations, although this is the first demonstration in transmurally-uncoupled tissue slices - supporting the concept that these differences are inherent to the myocardial region and not dictated by the transmural activation sequence.[2-5]

Interestingly, coupled with these transmural repolarisation differences, there was a transmural gradient in conduction velocity, with epicardial conduction velocity significantly faster than endocardial (**Figure 3.2C & D**). No previous studies have reported intramural conduction velocity in the endocardium. There are, however,

numerous epicardial studies yielding conduction velocities consistent with epicardial data presented here, supporting the validity of this novel finding.[19, 20] The role of this conduction velocity gradient is not clear, but may reduce the potential for transmural reentry working in conjunction with the action potential duration gradient to synchronise transmural repolarisation. As the myocardium activates from endocardium to epicardium, this dictates a delay between endocardial and epicardial depolarisation.[1] To ensure the epicardium completes its activation cycle before the endocardium is re-excitable, it might be necessary that the propagation velocity of the action potential increases as it travels towards the epicardium.

This interpretation is somewhat consistent with the finding that conduction velocity in the transverse direction (i.e. lateral propagation between cardiomyocytes), and not the longitudinal (end-end propagation between cardiomyocytes) direction, is driving the endocardial-epicardial difference (**Figure 3.2F & G**). Although the slice preparation only allows conduction mapping in the two-dimensional plane, cardiomyocyte alignment (and hence conduction) in the transmural axis would be consistent with the measurable transverse axis here. A modified mouse ventricular optical mapping protocol, capable of detecting delay in activation between 50-450µm tissue depth, demonstrated similar conduction velocities in the transmural axis to what we report in the transverse axis. This supports our contention of transverse conduction as a surrogate measure for transmural conduction.[21]

These intramural endocardial-epicardial conduction velocity differences might also be partially related to the geometrical shape of the heart. The endocardium is concave, whilst the epicardium is convex – dictating that the surface area, and therefore

pathlength of the epicardium is greater than the endocardium, necessitating a faster native conduction velocity to maintain endocardial-epicardial activation-repolarisation balance.

High fat feeding associates with elevated pericardial adiposity and loss of the transmural conduction velocity gradient

Emerging evidence implicates a role for augmented pericardial adiposity and ventricular arrhythmia risk, but there a few reports of the structural and electrical remodelling that must occur on a cellular level to predispose to arrhythmia.[11, 12] We used a rat model of elevated pericardial adiposity, induced through high fat diet feeding, which associated with lipid accumulation throughout the myocardium (**Figure 3.3C-E**). HFD feeding abolished the transmural conduction velocity gradient through slowing in the epicardium and no change in the endocardium (**Figure 3.5B**). Slowed conduction velocity is a key cellular feature which can predispose to reentrant arrhythmias, such as ventricular fibrillation. Reentry in this situation could occur intramurally (i.e. within the epicardium) or transmurally in a retrograde direction due to the regional effect of the conduction slowing. Previous studies using plunge electrodes or wedge preparations visualising the intact ventricular wall indicate that such types of reentry are the primary mechanisms driving ventricular fibrillation, but these approaches lack the intramural spatial resolution of the cardiac slice preparation used here.[6, 7]

Pericardial adiposity associates with fibrosis and absence of a conduction gradient

In control rats, fibrosis was greater in the epicardium compared to the endocardium. This may explain the gradient in conduction, with greater endocardial fibrosis disrupting cell-cell connectivity/conduction. Observationally, fibrosis was predominantly located laterally between adjacent cardiomyocytes, rather than at the longitudinal ends (**Figure 3.6A**). This is consistent with the transmural change in conduction being driven by changes in the transverse, and not longitudinal, axis (**Figure 3.2G**). It is not clear why fibrosis differs transmurally in the myocardium. This may be a result of greater sheer stress in the endocardium or perhaps necessary to provide greater structural support during diastole. There are few other reports quantitatively examining transmural differences in fibrosis. A similar trend in transmural fibrosis has been demonstrated in the mouse ventricle.[21] Others using the rat slice preparation have not seen such transmural differences in fibrosis.[22] This discrepancy might be a product of grouping endocardial and sub-endocardial, and epicardial and sub-epicardial regions, which was not done in the present study.

Previous studies have implicated the potential pro-fibrotic role of pericardial adipose tissue, with various adipokines (including activin A, TGF-β1, metalloproteinases and connective tissue growth factor) being detected with potential for promoting fibrosis.[23-26] Secretome from human epicardial adipose tissue has been shown to directly stimulate fibrosis of rat atrial tissue in organo-culture conditions.[23] Others have implicated pericardial adipose tissue as a mediator of ventricular fibrosis in high fat-fed pigs[27] and a driver for fibrotic infiltration post myocardial infarction in mice.[28] Following these data,

we hypothesised that augmented pericardial adiposity was promoting epicardial fibrosis, disrupting inter-myocyte connectivity to slow conduction in HFD rats. Consistent with this hypothesis, epicardial fibrosis was elevated in HFD animals (**Figure 3.6B**) and correlated with the extent of pericardial adiposity (**Figure 3.6C & D**). The degree of epicardial fibrosis associated with the absence of a transmural conduction velocity gradient (**Figure 3.6E & F**). As with control animals, HFD epicardial fibrosis was primarily located parallel to cardiomyocyte longitudinal axes, and so is consistent with a conduction slowing in the transverse axis. Together, these data reinforce our contention that locally derived adipokines promote fibrosis to slow epicardial conduction.

Transmural repolarisation is unaffected in the setting of augmented pericardial adiposity

Control and HFD slices exhibited similar rate-dependent repolarisation times, which were longer in the endocardium than the epicardium (**Figure 3.4B**). Other studies have demonstrated Q-T prolongation in HFD mice and prolonged action potential duration in ventricular cardiomyocytes isolated from HFD Wistar rats.[29, 30] Neither of these studies examined the extent of pericardial adiposity, and HFD feeding induced obesity – a feature not seen in the Sprague Dawley rats used here. The magnitude of steady-state repolarisation rate dependency was similar between the endocardium and epicardium (**Figure 3.4C**). This has not been previously investigated in the rat, and existing literature indicates this as species-dependent, with guinea cardiomyocytes exhibiting greater endocardial rate dependency, whilst dogs show the inverse.[31, 32]

Whilst there are no published investigations into the effects of pericardial adiposity on ventricular repolarisation, prolonged repolarisation has been shown in rabbit atrial cardiomyocytes following short-term incubation with epicardial adipose.[33] We have also shown that obese mice have prolonged atrial repolarisation and human induced pluripotent stem cell-derived cardiomyocyte repolarisation is prolonged by epicardial adipose through a paracrine mechanism (present thesis, Chapter 5). These stem cell-derived human cardiomyocytes were primarily of ventricular origin, indicating prolonged repolarisation is not a chamber specific effect. It might be that prolonged repolarisation is driven primarily by epicardial adipose-specific derived factors. Although epicardial adipose tissue is minimal in rodents, it is situated near the atria whereas the ventricle is in proximity to paracardial adipose.

It is also worth noting the limited scope to assess repolarisation using rodent tissue on the microelectrode array platform. As others have noted, determining the completion of repolarisation is not always possible.[13] This is likely due to the combined effect of rapid repolarisation inherent to rodent tissue and contraction of the tissue during the refractory period, conferring lateral tissue movement away from the electrode where depolarisation was detected.

3.5 Conclusions

In summary, we show that a positive gradient in conduction velocity consistent with the transmural activation sequence exists in the ventricular myocardium. The presence of this gradient is likely important in protecting against reentry and is abolished in the setting of elevated pericardial adiposity via slowed epicardial conduction linked with localised fibrosis (as summarised in **Figure 3.7**). We conclude that high fat feeding induces epicardial structural and electrical remodelling which may predispose to reentrant arrhythmias such as ventricular fibrillation. Further studies are required to confirm the role of adipocytokines in mediating this effect.

Funding

This research was supported by the National Health and Medical Research Council (nos. 1099352 and 1125453; L. M. D. Delbridge, J. R. Bell) and the Australian Research Council (no. DP160102404; L. M. D. Delbridge).

Acknowledgements

MATLAB script for generation of activation maps and conduction velocity analysis was kindly provided by Professor Cesare Terracciano, Imperial College London, and is gratefully acknowledged. Technical support and assistance with mapping analysis and histology was provided by Dr Chris O'Shea (University of Birmingham) and the University of Melbourne histopathology platform, respectively.

3.6 References

1. Durrer D, Dam RTV, Freud GE, Janse MJ, Meijler FL, Arzbaecher RC. Total Excitation of the Isolated Human Heart. Circulation 1970;41:899-912.

2. Bányász T, Fülöp L, Magyar J, Szentandrássy N, Varró A, Nánási PP. Endocardial versus epicardial differences in L-type calcium current in canine ventricular myocytes studied by action potential voltage clamp. Cardiovasc Res 2003;58:66-75.

3. Boukens BJ, Sulkin MS, Gloschat CR, Ng FS, Vigmond EJ, Efimov IR. Transmural APD gradient synchronizes repolarization in the human left ventricular wall. Cardiovasc Res Oct 1 2015;108:188-196.

4. Volk T, Nguyen TH, Schultz JH, Ehmke H. Relationship between transient outward K+ current and Ca2+ influx in rat cardiac myocytes of endo- and epicardial origin. J Physiol 1999;519 Pt 3:841-850.

5. Wen Q, Gandhi K, Capel RA, et al. Transverse cardiac slicing and optical imaging for analysis of transmural gradients in membrane potential and Ca(2+) transients in murine heart. J Physiol 2018;596:3951-3965.

6. Nair K, Umapathy K, Farid T, Masse S, Mueller E, Sivanandan RV, Poku K, Rao V, Nair V, Butany J, Ideker RE, Nanthakumar K. Intramural Activation During Early Human Ventricular Fibrillation. Circ Arrhythm Electrophysiol 2011;4:692-703.

7. Valderrábano M, Lee M-H, Ohara T, Lai AC, Fishbein MC, Lin S-F, Karagueuzian HS, Chen P-S. Dynamics of Intramural and Transmural Reentry During Ventricular Fibrillation in Isolated Swine Ventricles. Circ Res 2001;88:839-848.

8. Wong CX, Abed HS, Molaee P, et al. Pericardial fat is associated with atrial fibrillation severity and ablation outcome. J Am Coll Cardiol 2011;57:1745-1751.

9. Lee DS, Gona P, Albano I, Larson MG, Benjamin EJ, Levy D, Kannel WB, Vasan RS. A systematic assessment of causes of death after heart failure onset in the community: impact of age at death, time period, and left ventricular systolic dysfunction. Circ Heart Fail Jan 2011;4:36-43.

10. Nerlekar N, Muthalaly RG, Wong N, Thakur U, Wong DTL, Brown AJ, Marwick TH. Association of Volumetric Epicardial Adipose Tissue Quantification and Cardiac Structure and Function. J Am Heart Assoc 2018;7:e009975.

11. Wu CK, Tsai HY, Su MY, Wu YF, Hwang JJ, Tseng WY, Lin JL, Lin LY. Pericardial fat is associated with ventricular tachyarrhythmia and mortality in patients with systolic heart failure. Atherosclerosis 2015;241:607-614.

12. Sepehri Shamloo A, Schoene K, Stauber A, et al. Epicardial adipose tissue thickness as an independent predictor of ventricular tachycardia recurrence following ablation. Heart Rhythm 2019/10/01/ 2019;16:1492-1498.

13. Bussek A, Wettwer E, Christ T, Lohmann H, Camelliti P, Ravens U. Tissue slices from adult mammalian hearts as a model for pharmacological drug testing. Cell Physiol Biochem 2009;24:527-536.

14. Watson SA, Scigliano M, Bardi I, Ascione R, Terracciano CM, Perbellini F. Preparation of viable adult ventricular myocardial slices from large and small mammals. Nat Prot 2017;12:2623-2639.

15. Chowdhury RA, Tzortzis KN, Dupont E, Selvadurai S, Perbellini F, Cantwell CD, Ng FS, Simon AR, Terracciano CM, Peters NS. Concurrent micro- to macro-cardiac electrophysiology in myocyte cultures and human heart slices. Sci Rep 2018;8:6947.

16. Curl CL, Danes VR, Bell JR, et al. Cardiomyocyte Functional Etiology in Heart Failure With Preserved Ejection Fraction Is Distinctive - A New Preclinical Model. J Am Heart Assoc 2018;7:e007451.

17. Shattock MJ, Park KC, Yang H-Y, Lee AWC, Niederer S, MacLeod KT, Winter J. Restitution slope is principally determined by steady-state action potential duration. Cardiovasc Res 2017;113:817-828.

18. Wells SP, Waddell HM, Sim CB, Lim SY, Bernasochi GB, Pavlovic D, Kirchhof P, Porrello ER, Delbridge LMD, Bell JR. Cardiomyocyte functional screening: interrogating comparative electrophysiology of high-throughput model cell systems. Am J Physiol Cell Physiol 2019;317:C1256-c1267.

19. O'Shea C, Pavlovic D, Rajpoot K, Winter J. Examination of the Effects of Conduction Slowing on the Upstroke of Optically Recorded Action Potentials. Front Physiol 2019;10:1295-1295.

20. Takanari H, Bourgonje VJA, Fontes MSC, et al. Calmodulin/CaMKII inhibition improves intercellular communication and impulse propagation in the heart and is antiarrhythmic under conditions when fibrosis is absent. Cardiovasc Res 2016;111:410-421.

21. Kelly A, Salerno S, Connolly A, Bishop M, Charpentier F, Stølen T, Smith GL. Normal interventricular differences in tissue architecture underlie right ventricular susceptibility to conduction abnormalities in a mouse model of Brugada syndrome. Cardiovasc Res 2018;114:724-736.

22. Pitoulis FG, Hasan W, Papadaki M, Clavere NG, Perbellini F, Harding SE, Kirk JA, Boateng SY, de Tombe PP, Terracciano CM. Intact myocardial preparations reveal intrinsic transmural heterogeneity in cardiac mechanics. J Mol Cell Cardiol Mar 19 2020;141:11-16.

23. Venteclef N, Guglielmi V, Balse E, Gaborit B, Cotillard A, Atassi F, Amour J, Leprince P, Dutour A, Clément K, Hatem SN. Human epicardial adipose tissue induces fibrosis of the atrial myocardium through the secretion of adipo-fibrokines. Eur Heart J 2015;36:795-805.

24. Miksztowicz V, Morales C, Barchuk M, Lopez G, Poveda R, Gelpi R, Schreier L, Rubio M, Berg G. Metalloproteinase 2 and 9 Activity Increase in Epicardial Adipose Tissue of Patients with Coronary Artery Disease. Curr Vasc Pharmacol 2017;15:135-143.

25. Zeller J, Kruger C, Lamounier-Zepter V, Sag S, Strack C, Mohr M, Loew T, Schmitz G, Maier L, Fischer M, Baessler A. The adipo-fibrokine activin A is associated with metabolic abnormalities and left ventricular diastolic dysfunction in obese patients. ESC Heart Fail 2019;6:362-370.

26. Wang Q, Xi W, Yin L, Wang J, Shen H, Gao Y, Min J, Zhang Y, Wang Z. Human Epicardial Adipose Tissue cTGF Expression is an Independent Risk Factor for Atrial Fibrillation and Highly Associated with Atrial Fibrosis. Sci Rep Feb 26 2018;8:3585.

27. Li SJ, Wu TW, Chien MJ, Mersmann HJ, Chen CY. Involvement of pericardial adipose tissue in cardiac fibrosis of dietary-induced obese minipigs- Role of mitochondrial function. Biochim Biophys Acta Mol Cell Biol Lipids Jul 2019;1864:957-965.

28. Horckmans M, Bianchini M, Santovito D, Megens RTA, Springael JY, Negri I, Vacca M, Di Eusanio M, Moschetta A, Weber C, Duchene J, Steffens S. Pericardial Adipose Tissue Regulates Granulopoiesis, Fibrosis, and Cardiac Function After Myocardial Infarction. Circulation Feb 27 2018;137:948-960.

29. Huang H, Amin V, Gurin M, Wan E, Thorp E, Homma S, Morrow JP. Diet-induced obesity causes long QT and reduces transcription of voltage-gated potassium channels. J Mol Cell Cardiol 2013;59:151-158.

30. Bai Y, Su Z, Sun H, Zhao W, Chen X, Hang P, Zhu W, Du Z. Aloe-Emodin Relieves High-Fat Diet Induced QT Prolongation via MiR-1 Inhibition and IK1 Up-Regulation in Rats. Cell Physiol Biochem 2017;43:1961-1973.

31. Main MC, Bryant SM, Hart G. Regional differences in action potential characteristics and membrane currents of guinea-pig left ventricular myocytes. Exp Physiol Nov 1998;83:747-761.

32. Tande PM, Mortensen E, Refsum H. Rate-dependent differences in dog epi- and endocardial monophasic action potential configuration in vivo. Am J Physiol Heart Circ Physiol Nov 1991;261:H1387-1391.

33. Lin YK, Chen YC, Chen JH, Chen SA, Chen YJ. Adipocytes modulate the electrophysiology of atrial myocytes: implications in obesity-induced atrial fibrillation. Basic Res Cardiol Sep 2012;107:293.

3.7 Figures

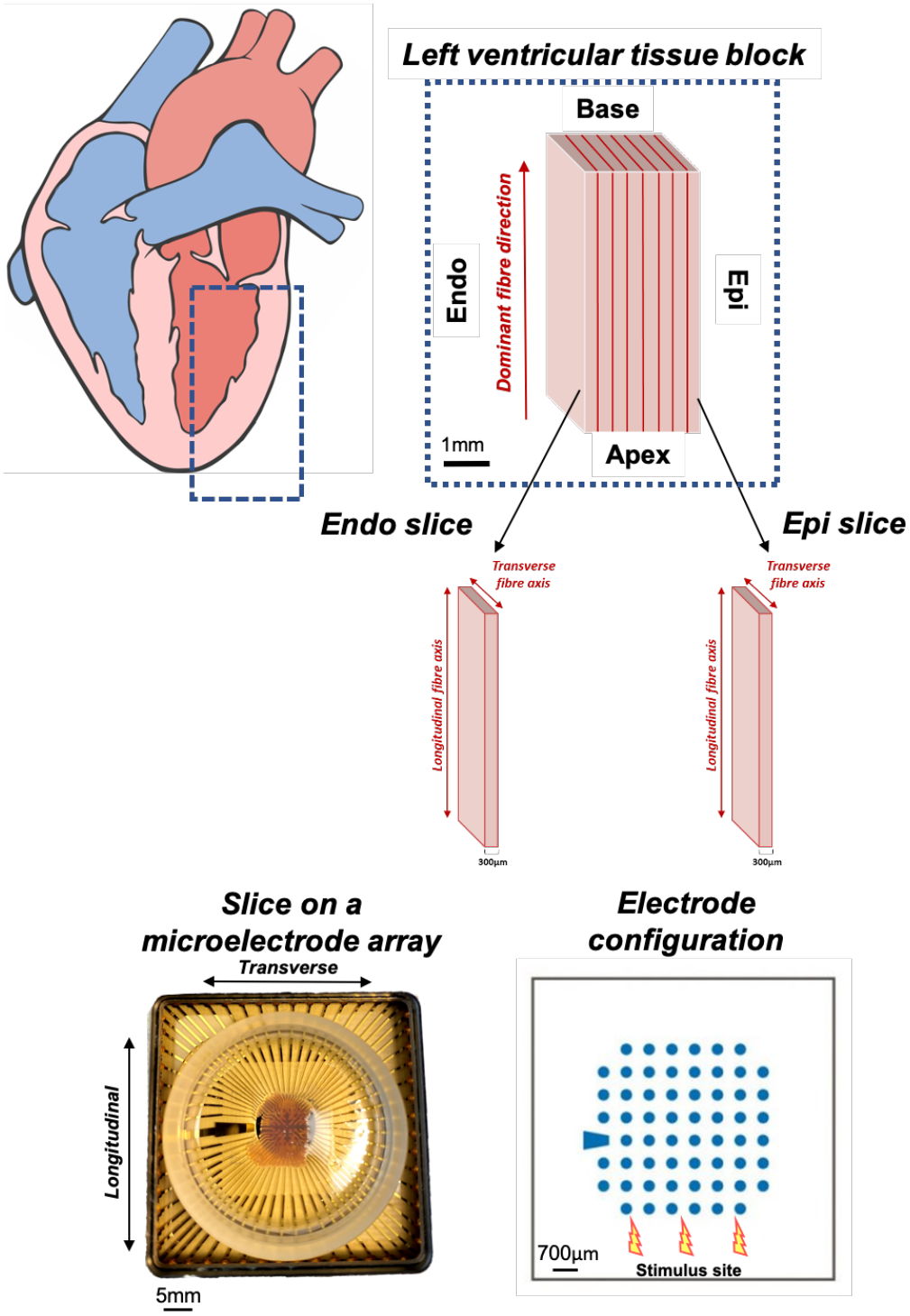

Figure 3.1 Generation of tangential left ventricular cardiac slices. The left ventricular free wall was dissected out of freshly isolated rat hearts. This left ventricular tissue block was then sectioned tangentially to generate individual 300µm slices from each layer of the heart wall, from endocardium to epicardium. Local field potentials were mapped from electrically paced slices using a microelectrode array.

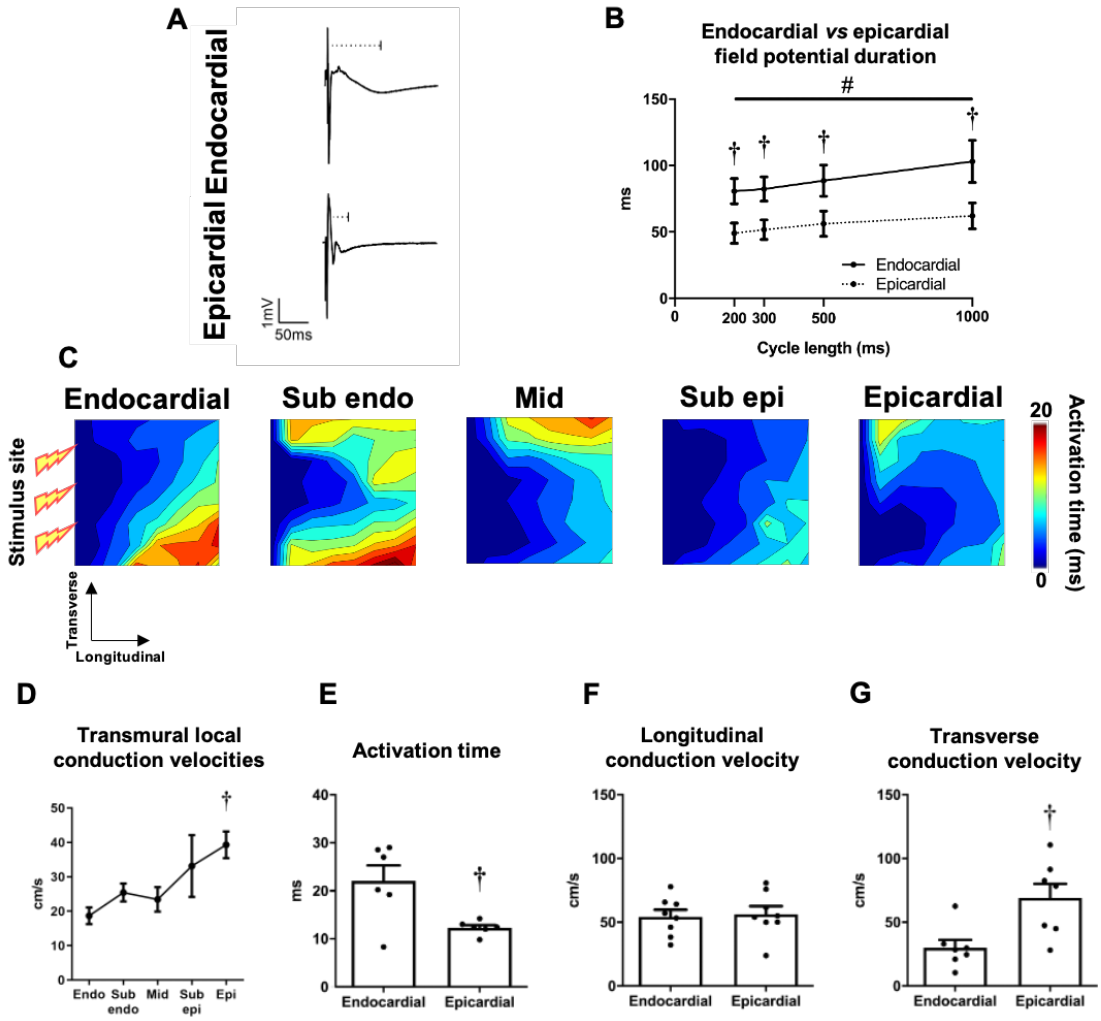

Figure 3.2 A transmural activation and repolarisation gradient is present in the ventricular myocardium. **(A)** exemplar field potential traces from the endocardium and epicardium, with dashed line indicating field potential duration. **(B)** endocardial and epicardial field potential duration:cycle length relationship. **(C)** exemplar activation maps from endocardial through to epicardial slices (isochrones indicate 2ms), with **(D)** mean local conduction velocities. Mean endocardial vs epicardial: activation time **(E)**, longitudinal conduction velocity **(F)** and transverse conduction velocity **(G)**. Two-way repeated measures ANOVA with Sidak's multiple comparisons **(B)**, one-way repeated measures ANOVA with Dunnett's multiple comparisons **(D)** or paired t-tests **(E-G)**. $^{\#}P<0.05$, cycle length effect and $^{\dagger}P<0.05$ transmural region effect (*vs* endocardium), respectively; $n=7$.

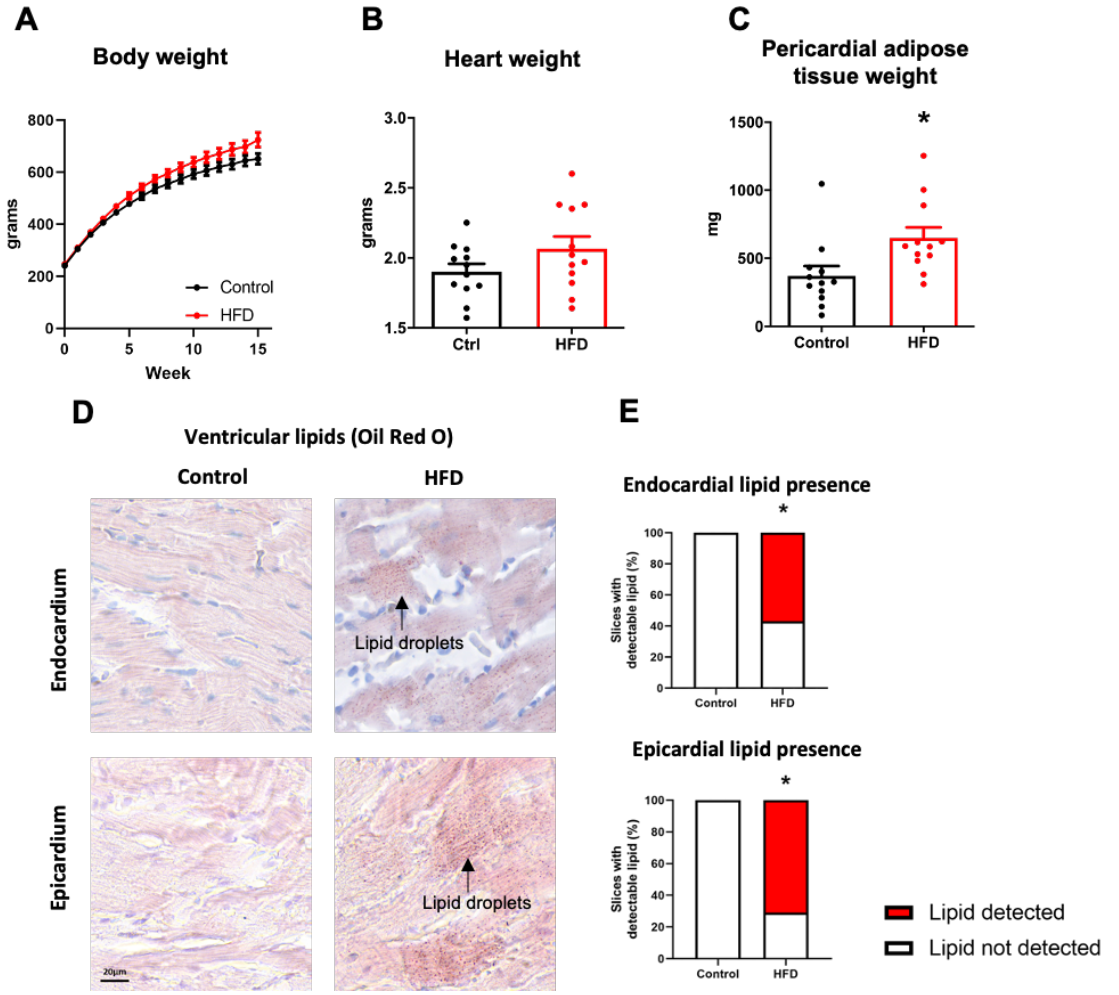

Figure 3.3 High fat feeding is associated with augmented pericardial adiposity and cardiac lipid accumulation. **(A)** body weight, **(B)** heart weight and **(C)** pericardial adipose tissue weight from control fed and high fat diet (HFD) fed animals. **(D)** exemplar endocardial and epicardial sections stained with Oil Red O (lipid staining is indicated and stained as red puncta). **(E)** Quantified detection of lipid in the endocardium (top) and epicardium (bottom) of control and HFD rats. Two-way repeated measures ANOVA **(A)**, unpaired t-tests **(B-C)** and Fisher's exact test **(E)**. **P*<0.05 between diets; *n*=7-12.

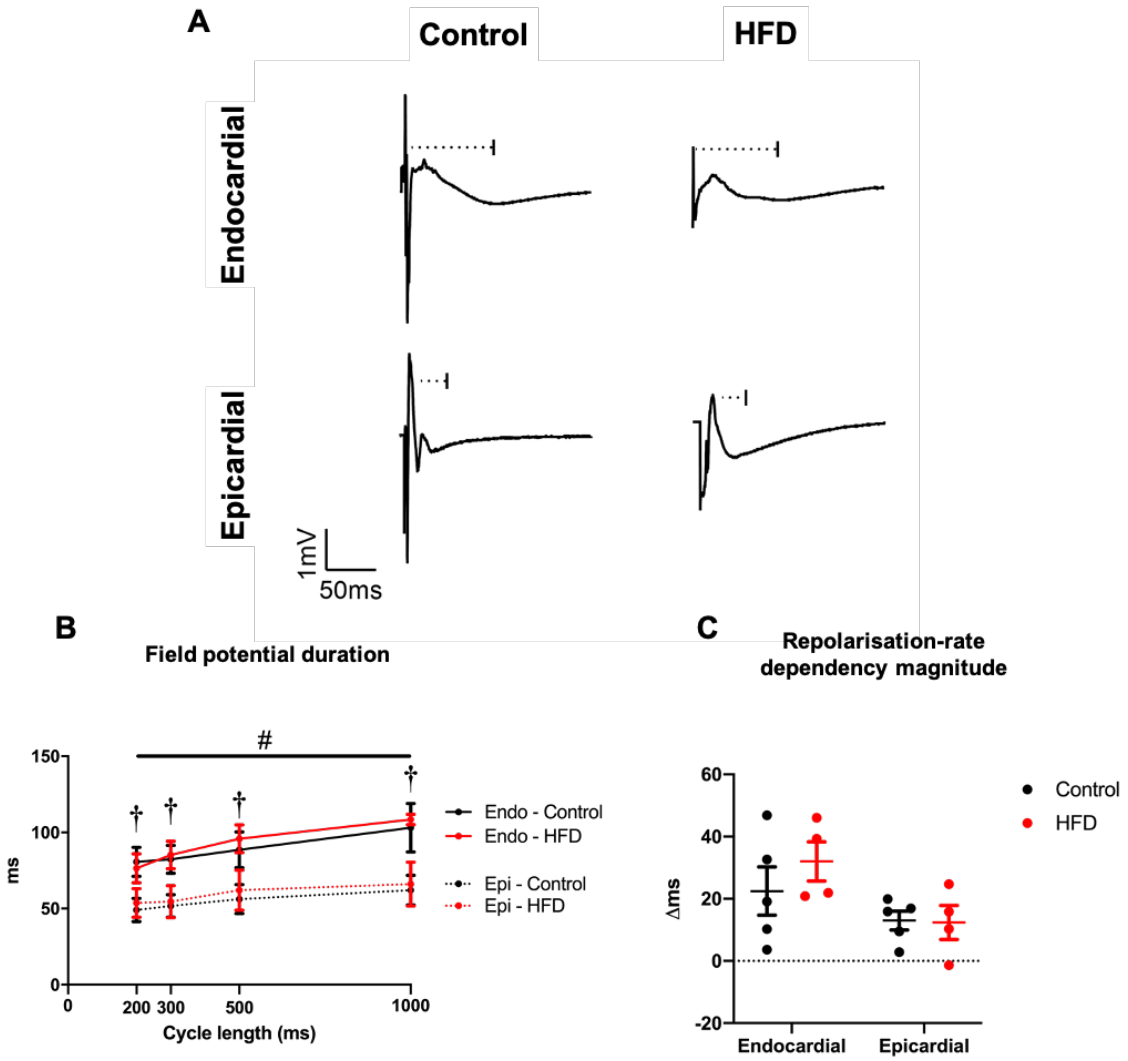

Figure 3.4 High fat feeding does not affect ventricular repolarisation. **(A)** exemplar endocardial and epicardial field potentials from control and high fat diet (HFD) rats (dashed line indicates the measure of field potential duration). **(B)** endocardial and epicardial field potential duration in control and HFD rats. **(C)** magnitude of the repolarisation-rate dependency relationship (calculated as the difference between field potential duration at 1000ms and 200ms cycle length). Three-way **(B)** or two-way **(C)** repeated measures ANOVAs. $^{\#}P<0.05$ for cycle length effect and $^{\dagger}P<0.05$ for transmural region effect for both diets; n=4-5.

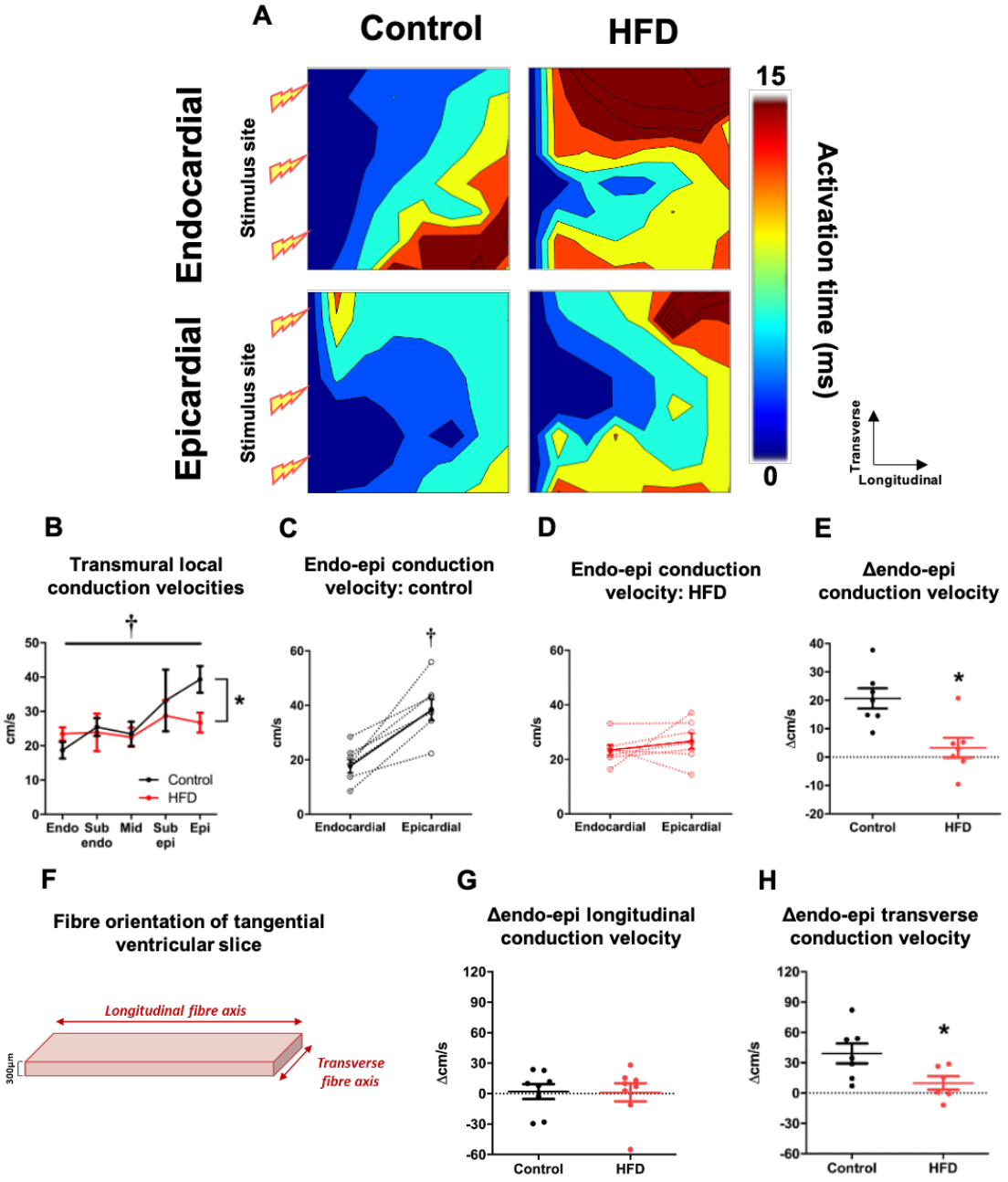

Figure 3.5 High fat feeding is associated with slowed epicardial conduction velocity. **(A)** exemplar activation maps from endocardial and epicardial slices in control and high fat diet (HFD) rats (isochrones indicate 3ms). **(B)** Local conduction velocities from slices across the heart wall. Endocardial to epicardial conduction velocity gradient in control **(C)** and high fat diet **(D)** rats (dashed line indicates individual animals; solid line is mean±standard error) and **(E)** change in conduction velocity from endocardium to epicardium. **(F)** slice schematic indicating longitudinal and transverse fibre/conduction pathways, with change from endocardium to epicardium in longitudinal **(G)** and transverse **(H)** conduction velocities. Two-way repeated measures ANOVA and Sidak's multiple comparisons test **(B)** or unpaired t-tests **(C-E; G & H)**. * and † indicate $P<0.05$ for diet and transmural region effects, respectively; $n=7$.

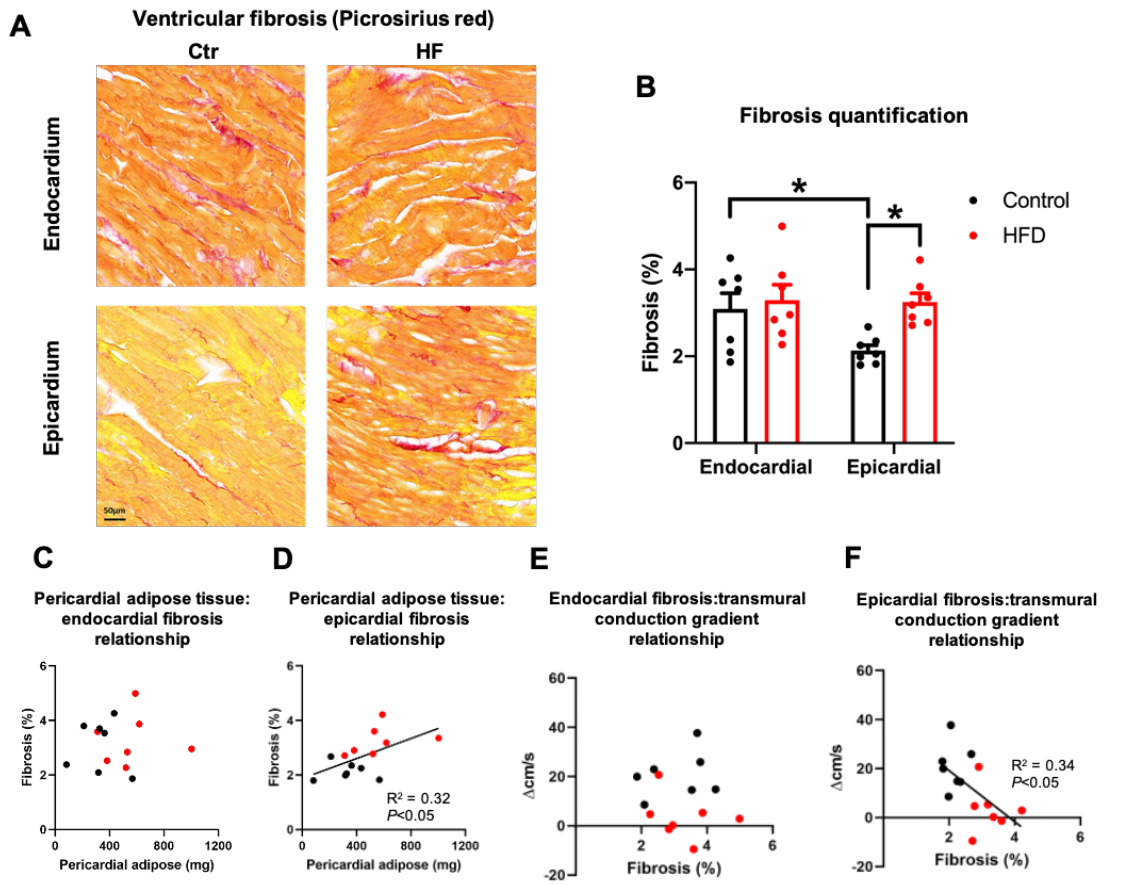

Figure 3.6 Augmented pericardial adiposity associates with epicardial fibrosis to dictate the transmural conduction gradient magnitude. **(A)** exemplar Picrosirius red-stained sections, indicating fibrosis (red) and quantified percentage fibrosis **(B)**. Pericardial adipose:endocardial fibrosis **(C)** and pericardial adipose:epicardial fibrosis **(D)** relationships. **(E)** endocardial fibrosis:transmural conduction velocity gradient relationship and **(F)** epicardial fibrosis:transmural conduction velocity gradient relationship. Two-way repeated measures ANOVA and Sidak's multiple comparisons test **(B)** or linear regression **(C-F)**, **P*<0.05; *n*=7.

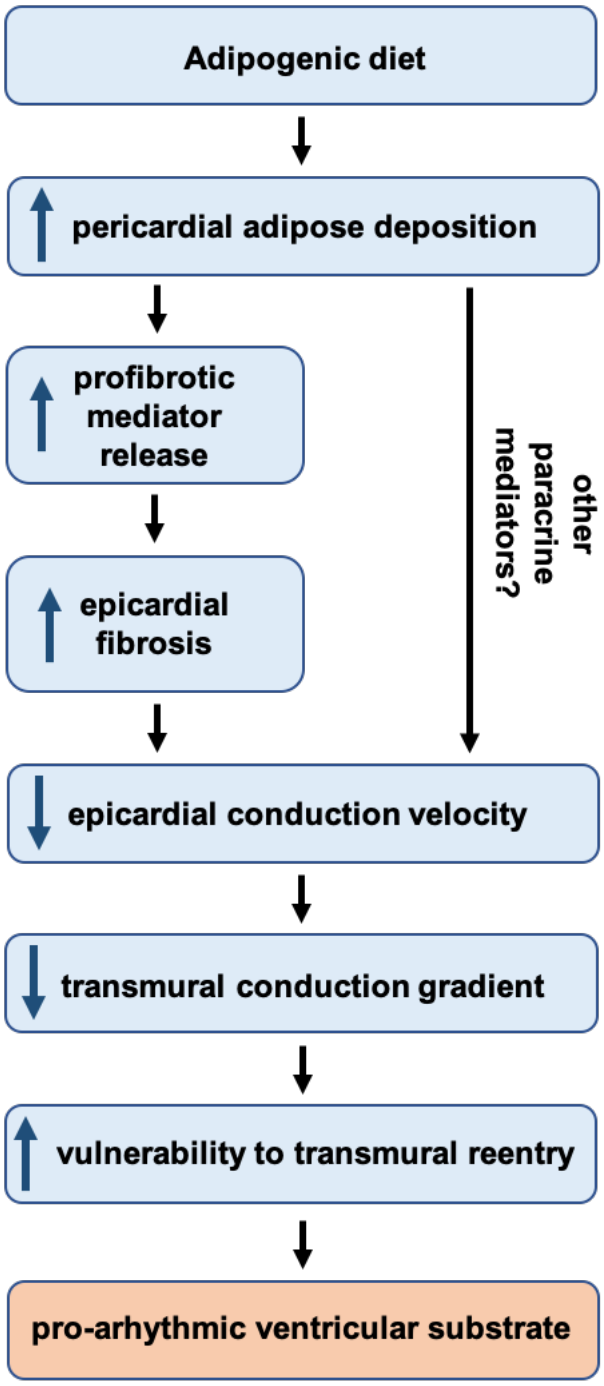

Figure 3.7 Illustrative summary of the potential relationship between elevated pericardial adiposity and ventricular arrhythmia vulnerability. A diet with a high fat content increases the amount of pericardial adipose. This potentially increases the amount of pericardial adipose-derived profibrotic mediators being released onto the epicardium – promoting local epicardial fibrosis. Fibrosis disrupts cell-cell conduction velocity in the epicardium, diminishing the normal endocardial-epicardial conduction gradient. This potentially predisposes to action potential reentry (i.e. retrograde action potential propagation from epicardium to endocardium), generating a pro-arrhythmic left ventricular substrate.

3.8 Supplementary Methods

Animal details

Experiments were conducted in accordance with the Guide for the Care and Use of Laboratory Animals, National Health and Medical Research Council/Commonwealth Scientific and Industrial Research Organisation/ACC Australian Code of Practice for the Care and Use of Animals for Scientific Purposes (1997), as approved (University of Melbourne Animal Ethics Committee).

8-week-old Male Sprague Dawley rats were fed either a control (Specialty Feeds, SF13-081; 12% lipid energy intake) or high fat diet (HFD; SF04-001; 43% lipid intake) for 15-16 weeks. Food and water were available *ad libitum* and intake and body weights monitored weekly.

Cardiac slice preparation

Tangential left ventricular slices were generated using a modified version of previously published protocols (**Figure 3.1**).[13, 14] At age 23-24 weeks, rats were anaesthetised with isoflurane and decapitated. Pericardial adipose tissue and hearts quickly excised, then manually massaged for 5-10s to clear blood in 37^{o}C heparinised superfusion Tyrode's buffer (in mM: NaCl, 140; KCl, 4.5; glucose, 10; $MgCl_2$, 1; HEPES, 10; $CaCl_2$, 1.8; all purchased from Sigma-Aldrich, New South Wales, Australia). Hearts were then weighed and transferred to heparinised ice-cold oxygenated Tyrode's slicing buffer (in mM: NaCl, 140; KCl, 6; glucose, 10; $MgCl_2$, 1; HEPES, 10; $CaCl_2$, 1.8; 2,3-Butanedione, 30). Atria were resected, then the left ventricular free wall was carefully dissected away and glued epicardial side down onto an agarose-coated specimen holder using Histoacryl surgical

glue (B. Braun, Hessen, Germany). The specimen holder was then transferred into a vibratome bath (7000smz-2, Campden Instruments, UK) containing oxygenated Tyrode's slicing buffer (4°C).

300µm tangential sections were made from endocardium to epicardium, cutting along the longitudinal axis of the myocardium using a ceramic blade (0.03mm/s advance speed, 2mm amplitude, 80Hz frequency, <1µm z-axis error), yielding 8-10 slices/heart on average. Slices were immediately placed on cell strainers and incubated in oxygenated Tyrode's slicing buffer (4°C) for <3hr before electrophysiological mapping.

The endocardial slice was defined as the first (after trabeculae carneae removal), and the epicardial slice the final, intact section to detach from the tissue block. Since the tissue was glued epicardial side down, approximately 100µm of epicardium remained attached to the tissue block and was not viable for recordings.

Microelectrode array recordings

For electrophysiological mapping, slices were trimmed into a rectangular shape so longitudinal and transverse muscle fibres were clearly distinguishable. Fibre-aligned slices were then positioned on a microelectrode array consisting of 60 gold recording electrodes embedded into a glass substrate in an 8x8 matrix (100µm electrode diameter, 700µm spacing; 60EcoMEA-Glass-pr, Multichannel systems, Reutlingen, Germany). Slices were secured using a custom-made tissue weight and continuously superfused with oxygenated Tyrode's superfusion buffer (37°C, 4ml/min). Extracellular field potentials were recorded (MEA2100-System, Multichannel Systems) using MC_Rack

(V4.6.2, Multichannel Systems) software sampling at 10KHz (low pass filter: 3,500Hz, high pass filter: 10Hz).

Slices were given a 3-5min equilibration period, then paced along their longitudinal axis using electrodes at the periphery of the tissue at a cycle length of 1000ms (biphasic pulse at ±1.5V [approx. twice diastolic threshold], 1ms pulse width) for a further 2-3min. After this period, slices were subjected to a ramp pacing protocol of: 1000ms, 500ms, 300ms and 200ms cycle lengths (50 pulses/cycle length).

Electrophysiological analysis

All analyses were performed using the last beats of a single cycle length in the ramp protocol to allow for sufficient rate adaptation. Analysis of conduction velocity and generation of activation maps was performed using a MATLAB-based script[14, 15] at a cycle length of 200ms. Field potential duration was calculated as the interval between the first negative peak on the field potential and the final negative deflection.

Histology

At the end of the electrophysiological mapping protocol, slices were fixed in 10% formalin (Sigma Aldrich, Cat #: HT501128-4L). Slices were serially dehydrated in 15% and 30% sucrose solutions, embedded in optimal cutting temperature compound (Agar Scientific, Essex, UK, Cat #: AGR1180) and frozen gradually using isopentane. Frozen tissue was then cryosectioned to generate 10µm sections and stained with either Picrosirius red to identify Collagen Type I and III or Oil Red O to identify lipids.

Stained tissue sections were scanned using the Panoramic SCAN II slide scanner (3DHISTECH, Budapest, Hungary). For collagen analysis, five regions of interest per tissue

section were exported from CaseViewer (V2.3, 3D HISTECH) for analysis in ImageJ (V1.8, Maryland, USA; *n*=15-20 regions of interest across 3-4 10µm sections per left ventricular slice). The images were converted to RGB stacks and a thresholding approach used to detect presence of collagen.[16] Oil Red O-stained whole sections were visualised to detect presence or absence of lipid staining. All histological analyses were performed blinded.

Statistical analysis

Normally distributed data are presented as mean± standard error of the mean. Outliers were excluded if >2 standard deviations from the mean, and only data where paired endo-epi recordings from a single heart are included. Statistical tests performed are indicated in the Figure legends throughout. $P<0.05$ was deemed significant and *n* denoted the number of animals/slices used.

Chapter 4

High-throughput examination of the electrophysiological properties of cultured cardiomyocytes from different origins

Manuscripts generated from this chapter:

Wells SP, Waddell HM, Sim CB, Lim SY, Bernasochi GB, Pavlovic D, Kirchhof P, Porrello ER, Delbridge LMD, Bell JR. Cardiomyocyte functional screening - interrogating comparative electrophysiology of high-throughput model cell systems. ***Am J Physiol Cell Physiol***, 317: (6), C1256-C1267

Abstract

Arrhythmias are characteristic of many cardiovascular diseases in males and females, though onset and outcomes differ markedly between sexes. Novel anti-arrhythmia therapies are required to overcome current drug limitations associated with efficacy and side effects. Cardiomyocytes cultured on microelectrode arrays (MEAs) offer a high-throughput anti-arrhythmic drug screening platform, but comparative information about electrophysiological properties of commonly used culture types is lacking. Cultured cardiomyocyte-MEA preparation standardisation is required to advance its application as a high-throughput system for anti-arrhythmic drug screening. The aims of this study were to characterise the electrophysiology of male and female primary cardiomyocyte cultures, and to directly compare the electrophysiological properties of two frequently used cardiomyocyte cultures. Neonatal rat ventricular myocytes (NRVMs) and custom-generated human iPSC-derived cardiomyocytes (hiPSC-CMs) were cultured on MEAs for 48-120 hours. Field potentials and activation patterns were recorded in the absence/presence of the β-adrenoceptor agonist isoproterenol (1µM). Basal and β-stimulated electrophysiology did not differ between male and female NRVMs. Both NRVMs and hiPSC-CMs exhibited rate-dependent field potential durations and were similarly responsive to isoproterenol. Field potential amplitude was greater in NRVM *vs* hiPSC-CM. Time post differentiation induction was a key factor in hiPSC-CM electrical stability. This is the first study to compare intrinsic electrophysiological properties of commonly used cardiomyocyte cultures. These findings offer important comparative data informing on methodological approaches for functional screening investigations into cardiomyocyte arrhythmogenesis and anti-arrhythmic compounds.

Key words

Microelectrode array, cardiomyocyte electrophysiology, neonatal rat ventricular myocytes, human iPS-derived cardiomyocytes.

Abbreviations

human induced pluripotent stem cell-derived cardiomyocytes, hiPSC-CMs; microelectrode array, MEA; neonatal rat ventricular myocytes, NRVMs.

4.1 Introduction

Cardiac arrhythmia is a clinical feature of various cardiovascular diseases, including heart failure, stroke, and ischemic heart disease. The most common arrhythmia is atrial fibrillation which has multiple risk factors/comorbidities including aging, obesity and genetic mutations (1-3). Atrial fibrillation alone is not lethal but increases the risk of thrombotic stroke and heart failure. Ventricular arrhythmias are less common, but often severe and increase susceptibility to sudden cardiac death (4). Patients at risk of ventricular arrhythmias can undergo defibrillator implantation, which is effective in some settings, but is expensive and coupled with a considerable morbidity profile (5). Numerous anti-arrhythmic therapies are available, although there is often incomplete effectiveness or significant side effects restricting their use (5-7). Improving the current cellular electrophysiological understanding of cardiac arrhythmogenesis is required to further the development of more efficacious novel treatments.

Microelectrode array (MEA) technology is commonly used in pre-clinical studies of cardiomyocyte electrophysiology and arrhythmogenesis. MEAs are devices embedded with low-impedance electrodes arranged in a grid matrix, designed for synchronised, non-invasive, multifocal recordings across cardiac preparations. Cardiomyocytes cultured on MEAs offer a high-throughput screening platform for compounds with anti-arrhythmic/cardiac electrophysiology-modifying potential, enabling the evaluation of conduction properties (8).

Cardiomyocyte studies have traditionally relied on isolated neonatal rodent ventricular myocytes or a limited number of immortalised cell lines (9,10). Recently, inducible

pluripotent stem cell preparations have become more widely utilised (11). Comparative benchmarking of the electrophysiological properties of these cells has not been extensively examined in a direct approach.

Neonatal rat ventricular myocytes (NRVMs) and human induced pluripotent stem cell-derived cardiomyocytes (hiPSC-CMs) can be maintained in culture over multiple days-weeks. NRVMs cultured as a monolayer are immature cardiomyocytes, exhibiting minimal proliferation with ability to re-form "native-like" gap junctions (10). NRVM cultures are usually sourced from mixed male and female litters, without concern for potential sex-specific cardiac electrophysiological differences. This may be an important oversight, as a growing literature base describes numerous differences in male and female cardiac physiology and pathology. Women have faster heart rates, longer rate-corrected Q-T intervals and steeper electrical restitution (QT-RR relationship) than men (12-14). On a cellular level, action potential durations are typically greater in females (particularly at long cycle lengths), and Ca^{2+} transient rise time and decay is prolonged compared to males (15,16). The incidence of atrial fibrillation is 1.6-2.7% in women *vs* 3.8-4.7% in men (17). Conversely, mortality and incidence of arrhythmias caused by antiarrhythmic drugs is lower in men than age-matched women (16,18,19).

hiPSC-CMs are generated from induced pluripotent stem cells differentiated toward the cardiac lineage. Though expensive, they can be mass produced, recapitulate the adult human cardiac ion channel profile action potential characteristics to a degree, and can be commercially obtained or created locally by established differentiation protocols (11,20). Similar to NRVMs, hiPSC-CMs are immature and beat spontaneously (11). Therapeutically, there is developing interest in the regenerative ability of hiPSC-CMs and

hence usage of these cells to advance the cardiomyocyte electrophysiology knowledgebase (21).

Both NRVMs and hiPSC-CMs have been used for disease modelling and drug screening; however, a direct electrophysiological comparison between these cultures has not been previously reported, hence little information is available to assist in determining which culture type is best suited to specific experimental applications. Here, the basal and β-adrenergic-stimulated electrophysiological characteristics of spontaneously beating NRVMs and hiPSC-CMs were directly examined.

The aims of this investigation were to:

1. characterise the electrophysiology of male and female primary cardiomyocyte cultures
2. compare the electrophysiological characteristics of two routinely used cardiomyocyte cultures to provide a standardised framework for potential purpose-driven modelling of disease scenarios, aiding researchers with the appropriate selection of cultures for their enquiries.

This study demonstrates for the first time that primary cardiomyocytes derived from different sexes exhibit similar beating rates, conduction velocities, repolarisation durations and β-adrenergic sensitivity. Beating rates are different between NRVMs and hiPSC-CMs, but repolarisation characteristics and β-adrenergic responsiveness is comparable. These findings provide key novel insight for pre-clinical studies and high-throughput drug screening trials using cultured cardiomyocytes and the MEA platform.

4.2 Materials and methods

Neonatal rat ventricular myocyte culture

Experiments were conducted, and animals handled in the manner specified by the NHMRC/CSIRO/ACC Australian Code of Practice for the Care and Use of Animals for Scientific Purposes (2013) and the EU Directive 2010/63/EU for animal experiments, with approval and oversight of the project by the University of Melbourne Animal Ethics Committee. For NRVMs, cells were isolated from Sprague Dawley litters (postnatal day 2) as previously described (22). Briefly, pups were decapitated, hearts quickly excised, and atria resected. Ventricles were dissected into small fragments and gently swirled in 0.5% collagenase II (Worthington, LS004176) for 15min at 37^{o}C.

Single NRVMs were isolated by Trypsin digestion (0.06%, Sigma, T9201) in Hanks' balanced salt solution + 0.02% DNAse 1 (Calibiochem, 260913), then digestion inhibited with the addition of new-born calf serum. NRVMs were centrifuged at 990g at 4^{o}C for 10min and the cell pellet resuspended in Dulbecco's Modified Eagle Medium + GlutaMAX (ThermoFisher, 10565-042), supplemented with: 5% horse serum (ThermoFisher, 16050-122), pyruvic acid (3mM, Sigma, P-8574), bovine serum albumin (2g/L, Sigma, A-7030), ampicillin (100µg/ml, Sigma, A-0166), insulin-transferrin-selenium 100x (ThermoFisher, 41400045), antibiotic/antimycotic (1%, ThermoFisher, 15240062), linoleic acid (5µg/ml, Sigma, L5900) and ascorbic acid (100µM, Sigma, A4544), then pre-plated to remove fibroblasts (2x30min, 37^{o}C, 5% CO_2). Purified NRVMs were seeded onto MEAs pre-coated with fibronectin (10µg/ml, Sigma, F2006) by pipetting a 75µl droplet of 300,000 NRVMs across the central recording matrix. Stable droplet formation was facilitated through increasing MEA hydrophobicity by heating to

70°C for ≥2hr prior to fibronectin coating. Droplet-seeded NRVMs were incubated for 2hr to promote adhesion, with culture media subsequently added to a final volume of 1ml (300,000 cell/ml of media, final density of ~1,000,000 cells/cm^2). Media was changed after 48hr. MEA experiments were performed 5-6 days post isolation – a timepoint previously established to demonstrate stable beating rate, field potential amplitude and conduction velocity (10,23).

Human induced pluripotent stem cell-derived cardiomyocyte culture

hiPSC-CMs were cultured and differentiated as previously described (24-26). Briefly, hiPSCs (line PB004.4 female, Murdoch Children's Research Institute) were cultured in a 75cm^2 tissue culture flask with hiPSC media (DMEM/F12 (Gibco, 11320033), 20% (v/v) knockout serum replacement (Gibco, 10828028), 1X non-essential amino acids (Gibco, 11140050), 1X GlutaMAX (Gibco, 35050061), penicillin/streptomycin (Gibco, 15140122), 110µM 2-mercaptoethanol (Gibco, 21985023), 5ng/mL recombinant human FGF (R&D, 233-FB-025)) on irradiated mouse embryonic fibroblasts and passaged using TrypLE Express enzyme (ThermoFisher, 12604013). One day before differentiation, 1.6x10^5 cells/cm^2 were seeded. To induce differentiation (Day 0), cells were treated with basal differentiation media [RPMI (Gibco, 21870076), B27 minus vitamin A (Gibco, 12587010) and 50µg/ml ascorbic acid (Sigma, A8960) supplemented with 10µM CHIR99021 (Tocris Bioscience, 4423) and 80ng/ml Activin A (Peprotech)]. On Days 1, 3 and 5, media were changed to basal differentiation media supplemented with 5µM IWR-1 (Sigma, I0161). Cells were maintained in basal differentiation medium from Day 7 until used.

For experiments, cells were dissociated with TrypLE, centrifuged (200g, 4°C, 3min), carefully resuspended in basal differentiation medium and re-plated at 800,000 cells/ml

as clusters across Geltrex-coated microelectrode arrays (Geltrex, 1:100, Life Technologies, A1413202). Media was changed after 48hr and experiments performed the following day.

Microelectrode array configurations

The MEA2100 2x60 system (Multichannel systems, Reutlingen, Germany) was used to record extracellular field potentials (**Figure 4.1**). An MEA was composed of 60 gold electrodes implanted into a glass plate fabricated with a layer of the conductive polymer poly(3,4-ethylenedioxythiophene). Two electrode layouts were used (1) 30µm diameter with 200µm spacing or (2) 100µm diameter with 700µm spacing – recordings were consistent between configurations.

Electrophysiological recordings

Cardiomyocyte cultures were maintained at 37^{o}C and field potential recordings acquired at 10kHz using Cardio2D (Multichannel Systems). All comparable experimental recordings began after a 10min equilibration period. To assess NRVM stability, 2min recordings were obtained at 0, 15 and 35min. To assess hiPSC-CM stability, 2min recordings were made at 10min intervals over 1hr. A subgroup of NRVMs and hiPSC-CMs were treated with the β-adrenergic agonist, isoproterenol (1µM, 3-5min), which has previously evidenced strong electrophysiological responses in NRVMs (27).

Electrophysiology analysis

Spontaneous beating rate was calculated by averaging the inter-spike interval between 10 consecutive beats. Field potential duration was determined as the time between the maximal negative deflection and the peak of the final positive deflection (**Figure 4.1D**;

(28,29). For NRVMs, this was computed by ensemble averaging across 10 beats at 10 sites across an MEA. Activation maps for NRVMs were generated by calculating the delay in depolarisation between neighbouring electrodes using a multi-vector approach and mean conduction velocity computed across 10 consecutive beats. Due to the clustered nature of hiPSC-CMs, field potential duration was averaged from 10 consecutive beats at a single site, and it was not possible to reliably map signal propagation to study activation patterns. Analysis was completed using Cardio2D+ software, with arrhythmic cardiomyocyte cultures omitted.

Statistics

Data are expressed as mean±standard error. Statistical analysis was performed, and graphs generated using GraphPad Prism 8.0. Relevant statistical analyses are indicated throughout and $P<0.05$ defining statistical significance. *N* denotes the number of cultures and *n* denotes the number of MEAs.

4.3 Results

NRVM cultures from both sexes display comparable electrophysiology

Basal electrophysiology was compared in NRVMs isolated from males and females. In both sexes, spontaneous beating rate and conduction velocity was consistent over a 35min recording period, and only slight changes in the morphology of field potentials were observed (**Figure 4.2A-D**). Field potential amplitude:conduction velocity relationships were similar between male and female NRVMs (**Figure 4.2E**).

A subset of cardiomyocytes was subsequently treated acutely with 1μM isoproterenol to evaluate the response to β-adrenergic stimulation. Male and female NRVMs both showed an increase in spontaneous beating rate, decrease in field potential duration, and unchanged field potential amplitude (**Figure 4.3A-E** and **S4.1A-C**). Conduction velocity significantly increased comparably in NRVMs from both sexes (**Figure 4.3F** and **S4.1D**).

Basal electrophysiology is defined by cardiomyocyte origin

The electrophysiology of two routinely used cardiomyocyte culture types, NRVMs and hiPSC-CMs, were compared. Significant differences in the electrophysiology of both cell types were apparent (**Figure 4.4A**). Spontaneous beating rate was faster in hiPSC-CMs compared with NRVMs (**Figure 4.4B**, beats per minute; NRVMs *vs* hiPSC-CMs; 81.5±6.9 *vs* 162.5±38.0, $P<0.05$). NRVMs exhibited a significantly larger field potential amplitude compared with hiPSC-CMs (**Figure 4.4C**, mV; 2.95±0.58 *vs* 0.40±0.09; $P<0.05$), whilst field potential duration was comparable (**Figure 4.4D**, ms; 184.0±10.5 *vs* 146.9±23.2; $P<0.05$). NRVMs and hiPSC-CMs displayed distinct beating rate:field potential duration

relationships, although both cell types did demonstrate faster repolarisation at higher beating rates (**Figure 4.4E**, $P<0.05$). The gradient of this relationship was significantly steeper in NRVMs ($P<0.05$), although when excluding hiPSC-CMs with a beating rate >150BPM, gradients were comparable (**Figure 4.4F**, $P<0.05$, linear regression).

β-adrenergic stimulated responses were not different between NRVMs and hiPSC-CMs, with similar increases in spontaneous beating rate (**Figure 4.5A-C** and **S4.2A**) and concomitant shortening of field potential duration (**Figure 4.5D-F** and **S4.2B**).

hiPSC-CM electrophysiology is dependent upon time post differentiation

Greater variability between experimental replicates was displayed in hiPSC-CMs *vs* NRVMs. Further analysis was performed to determine whether the hiPSC-CMs needed longer on the MEA to stabilise before making a comparable recording, or whether the timepoint between differentiation induction (D0) and plating onto the MEA was a determining factor (**Figure 4.6**). Spontaneously beating hiPSC-CMs were recorded over 1hr, with a measurement made every 10min (in this instance, the first was immediately after securing the MEA onto the recording headstage). Over 1hr, there was no significant change in spontaneous beating rate, field potential duration or amplitude (**Figure 4.6A-D**). In the first 10min (t=-10min to 0min), however, there was a strong trend for an increase in beating rate and paired reduction in field potential duration, which stabilised thereafter – indicating the decision to make comparisons after this 10min was important.

hiPSC-CMs reseeded onto MEAs early post differentiation induction displayed faster spontaneous beating rates and shorter repolarisation times (**Figure 4.6E-G**).

Isoproterenol sensitivity decreased in cells reseeded at a later timepoints. Cells reseeded onto MEAs at Day 20 and 44 displayed greater increases in spontaneous beating rate than those replated at Day 69 (**Figure 4.6H**). Change in field potential duration in response to isoproterenol treatment was, however, consistent across all reseeding timepoints (**Figure 4.6I**).

4.4 Discussion

This is the first study to directly compare the inherent electrophysiological differences between commonly used cultured cardiomyocytes of different sex and origin. This investigation highlights that NRVM monolayer electrophysiology does not differ with sex – supporting the established use of combined male and female cardiomyocytes. Importantly, this study yields new insight into the electrophysiology of two commonly used cardiomyocyte cultures from different origin. NRVMs exhibit a slower beating rate and greater amplitude than hiPSC-CMs yet have similar repolarisation times and β-adrenergic responsiveness. Also shown is the association between hiPSC-CM electrophysiological variability with time post differentiation induction. These results give novel insights into the selection criteria of appropriate culture models to specific experimental questions.

Cultured primary cardiomyocyte sex does not influence electrophysiology

NRVMs and hiPSC-CMs are two of the most routinely used cultures for drug screening investigations. NRVMs exhibited rapid conduction velocities (**Figure 4.3B&F**), particularly in comparison to HL-1 cells (approximately 20-fold faster than HL-1 (30)), though slower than typical conduction velocities of 60-75cm/s intact rodent and human tissue preparations (31-33).

A possible oversight in the traditional use of NRVMs has been pooling cells from male and female pups. Although cardiovascular disease is the primary cause of death in both sexes, onset, progression and pathological profile differs between males and females (34). Sex differences in cardiomyocyte electrical and mechanical function is being

progressively recognised (35,36). NRVM data here indicate sex does not influence basal or β-stimulated electrophysiological characteristics in the cultured neonatal cells. This contrasts with data from freshly-isolated adult ventricular cardiomyocytes (19,37,38), potentially implicating a role for sexual maturity and differences in sex steroid balance. There may also be a role for absence of sex steroids in the culture medium over the 5-6 days of culture. This may cause changes in gene expression that attenuate the sex differences. Regardless, our data validate the pooling NRVMs from both sexes as a model for studying cardiomyocyte electrophysiology.

NRVMs and hiPSC-CMs exhibit distinct basal, but similar β-stimulated, electrophysiology

Simultaneous extracellular-intracellular recordings on cell and tissue preparations have previously demonstrated positive interactions between action potential and field potential waveforms (28,29). Our data add to this, showing that the action potential amplitude:conduction velocity relationship is also evident in extracellular recordings - whereby field potential amplitude correlated with conduction velocity in NRVMs (**Figure 4.2E**) and cultures displayed repolarisation-rate dependency (**Figure 4.4E&F**). In cultures with a beating rate of ≤150beats per minute, the rate-dependency relationships were comparable between hiPSC-CMs and NRVM monolayers (**Figure 4.4F**). This relationship between pacing rate and action potential duration is a fundamental property of cardiomyocytes (39). Exhibition of these adult cardiomyocyte properties (traditionally recorded with intracellular electrodes) in both cultured cardiomyocyte preparations indicates their validity as a model for anti-arrhythmic drug screening on the MEA platform.

The hiPSC-CM differentiation protocols used in experiments presented here yields cells primarily of ventricular origin (24). It is not, therefore, surprising that hiPSC-CMs exhibited similar electrophysiological characteristics to NRVMs, especially in relation to repolarisation durations and β-adrenergic stimulated responsiveness.

One single stem cell pool was used to re-differentiate hiPSC-CMs used for each culture (*N*) presented in these data. Although good reproducibility in electrophysiological parameters was evident, spontaneous beating rate and therefore field potential duration were dependent on the number of days post-differentiation. hiPSC-CM electrophysiology was unstable at 20 days post differentiation induction, potentially indicating an immature/developing phenotype. This emphasizes the importance of using cultures which have undergone a sufficient period of maturation (≥30 days) post induction of differentiation. Consistency in beating rates from Day 30-60 and reduced isoproterenol responsiveness (**Figure 4.6E&H**) was apparent and is supported by data from others (40). The responsiveness of these cultures to isoproterenol, particularly from Day 30-44, indicates their potential usefulness as a platform to study repolarisation-rate dependency interactions in arrhythmogenesis processes. In particular, they may be useful for screening drugs which modulate β-adrenergic stimulation/sympathetic innervation and alternans-based arrhythmias.

In this study, hiPSC-CMs did not form confluent monolayers and the capacity to assess conduction velocity was limited across large microelectrode arrays (area, 1.6-5.6mm^2). Similar clustered recordings have been reported (20,41). Unlike hiPSC-CMs used here, commercially available hiPSC-CMs can form electrically coupled monolayers; however, often lack responsiveness to β-adrenergic stimulation, suggesting less mature

phenotypes (42-44). This lack of monolayer connectivity may too be a factor responsible for lower field potential amplitudes seen in hiPSC-CMs than NRVM (**Figure 4.4A&C**). A component, namely the upstroke, of the field potential amplitude is a result of capacitive currents flowing from cell-to-cell (45). This current is likely lower in hiPSC-CM clusters *vs* NRVM monolayers, explaining, at least in part, the reduced amplitude.

Potential purpose-driven uses for NRVMs and hiPSC-CMs

The direct comparison between NRVM and hiPSC-CM electrophysiology can be used to provide insight into scenarios where it might be important to use a particular cell type to model a disease or test a specific drug. Although cultured cardiomyocytes do not recapitulate the complexity of an *in vivo* situation, they do allow study of the direct effects of compounds on cardiomyocytes without the complexity of other organ systems (*in vivo*) and tissue types (slice preparations). Cultured cardiomyocytes are relatively simple to establish and maintain in a laboratory and deliver unrivalled high-throughput capabilities. The differences in cardiomyocyte electrophysiological properties presented here may even be exploited to enable targeting of specific cellular phenotypes that most closely model specific arrhythmia or drug response scenarios. Our findings suggest that NRVM and hiPSC-CM cultures may both be equally suited for modelling triggered and alternans arrhythmias – with good scope to detect changes in repolarisation times. The benefit of hiPSC-CMs over NRVMs is they more reliability recapitulate the human cardiac action potential. This is important because human repolarisation is mediated primarily by delayed rectifier currents, which contribute minimally to rodent repolarisation (46). 40-70% of all new pharmacological agents have capacity to modulate KCNH2 – the channel which carried the rapid component of the delayed rectifier current (47,48). This

indicates the importance of appreciating species difference in repolarisation and the potential greater relevance of using hiPSC-CMs in screening novel compounds which might modulate repolarisation.

Cells with slow conduction velocity (e.g. HL-1 (30)) may be more appropriate for the setting of reentrant arrhythmias, although establishment of reentrant circuits in small microelectrode array dishes is likely difficult with limited wavelength capacity for rotor formation. NRVMs, given their relatively fast conduction, may be particularly useful in studies screening the effects of compounds on cardiomyocyte conduction. This may be important for antiarrhythmic drug studies, but also novel non-cardiac-focussed medications which may have off-target effects on cardiac conduction.

4.5 Conclusions

In conclusion, this is the first study to demonstrate that male and female primary cardiomyocytes demonstrate similar electrophysiology. NRVMs and hiPSC-CMs display comparable, modifiable, repolarisation characteristics (supporting their use in scenarios of triggered arrhythmia) but differ with regard to beating rates and amplitudes. These data provide important protocol and physiological benchmarks for other investigators, detailing insight into appropriate culture choice for specific disease/drug screening scenarios.

4.6 References

1. Jansen HJ, Moghtadaei M, Mackasey M et al. Atrial structure, function and arrhythmogenesis in aged and frail mice. Sci Rep 2017;7:44336-44336.

2. Lane DA, Skjøth F, Lip GYH, Larsen TB, Kotecha D. Temporal Trends in Incidence, Prevalence, and Mortality of Atrial Fibrillation in Primary Care. J Am Heart Assoc 2017;6:e005155.

3. Lubitz SA, Sinner MF, Lunetta KL et al. Independent susceptibility markers for atrial fibrillation on chromosome 4q25. Circulation 2010;122:976-84.

4. Vandenberg J, Perry M, Hill A. Recent advances in understanding and prevention of sudden cardiac death. F1000Research 2017;6.

5. Kirchhof P, Benussi S, Kotecha D et al. 2016 ESC Guidelines for the management of atrial fibrillation developed in collaboration with EACTS. Eur Heart J 2016;37:2893-2962.

6. Heist EK, Ruskin JN. Drug-induced arrhythmia. Circulation 2010;122:1426-35.

7. Lafuente-Lafuente C, Valembois L, Bergmann JF, Belmin J. Antiarrhythmics for maintaining sinus rhythm after cardioversion of atrial fibrillation. Cochrane Database of Syst Rev 2015.

8. Braam SR, Tertoolen L, van de Stolpe A, Meyer T, Passier R, Mummery CL. Prediction of drug-induced cardiotoxicity using human embryonic stem cell-derived cardiomyocytes. Stem Cell Res 2010;4:107-16.

9. Boyle PM, Franceschi WH, Constantin M et al. New insights on the cardiac safety factor: Unraveling the relationship between conduction velocity and robustness of propagation. J Mol Cell Cardiol 2019;128:117-128.

10. Meiry G, Reisner Y, Feld Y et al. Evolution of Action Potential Propagation and Repolarization in Cultured Neonatal Rat Ventricular Myocytes. J Cardiovasc Electrophys 2001;12:1269-1277.

11. Sala L, Ward-van Oostwaard D, Tertoolen LGJ, Mummery CL, Bellin M. Electrophysiological Analysis of human Pluripotent Stem Cell-derived Cardiomyocytes (hPSC-CMs) Using Multi-electrode Arrays (MEAs). J Vis Exp 2017:e55587.

12. H B. An analysis of the time-relations of electrocardiograms. Heart 1920;7:353-370.

13. Kligfield P, Lax KG, Okin PM. QT interval-heart rate relation during exercise in normal men and women: definition by linear regression analysis. J Am Coll Cardiol 1996;28:1547-55.

14. Stramba-Badiale M, Locati EH, Martinelli A, Courville J, Schwartz PJ. Gender and the relationship between ventricular repolarization and cardiac cycle length during 24-h Holter recordings. Eur Heart J 1997;18:1000-6.

15. Curl CL, Wendt IR, Kotsanas G. Effects of gender on intracellular [Ca2+] in rat cardiac myocytes. Pflugers Arch 2001;441:709-16.

16. Pham TV, Rosen MR. Sex, hormones, and repolarization. Cardiovasc Res 2002;53:740-751.

17. Kim MH, Johnston SS, Chu B-C, Dalal MR, Schulman KL. Estimation of Total Incremental Health Care Costs in Patients With Atrial Fibrillation in the United States. Circulation 2011;4:313-320.

18. Bell JR, Curl CL, Harding TW, Vila Petroff M, Harrap SB, Delbridge LMD. Male and female hypertrophic rat cardiac myocyte functional responses to ischemic stress and β-adrenergic challenge are different. Biol Sex Differ 2016;7:32.

19. Trépanier-Boulay V, St-Michel C, Tremblay A, Fiset C. Gender-based differences in cardiac repolarization in mouse ventricle. Circ Res 2001;89:437-444.

20. Mills RJ, Titmarsh DM, Koenig X et al. Functional screening in human cardiac organoids reveals a metabolic mechanism for cardiomyocyte cell cycle arrest. Proc Natl Acad Sci U S A 2017;114:E8372-E8381.

21. Sayed N, Liu C, Wu JC. Translation of Human-Induced Pluripotent Stem Cells: From Clinical Trial in a Dish to Precision Medicine. J Am Coll Cardiol 2016;67:2161-2176.

22. Porrello ER, Bell JR, Schertzer JD et al. Heritable pathologic cardiac hypertrophy in adulthood is preceded by neonatal cardiac growth restriction. Am J Physiol Regul Integr Comp Physiol 2009;296:R672-R680.

23. Chan Y-C, Tse H-F, Siu C-W, Wang K, Li RA. Automaticity and conduction properties of bio-artificial pacemakers assessed in an in vitro monolayer model of neonatal rat ventricular myocytes. EP Europace 2010;12:1178-1187.

24. Anderson DJ, Kaplan DI, Bell KM et al. NKX2-5 regulates human cardiomyogenesis via a HEY2 dependent transcriptional network. Nat Commun 2018;9:1373.

25. Costa M, Dottori M, Sourris K et al. A method for genetic modification of human embryonic stem cells using electroporation. Nat Protoc 2007;2:792-6.

26. Elliott DA, Braam SR, Koutsis K et al. NKX2-5(eGFP/w) hESCs for isolation of human cardiac progenitors and cardiomyocytes. Nat Methods 2011;8:1037-40.

27. Nguyen PD, Hsiao ST, Sivakumaran P, Lim SY, Dilley RJ. Enrichment of neonatal rat cardiomyocytes in primary culture facilitates long-term maintenance of contractility in vitro. Am J Physiol Cell Physiol 2012;303:C1220-C1228.

28. Chowdhury RA, Tzortzis KN, Dupont E et al. Concurrent micro- to macro-cardiac electrophysiology in myocyte cultures and human heart slices. Sci Rep 2018;8:6947.

29. Halbach M, Egert U, Hescheler J, Banach K. Estimation of Action Potential Changes from Field Potential Recordings in Multicellular Mouse Cardiac Myocyte Cultures. Cell Physiol Biochem 2003;13:271-84.

30. Wells SP, Waddell HM, Sim CB et al. Cardiomyocyte functional screening: interrogating comparative electrophysiology of high-throughput model cell systems. Am J Physiol Cell Physiol 2019;317:C1256-c1267.

31. Camelliti P, Al-Saud SA, Smolenski RT et al. Adult human heart slices are a multicellular system suitable for electrophysiological and pharmacological studies. J Mol Cell Cardiol 2011;51:390-398.

32. O'Shea C, Holmes AP, Yu TY et al. ElectroMap: High-throughput open-source software for analysis and mapping of cardiac electrophysiology. Sci Rep 2019;9:1389.

33. Wen Q, Gandhi K, Capel RA et al. Transverse cardiac slicing and optical imaging for analysis of transmural gradients in membrane potential and Ca2+ transients in murine heart. J Physiol 2018;596:3951-3965.

34. Garcia M, Mulvagh SL, Merz CNB, Buring JE, Manson JE. Cardiovascular Disease in Women. Circ Res 2016;118:1273-1293.

35. Bell JR, Bernasochi GB, Varma U, Raaijmakers AJA, Delbridge LMD. Sex and sex hormones in cardiac stress—Mechanistic insights. J Steroid Biochem Mol Biol 2013;137:124-135.

36. Parks RJ, Howlett SE. Sex differences in mechanisms of cardiac excitation-contraction coupling. Pflugers Archiv : Eur J Physiol 2013;465:747-763.

37. Brouillette J, Rivard K, Lizotte E, Fiset C. Sex and strain differences in adult mouse cardiac repolarization: importance of androgens. Cardiovasc Res 2005;65:148-157.

38. Graham EL, Balla C, Franchino H, Melman Y, del Monte F, Das S. Isolation, culture, and functional characterization of adult mouse cardiomyoctyes. J Vis Exp 2013:e50289.

39. Hund TJ, Rudy Y. Rate Dependence and Regulation of Action Potential and Calcium Transient in a Canine Cardiac Ventricular Cell Model. Circulation 2004;110:3168-3174.

40. Wu H, Lee J, Vincent LG et al. Epigenetic Regulation of Phosphodiesterases 2A and 3A Underlies Compromised β-Adrenergic Signaling in an iPSC Model of Dilated Cardiomyopathy. Cell Stem Cell 2015;17:89-100.

41. Mummery CL, Zhang J, Ng ES, Elliott DA, Elefanty AG, Kamp TJ. Differentiation of Human Embryonic Stem Cells and Induced Pluripotent Stem Cells to Cardiomyocytes. Circ Res 2012;111:344-358.

42. Goineau S, Castagné V. Electrophysiological characteristics and pharmacological sensitivity of two lines of human induced pluripotent stem cell derived cardiomyocytes coming from two different suppliers. J Pharmacol Toxicol Meth 2018;90:58-66.

43. Hernandez D, Millard R, Sivakumaran P et al. Electrical Stimulation Promotes Cardiac Differentiation of Human Induced Pluripotent Stem Cells. Stem Cells Int 2016;2016:1718041.

44. Ribeiro MC, Tertoolen LG, Guadix JA et al. Functional maturation of human pluripotent stem cell derived cardiomyocytes in vitro – Correlation between contraction force and electrophysiology. Biomaterials 2015;51:138-150.

45. Egert U, Meyer T. Heart on a Chip - Extracellular Multielectrode Recordings from Cardiac Myocytes in Vitro. In: S D, FW M, M D, editors. Practical Methods in Cardiovascular Research. Berlin: Springer, 2005:32-453.

46. O'Hara T, Rudy Y. Quantitative comparison of cardiac ventricular myocyte electrophysiology and response to drugs in human and nonhuman species. Am J Physiol Heart Circ Physiol 2012;302:H1023-30.

47. Redfern WS, Carlsson L, Davis AS et al. Relationships between preclinical cardiac electrophysiology, clinical QT interval prolongation and torsade de pointes for a broad range of drugs: evidence for a provisional safety margin in drug development. Cardiovasc Res 2003;58:32-45.

48. Witchel HJ. The hERG potassium channel as a therapeutic target. Expert Opin Ther Targets 2007;11:321-36.

4.7 Figures

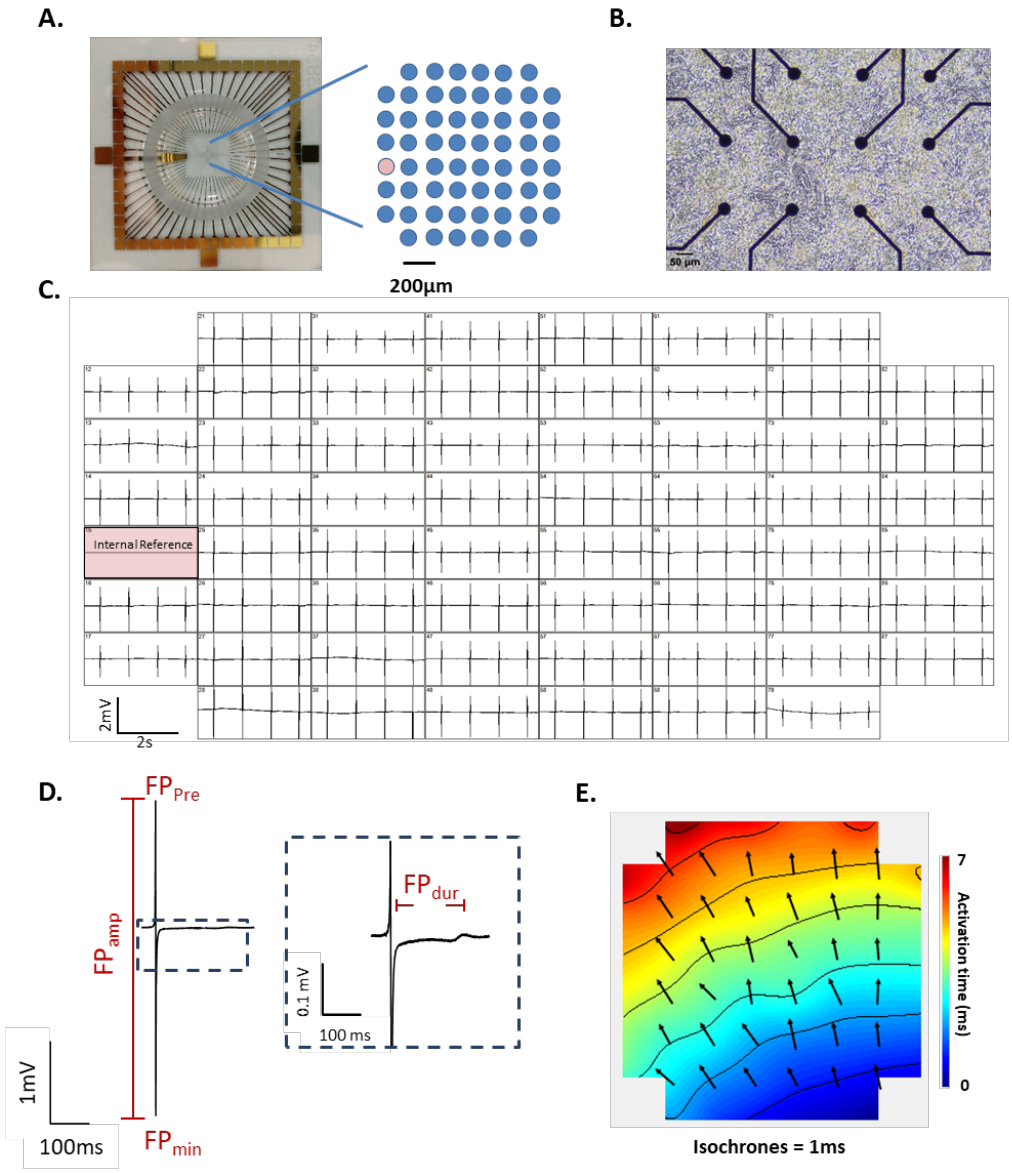

Figure 4.1 Visual overview of MEAs and measurable electrophysiological parameters. **(A)** Exemplar images of an MEA (200µm electrode spacing, 30µm electrode diameter; 1 internal reference in red), **(B)** NRVM seeding on MEA electrodes, and **(C)** multi-channel recordings of field potentials. **(D)** Exemplar field potential trace ($FP_{pre,}$ field potential upstroke maximum; FP_{min} field potential downstroke minimum; FP_{amp}, field potential amplitude; FP_{dur}, field potential duration) and **(E)** activation map showing propagation of a single field potential across an NRVM monolayer over 7ms. Arrows indicate propagation pathway and are situated at approximate electrode positioning, contours indicate 1ms delay).

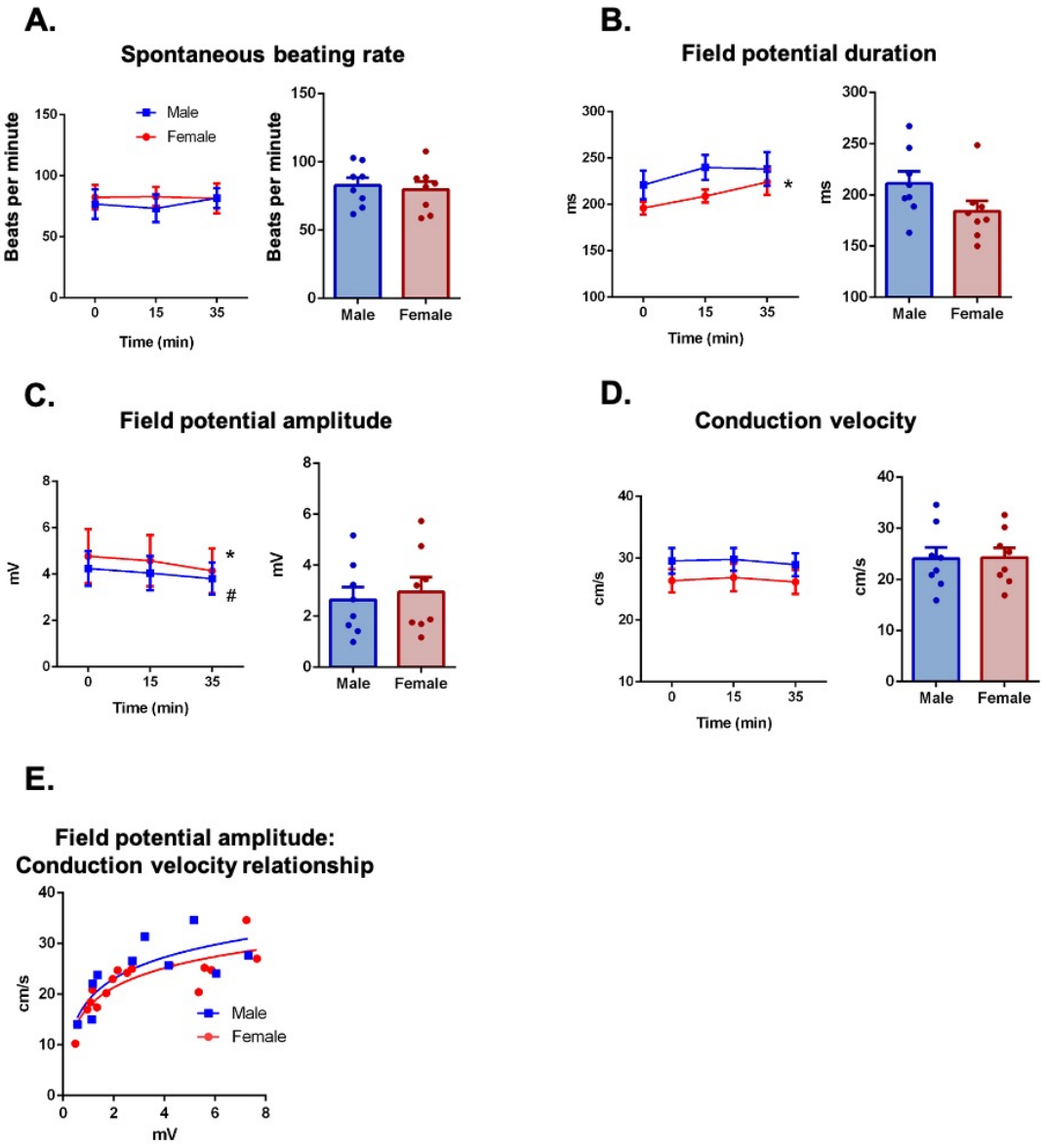

Figure 4.2 Comparable electrophysiology in cultured male (blue) and female (red) neonatal rat ventricular myocytes (NRVMs). Assessment of prep stability in male and female NRVM electrophysiology with time (*left*) and direct sex comparison at 0 min (*right*), including spontaneous beating rate **(A)**, field potential duration **(B)**, field potential amplitude **(C)**, and conduction velocity **(D)**. **E:** field potential amplitude-conduction velocity relationships in male and female NRVM cultures. $P<0.05$ females 0 *vs* 35 min (*) and males 0 *vs* 35min (#), $N=3–4$ cultures, $n=6–9$ microelectrode arrays. No between-sex differences at any time point. Repeated-measures 2-way ANOVA and Holm-Sidak's multiple-comparison tests.

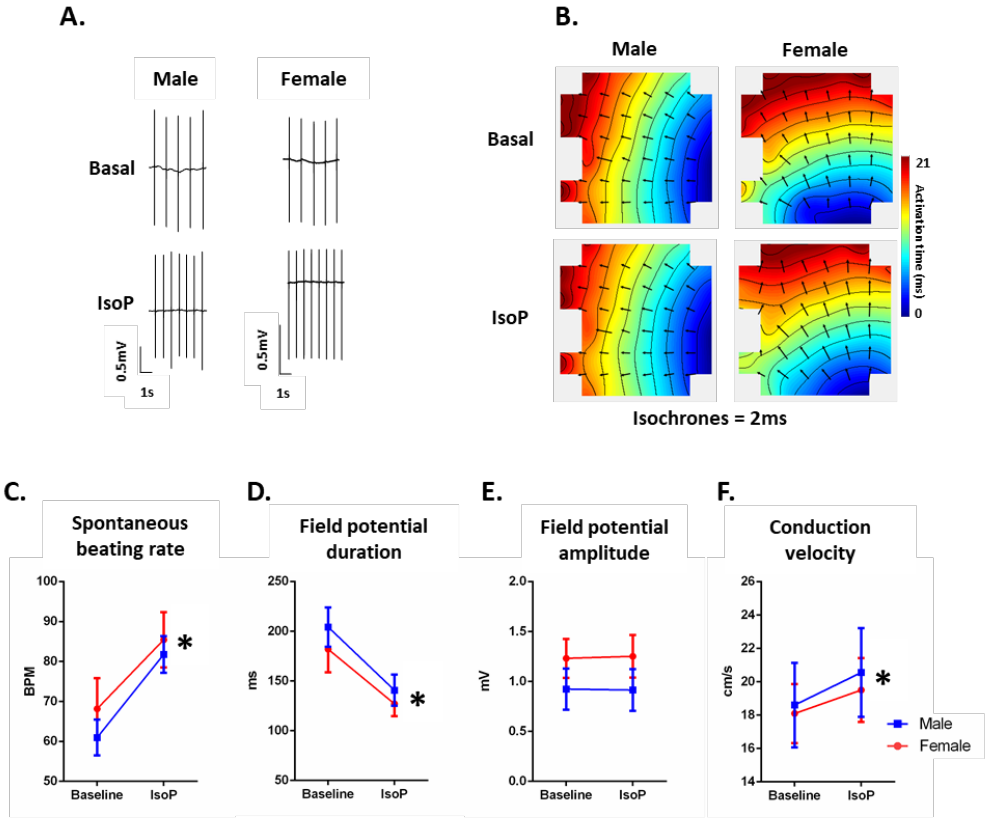

Figure 4.3 Responsiveness of male and female NRVMs to isoproterenol. Comparable electrophysiology in cultured male and female NRVMs. **(A)** Exemplar field potential traces and **(B)** activation maps in male and female NRVMs at baseline and after 5 min of isoproterenol (IsoP) treatment. **(C)** Spontaneous beating rate, **(D)** field potential duration, **(E)** field potential amplitude and **(F)** conduction velocity of male and female NRVMs acutely treated with 1µM isoproterenol (IsoP). $^{*}P<0.05$ Baseline *vs* IsoP for both sexes. No between sex differences. Repeated measures two-way ANOVA. *N*=5-6 cultures, *n*=6-7 MEAs.

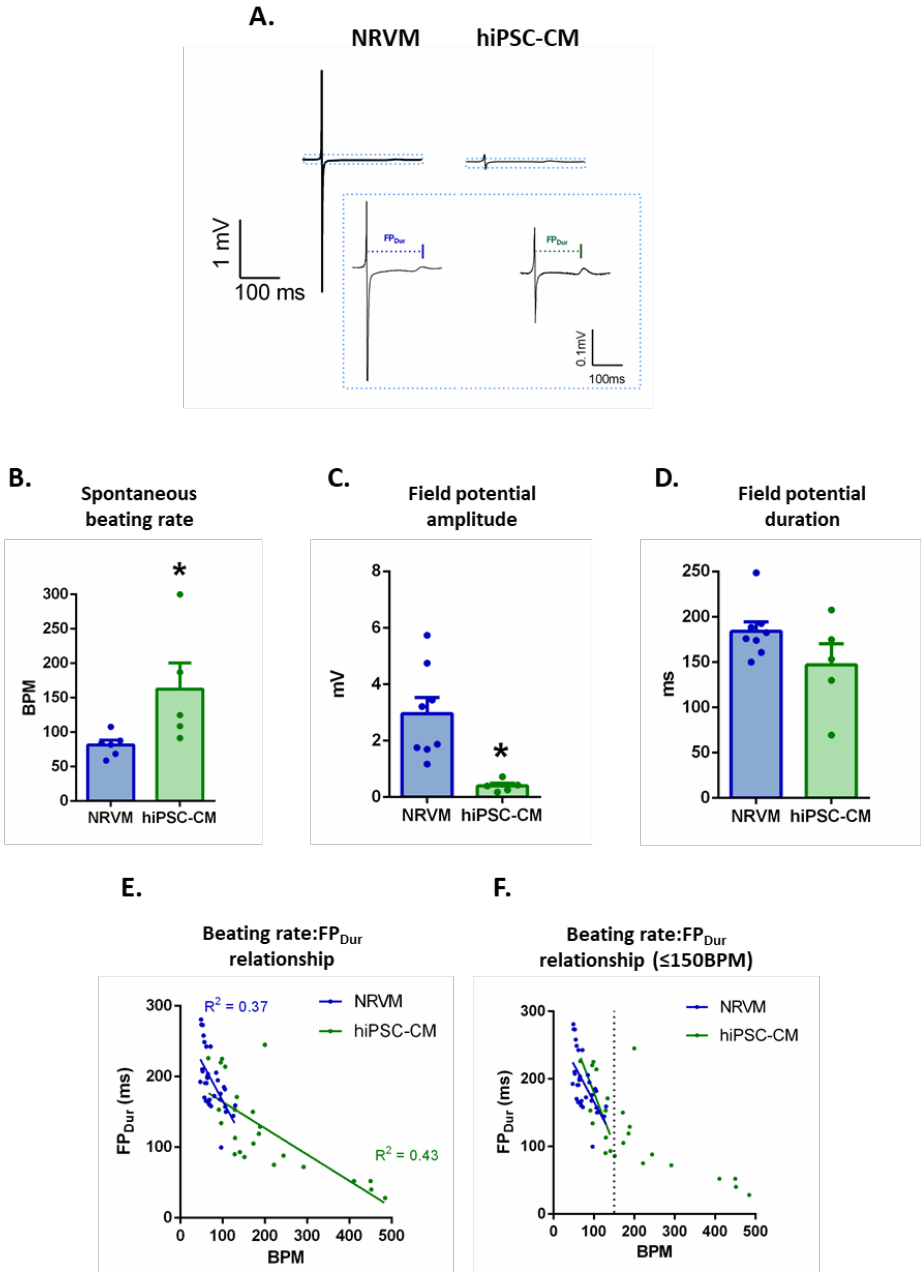

Figure 4.4 Basal electrophysiology differs between female cardiomyocyte cultures of different origin. **(A)** Exemplar field potential traces from NRVMs and hiPSC-CMs, with cropped field potentials inset to highlight repolarisation waves. **(B)** Spontaneous beating rate, **(C)** field potential amplitude and **(D)** field potential duration in NRVMs and hiPSC-CMs at baseline. **(E)** Relationship between spontaneous beating rate and field potential duration in NRVMs and hiPSC-CMs and **(F)** the same relationship with linear regression fitted only to cultures with a beating rate ≤150BPM. **P*<0.05, unpaired t-tests. NRVM: *N*=8 cultures, *n*=19 MEAs; hiPSC-CMs: *N*=5 (3 separate cultures, 5 plating runs), *n*=22 MEAs.

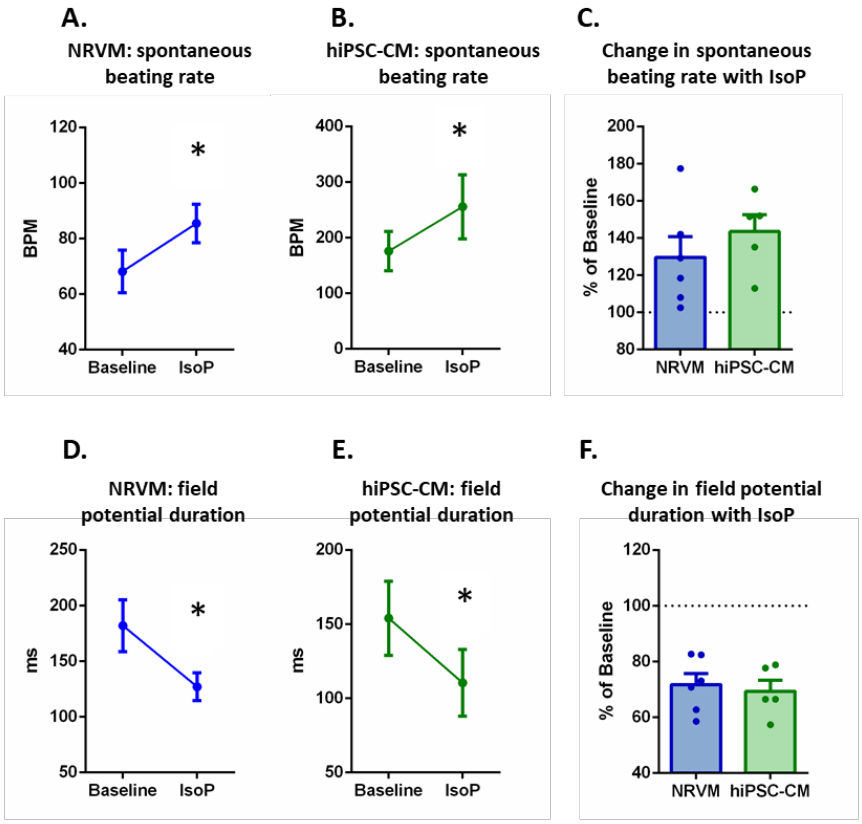

Figure 4.5 Isoproterenol-stimulated electrophysiology differs between female cardiomyocyte cultures of different origin. Mean spontaneous beating rate for **(A)** NRVMs and **(B)** hiPSC-CMs in response to 1µM isoproterenol (IsoP). **(C)** Percent change in beating rate in response to IsoP in both culture types. Mean field potential duration for **(D)** NRVMs and **(E)** hiPSC-CMs in response to IsoP. **(F)** Percent change in field potential duration in response to IsoP in both culture types. **P*<0.05, paired t-test; NRVM: *N*=8 cultures, *n*=19 MEAs; hiPSC-CMs: *N*=5 (3 separate cultures, 5 plating runs), *n*=22 MEAs.

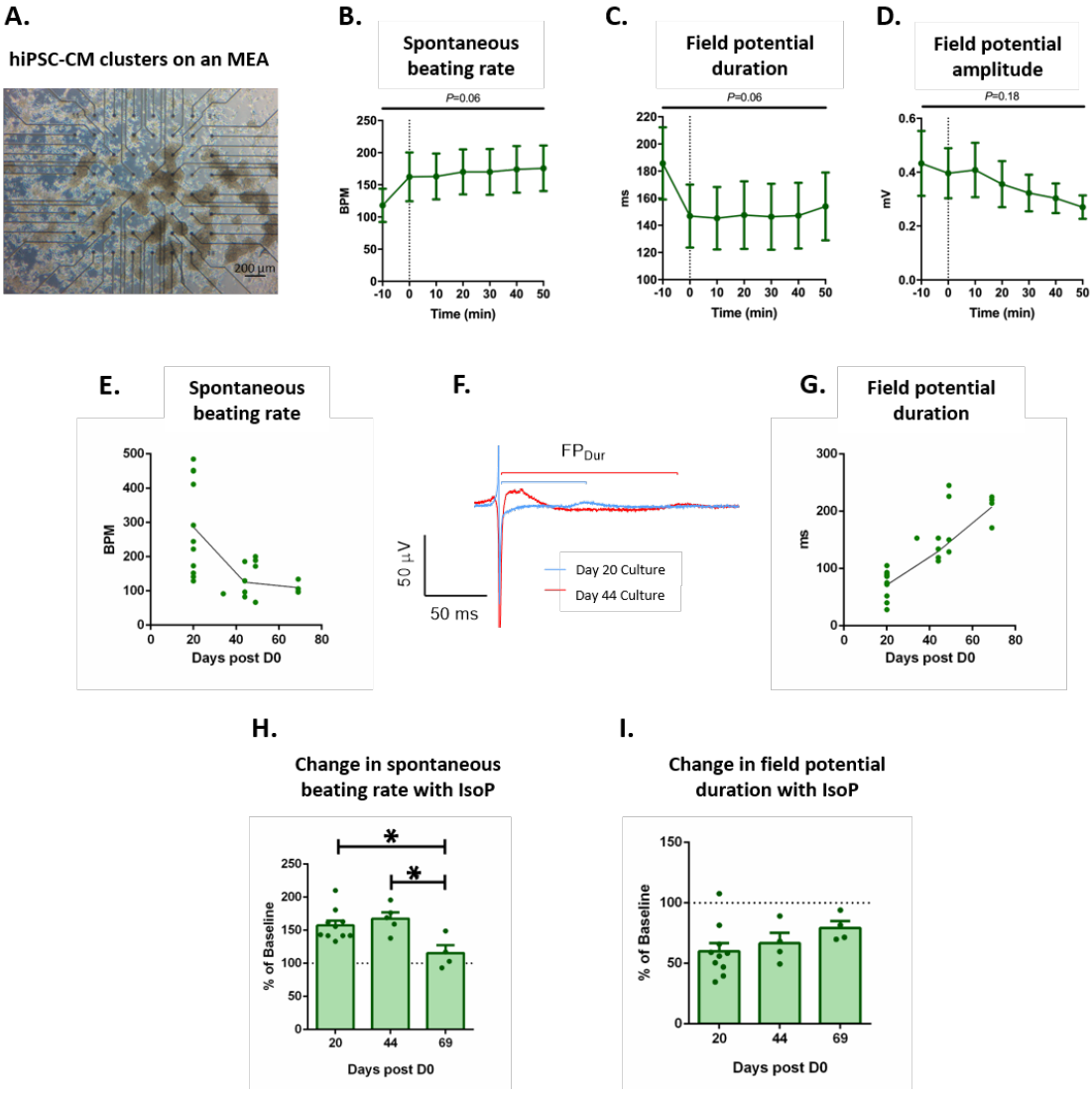

Figure 4.6 hiPSC-CM electrophysiology is stable over a 1hr recording period but varies with time post differentiation induction. **(A)** Exemplar image of hiPSC-CM clusters cultured on an MEA. **(B)** Spontaneous beating rate, **(C)** field potential duration and **(D)** field potential amplitude from hiPSC-CMs recorded over a 1hr period. Repeated measures one-way ANOVAs, *N*=5 cultures, *n*=22 MEAs. Relationship between spontaneous beating rate **(E)** and field potential duration **(F and G)** and the duration of the period post-differentiation induction. *n*=22 MEAs (lines plotted through Day 22, 44 and 69 means, as these timepoints had the most datapoints). **(H)** spontaneous beating rate and **(I)** field potential duration changes induced by 1µM isoproterenol (IsoP) in cultures examined at different timepoints post differentiation induction. *n*=16-22 MEAs, **P*<0.05, one-way ANOVA with Holm-Sidak's multiple comparisons.

4.8 Appendices

Appendix A

Supplementary Figures

- Figure S4.1
- Figure S4.2

Appendix B

Published journal article arising from this chapter and copyright approval statement for inclusion of data in this thesis.

Appendix A – Supplementary Figures

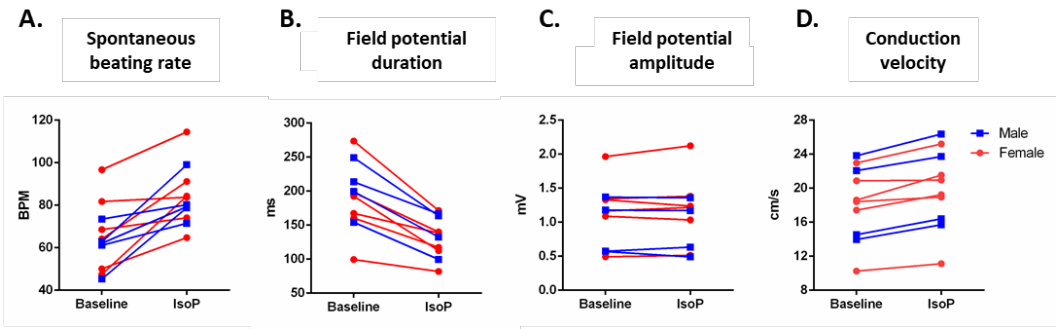

Figure S4.1 Individual responses of male (blue) and female (red) NRVMs to 1µM isoproterenol (IsoP). **(A)** Spontaneous beating rate **(B)** field potential duration, **(C)** field potential amplitude and **(D)** conduction velocity. *N*=5–6 cultures, *n*=6–7 MEAs.

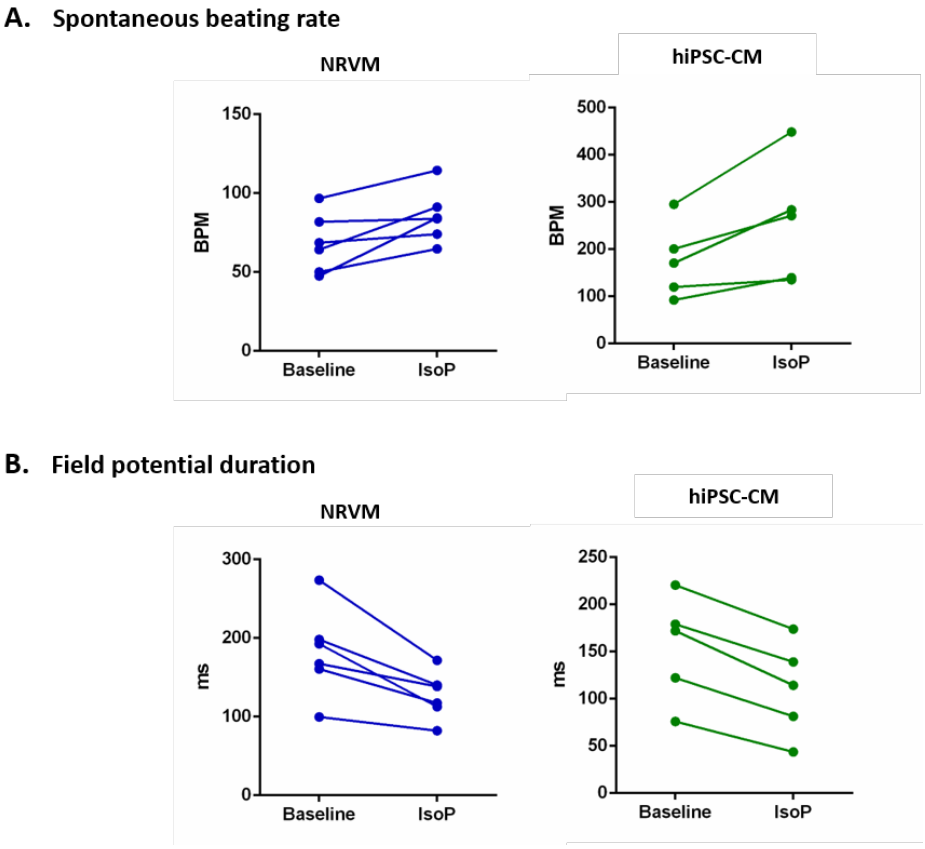

Figure S4.2 Individual responses of NRVM and hiPSC-CM to 1µM isoproterenol. (**A**) Spontaneous beating rate **(B)** field potential duration. NRVM: *N*=6 cultures, *n*=7 MEAs; hiPSC-CMs: *N*=5, *n*=22 MEAs.

Appendix B – Copyright permissions and published manuscript

From: APS Subscriptions
To: Simon Wells
Subject: RE: Copyright enquiry for reproducing published article in thesis
Date: 10 December 2019 01:41:56

Dear Simon,

Yes, this type of use is allowed. You do not need to use the whole article as long as you cite the article in your thesis.

Kind Regards,
Stephani

Stephani Rozier
Subscription Database Specialist/Permissions
w 301.634.7796 f 301.634.7418
6120 Executive Boulevard, Suite 600
Rockville, MD 20852-4911
Visit APS' website. Explore our Journals.

From: Simon Wells [mailto:wellss1@student.unimelb.edu.au]
Sent: Monday, December 9, 2019 12:48 AM
To: APS Subscriptions
Subject: Copyright enquiry for reproducing published article in thesis

Dear Sir/Madam,

We have recently published an original research article in AJP-Cell (https://www-physiology-org.ezp.lib.unimelb.edu.au/doi/full/10.1152/ajpcell.00306.2019) and I wish to reuse this in my PhD thesis.

I have read through the copyright & permissions on your website, but just wanted further clarification that it is ok to reproduce **part** of this published work in a thesis (online only states that "Authors may reproduce **whole** published articles in dissertations and post to thesis repositories without charge and without requesting permission. Full citation is required.")?

Best wishes,
Simon.

Simon P Wells
PhD Candidate, Cardiac Phenomics Laboratory
Department of Physiology
University of Melbourne
Australia
Tel: +61 (0) 412384562
Email: wellss1@student.unimelb.edu.au

Am J Physiol Cell Physiol 317: C1256–C1267, 2019.
First published October 2, 2019; doi:10.1152/ajpcell.00306.2019.

METHODS IN CELL PHYSIOLOGY | *Making Cell Culture More Physiological*

Cardiomyocyte functional screening: interrogating comparative electrophysiology of high-throughput model cell systems

Simon P. Wells,[1,2]* Helen M. Waddell,[1]* Choon Boon Sim,[3] Shiang Y. Lim,[4,5] Gabriel B. Bernasochi,[1] Davor Pavlovic,[2] Paulus Kirchhof,[2,6] Enzo R. Porrello,[1,3] Lea M. D. Delbridge,[1]* and James R. Bell[1,7]*

[1]*Department of Physiology, School of Biomedical Sciences, University of Melbourne, Melbourne, Victoria, Australia;* [2]*Institute of Cardiovascular Sciences, College of Medical and Dental Sciences, University of Birmingham, United Kingdom;* [3]*Murdoch Children's Research Institute, Royal Children's Hospital, Melbourne, Victoria, Australia;* [4]*St. Vincent's Institute of Medical Research, Fitzroy, Victoria, Australia;* [5]*Departments of Medicine and Surgery, University of Melbourne, Melbourne, Victoria, Australia;* [6]*Departments of Cardiology, University Hospitals Birmingham and Sandwell and West Birmingham Hospitals National Health Service Trusts, Birmingham, United Kingdom; and* [7]*Department of Physiology, Anatomy and Microbiology, La Trobe University, Bundoora, Victoria, Australia*

Submitted 5 August 2019; accepted in final form 12 September 2019

Wells SP, Waddell HM, Sim CB, Lim SY, Bernasochi GB, Pavlovic D, Kirchhof P, Porrello ER, Delbridge LMD, Bell JR. Cardiomyocyte functional screening: Interrogating comparative electrophysiology of high-throughput model cell systems. *Am J Physiol Cell Physiol* 317: C1256–C1267, 2019. First published October 2, 2019; doi:10.1152/ajpcell.00306.2019.—Cardiac arrhythmias of both atrial and ventricular origin are an important feature of cardiovascular disease. Novel antiarrhythmic therapies are required to overcome current drug limitations related to effectiveness and pro-arrhythmia risk in some contexts. Cardiomyocyte culture models provide a high-throughput platform for screening antiarrhythmic compounds, but comparative information about electrophysiological properties of commonly used types of cardiomyocyte preparations is lacking. Standardization of cultured cardiomyocyte microelectrode array (MEA) experimentation is required for its application as a high-throughput platform for antiarrhythmic drug development. The aim of this study was to directly compare the electrophysiological properties and responses to isoproterenol of three commonly used cardiac cultures. Neonatal rat ventricular myocytes (NRVMs), immortalized atrial HL-1 cells, and custom-generated human induced pluripotent stem cell-derived cardiomyocytes (hiPSC-CMs) were cultured on microelectrode arrays for 48–120 h. Extracellular field potentials were recorded, and conduction velocity was mapped in the presence/absence of the β-adrenoceptor agonist isoproterenol (1 μM). Field potential amplitude and conduction velocity were greatest in NRVMs and did not differ in cardiomyocytes isolated from male/female hearts. Both NRVMs and hiPSC-CMs exhibited longer field potential durations with rate dependence and were responsive to isoproterenol. In contrast, HL-1 cells exhibited slower conduction and shorter field potential durations and did not respond to 1 μM isoproterenol. This is the first study to compare the intrinsic electrophysiologic properties of cultured cardiomyocyte preparations commonly used for in vitro electrophysiology assessment. These findings offer important comparative data to inform methodological approaches in the use of MEA and other techniques relating to cardiomyocyte functional screening investigations of particular relevance to arrhythmogenesis.

cardiomyocyte electrophysiology; HL-1 cells; human iPS-derived cardiomyocytes; microelectrode array; neonatal rat ventricular myocytes

* S.P. Wells and H.M. Waddell contributed equally to this work. L.M.D. Delbridge and J.R. Bell contributed equally to this work.

Address for reprint requests and other correspondence: J. R. Bell, Cardiac Phenomics Laboratory, School of Biomedical Sciences, University of Melbourne, VIC, Australia, 3010 (e-mail: belljr@unimelb.edu.au).

INTRODUCTION

Cardiac arrhythmias are an important feature of numerous cardiovascular diseases, including heart failure and ischemic heart disease. Arrhythmias can be of atrial or ventricular origin, disrupting the capacity and stability of the heart pump. Patients with ventricular arrhythmias, including ventricular tachycardia and fibrillation, are especially vulnerable to sudden cardiac death, and immediate defibrillatory intervention is required (42). Atrial fibrillation is the most common sustained arrhythmia, associated with multiple risk factors, including aging, obesity, and genetic predisposition (23, 26, 27). Although atrial fibrillation in isolation may not be lethal, it can lead to thrombotic stroke and heart failure. Implantation of a cardioverter defibrillator can be effective in patients at risk of ventricular arrhythmias but are expensive and associated with significant morbidity (24). Numerous antiarrhythmic treatment strategies are available although risk of side effects and incomplete effectiveness limit their clinical use (19, 24, 25). A better understanding of the subcellular mechanisms underpinning arrhythmias is required for the development of more effective novel antiarrhythmia strategies.

Preclinical experimental models to study cardiomyocyte electrophysiology have proved a useful tool in understanding the basic mechanisms of arrhythmogenesis. Substrate-integrated microelectrode arrays (MEAs) are devices embedded with multiple low-impedance electrodes arranged in a grid formation, designed for noninvasive synchronous multifocal recordings across cardiac slices and cardiomyocyte monolayers.

Cardiomyocytes cultured on MEAs have enabled assessment of electrophysiology and conduction properties and provide a high-throughput platform for screening compounds for antiarrhythmic properties (6). In vitro cardiomyocyte studies have historically relied on a limited number of immortalized cell lines and/or dissociated neonatal rodent ventricular myocytes (5, 28). Recently, inducible pluripotent stem cell preparations

have become more widely utilized (37). Comparative benchmarking of these different cell types relative to various functional readouts has not been previously reported.

Commonly used spontaneously beating cardiomyocytes that can be maintained in culture over multiple days/weeks include neonatal rat ventricular myocytes (NRVMs), immortalized mouse atrial HL-1 cell lines, and human induced pluripotent stem cell-derived cardiomyocytes (hiPSC-CMs). NRVMs in culture are minimally proliferative, immature, and able to reestablish gap junction connections when seeded as a dense confluent monolayer (28). Typically, NRVM cultures are sourced from a mixed male/female population, without regard for potential sex-specific cardiac electrophysiological differences. This may be an important oversight, since a growing body of literature describes numerous differences in male and female cardiac physiology, including action potential and Ca^{2+}-handling characteristics, arrhythmia vulnerability, and interventional drug responses (4, 41).

The HL-1 cell line was derived from an atrial tumor excised from an adult female C57BL/6J mouse and is readily commercially available (11). Although immortalized, HL-1 cells substantially maintain their terminally differentiated phenotype in culture even after multiple passages and, like NRVMs, form an electrically coupled syncytia allowing mapping of electrical signal propagation. hiPSC-CMs are generated from induced pluripotent stem cells differentiated toward the cardiac lineage. They can be generated in high quantity, recapitulate the adult human cardiac action potential and ion channel profile to an extent, and can be sourced commercially or produced locally by a defined differentiation protocol (29, 37). Like NRVMs, hiPSC-CMs are immature and beat spontaneously (37). The therapeutic regenerative potential of hiPSC-CMs is intriguing; hence, there is considerable interest in using these human-derived cardiomyocytes as a model to better understand cardiac electrophysiology (38).

All three cell types (hiPSC-CMs, HL-1, and NRVMs) are used for disease modeling and drug screening. However, a direct comparison of electrophysiology/conduction properties across these commonly used cardiomyocyte cultures has not been reported, and there is little information available to assist in determining which cardiomyocyte type is best suited to specific experimental applications and arrhythmia models. The spontaneous pacing properties of these three cell types were hence compared under basal conditions and in the presence of the β-adrenergic agonist, isoproterenol, to assess cardiomyocyte electrophysiology responses in settings known to induce arrhythmias in the intact heart. The aim of this study was to compare the electrophysiological characteristics of three commonly used cardiomyocyte cultures to standardize their use for potential purpose-specific modeling of relevant disease scenarios and aid researchers in the field with the selection of appropriate cultured cardiomyocyte preps for their studies.

Here, we show for the first time that primary cardiomyocytes, immortalized cardiac cell lines, and induced pluripotent stem cell-derived cardiomyocytes (NRVM, HL-1, and hiPSC-CM) exhibit marked difference in relation to beating rates, conduction velocities, rate adaptations of repolarization, and β-adrenergic responsiveness. By describing the distinct electrophysiological characteristics of these cell preparations, these findings provide important new insights for the use of cultured cardiomyocyte MEA as a high-throughput platform for antiarrhythmic drug development.

MATERIALS AND METHODS

Cell Culture

Neonatal rat ventricular myocyte culture. Experiments were conducted and animals were handled in the manner specified by the National Health and Medical Research Council/Commonwealth Scientific and Industrial Research Organisation Australian Code of Practice for the Care and Use of Animals for Scientific Purposes (2013) and the European Union (EU) Directive 2010/63/EU for animal experiments, with approval and oversight of the project by the University of Melbourne Animal Ethics Committee. For NRVM cultures, cardiomyocytes were isolated from *postnatal day 2* Sprague-Dawley litters as previously described (35). Briefly, pups were decapitated, hearts were rapidly excised, and atria were resected. Ventricles were dissected into chunks and gently swirled in 0.5% collagenase II (LS004176; Worthington) for 15 min at 37°C. Single NRVMs were isolated by Trypsin digestion (0.06%, T9201; Sigma) in Hanks' balanced salt solution + 0.02% DNAse 1 (260913; Calbiochem) and then digestion inhibited with the addition of newborn calf serum. NRVMs were centrifuged at 990 *g* at 4°C for 10 min, and cell pellets were resuspended in Dulbecco's modified Eagle's medium + GlutaMAX (10565–042; ThermoFisher), supplemented with 5% horse serum (16050–122; ThermoFisher), pyruvic acid (3 mM, P-8574; Sigma), bovine serum albumin (2 g/L, A-7030; Sigma), ampicillin (100 μg/mL, A-0166; Sigma), 100× insulin-transferrin-selenium (41400045; ThermoFisher), antibiotic/antimycotic (1%, 15240062; ThermoFisher), linoleic acid (5 μg/mL, L5900; Sigma), and ascorbic acid (100 μM, Sigma; A4544), and then preplated to remove fibroblasts (2 × 30 min, 37°C, 5% CO_2). Purified NRVMs were seeded on MEAs precoated with fibronectin (10 μg/mL, F2006; Sigma) by either coating the whole MEA well (1 mL at 1,400,000 cells/mL, final density of 500,000 cells/cm^2) or only the central recording matrix with a 75 μl droplet of 300,000 NRVMs. To ensure stable droplet formation critical to establishing a confluent cardiomyocyte monolayer, MEA hydrophobicity was increased by heating to 70°C for ≥2 h before seeding. Droplet-seeded NRVMs were then incubated for 2 h to promote adhesion, with culture media subsequently added to a final volume of 1 mL (300,000 cell/mL of media, final density of ~1,000,000 cells/cm^2). Media was changed after 48 h, typically when spontaneously beating monolayers had formed. MEA experiments were performed 5–6 days postisolation, since spontaneous beating rate, field potential amplitude, and conduction velocity have previously been shown to decline from 7 to 8 days postisolation (9, 28).

HL-1 cardiomyocyte culture. The immortalized atrial cardiomyocyte cell line, HL-1, was purchased from Merck (SCC065). HL-1 cells were cultured in Claycomb media (51800C; Sigma) supplemented with 10% fetal bovine serum (A3160601; ThermoFisher), penicillin/streptomycin (100 $U \cdot mL^{-1} \cdot 100\ \mu g^{-1} \cdot mL^{-1}$, 15140122; ThermoFisher), norepinephrine (0.1 mM, A0937; Sigma), ascorbic acid (0.3 mM, A7631; Sigma), and L-glutamine (2 mM, 25030081; ThermoFisher) and were maintained as per the manufacturer's instructions. For MEA experiments, 100,000 cardiomyocytes were seeded as a droplet on gelatin- and/or fibronectin-coated MEAs [0.02% gelatin, G9391 (Sigma); 0.5 μg/mL fibronectin, F1141 (Sigma)], similar to the process described for NRVMs. Media were changed daily, and cell recordings were obtained from 2 days postseeding. HL-1 cultures exhibiting spontaneous beating rates in excess of 200 beats/min were excluded from MEA analysis.

Human induced pluripotent stem cell-derived cardiomyocyte culture. hiPSC-CMs were cultured and differentiated as previously described (1, 13, 14). Briefly, hiPSCs (line PB004.4 female; Murdoch Children's Research Institute) were cultured in a 75 cm^2 tissue culture flask with hiPSC media [DMEM-F-12 (11320033; Gibco), 20% (vol/

vol) knockout serum replacement (10828028; Gibco), 1× nonessential amino acids (11140050; Gibco), 1× GlutaMAX (35050061; Gibco), penicillin/streptomycin (15140122; Gibco), 110 μM 2-mercaptoethanol (21985023; Gibco), and 5 ng/mL recombinant human fibroblast growth factor (233-FB-025; R&D)] on irradiated mouse embryonic fibroblasts and passaged using TrypLE Express enzyme (12604013; ThermoFisher). Before differentiation (1 day), 1.6×10^5 cells/cm^2 were seeded. To induce differentiation (*day 0*), cells were treated with basal differentiation media [RPMI (21870076; Sigma), B27 minus vitamin A (12587010; Gibco), and 50 μg/mL ascorbic acid (A8960; Sigma) supplemented with 10 μM CHIR-99021 (4423; Tocris Bioscience) and 80 ng/mL activin A (Peprotech)]. On *days 1*, *3*, and *5*, media were changed to basal differentiation media supplemented with 5 μM IWR-1 (I0161; Sigma). Cells were maintained in basal differentiation media from *day 7* until used.

For experiments, cells were dissociated with TrypLE, centrifuged (200 *g*, 4°C, 3 min), carefully resuspended in basal differentiation medium, and replated at 800,000 cells/mL as clusters across Geltrex-coated microelectrode arrays (Geltrex, 1:100, A1413202; Life Technologies). Media was changed after 48 h, and experiments were performed the following day.

Microelectrode Array Configuration

Extracellular electrophysiological field potentials were recorded from cardiomyocyte cultures using the MEA2100 2 × 60 system (Fig. 1; Multichannel Systems, Reutlingen, Germany). MEAs consisted of 60 gold recording electrodes embedded in a glass substrate fabricated with a layer of the conductive polymer poly(3,4-ethylenedioxythiophene) during the manufacturing process to produce the most robust signal amplitudes. Two different electrode configurations were used, either 100 μm diameter with 700 μm spacing or 30 μm diameter with 200 μm spacing (one of the 60 electrodes was used as an internal reference), with data sets comparable across the two configurations.

Electrophysiology Recordings

Spontaneously beating cultures were maintained at 37°C, and field potential recordings were acquired using Cardio2D software (Multichannel Systems) sampling at 10 kHz (low pass filter: 3,500 Hz, high pass filter: 10 Hz). All experimental recordings began after a 10-min equilibration period. To assess NRVM stability, 2-min recordings were obtained at 0, 15, and 35 min. A subset of NRVM, HL-1, and hiPSC-CM cultures was treated with the β-adrenergic agonist, isoproterenol (1 μM, 3–5 min), which we have shown previously to induce robust maximal electrophysiological responses in NRVM cultures (32).

Electrophysiology Analysis

Spontaneous beating rate was calculated by averaging the interspike interval between 10 consecutive beats. Field potential duration was determined as the time between the peak negative deflection and the peak of the final positive deflection (Fig. 1*D*; 10, 18). For NRVM and HL-1 cells, this was calculated by averaging across 10 beats at 10 sites across an MEA. Activation maps for NRVMs and HL-1 monolayers were generated in Cardio2D+ software (Multichannel Systems). Delay in activation between neighboring electrodes was computed using a multivector approach, and mean conduction velocity was calculated on a beat-beat basis. Conduction velocity was then averaged across 10 consecutive beats for each MEA. Because of the clustered nature of hiPSC-CMs, field potential duration was averaged from 10 consecutive beats at a single site. All analysis was performed using Cardio2D+, and arrhythmic cultures were excluded.

Statistics

All data are expressed as means ± SE. Statistical analysis was performed and graphs were generated using GraphPad Prism 6.0. Relevant statistical analyses are indicated throughout and $P < 0.05$ was deemed significant. *N* denotes the number of cultures, and *n* denotes the number of MEAs.

RESULTS

Optimizing Methodology to Plate Cardiomyocytes on MEAs

NRVMs seeded on MEAs formed a confluent spontaneously beating monolayer over 5 days in culture, allowing the detection of field potentials across the 59 recording electrodes. Activation maps were derived from detection of the field potential propagation across the monolayer, with isochrones indicating activation latency and arrows showing the dominant regional propagation pathways.

To assess the optimal plating methodology for detecting cardiomyocyte field potentials, mixed-sex NRVMs were either seeded across the whole MEA or as a droplet exclusively over the central recording region without covering the internal reference electrode (Fig. 2, *A* and *B*). Following a 10-min stabilization period, basal measurements (time = 0 min) showed plating cardiomyocytes as a droplet-enhanced capacity to detect field potentials (Fig. 2*C*) and significantly reduced interprep variability (*F* test, $P < 0.001$). This was associated with a significantly greater field potential amplitude (4.48 ± 0.83 vs. 0.79 ± 0.20 mV, $N = 3$–4, $P < 0.05$; Fig. 2*D*). The droplet seeding of cells over the central recording region was hence adopted for the remainder of the study. Interestingly, NRVMs plated as a central droplet exhibited a lower spontaneous beating rate (99.1 ± 10.3 vs. 320.5 ± 48.3 beats/min, $N = 3$–4, $P < 0.05$; Fig. 2*E*) with less interprep variability (*F* test, $P < 0.001$) compared with those cells plated across the whole MEA.

Male and Female NRVM Monolayers Exhibit Similar Electrophysiology

Basal electrophysiology parameters were compared in NRVM monolayers from male and female rat hearts harvested at *postnatal day 2*. No significant differences in spontaneous beating rate, field potential duration, field potential amplitude, or conduction velocity were evident between male and female NRVM monolayers (Fig. 3, *A*–*D*). Both sexes also displayed similar field potential amplitude-conduction velocity relationships (Fig. 3*E*). MEA recordings of male and female cardiomyocytes were then either continued under basal conditions to assess electrophysiological stability over a 35-min period or treated with 1 μM isoproterenol to determine responsiveness to β-adrenergic stimulation. Spontaneous beating rate did not change in either male or female NRVM monolayers during the 35-min assessment, with evidence of only minor changes in field potential morphology and no change in conduction velocity (Fig. 3, *A*–*D*). Male and female NRVMs acutely treated with 1 μM isoproterenol exhibited no significant differences in electrophysiologic response parameters, with both sexes displaying an expected significant increase in spontaneous beating rate, shortening of field potential duration, and no change in field potential amplitude (Fig. 4, *A*–*D*, and Supplemental Fig. S1; Supplemental Material is available at https://doi.org/10.26188/5d71e20d43c5e). Conduction velocity increased similarly in cells of both sexes (Fig. 4*F* and Supplemental Fig. S1).

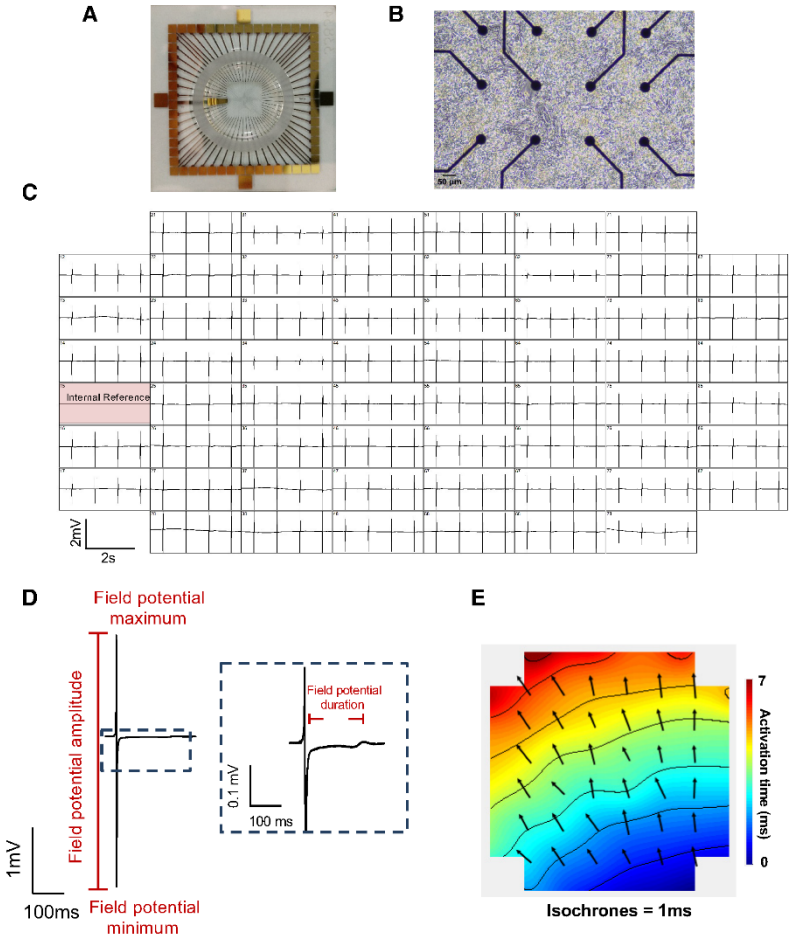

Fig. 1. Visual overview of microelectrode arrays (MEAs) and measurable electrophysiological parameters. Exemplar images of MEA chip (200 μm electrode spacing, 30 μm electrode diameter, *A*), neonatal rat ventricular myocyte (NRVM) seeding on MEA electrodes (*B*), and multichannel recordings of field potentials (*C*). Exemplar field potential traces (*D*) and activation map (*E*) showing propagation of a single field potential across the NRVM monolayer over 7 ms. Arrows indicate propagation pathway and are situated at approximate electrode positioning; contours indicate 1-ms delay.

Differences in Basal Electrophysiology Depend on Cardiomyocyte Culture Type

The optimized MEA recording methodology was next used to compare the electrophysiological characteristics of three cardiomyocyte culture types, all of female origin. Significant differences in the electrical properties of female NRVMs, HL-1 cells, and hiPSC-CMs were observed (Fig. 5*A*). Spontaneous beating rate was significantly faster in hiPSC-CMs compared with both NRVM and HL-1 cells (NRVM vs. HL-1 vs. hiPSC-CM; 81.5 ± 6.9 vs. 49.7 ± 5.6 vs. 162.5 ± 38.0 beats/min, $P < 0.05$; Fig. 5*B*). Field potential morphology differed across the three cell types, with NRVMs exhibiting a substantially greater field potential amplitude compared with other cardiomyocyte cultures (2.95 ± 0.58 vs. 0.26 ± 0.02 vs. 0.40 ± 0.09 mV, $P < 0.05$; Fig. 5*C*). Field potential duration was similar in NRVMs and hiPSC-CMs but significantly shorter in HL-1 cells (184.0 ± 10.5 vs. 40.2 ± 1.4 vs. 146.9 ± 23.2 ms, $P < 0.05$; Fig. 5*D*). Derivation of the beating

AJP-Cell Physiol • doi:10.1152/ajpcell.00306.2019 • www.ajpcell.org

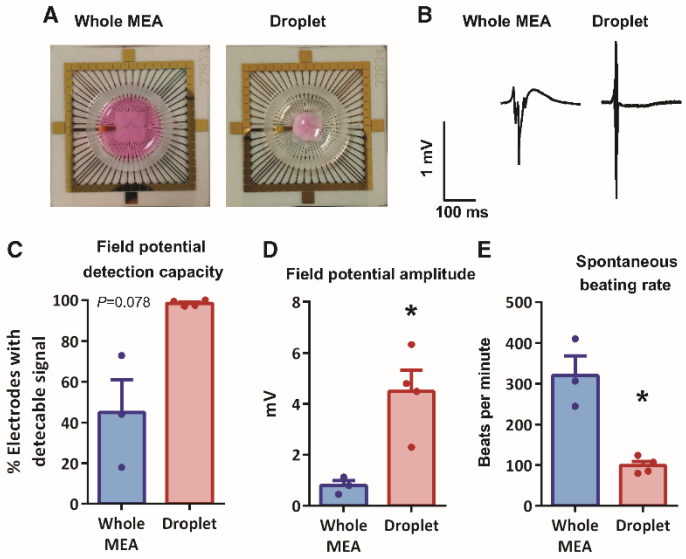

Fig. 2. Optimal cell seeding conditions for measuring cultured neonatal rat ventricular myocyte (NRVM) field potentials. Exemplar images of NRVM seeding across the entire microelectrode array (MEA) or as a droplet over the central recording zone of the electrode array (*A*), with respective exemplar field potential traces (*B*) and percentage of electrodes detecting field potentials (*C*). Mean field potential amplitude (*D*) and spontaneous beating rate from MEAs (*E*). All data were acquired from mixed-sex NRVMs, immediately after a 10-min stabilization period. *$P < 0.05$, unpaired *t* tests, $N = 3$–4 cultures, $n = 3$–10 MEAs.

rate-field potential duration relationship showed that both NRVMs and hiPSC-CMs (but not HL-1 cells) displayed field potential duration rate dependency. Both cell types exhibited faster repolarization at higher beating rates ($P < 0.05$, Fig. 5*E* and Supplemental Fig. S2), although the gradient of this relationship differed significantly ($P < 0.05$). Monolayer conduction rates were assessed in NRVM and HL-1 cells (but not in hiPSC-CMs because of their cluster morphology on plating). Conduction velocity was significantly faster in NRVM vs. HL-1 (24.25 ± 1.91 vs. 0.83 ± 0.03 cm/s, $P < 0.05$; Fig. 5, *F* and *G*).

To assess differences in responsiveness to β-adrenergic stimulation among cardiomyocyte cultures, cells were treated with 1 μM isoproterenol for 3–5 min. A significant increase in spontaneous beating rate was detected in both NRVMs and hiPSC-CMs but not HL-1 cells (Fig. 6, *A–D*, and Supplemental Fig. S3). Concomitant changes in field potential duration were observed, with a significant reduction evident in both NRVMs and hiPSC-CMs, but not HL-1 cells (Fig. 6, *E–G*, and Supplemental Fig. S3). The percentage decrease in field potential duration was hence significantly greater in both NRVMs and hiPSC-CMs compared with HL-1 cells (71.7 ± 4.0 vs. 102.1 ± 2.0 vs. 69.4 ± 4.0% basal, $P < 0.05$; Fig. 6*H*). It was evident that hiPSC-CM displayed greater variability between experimental replicates compared with NRVMs and HL-1 preps, and hence additional analysis was performed to determine whether the time point between differentiation induction (D0) and plating on the MEA was a determining factor (Fig. 7). hiPSCs plated earlier postdifferentiation induction demonstrated faster beating rates and shorter field potential durations (Fig. 7, *B–D*). hiPSC-CM isoproterenol responsiveness decreased in cells plated at a later time point postdifferentiation induction. An increase in beating rate in hiPSC-CMs treated with isoproterenol was not evident at 69 days postdifferentiation induction, with a similar trend evident in the field potential duration shortening response (Fig. 7, *E* and *F*).

DISCUSSION

This is the first study to systematically contrast the intrinsic differences in cardiomyocyte culture electrophysiologic function, comparing cultures of different cellular origin and prepared using different seeding methodologies. Our findings with NRVM monolayers showed that field potential detection/amplitude is greatly improved when cardiomyocytes are seeded exclusively over the central recording matrix of MEAs. We demonstrate that NRVM monolayer electrophysiology does not differ in cardiomyocytes isolated from male and female hearts, supporting the systematic use of combined male/female NRVM reported in the literature. Importantly, this study provides novel insight into the electrophysiological characteristics of different cardiomyocyte cultures. Both NRVMs and hiPSC-CMs exhibit a rate-dependent field potential duration and are responsive to β-adrenergic stimulation, contrasting with the relatively slower conduction and shorter field potential duration in HL-1 cells. This highlights the limitations with selecting a cardiomyocyte culture based primarily on cellular origin. Additionally, we report that hiPSC-CM electrophysiological characteristics are dependent on the number of days postdifferentiation at which the cells are plated on the MEA. Together, these findings provide important insights to assist in the selection of cell culture type appropriate for modeling cardiomyocyte conduction, novel comparative information that has not been previously available.

AJP-Cell Physiol • doi:10.1152/ajpcell.00306.2019 • www.ajpcell.org

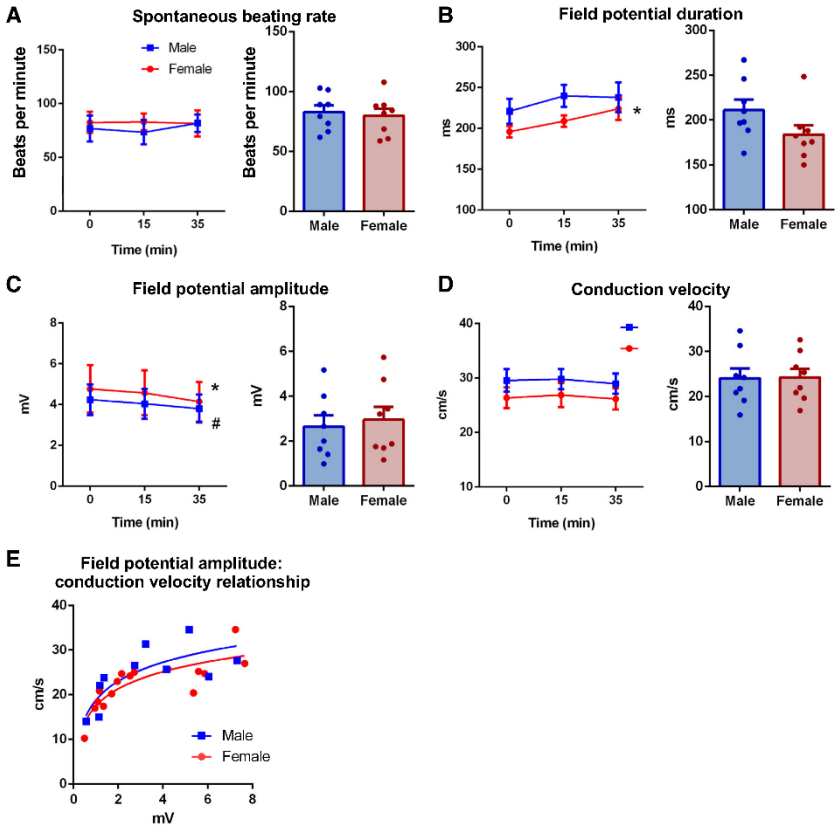

Fig. 3. Comparable electrophysiology in cultured male (blue) and female (red) neonatal rat ventricular myocytes (NRVMs). Assessment of prep stability in male and female NRVM electrophysiology with time (*left*) and direct sex comparison at 0 min (*right*), including spontaneous beating rate (*A*), field potential duration (*B*), field potential amplitude (*C*), and conduction velocity (*D*). *E*: field potential amplitude-conduction velocity relationships in male and female NRVM cultures. $P < 0.05$ females 0 vs. 35 min (*) and males 0 vs. 35min (#), $N = 3–4$ cultures, $n = 6–9$ microelectrode arrays (MEAs). No between-sex differences at any time point. Repeated-measures 2-way ANOVA and Holm-Sidak's multiple-comparison tests.

MEAs have been used to assess cardiomyocyte culture conduction properties for over a decade, yet there is a surprising lack of information in the literature with regard to optimizing seeding conditions. We have demonstrated important technical factors that significantly enhance field potential detection in cardiomyocyte monolayers. Seeding cardiomyocytes exclusively over the central recording matrix of the MEA increased the capacity to detect field potentials, with improved field potential morphology and significantly greater amplitude (Fig. 2). This is at least partly attributable to keeping the internal reference electrode free of the cell monolayer, increasing the signal-to-noise ratio, and enhancing the capacity to detect field potentials even at low field potential amplitudes. It is not clear whether the greater cell density over the central recording matrix in "droplet"-seeded MEAs (~1,000,000 vs. 500,000 cells/cm^2) is a factor in the capacity to detect field potentials. The considerably lower total number of cells in the 1 mL of media in droplet-seeded MEAs (300,000 vs. 1,400,000) may be important, likely enhancing glucose availability and minimizing accumulation of metabolic by-products. This would be expected to better maintain ATP-dependent ion homeostatic processes that contribute to action potential amplitude/duration.

The use of cardiac cell cultures adds a high-throughput capacity to the MEA that can be exploited for more rapid screening of novel antiarrhythmia drugs not limited by propensity for context-specific proarrhythmic actions. NRVMs, HL-1 cells, and hiPSC-CMs are three of the most commonly used cardiomyocyte cultures for these screening investigations. NRVMs exhibited rapid conduction velocities, particularly

AJP-Cell Physiol • doi:10.1152/ajpcell.00306.2019 • www.ajpcell.org

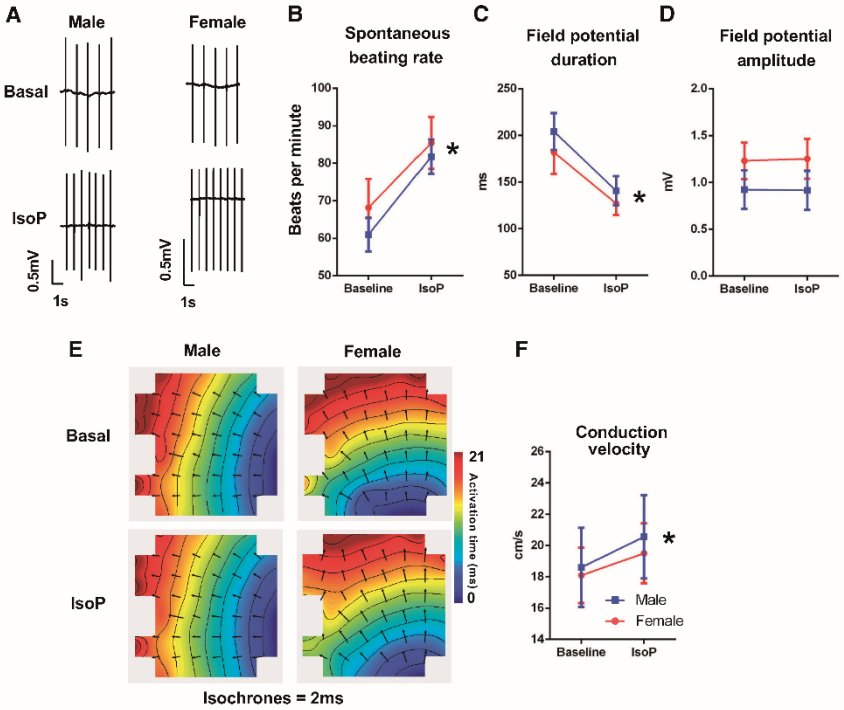

Fig. 4. Comparable isoproterenol (IsoP) response in cultured male (blue) and female (red) neonatal rat ventricular myocytes (NRVMs). *A*: exemplar field potential traces in male and female NRVMs in basal and 1 μM isoproterenol conditions. Mean spontaneous beating rate (*B*), field potential duration (*C*), and amplitude (*D*), exemplar conduction maps (*E*), and conduction velocity (*F*) of male and female NRVMs before (basal) and following an acute treatment of 1 μM isoproterenol. *$P < 0.05$, baseline vs. isoproterenol for both sexes. No between-sex differences. Repeated-measures 2-way ANOVA and Holm-Sidak's multiple-comparison tests. $N = 5–6$ cultures, $n = 6–7$ microelectrode arrays (MEAs).

compared with HL-1 cells (~20-fold faster than HL-1; Fig. 5, *F* and *G*), although slower than the typical conduction velocities of 60–75 cm/s recorded in mouse, guinea pig, and human ventricular slices (8, 33, 44). In addition to the inherent differences between neonatal rat and adult human electrophysiology, the slower conduction of NRVMs in vitro possibly reflects the more disorganized and polymorphic nature of these cells in culture following the cell isolation process.

Clearly, NRVMs provide a useful platform for exploring ventricular conduction properties and drug development. However, a potential oversight in the use of NRVMs in the past has been that these cells are almost exclusively isolated from litters without consideration for the sex of the pups. Cardiovascular disease is the primary cause of death in men and women, although the onset, development, and pathological characteristics of disease differ between sexes (15). Sexual dimorphism in cardiomyocyte electromechanical function is increasingly recognized (3, 34). Our novel NRVM data indicate sex does not influence basal or isoproterenol-induced electrophysiological characteristics in the neonatal rat, contrasting with previous studies in freshly isolated male/female adult cardiomyocytes (7, 17, 41). This suggests either the inherent influence of sex and sex steroids is absent in the neonate and/or that an absence of androgens/estrogens in the media over the 5–6 days of culture may convey transcriptional changes that attenuate fundamental sex differences in cardiomyocyte electrophysiology. Nonetheless, our findings indicate that pooled male and female NRVM cultures provide a valid model for studying at least some aspects of cardiomyocyte electrophysiology on the MEA. The comparison of NRVM, HL-1, and hiPSC-CM electrophysiology in this study used cells derived from females only, allowing for direct sex-controlled comparison of cellular phenotypes. Unfortunately, a parallel comparison of these three cardiomyocyte types in male-derived cells is not possible, since HL-1 cells were developed from an adult female C57BL/6J mouse.

Our hiPSC-CM differentiation protocol has been shown to produce cells expressing ventricular-specific markers (1), indicating the hiPSC-CMs used in this study are primarily of ventricular origin. Accordingly, hiPSC-CMs exhibited similar

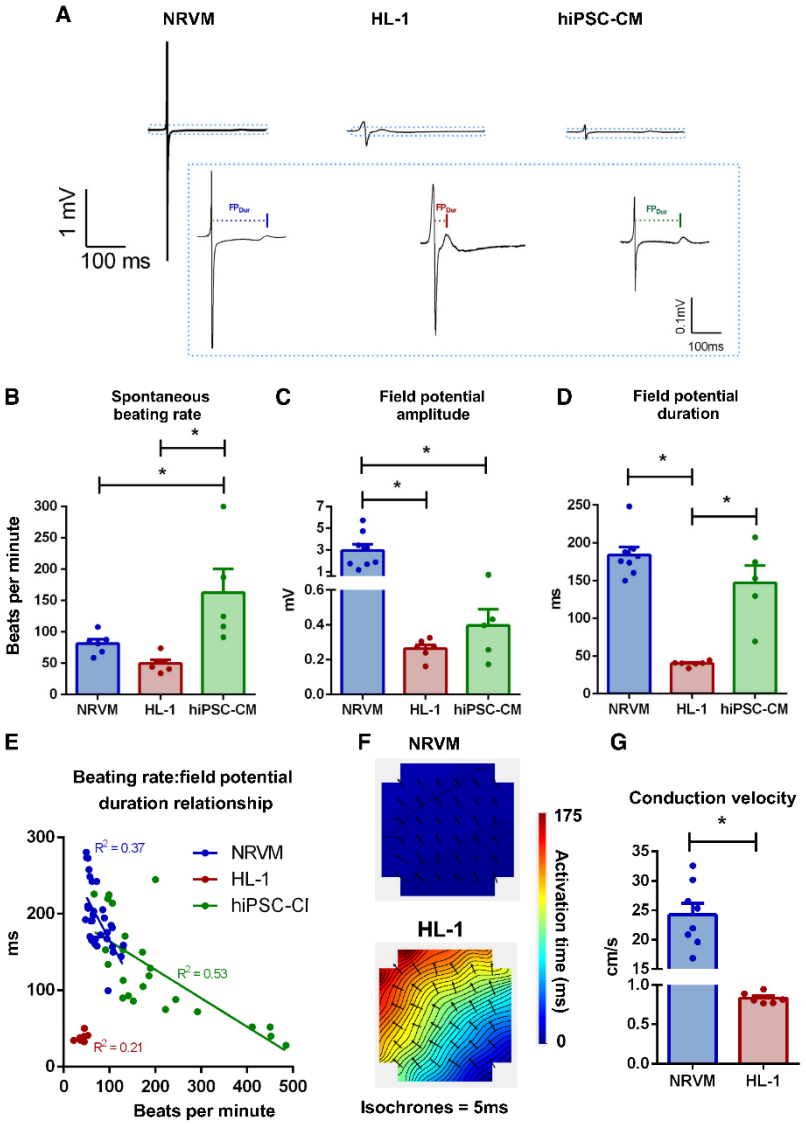

Fig. 5. Basal electrophysiology differs among female cardiomyocyte cultures of different origin. *A*: exemplar field potential traces from neonatal rat ventricular myocytes (NRVMs), HL-1, and human induced pluripotent stem cell-derived cardiomyocytes (hiPSC-CMs) at full scale and cropped (at the dotted lines) to highlight repolarization. Mean spontaneous beating rate (*B*), field potential amplitude (*C*), and field potential duration (*D*) from all 3 cell types. *E*: spontaneous beating rate-field potential duration relationship was examined on a single microelectrode array (MEA) basis among NRVM, HL-1, and hiPSC-CMs. Representative activation maps (*F*) and mean conduction velocity (*G*) in NRVM and HL-1 monolayers. $^*P < 0.05$, unpaired *t* tests or 1-way ANOVA with Holm-Sidak's multiple-comparison tests. NRVM: $N = 8$ cultures, $n = 19$ MEAs; HL-1: $N = 4–6$ passages, $n = 7–11$ MEAs; hiPSC-CMs: $N = 5$ (3 separate cultures, 5 plating runs), $n = 22$ MEAs.

AJP-Cell Physiol • doi:10.1152/ajpcell.00306.2019 • www.ajpcell.org

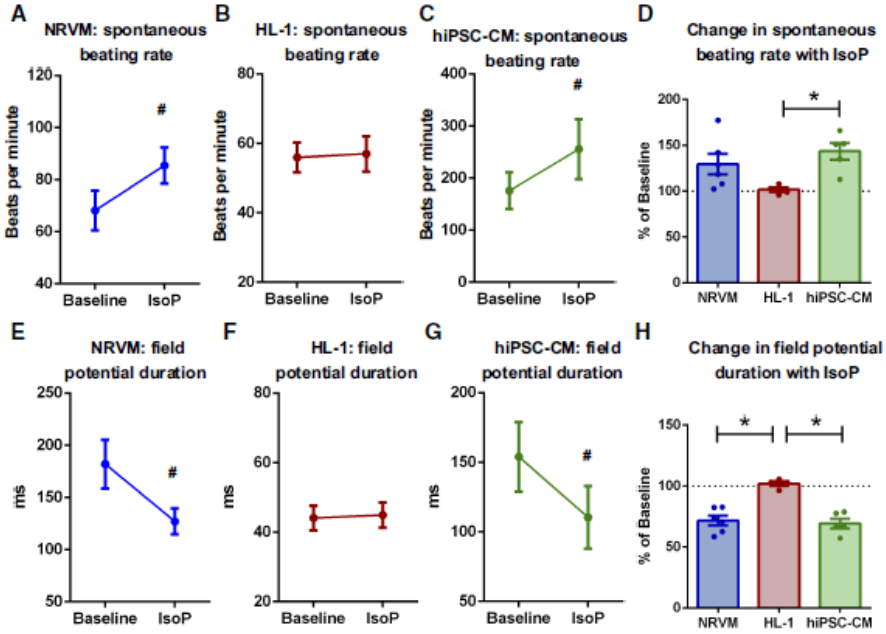

Fig. 6. Isoproterenol-stimulated (IsoP) electrophysiology differs among female cardiomyocyte cultures of different origin. Mean spontaneous beating rate for neonatal rat ventricular myocyte (NRVM, *A*), HL-1 (*B*), and human induced pluripotent stem cell-derived cardiomyocytes (hiPSC-CM, *C*) in response to 1 μM isoproterenol. *D*: %change in beating rate in response to 1 μM isoproterenol in all cell types. Mean field potential duration for NRVM (*E*), HL-1 (*F*), and hiPSC-CM (*G*) in response to 1 μM isoproterenol. *H*: %change in field potential duration in response to 1 μM isoproterenol in all cell types. $P < 0.05$, paired *t* test (#) and ordinary 1-way ANOVAs with Holm-Sidak's multiple comparisons (*). NRVM: $N = 8$ cultures, $n = 19$ MEAs; HL-1: $N = 4$ passages, $n = 7$–11 MEAs; hiPSC-CMs: $N = 5$ (3 separate cultures, 5 plating runs), $n = 22$ MEAs.

electrophysiological characteristics to NRVMs, particularly in relation to field potential duration and response to β-adrenergic receptor stimulation with isoproterenol. hiPSC-CMs were redifferentiated separately for each culture (*N*) from a single pool of stem cells, with reproducibility in the electrophysiological parameters evident between cultures/MEA runs. However, field potential duration and spontaneous beating rate were highly dependent on the number of days postdifferentiation at which the hiPSC-CMs were plated on the MEA. Our data showing that hiPSC-CM electrophysiology was not stable at 20 days postdifferentiation indicate an immature phenotype at this time point and highlight the need to ensure a sufficient period (≥30 days) between hiPSC-CM differentiation induction and MEA plating. Our demonstration of stable beating rates from *day 30* and reduced isoproterenol responsiveness in *day 60* cultures (vs. *day 30* cultures; Fig. 7, *F* and *G*) is consistent with previous studies. Paradoxically, β-adrenoreceptor expression has been shown to be increased in hiPSC-CMs at these time points (46). It is not clear why β-adrenoreceptor expression increases at a time when isoproterenol responsiveness is reduced. We speculate the greater β-adrenoreceptor expression reported in hiPSC-CMs could be indicative of extensive β-adrenoreceptor internalization or a compensatory upregulation to overcome potential disruption to downstream signaling pathways, although additional studies would be required to confirm this.

In this study, hiPSC-CMs did not form confluent coupled monolayers, and the capacity to assess conduction velocity was limited. As has been previously observed, the hiPSC-CMs formed clusters when plated, and conduction across the full array could not usually be evaluated (29, 31). There may be differences in culture morphology between commercially sourced and locally generated hiPSC-CMs. Although commercially available hiPSC-CMs can form electrically coupled monolayers, the lack of responsiveness to β-adrenergic stimulation suggests a less mature phenotype (16, 20, 36). Therefore, the hiPSC-CM source may limit the scope of investigation that may be undertaken.

Previous studies performing simultaneous intracellular and extracellular recordings on cell and tissue preparations have shown strong relationships between the action potential and field potential waveforms (10, 18). Our findings show that this action potential-conduction velocity relationship is also evident in the extracellular recording setup, with field potential amplitude correlating strongly with conduction velocity in NRVM monolayers (Fig. 3*E*). Also, our finding that different cardiomyocyte culture types display different rate adaptation properties has not been reported previously. Both hiPSC-CMs

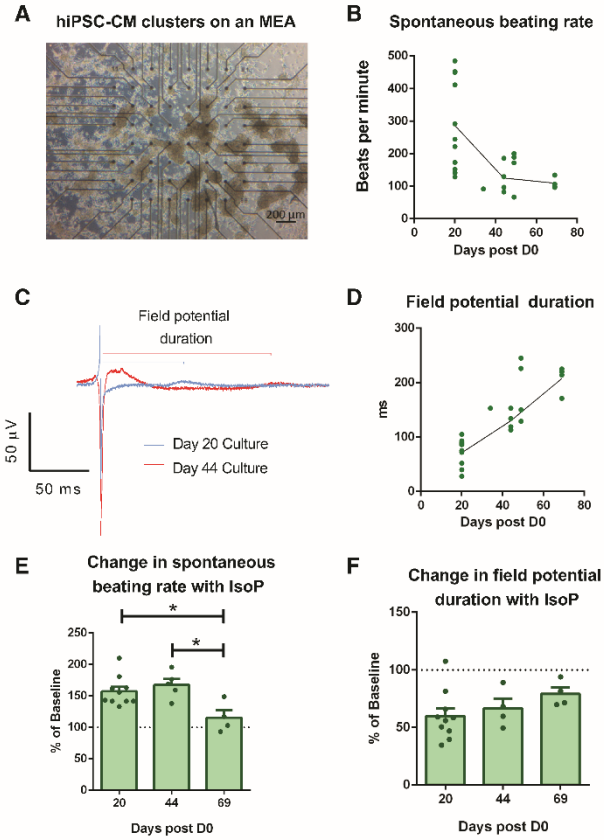

Fig. 7. Human induced pluripotent stem cell-derived cardiomyocyte (hiPSC-CM) electrophysiology changes with time postdifferentiation induction. *A*: exemplar image of hiPSC-CM clusters cultured on a microelectrode array (MEA). Relationship between spontaneous beating rate (*B*) and field potential duration (*C* and *D*) and the duration of the period postdifferentiation induction. n = 22 MEAs (lines plotted through *day 22*, *44*, and *69* means, since these time points had the most data points). Spontaneous beating rate (*E*) and field potential duration (*F*) changes induced by 1 µM isoproterenol (IsoP) in cultures examined at different time points postdifferentiation induction. n = 16–22 MEAs. *$P < 0.05$, 1-way ANOVA with Holm-Sidak's multiple comparisons.

and NRVMs exhibited a rate dependency in relation to field potential duration. When comparing NRVMs and those hiPSC-CMs with a beating rate of ≤150 beats/min, the rate-dependency relationships were comparable (Supplemental Fig. S2). The relationship between pacing rate and action potential duration is a fundamental property of cardiac myocytes (22), as evidenced by the similarities of the hiPSC-CMs used here with neonatal immature rat cardiomyocytes. Given the relationship between beating rate, action potential duration, and arrhythmia occurrence, our findings highlight the utility of these cell types as a model for drug screening.

HL-1 cells in our study did not show rate dependency, at least partly because of the low variability in observed beating rate, which may in turn reflect the minimal murine intrinsic rate adaptation in vivo (30, 46). As was observed for hiPSC-CMs, HL-1 cells exhibited low field potential amplitudes. More strikingly though, were the markedly shorter field potentials and slower conduction velocities compared with the other cell types. The conduction velocities reported here are similar to those reported for HL-1 cells in the literature (5, 39), although this is slower than that reported in NRVMs. It is not clear why conduction velocity is slower in HL-1 cells compared with the other cardiomyocyte cultures studied. HL-1 cells express both connexins (40 and 43 subtypes) and the fast voltage-gated sodium channel ($Na_V1.5$) that are essential for the formation of an electrically coupled excitable syncytium (2, 40, 43). We are not aware of any direct comparison of ion channel expression between cell types. To what extent the immortal nature of HL-1 cells yields a less organized monolayer compared with NRVMs is unknown. Interestingly, shorter field potentials and slower conduction velocities can both be characteristic electrophysiological features of atrial fibrillation. Indeed, several studies have used HL-1 cultures to model reentrant rotors (12, 21) and hence provide a valuable model for determining the underlying mechanisms of these waveforms required to develop new atrial fibrillation therapies.

Our direct comparisons of the three cell types provide novel evidence that β-adrenergic responses differ between cardiomy-

AJP-Cell Physiol • doi:10.1152/ajpcell.00306.2019 • www.ajpcell.org

ocyte cultures. HL-1 cell cultures in our study were not responsive to β-adrenergic stimulation with isoproterenol, contrasting with the significant acceleration of beating rate in both NRVM and hiPSC-CMs. This may be related to the presence of norepinephrine in the culture medium specifically formulated for HL-1 cells (45). Prolonged adrenergic stimulation induces a downregulation of adrenergic receptors (47), which may explain the lack of response of HL-1 cells to 1 μM isoproterenol in the current study. Considering the apparent lack of field potential duration rate dependency in the HL-1 cells, this suggests that NRVM and hiPSC-CMs may be better suited for modeling the relationship between heart rate, action potential duration, and arrhythmogenesis.

The direct comparison of the electrophysiological properties of commonly used cardiomyocyte cultures provides phenotypic benchmarking of important criteria for optimizing drug screening and development. Although these in vitro models cannot emulate in vivo characteristics, cardiomyocyte cultures offer clear advantages for electrophysiological investigations compared with in vivo/ex vivo/tissue slice alternatives. The preparations are relatively simple to set up and provide a high-throughput capacity. The differences in cultured cardiomyocyte electrophysiological properties described here may even be exploited, enabling the targeting of specific cellular phenotypes that most closely model specific arrhythmia or drug response scenarios. Our findings suggest that NRVM and hiPSC-CM cultures may be suitable for modeling-triggered arrhythmia scenarios, with HL-1 cells better suited to model conduction rotors and reentrant arrhythmias.

In conclusion, our study provides a methodologic advance as the first study to demonstrate the intrinsic differences in electrophysiology of cultured cardiomyocyte preparations commonly used for in vitro electrophysiology assessment. Considering the interest in the MEA as a drug-screening platform, these differences can be considered for an appropriate experimental design when selecting cardiomyocyte in vitro approaches for modeling triggered and reentrant arrhythmia scenarios. Together with our optimization of the culture-seeding technique, these findings offer important comparative data to inform methodological approaches in the use of MEA and other techniques relating to cardiomyocyte functional screening investigations.

GRANTS

This research was supported by the National Health and Medical Research Council (nos. 1099352 and 1125453; L. M. D. Delbridge, J. R. Bell) and the Australian Research Council (no. DP160102404; L. M. D. Delbridge).

DISCLOSURES

P. Kirchhof receives research support for basic, translational, and clinical research projects from European Union, British Heart Foundation, Leducq Foundation, Medical Research Council (UK), and German Centre for Cardiovascular Research, from several drug and device companies active in atrial fibrillation, and has received honoraria from several such companies in the past. P. Kirchhof is listed as inventor on two patents held by University of Birmingham (Atrial Fibrillation Therapy WO 2015140571, Markers for Atrial Fibrillation WO 2016012783). None of the other authors has any conflicts of interest, financial or otherwise, to disclose.

AUTHOR CONTRIBUTIONS

S.P.W., H.M.W., E.R.P., L.M.D.D., and J.R.B. conceived and designed research; S.P.W., H.M.W., C.B.S., S.Y.L., and G.B.B. performed experiments; S.P.W., H.M.W., and G.B.B. analyzed data; S.P.W., H.M.W., G.B.B., D.P., P.K., E.R.P., L.M.D.D., and J.R.B. interpreted results of experiments; S.P.W., H.M.W., G.B.B., L.M.D.D., and J.R.B. prepared figures; S.P.W., H.M.W., L.M.D.D., and J.R.B. drafted manuscript; S.P.W., H.M.W., C.B.S., S.Y.L., G.B.B., D.P., P.K., E.R.P., L.M.D.D., and J.R.B. edited and revised manuscript; S.P.W., H.M.W., C.B.S., S.Y.L., G.B.B., D.P., P.K., E.R.P., L.M.D.D., and J.R.B. approved final version of manuscript.

REFERENCES

1. **Anderson DJ, Kaplan DI, Bell KM, Koutsis K, Haynes JM, Mills RJ, Phelan DG, Qian EL, Leitoguinho AR, Arasaratnam D, Labonne T, Ng ES, Davis RP, Casini S, Passier R, Hudson JE, Porrello ER, Costa MW, Rafii A, Curl CL, Delbridge LM, Harvey RP, Oshlack A, Cheung MM, Mummery CL, Petrou S, Elefanty AG, Stanley EG, Elliott DA.** NKX2-5 regulates human cardiomyogenesis via a HEY2 dependent transcriptional network. *Nat Commun* 9: 1373, 2018. doi:10.1038/s41467-018-03714-x.
2. **Barriga M, Cal R, Cabello N, Llach A, Vallmitjana A, Benítez R, Badimon L, Cinca J, Llorente-Cortés V, Hove-Madsen L.** Low density lipoproteins promote unstable calcium handling accompanied by reduced SERCA2 and connexin-40 expression in cardiomyocytes. *PLoS One* 8: e58128, 2013. doi:10.1371/journal.pone.0058128.
3. **Bell JR, Bernasochi GB, Varma U, Raaijmakers AJA, Delbridge LMD.** Sex and sex hormones in cardiac stress--mechanistic insights. *J Steroid Biochem Mol Biol* 137: 124–135, 2013. doi:10.1016/j.jsbmb.2013.05.015.
4. **Bell JR, Curl CL, Harding TW, Vila Petroff M, Harrap SB, Delbridge LMD.** Male and female hypertrophic rat cardiac myocyte functional responses to ischemic stress and β-adrenergic challenge are different. *Biol Sex Differ* 7: 32, 2016. doi:10.1186/s13293-016-0084-8.
5. **Boyle PM, Franceschi WH, Constantin M, Hawks C, Desplantez T, Trayanova NA, Vigmond EJ.** New insights on the cardiac safety factor: unraveling the relationship between conduction velocity and robustness of propagation. *J Mol Cell Cardiol* 128: 117–128, 2019. doi:10.1016/j.yjmcc.2019.01.010.
6. **Braam SR, Tertoolen L, van de Stolpe A, Meyer T, Passier R, Mummery CL.** Prediction of drug-induced cardiotoxicity using human embryonic stem cell-derived cardiomyocytes. *Stem Cell Res (Amst)* 4: 107–116, 2010. doi:10.1016/j.scr.2009.11.004.
7. **Brouillette J, Rivard K, Lizotte E, Fiset C.** Sex and strain differences in adult mouse cardiac repolarization: importance of androgens. *Cardiovasc Res* 65: 148–157, 2005. doi:10.1016/j.cardiores.2004.09.012.
8. **Camelliti P, Al-Saud SA, Smolenski RT, Al-Ayoubi S, Bussek A, Wettwer E, Banner NR, Bowles CT, Yacoub MH, Terracciano CM.** Adult human heart slices are a multicellular system suitable for electrophysiological and pharmacological studies. *J Mol Cell Cardiol* 51: 390–398, 2011. doi:10.1016/j.yjmcc.2011.06.018.
9. **Chan YC, Tse HF, Siu CW, Wang K, Li RA.** Automaticity and conduction properties of bio-artificial pacemakers assessed in an in vitro monolayer model of neonatal rat ventricular myocytes. *Europace* 12: 1178–1187, 2010. doi:10.1093/europace/euq120.
10. **Chowdhury RA, Tzortzis KN, Dupont E, Selvadurai S, Perbellini F, Cantwell CD, Ng FS, Simon AR, Terracciano CM, Peters NS.** Concurrent micro- to macro-cardiac electrophysiology in myocyte cultures and human heart slices. *Sci Rep* 8: 6947, 2018. doi:10.1038/s41598-018-25170-9.
11. **Claycomb WC, Lanson NA Jr, Stallworth BS, Egeland DB, Delcarpio JB, Bahinski A, Izzo NJ Jr.** HL-1 cells: a cardiac muscle cell line that contracts and retains phenotypic characteristics of the adult cardiomyocyte. *Proc Natl Acad Sci USA* 95: 2979–2984, 1998. doi:10.1073/pnas.95.6.2979.
12. **Climent AM, Guillem MS, Fuentes L, Lee P, Bollensdorff C, Fernández-Santos ME, Suárez-Sancho S, Sanz-Ruiz R, Sánchez PL, Atienza F, Fernández-Avilés F.** Role of atrial tissue remodeling on rotor dynamics: an in vitro study. *Am J Physiol Heart Circ Physiol* 309: H1964–H1973, 2015. doi:10.1152/ajpheart.00055.2015.
13. **Costa M, Dottori M, Sourris K, Jamshidi P, Hatzistavrou T, Davis R, Azzola L, Jackson S, Lim SM, Pera M, Elefanty AG, Stanley EG.** A method for genetic modification of human embryonic stem cells using electroporation. *Nat Protoc* 2: 792–796, 2007. doi:10.1038/nprot.2007.105.
14. **Elliott DA, Braam SR, Koutsis K, Ng ES, Jenny R, Lagerqvist EL, Biben C, Hatzistavrou T, Hirst CE, Yu QC, Skelton RJ, Ward-van Oostwaard D, Lim SM, Khammy O, Li X, Hawes SM, Davis RP, Goulburn AL, Passier R, Prall OW, Haynes JM, Pouton CW, Kaye DM, Mummery CL, Elefanty AG, Stanley EG.** NKX2-5(eGFP/w)

hESCs for isolation of human cardiac progenitors and cardiomyocytes. *Nat Methods* 8: 1037–1040, 2011. doi:10.1038/nmeth.1740.

15. **Garcia M, Mulvagh SL, Merz CNB, Buring JE, Manson JE.** Cardiovascular disease in women: clinical perspectives. *Circ Res* 118: 1273–1293, 2016. doi:10.1161/CIRCRESAHA.116.307547.
16. **Goineau S, Castagné V.** Electrophysiological characteristics and pharmacological sensitivity of two lines of human induced pluripotent stem cell derived cardiomyocytes coming from two different suppliers. *J Pharmacol Toxicol Methods* 90: 58–66, 2018. doi:10.1016/j.vascn.2017.12.003.
17. **Graham EL, Balla C, Franchino H, Melman Y, del Monte F, Das S.** Isolation, culture, and functional characterization of adult mouse cardiomyoctyes. *J Vis Exp* 79: e50289, 2013. doi:10.3791/50289.
18. **Halbach M, Egert U, Hescheler J, Banach K.** Estimation of action potential changes from field potential recordings in multicellular mouse cardiac myocyte cultures. *Cell Physiol Biochem* 13: 271–284, 2003. doi:10.1159/000074542.
19. **Heist EK, Ruskin JN.** Drug-induced arrhythmia. *Circulation* 122: 1426–1435, 2010. doi:10.1161/CIRCULATIONAHA.109.894725.
20. **Hernández D, Millard R, Sivakumaran P, Wong RC, Crombie DE, Hewitt AW, Liang H, Hung SS, Pébay A, Shepherd RK, Dusting GJ, Lim SY.** Electrical stimulation promotes cardiac differentiation of human induced pluripotent stem cells. *Stem Cells Int* 2016: 1718041, 2016. doi:10.1155/2016/1718041.
21. **Houston C, Tzortzis KN, Roney C, Saglietto A, Pitcher DS, Cantwell CD, Chowdhury RA, Ng FS, Peters NS, Dupont E.** Characterisation of re-entrant circuit (or rotational activity) in vitro using the HL1-6 myocyte cell line. *J Mol Cell Cardiol* 119: 155–164, 2018. doi:10.1016/j.yjmcc.2018.05.002.
22. **Hund TJ, Rudy Y.** Rate dependence and regulation of action potential and calcium transient in a canine cardiac ventricular cell model. *Circulation* 110: 3168–3174, 2004. doi:10.1161/01.CIR.0000147231.69595.D3.
23. **Jansen HJ, Moghtadaei M, Mackasey M, Rafferty SA, Bogachev O, Sapp JL, Howlett SE, Rose RA.** Atrial structure, function and arrhythmogenesis in aged and frail mice. *Sci Rep* 7: 44336–44336, 2017. doi:10.1038/srep44336.
24. **Kirchhof P, Benussi S, Kotecha D, Ahlsson A, Atar D, Casadei B, Castella M, Diener HC, Heidbuchel H, Hendriks J, Hindricks G, Manolis AS, Oldgren J, Popescu BA, Schotten U, Van Putte B, Vardas P, Group ESCSD; ESC Scientific Document Group.** 2016 ESC Guidelines for the management of atrial fibrillation developed in collaboration with EACTS. *Eur Heart J* 37: 2893–2962, 2016. doi:10.1093/eurheartj/ehw210.
25. **Lafuente-Lafuente C, Valembois L, Bergmann JF, Belmin J.** Antiarrhythmics for maintaining sinus rhythm after cardioversion of atrial fibrillation. *Cochrane Database Syst Rev* 3: CD005049, 2015. doi:10.1002/14651858.CD005049.pub4.
26. **Lane DA, Skjøth F, Lip GYH, Larsen TB, Kotecha D.** Temporal trends in incidence, prevalence, and mortality of atrial fibrillation in primary care. *J Am Heart Assoc* 6: e005155, 2017. doi:10.1161/JAHA.116.005155.
27. **Lubitz SA, Sinner MF, Lunetta KL, Makino S, Pfeufer A, Rahman R, Veltman CE, Barnard J, Bis JC, Danik SP, Sonni A, Shea MA, Del Monte F, Perz S, Müller M, Peters A, Greenberg SM, Furie KL, van Noord C, Boerwinkle E, Stricker BH, Witteman J, Smith JD, Chung MK, Heckbert SR, Benjamin EJ, Rosand J, Arking DE, Alonso A, Kääb S, Ellinor PT.** Independent susceptibility markers for atrial fibrillation on chromosome 4q25. *Circulation* 122: 976–984, 2010. doi:10.1161/CIRCULATIONAHA.109.886440.
28. **Meiry G, Reisner Y, Feld Y, Goldberg S, Rosen M, Ziv N, Binah O.** Evolution of action potential propagation and repolarization in cultured neonatal rat ventricular myocytes. *J Cardiovasc Electrophysiol* 12: 1269–1277, 2001. doi:10.1046/j.1540-8167.2001.01269.x.
29. **Mills RJ, Titmarsh DM, Koenig X, Parker BL, Ryall JG, Quaife-Ryan GA, Voges HK, Hodson MP, Ferguson C, Drowley L, Plowright AT, Needham EJ, Wang Q-D, Gregorevic P, Xin M, Thomas WG, Parton RG, Nielsen LK, Launikonis BS, James DE, Elliott DA, Porrello ER, Hudson JE.** Functional screening in human cardiac organoids reveals a metabolic mechanism for cardiomyocyte cell cycle arrest. *Proc Natl Acad Sci USA* 114: E8372–E8381, 2017. doi:10.1073/pnas.1707316114.
30. **Mulla W, Gillis R, Murninkas M, Klapper-Goldstein H, Gabay H, Mor M, Elyagon S, Liel-Cohen N, Bernus O, Etzion Y.** Unanesthetized rodents demonstrate insensitivity of qt interval and ventricular refractory period to pacing cycle length. *Front Physiol* 9: 897, 2018. doi:10.3389/fphys.2018.00897.
31. **Mummery CL, Zhang J, Ng ES, Elliott DA, Elefanty AG, Kamp TJ.** Differentiation of human embryonic stem cells and induced pluripotent stem cells to cardiomyocytes: a methods overview. *Circ Res* 111: 344–358, 2012. doi:10.1161/CIRCRESAHA.110.227512.
32. **Nguyen PD, Hsiao ST, Sivakumaran P, Lim SY, Dilley RJ.** Enrichment of neonatal rat cardiomyocytes in primary culture facilitates long-term maintenance of contractility in vitro. *Am J Physiol Cell Physiol* 303: C1220–C1228, 2012. doi:10.1152/ajpcell.00449.2011.
33. **O'Shea C, Holmes AP, Yu TY, Winter J, Wells SP, Correia J, Boukens BJ, De Groot JR, Chu GS, Li X, Ng GA, Kirchhof P, Fabritz L, Rajpoot K, Pavlovic D.** ElectroMap: High-throughput open-source software for analysis and mapping of cardiac electrophysiology. *Sci Rep* 9: 1389, 2019. doi:10.1038/s41598-018-38263-2.
34. **Parks RJ, Howlett SE.** Sex differences in mechanisms of cardiac excitation-contraction coupling. *Pflugers Arch* 465: 747–763, 2013. doi:10.1007/s00424-013-1233-0.
35. **Porrello ER, Bell JR, Schertzer JD, Curl CL, McMullen JR, Mellor KM, Ritchie RH, Lynch GS, Harrap SB, Thomas WG, Delbridge LMD.** Heritable pathologic cardiac hypertrophy in adulthood is preceded by neonatal cardiac growth restriction. *Am J Physiol Regul Integr Comp Physiol* 296: R672–R680, 2009. doi:10.1152/ajpregu.90919.2008.
36. **Ribeiro MC, Tertoolen LG, Guadix JA, Bellin M, Kosmidis G, D'Aniello C, Monshouwer-Kloots J, Goumans M-J, Wang YL, Feinberg AW, Mummery CL, Passier R.** Functional maturation of human pluripotent stem cell derived cardiomyocytes in vitro--correlation between contraction force and electrophysiology. *Biomaterials* 51: 138–150, 2015. doi:10.1016/j.biomaterials.2015.01.067.
37. **Sala L, Ward-van Oostwaard D, Tertoolen LGJ, Mummery CL, Bellin M.** Electrophysiological analysis of human pluripotent stem cell-derived cardiomyocytes (hPSC-CMs) using multi-electrode arrays (MEAs). *J Vis Exp* 123: 55587, 2017. doi:10.3791/55587.
38. **Sayed N, Liu C, Wu JC.** Translation of human-induced pluripotent stem cells: from clinical trial in a dish to precision medicine. *J Am Coll Cardiol* 67: 2161–2176, 2016. doi:10.1016/j.jacc.2016.01.083.
39. **Schinner C, Erber BM, Yeruva S, Waschke J.** Regulation of cardiac myocyte cohesion and gap junctions via desmosomal adhesion. *Acta Physiol (Oxf)* 226: e13242, 2019. doi:10.1111/apha.13242.
40. **Severino A, Narducci ML, Pedicino D, Pazzano V, Giglio AF, Biasucci LM, Liuzzo G, Casella M, Bartoletti S, Dello Russo A, Pelargonio G, Santangeli P, Di Biase L, Natale A, Crea F.** Reversible atrial gap junction remodeling during hypoxia/reoxygenation and ischemia: a possible arrhythmogenic substrate for atrial fibrillation. *Gen Physiol Biophys* 31: 439–448, 2012. doi:10.4149/gpb_2012_047.
41. **Trépanier-Boulay V, St-Michel C, Tremblay A, Fiset C.** Gender-based differences in cardiac repolarization in mouse ventricle. *Circ Res* 89: 437–444, 2001. doi:10.1161/hh1701.095644.
42. **Vandenberg JI, Perry MD, Hill AP.** Recent advances in understanding and prevention of sudden cardiac death. *F1000 Res* 6: 1614, 2017. doi:10.12688/f1000research.11855.1.
43. **Wang N, Huo R, Cai B, Lu Y, Ye B, Li X, Li F, Xu H.** Activation of Wnt/β-catenin signaling by hydrogen peroxide transcriptionally inhibits NaV1.5 expression. *Free Radic Biol Med* 96: 34–44, 2016. doi:10.1016/j.freeradbiomed.2016.04.003.
44. **Wen Q, Gandhi K, Capel RA, Hao G, O'Shea C, Neagu G, Pearcey S, Pavlovic D, Terrar DA, Wu J, Faggian G, Camelliti P, Lei M.** Transverse cardiac slicing and optical imaging for analysis of transmural gradients in membrane potential and Ca^{2+} transients in murine heart. *J Physiol* 596: 3951–3965, 2018. doi:10.1113/JP276239.
45. **White SM, Constantin PE, Claycomb WC.** Cardiac physiology at the cellular level: use of cultured HL-1 cardiomyocytes for studies of cardiac muscle cell structure and function. *Am J Physiol Heart Circ Physiol* 286: H823–H829, 2004. doi:10.1152/ajpheart.00986.2003.
46. **Wu H, Lee J, Vincent LG, Wang Q, Gu M, Lan F, Churko JM, Sallam KI, Matsa E, Sharma A, Gold JD, Engler AJ, Xiang YK, Bers DM, Wu JC.** Epigenetic regulation of phosphodiesterases 2A and 3A underlies compromised β-adrenergic signaling in an iPSC model of dilated cardiomyopathy. *Cell Stem Cell* 17: 89–100, 2015. doi:10.1016/j.stem.2015.04.020.
47. **Zhao M, Hagler HK, Muntz KH.** Regulation of α_{1}-, β_{1}-, and β_{2}-adrenergic receptors in rat heart by norepinephrine. *Am J Physiol Heart Circ Physiol* 271: H1762–H1768, 1996. doi:10.1152/ajpheart.1996.271.5.H1762.

Appendix A – Supplemental Data

Cardiomyocyte functional screening – interrogating comparative electrophysiology of high-throughput model cell systems

Simon P. Wells, Helen M. Waddell, Choon Boon Sim, Shiang Y. Lim, Gabriel B. Bernasochi, Davor Pavlovic, Paulus Kirchhof, Enzo R. Porrello, Lea M. D. Delbridge, James R. Bell

Index

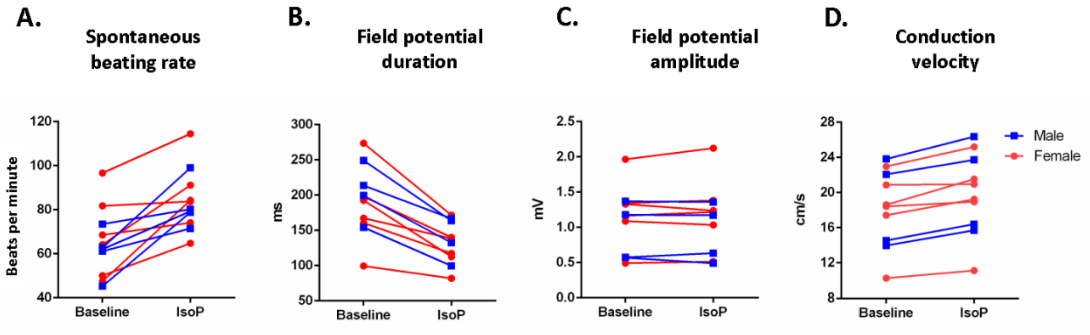

Fig S1 | Individual responses of male (blue) and female (red) NRVMs to 1μM isoproterenol. (**A**) Spontaneous beating rate (**B**) field potential duration, (**C**) field potential amplitude and (**D**) conduction velocity. *N*=5–6 cultures, *n*=6–7 MEAs.

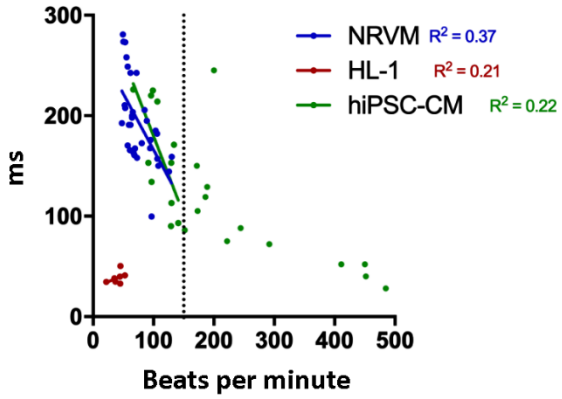

Fig S2 | Spontaneous beating rate:Field potential duration relationship among NRVMs, HL-1 and hiPSC-CMs, with a linear regression fitted only to cells with rates ≤150BPM.

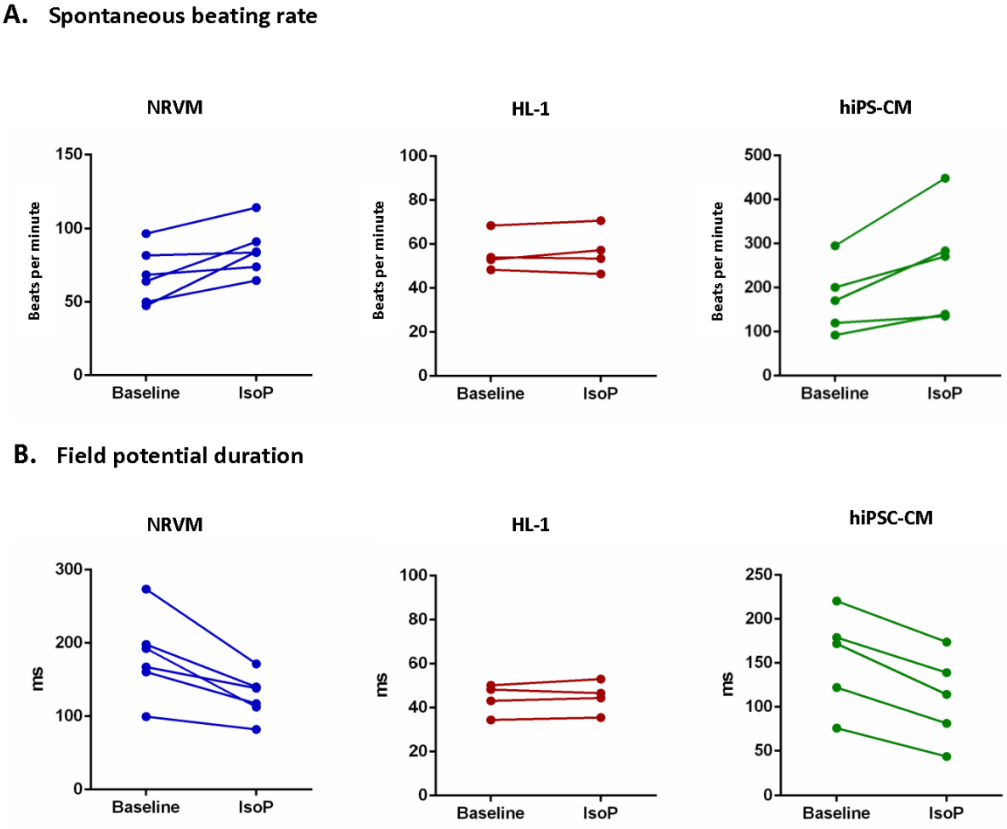

Fig S3 | Individual responses of NRVMs, HL-1 and hiPSC-CMs to 1μM isoproterenol. (A) Spontaneous beating rate **(B)** field potential duration. NRVMs: *N*=6 cultures, *n*=7 MEAs; HL-1: *N=4* passages, *n*=7 MEAs; hiPSC-CMs: *N*=5, *n*=22 MEAs.

Chapter 5

Obesity and epicardial adipose tissue associate with prolonged repolarisation in murine atria and human cardiomyocytes

This chapter contains data from two proposed manuscripts under finalisation.

Wells SP, O'Shea C, Sim CB, …, Porrello ER, Kirchhof P, Pavlovic D, Delbridge LMD and Bell JR. Obesity and epicardial adipose tissue associate with prolonged repolarisation in murine atria and human cardiomyocytes. **In preparation**. (**Figures: 5.1-5.5, 5.6A & F, 5.7 and 5.8**)

Nalliah CJ[*], Bell JR[*], Raaijmakers AJA, Waddell HW, **Wells SP**, Bernasochi GB, Montgomery MK, Binny S, Watts TM, Joshi S, Lui E, Sim CB, Larobina M, O'Keefe M, Goldblatt J, Royse A, Lee G, Porrello ER, Watt MJ, Kistler PM, Sanders P, Delbridge LMD[#], Kalman JM[#]. Epicardial Adipose Tissue Accumulation Confers Atrial Conduction Abnormality *J Am Coll Cardiol*, 2020; 76: (10), 1197-1211. (**Figures: 5.6B-E**)

Abstract

Background

Atrial fibrillation (AF) is a significant global healthcare burden, particularly in the aged and overweight/obese populations. Obesity associates with increased epicardial adiposity and recent clinical studies pose this as an independent risk factor for AF. The cellular electrophysiological mechanisms linking epicardial adiposity and AF are poorly understood. The aims of this study were to determine the extent of left atrial electrical remodelling in a murine model of obesity and determine how epicardial adipose tissue might modulate human cardiomyocyte electrophysiology.

Methods

C57BL/6 mice were fed chow (control) or a Western diet for 20 weeks (n=4-6). Left atria were isolated, and electrophysiology assessed using optical mapping. In parallel studies, human induced pluripotent stem cell-derived cardiomyocytes (hiPSC-CMs) were co-cultured in the absence/presence of sheep epicardial adipose tissue fragments (4-24hr) on microelectrode arrays and extracellular field potentials recorded ($N_{cultures}$=7, $n_{microelectrode\ arrays}$=17-33).

Results

Western diet feeding induced obesity (27% weight difference *vs* control) and significant left atrial action potential prolongation (action potential duration at 70% repolarisation, control *vs* Western diet: 17.0±1.0ms *vs* 23.5±1.0ms; P<0.05). Conduction velocity was unaffected. hiPSC-CMs co-cultured with epicardial adipose tissue for 4hr demonstrated prolonged field potential duration (29.5% increase, P<0.05), with unaffected conduction

velocity. When co-culture was extended to 24hr, effects on hiPSC-CM repolarisation were maintained, coupled with a drop in beating rate – steepening the repolarisation-rate dependency relationship *vs* control ($P<0.05$).

Conclusions

This is the first study to show that obesity associates with prolonged left atrial repolarisation and that epicardial adipose tissue exerts a similar paracrine effect on hiPSC-CM electrophysiology. Prolonged repolarisation predisposes to triggered arrhythmia – a key feature of AF onset, indicating a potential paracrine role for augmented epicardial adiposity in the initial formation of an unstable electrical substrate. Further studies are required to characterise which paracrine mediators might be implicated.

Key words

Atrial fibrillation ▪ Atrial repolarisation ▪ Epicardial adipose tissue ▪ Obesity ▪ Pericardial adipose tissue

Abbreviations

+Adip, epicardial adipose tissue co-culture ▪ AF, atrial fibrillation ▪ APD, action potential duration ▪ BPM, beats per minute ▪ Ctrl, control ▪ hiPSC-CM, human induced pluripotent stem cell-derived cardiomyocytes ▪ MEA, microelectrode array

5.1 Introduction

Epidemiology of obesity and atrial fibrillation

Obesity is a global public health problem and associates with a significant increase in atrial fibrillation (AF) risk (41). AF is the most common cardiac arrhythmia, affecting 4% of the population (13). For every 1 unit increase in BMI, there's a parallel 4% increase in AF risk (41). Although itself not lethal, AF has significant impact on life quality and associates with a greater risk of stroke and heart failure (11, 23, 29, 45). Current therapeutic strategies offer incomplete effectiveness, typically requiring repeated procedures or delivering off-target (potentially pro-arrhythmic) side effects (18). Development of novel therapeutic strategies requires a better understanding of the cellular electrophysiological mechanisms underpinning atrial fibrillation, particularly in the context of factors that make the aged/obese populations most at risk.

Cellular mechanisms of atrial fibrillation

It is well established that the left atrium is a key site for the onset and maintenance of AF (31). On a cellular level, the specific electrical remodelling involves regional action potential duration (APD) shortening/prolongation and/or conduction velocity slowing. APD shortening and conduction slowing predispose to a reentrant arrhythmia (typically seen in persistent/permanent AF), whilst APD prolongation is thought to underpin the electrical remodelling that initiates AF, increasing likelihood of early afterdepolarisation triggered arrhythmias (4, 14, 15, 24). Understanding the structural/electrical remodelling that predisposes to APD prolongation can give insight into the mechanisms of AF onset.

Epicardial adipose tissue and atrial fibrillation risk

Epicardial adipose tissue accumulation is an independent risk factor for AF (37). Epicardial adipose tissue (located on the myocardial epicardium) together with paracardial adipose tissue (located on the pericardial sac) comprises pericardial adipose tissue. Epicardial adipose tissue accumulation associates with AF progression, severity and worse treatment outcomes (44, 46). Tissue culture experimentation indicates that epicardial adipose tissue has capacity to release adipo-fibrokines, promoting epicardial fibrosis contributing to the formation of an electrically unstable AF substrate (40). It remains unknown how epicardial adipose tissue may directly modulate human cardiomyocyte electrophysiology. Lin *et al*., (2012) have demonstrated that rabbit atrial cardiomyocytes incubated with epicardial adipocytes exhibit a depolarised resting membrane potential and prolonged repolarisation (20).

Aims

The aims of this investigation were to determine whether left atrial electrophysiology is modulated in a murine model of obesity and examine whether epicardial adipose tissue influences human cardiomyocyte electrophysiology.

5.2 Methods

Animal details

Mouse experiments were conducted under the Animals (Scientific Procedures) Act 1986 and approved by the Home Office and the institutional review board at the University of Birmingham. 6-12-week-old C57BL/6 male mice were housed in individually ventilated cages, under 12hr light/dark cycles, at 22^{o}C, 55% humidity. Mice were fed either chow and drinking water or a Western diet (Special Diets Services, UK; Western RD, 829100; percentage dietary Kcal: fat, 42; protein, 15; carbohydrate, 43) supplemented with 15% fructose drinking water for 20 weeks. Food and water were available *ad libitum* and body weight, food intake and general health monitored weekly.

Sheep experiments were approved by the Animal Ethics Committee of the Florey Institute of Neuroscience that adheres to the Australian Code for the Care and Use of Animals for Scientific Purposes. Adult Merino ewes were maintained and fed as previously reported (1). Anaesthesia was induced and maintained with 1.5-2% isoflurane. Following thoracotomy and pericardial sac division, epicardial adipose tissue was dissected away from the heart and placed immediately in warm, sterile phosphate buffered saline (Life Technologies, Cat#: 14190-144) + 1% penicillin/streptomycin (Invitrogen, Cat#: 15070).

Isolated left atrial optical mapping

Optical mapping experiments were performed as previously published (16, 26). At 26-32 weeks of age, hearts were rapidly excised from mice under deep anaesthesia (4% isoflurane in O_2, 3L/min) and placed in ice-cold Krebs-Henseleit buffer (in mM: NaCl,

118.0; KCl, 3.52; $MgSO_4 7H_2O$, 0.83; KH_2PO_4, 1.18; $NaHCO_3$, 24.90; glucose, 11.0; $CaCl_2$, 1.80). The aorta was cannulated and the heart retrogradely perfused through a vertical Langendorff apparatus (Hugo Sachs, March-Hugstetten, Germany) with oxygenated Krebs-Henseleit buffer (37°C). The voltage-sensitive dye, Di-4-ANEPPS (5µM; Cambridge Biosciences, Cambridge, UK), was loaded via bolus injection into the perfusate over 5min. Dye-loaded hearts were removed from the Langendorff apparatus, the left atrium excised and pinned flat onto the silicone base of an organ bath. Isolated left atria were continuously superfused with oxygenated Krebs-Henseleit buffer (37°C). The contraction uncoupler blebbistatin (60µM) was introduced into the superfusate to reduce motion artefacts.

Left atria were paced from the posterior wall using a 2ms bipolar pulse via platinum electrodes at twice the diastolic threshold using an isolated constant voltage stimulator (Digitimer, Welwyn Garden City, UK). Di-4-ANEPPS was excited at 530nm by two twin LEDs (Cairn Research, Kent, UK). Emitted fluorescence (630nm) was recorded using a second generation, high spatial resolution (128 x 2048 pixels, single pixel area: 6.5µm x 6.5µm) ORCA flash 4.0 camera (Hamamatsu Photonics, Japan), sampling at 1KHz. Wide field macroscopic images of tissues paced at 120ms, 100ms and 80ms cycle lengths (100 pulses/cycle length) were acquired using WinFluor V3.4.9 software (Dr John Dempster, University of Strathclyde, UK).

Human induced pluripotent stem cell-derived cardiomyocyte differentiation and culture

hiPSC-CMs were derived and cultured, as previously published (3, 43)(**Fig 5.1A**). Briefly, hiPSCs (line PB004.4 female; Murdoch Children's Research Institute) were cultured in a 75cm^2 tissue culture flask with hiPSC media [DMEM-F-12 (11320033; Gibco), 20% (vol/vol) knockout serum replacement (10828028; Gibco), 1X nonessential amino acids (11140050; Gibco), 1X GlutaMAX (35050061; Gibco), penicillin/streptomycin (15140122; Gibco), 110µM 2-mercaptoethanol (21985023; Gibco), and 5ng/ml recombinant human fibroblast growth factor (233-FB-025; R&D)] on irradiated mouse embryonic fibroblasts and passaged using TrypLE Express enzyme (12604013; ThermoFisher). Before differentiation (1 day), 1.6X10^5 cells/cm^2 were seeded. To induce differentiation (Day 0), cells were treated with basal media [RPMI (21870076; Sigma), B27 minus vitamin A (12587010; Gibco), and 50 µg/ml ascorbic acid (A8960; Sigma) supplemented with 10µM CHIR-99021 (4423; Tocris Bioscience) and 80ng/ml activin A (Peprotech)]. On days 1, 3, and 5, media were changed to basal media supplemented with 5µM IWR-1 (I0161; Sigma). Cells were maintained in basal medium from day 6 until used. For experiments, cells were dissociated with TrypLE, centrifuged (200 g, 4°C, 3min), carefully resuspended in basal medium, and replated at 800,000cells/ml as clusters across Geltrex-coated microelectrode arrays (Geltrex, 1:100, A1413202; Life Technologies). Microelectrode arrays (MEAs; **Fig 5.1B**) consisted of six individual wells. At the base of each was a recording matrix of 3x3 titanium nitride electrodes interspaced by 200µm and 30µm in diameter (60-6wellMEA300/30iR-T-rcr; Multichannel Systems, Reutlingen, Germany).

hiPSC-CM-epicardial adipose tissue fragment co-culture

Excised sheep epicardial adipose tissue was washed 5-6 times in 37°C sterile phosphate-buffered saline (+1% penicillin/streptomycin). After extensive washing, epicardial adipose tissue was transferred to a fresh dish containing 3-4ml of basal culture medium. Epicardial adipose tissue fragments were then generated by cutting the tissue into 0.5mm pieces (2, 34). Approximately 10 x 0.5mm epicardial adipose tissue fragments were transferred to MEA wells containing hiPSC-CMs adhered to the base (48hr after re-plating; Day 32; **Fig 5.1A**). hiPSC-CMs and epicardial adipose tissue fragments were co-cultured together for 24hr (37°C, 5% CO_2/95% air) in a humidified incubator (**Fig 5.1C**).

At the 4hr and 24hr timepoints, synchronous multifocal spontaneous field potentials were recorded from hiPSC-CMs maintained at 37°C (MEA2100 2x60 system and Cardio2D software, Multichannel Systems). Recordings were made after a 10min equilibration period with a 10KHz sampling rate.

Electrophysiological analysis

Optical mapping data were analysed using ElectroMap software (25, 26). Ensemble averaging of the last 20 beats of each cycle length was used to assess: time to action potential peak, conduction velocity and action potential duration (APD) at 30%, 50% and 70% repolarisation (APD_{30}, APD_{50} and APD_{70}) across the whole left atrium. Images at these specific beats were spatially and temporally filtered with a 4x4 Gaussian filter and a 3rd order Savitzky-Golay filter, respectively. Non-physiological baseline deviations were corrected for using a Top-Hat filter (100ms).

APD_{70} spatial heterogeneity was defined as the standard deviation of the mean APD_{70} measure across the whole left atrium. Beat-to-beat variability of APD_{70} was assessed at 120ms cycle length and was calculated as the individual APD_{70} differences between 20 consecutive beats. These 19 values were then averaged together to give a mean APD_{70} variability for a single atrium.

hiPSC-CM spontaneous field potential recordings were analysed using Cardio2D+ (Multichannel Systems)(43). Due to the clustered nature of these cells (**Fig 5.1B**), it was not possible to calculate conduction velocity and activation time for all cultures. To ensure analysis was as consistent between cultures in this situation, these parameters were only calculated from cultures when a detectable signal (>50μV) was present on ≥6/9 electrodes (**Fig 5.1D**). Delay in activation between neighbouring electrodes was computed using a multi-vector approach on a beat-beat basis. Mean local conduction velocity and activation time were then calculated by averaging across 10 consecutive beats. "Nearest neighbour" interpolation was used when detectable signal was absent on some electrodes.

Spontaneous beating rate was calculated using the inter-spike interval across 10 consecutive beats. For field potential duration and amplitude, 10 consecutive beats (amplitude ≥50μV) were ensemble averaged to give a single "clean" signal. Field potential amplitude was calculated as the voltage between the field potential minimum and maximum. Field potential duration was calculated as the time between the field potential minimum and the final positive deflection (**Fig 5.1E**). A rate-corrected version of field potential duration was calculated using Bazett's formula (7). Both field potential

amplitude and duration were calculated from as many of the 9 electrodes in a single array as possible (typically 5-6), then these values averaged together.

Statistical analysis

All data are presented as mean ± standard error. Statistical analyses were performed in GraphPad Prism 8.4 and are indicated in the Figure legends throughout. $P<0.05$ was deemed significant.

5.3 Results

Western diet feeding induced obesity and prolonged left atrial repolarisation

20 weeks of Western diet feeding induced obesity, with a significant 27% increase in body weight over control-fed mice (34.4±2.3g *vs* 49.1±1.9g; **Fig 5.2A & B**). Obese animals had longer left atrial action potential durations (**Fig 5.2C & D**). This was not significant at early repolarisation (APD_{30}, **Fig 5.2E**; 120ms cycle length, control *vs* obese: 9.5±0.4ms *vs* 10.5±0.4ms, P=0.078); however, APD_{50} was significantly prolonged in obese mice at longer cycle lengths (**Fig 5.2F**; 12.9±0.8ms *vs* 16.0±0.8ms, P<0.05) and APD_{70} significantly longer across all cycle lengths (**Fig 5.2G**; 17.0±1.0ms *vs* 23.5±1.0ms, P<0.05). Mice on both diets demonstrated typical APD rate dependency, with longer repolarisation times at longer cycle lengths (**Fig 5.2E-G**).

There was a trend for greater APD_{70} spatial heterogeneity across intact left atria in obese mice (**Fig 5.2H**; 2.1±0.4ms *vs* 3.3±0.5ms, P=0.106). Temporal APD_{70} heterogeneity was assessed on a beat-beat basis over the final 20 consecutive beats in a 100 pulse, 120ms cycle length stimulus train. Beat-beat change in APD_{70} was not significantly different between control and obese mice **(Fig 5.2I & J)**.

Left atrial conduction velocity and time to action potential peak were also assessed in control and obese mice but did not significantly differ between groups (**Fig 5.3A-C**).

Epicardial adipose tissue prolongs repolarisation in hiPSC-CMs, through a paracrine mechanism

To address whether the prolonged left atrial repolarisation detected in obese mice was an effect mediated through epicardial adipose tissue-derived factors exerting a paracrine effect on cardiomyocytes, hiPSC-CMs were co-cultured with epicardial adipose tissue and spontaneous electrical activity recorded.

hiPSC-CMs co-cultured with epicardial adipose tissue fragments (+Adip) for 4hr showed no significant difference in beating rate compared with those hiPSC-CMs cultured alone (**Fig 5.4A & C**; Ctrl *vs* +Adip: 117.2±7.0BPM *vs* 128.8±10.5BPM, $P>0.05$). Interestingly, hiPSC-CMs co-cultured with epicardial adipose tissue demonstrated prolonged field potential duration (**Fig 5.4B & D**; 123±0.6ms *vs* 161±7.1ms, $P<0.05$), which was maintained when accounting for variability in beating rate (**Fig 5.4E**; 173.6±7.7ms *vs* 224.9±6.8ms, $P<0.05$). Repolarisation-rate dependency relationship was unaffected by epicardial adipose tissue co-culture at 4hr (**Fig 5.4F**; $R^2_{ctrl}=0.234$ *vs* $R^2_{+Adip}=0.629$, $P>0.05$ for difference in slopes).

Epicardial adipose tissue co-culture did not affect hiPSC-CM conduction velocity (**Fig 5.5A & B**) or activation time (**Fig 5.5A & C**). Field potential amplitude was unaffected by co-culture (**Fig 5.5D**; 0.38± 0.07mV *vs* 0.26 ± 0.04mV, $P=0.13$).

Epicardial adipose tissue-induced prolonged repolarisation in hiPSC-CMs is sustained beyond 4hr and modifies repolarisation rate dependency

To determine whether epicardial adipose tissue-derived factors exerted a genomic effect in addition to the more immediate acute signalling effects seen at 4hr, co-cultures were extended out to 24hr (see **Fig 5.1A**).

After 24hr of hiPSC-CM co-culture with/without epicardial adipose tissue, there was a significant reduction in spontaneous beating rate (**Fig 5.6A & C**; 109±4.0BPM *vs* 94.4±5.4BPM; $P<0.05$), and prolongation of field potential duration (**Fig 5.6B & D**; 138.6±3.8ms *vs* 193.0±10.6ms; $P<0.05$), maintained when correcting for the reduction in beating rate (**Fig 5.6E**; 185.3±4.8ms *vs* 233.5±8.2ms). These differences meant that the relationship between beating rate and field potential duration was significantly steeper in epicardial adipose tissue co-cultured hiPSC-CMs *vs* control at 24hr (**Fig 5.6D**; $R^2_{Ctrl}=0.144$ *vs* $R^2_{+Adip}=0.543$, $P<0.05$ between slopes). Conduction velocity and activation time remained unaffected (**Fig 5.7A-C**); however, field potential amplitude was significantly reduced (**Fig 5.7D**; 0.43±0.07mV *vs* 0.2±0.02mV; $P<0.05$).

When assessing the change in electrophysiological parameters between 4hr and 24hr, we saw a significant reduction in spontaneous beating rate in epicardial adipose tissue co-culture conditions (**Fig 5.8A**). There was no further field potential duration prolongation between 4hr and 24hr (**Fig 5.8B & C**). Change in conduction velocity and activation time between 4hr and 24hr were not significantly different between culture conditions (**Fig 5.8E & F**). There was a trend for a greater reduction in field potential

amplitude between 4hr and 24hr in epicardial adipose tissue co-cultured hiPSC-CMs (*P*=0.11; **Fig 5.8G**).

5.4 Discussion

Summary of key findings

This is the first study to show that obesity and epicardial adiposity associate with prolonged repolarisation across the intact left atrium and human cardiomyocyte cultures. Obesity is known to associate with augmented epicardial adipose tissue – itself a risk factor for AF. These data provide novel insight into the early electrophysiological remodelling that may underpin AF. Obesity may promote increased epicardial adiposity, which releases paracrine factors to prolong atrial repolarisation, increasing the risk of ectopic triggered activity.

Prolonged repolarisation in the obese adult mouse left atrium

AF is a progressive disease, beginning with paroxysmal symptoms which typically develop into persistent then permanent AF. The underlying mechanisms of paroxysmal and persistent/permanent AF are thought to be distinct, presenting as triggered activity and reentry, respectively (15). The shift from paroxysmal to permanent AF is associated with significant morbidity and mortality (30, 35), making this pre-transition period a key intervention timepoint. Our data indicate that obesity associates with prolonged left atrial repolarisation – particularly during the latter stages of repolarisation (**Fig 5.2C-G**). Prolonged repolarisation increases the likelihood of early afterdepolarisations (a type of triggered arrhythmia), through allowing L-type Ca^{2+} channels to reopen. This reopening facilitates transient Ca^{2+} influxes, seen as early afterdepolarisations during the action potential plateau phase (42). This might indicate that paroxysmal AF seen in obesity, is

a result of prolonged left atrial repolarisation, increasing the risk of triggered arrhythmia.

Clinical observations have associated prolonged ventricular repolarisation (Q-T interval) with obesity (10, 27, 28). It is not possible to measure atrial repolarisation clinically since this is masked under the QRS complex. Experimental studies using obese animal models attribute these ventricular repolarisation changes to decreased Kv1.5 (17) and Kir2.1 channel expression (6), ultimately leading to reduced K^+ currents. Similar K^+ currents are involved in mouse atrial repolarisation and so it could be hypothesised that similar changes underpin the atrial remodelling presented here (9, 39).

Takahashi *et al*., (2016) demonstrate that atrial action potential duration is unaffected in mice fed a high fat diet (36). The discrepancy between our findings and theirs might be explained by methodological differences. Although both studies used optical mapping, Takahashi and colleagues examined the right atrium in mice fed a different diet (60% fat for 8 weeks *vs* our 42% fat and 15% sucrose water, 20 weeks) and examined APD at 90% repolarisation, not at the 30%, 50% and 70% used here. Takahashi *et al.,* (2016) also do not report on weight difference between groups – which, as described earlier, is a potentially important factor in atrial electrical remodelling.

Epicardial adipose tissue exerts a paracrine effect to prolong hiPSC-CM repolarisation

Changes in atrial electrophysiology in obese mice might be due to increased pericardial adipose tissue deposition exerting an augmented paracrine effect directly on the cardiomyocytes. Although we did not measure pericardial adipose tissue content in this

study, we have previously reported that high fat diet feeding (42%), induces a significant increase in pericardial adiposity (8)(present thesis, Chapter 3). To test this hypothesis, we co-cultured epicardial adipose tissue with hiPSC-CMs and were able to demonstrate a prolongation in field potential duration – an extracellular measure of cardiomyocyte repolarisation (**Fig 5.4B, D & E** and **Fig 5.6B, D & E**). When co-culture was extended to 24hr, a steeper beating rate:repolarisation time relationship was seen (**Fig 5.6F**). This, although only a surrogate measure of APD restitution, indicates an increased likelihood of alternans-based arrhythmia (33).

Over the last decade there has been emerging interest in the processes linking epicardial adipose tissue accumulation and AF risk, however, there is a distinct lack of functional mechanistic insight. Lin *et al*., (2012) is one of the few studies to provide mechanistic data, obtaining patch clamp recordings from rabbit atrial cardiomyocytes co-incubated with isolated epicardial adipocytes for 2-4hr (20). Similar to our data, they demonstrate prolonged left atrial cardiomyocyte repolarisation (APD_{90}), elevated resting membrane potential and increased triggered activity upon isoproterenol treatment in cardiomyocytes cultured with adipocytes. Their data implicated increased late sodium current and L-type Ca^{2+} currents coupled with decreased delayed rectifier K^{+} currents as the mechanism for prolonged repolarisation (20). Similar cellular changes might be modulated in hiPSC-CMs studies here at the 4hr timepoint, however there may be further genomic-induced changes to sustain the prolonged repolarisation seen at 24hr.

Potential mechanisms linking pericardial adiposity and prolonged repolarisation

It is not known exactly which paracrine factors epicardial adipose tissue might be releasing to modulate cardiomyocyte repolarisation. Experimentation using HL-1 cells co-cultured with human epicardial adipose tissue fragments demonstrated intracellular lipid accumulation and upregulation of two fatty acid transporter proteins (FATP4 and CD36) in HL-1 cardiomyocytes (2). Others have shown that in high fat-fed mice prolonged ventricular repolarisation associates with intracellular lipid accumulation and reduced voltage-gated K^+ channel expression (17). It may be that in the mouse left atrium and hiPSC-CMs used for our experiments are in a similar state of lipid overload, driving changes in K^+ currents and prolonged repolarisation.

We have recently reported a local androgen-oestrogen system in the heart, indicating that rodent and human pericardial adipose tissue has capacity to locally synthesise oestrogens and modulate sex steroid balance (8). It has been shown that local pericardial adipose tissue aromatase expression correlates with vulnerability to atrial arrhythmias and so it could be possible that pericardial adipose tissue-derived sex steroids may locally modulate atrial electrophysiology. Clinically, there are consistent sex differences in cardiac electrophysiology and arrhythmia epidemiology – not least the longer female ventricular repolarisation time (Q-T interval) and greater AF incidence in males (21, 32). At the level of the cardiomyocyte, sex differences and responsiveness to sex steroids are less clear – with atrial data distinctly lacking and ventricular experimental findings complicated by differences in species, age, steroid concentration and treatment duration (21). There is good consensus, however, that females have

longer ventricular APDs at long cycle lengths and oestradiol can prolong APD through direct actions on K_v11.1 delayed rectifier channels (12, 19, 38). It is possible that pericardial adipose tissue-derived oestrogens may be at least partly responsible for the prolonged repolarisation seen in our experimental preparations, hence may play an important role in AF onset pathogenesis. Further investigations are required to confirm an atrial electrophysiological response to sex steroids, however.

Maintained conduction velocity in the obese murine left atrium and human cardiomyocytes co-cultured with epicardial adipose tissue

An important feature in the transition from paroxysmal to persistent AF is a shortening of APD and slowing in conduction velocity, transitioning from a triggered to reentrant arrhythmia-based substrate (4). Neither the obese mouse left atrium or hiPSC-CMs co-cultured with epicardial adipose tissue demonstrated these reentrant arrhythmia features. This may indicate these preparations as models of paroxysmal AF; however, it is possible this is a consequence of insufficient wavelength to allow rotors to form in the small mouse atrium or microelectrode array wells. Conduction slowing in the in the right atrium of high fat-fed mice has been reported, but as described earlier, there were several methodological differences between our studies, notably, they calculated conduction velocity using a single vector approach, contrasting with our multi-vector approach which accounts for the multidirectional fibre orientation in the atrium (36). Similar single vector approaches have also shown conduction slowing in ventricular tissue strip preparations of high fat-fed rats (5).

The preserved conduction velocity in our preparations is interesting and may indicate the mechanisms driving changes in APD and conduction are distinct. It could be that fibro-fatty infiltration into the myocardium is required to disrupt cell-cell action potential propagation or drive changes in connexin expression/localisation. Meng *et al*., (2017) investigated structural remodelling in high fat-fed rats, noting that a subpopulation became overweight and associated with increased atrial weight and fibrosis, coupled with reduced connexin 40 and 43 expression (22). This may indicate that a degree of structural remodelling is required to slow conduction velocity to trigger the transition to reentry and persistent AF, whilst changes in APD are mediated by paracrine actions from the overlying epicardial adipose tissue.

In line with preserved conduction velocity, both the mouse left atrium and hiPSC-CM preparations demonstrated preserved time to action potential peak and field potential amplitude at 4hr. These observations should be interpreted with a degree of caution, because of the nature of optically recorded action potentials (17) and the clustered nature of hiPSC-CMs/partial dependence of amplitude on adherence strength. A better insight into these parameters might be yielded using traditional intracellular microelectrode recordings.

Study limitations

Although we have previously shown that high fat feeding mice leads to an increase in pericardial adiposity (8), we did not record adipose tissue weights in this present study. We also note that in our co-culture experiments, there could be a degree of artificiality from release of free fatty acids – a result of the dissection process – and lack of a control group from another adipose depot.

Future steps

Our data indicate that in the setting of obesity, there is atrial repolarisation prolongation – potentially a result of elevated paracrine influence from the surrounding epicardial adipose tissue. Future experimentation should focus to identify which factors (e.g. sex steroids, proteins, lipids) might be implicated, to yield potential novel therapeutic targets to treat paroxysmal AF/slow disease progression.

5.5 Conclusions

In conclusion, we have shown for the first time that obesity associates with significant prolongation of left atrial repolarisation, increasing the likelihood of triggered arrhythmias. This effect is mimicked in human cardiomyocytes cultured with epicardial adipose tissue – indicating a paracrine role for epicardial adipose tissue in the electrical remodelling seen in paroxysmal AF.

Competing interests

PK receives research support from several drug and device companies active in atrial fibrillation and has received honoraria from several such companies. PK is also listed as an inventor on two patents held by University of Birmingham (Atrial Fibrillation Therapy WO 2015140571, Markers for Atrial Fibrillation WO 2016012783). All other authors declare no potential conflict of interest.

Funding

This research was supported by the National Health and Medical Research Council (nos. 1099352 and 1125453; L.M.D. Delbridge, J.R. Bell), the Australian Research Council (no. DP160102404; L.M.D. Delbridge), Wellcome Trust Seed Award Grant (109604/Z/15/Z, to DP) and British Heart Foundation Grants (PG/17/55/33087, RG/17/15/33106, to DP).

Acknowledgements

Provision of sheep tissue from Professor Clive May's research group at the Howard Florey Institute and assistance with mouse cohort management from Clara Apicella is gratefully acknowledged.

5.6 References

1. **Abukar Y, Ramchandra R, Hood SG, McKinley MJ, Booth LC, Yao ST, and May CN.** Increased cardiac sympathetic nerve activity in ovine heart failure is reduced by lesion of the area postrema, but not lamina terminalis. *Basic Research in Cardiology* 113: 35, 2018.

2. **Anan M, Uchihashi K, Aoki S, Matsunobu A, Ootani A, Node K, and Toda S.** A Promising Culture Model for Analyzing the Interaction between Adipose Tissue and Cardiomyocytes. *Endocrinology* 152: 1599-1605, 2011.

3. **Anderson DJ, Kaplan DI, Bell KM, Koutsis K, Haynes JM, Mills RJ, Phelan DG, Qian EL, Leitoguinho AR, Arasaratnam D, Labonne T, Ng ES, Davis RP, Casini S, Passier R, Hudson JE, Porrello ER, Costa MW, Rafii A, Curl CL, Delbridge LM, Harvey RP, Oshlack A, Cheung MM, Mummery CL, Petrou S, Elefanty AG, Stanley EG, and Elliott DA.** NKX2-5 regulates human cardiomyogenesis via a HEY2 dependent transcriptional network. *Nat Commun* 9: 1373, 2018.

4. **Andrade J, Khairy P, Dobrev D, and Nattel S.** The clinical profile and pathophysiology of atrial fibrillation: relationships among clinical features, epidemiology, and mechanisms. *Circ Res* 114: 1453-1468, 2014.

5. **Axelsen LN, Calloe K, Braunstein TH, Riemann M, Hofgaard JP, Liang B, Jensen CF, Olsen KB, Bartels ED, Baandrup U, Jespersen T, Nielsen LB, Holstein-Rathlou N-H, and Nielsen MS.** Diet-induced pre-diabetes slows cardiac conductance and promotes arrhythmogenesis. *Cardiovasc Diabetol* 14: 87, 2015.

6. **Bai Y, Su Z, Sun H, Zhao W, Chen X, Hang P, Zhu W, and Du Z.** Aloe-Emodin Relieves High-Fat Diet Induced QT Prolongation via MiR-1 Inhibition and IK1 Up-Regulation in Rats. *Cell Physiol Biochem* 43: 1961-1973, 2017.

7. **Bazett HC.** An analysis of the time-relations of electrocardiograms. *Heart* 7: 353-370, 1920.

8. **Bernasochi GB, Boon WC, Curl CL, Varma U, Pepe S, Tare M, Parry LJ, Dimitriadis E, Harrap SB, Nalliah CJ, Kalman JM, Delbridge LMD, and Bell JR.** Pericardial adipose and aromatase: A new translational target for aging, obesity and arrhythmogenesis? *J Mol Cell Cardiol* 111: 96-101, 2017.

9. **Bou-Abboud E, Li H, and Nerbonne JM.** Molecular diversity of the repolarizing voltage-gated K+ currents in mouse atrial cells. *J Physiol* 529 Pt 2: 345-358, 2000.

10. **Carella MJ, Mantz SL, Rovner DR, Willis PW, 3rd, Gossain VV, Bouknight RR, and Ferenchick GS.** Obesity, adiposity, and lengthening of the QT interval: improvement after weight loss. *Int J Obes Relat Metab Disord* 20: 938-942, 1996.

11. **Chen LY, Sotoodehnia N, Buzkova P, Lopez FL, Yee LM, Heckbert SR, Prineas R, Soliman EZ, Adabag S, Konety S, Folsom AR, Siscovick D, and Alonso A.** Atrial fibrillation and the risk of sudden cardiac death: the atherosclerosis risk in communities study and cardiovascular health study. *JAMA Intern Med* 173: 29-35, 2013.

12. **Cheng J, Ma X, Zhang J, and Su D.** Diverse modulating effects of estradiol and progesterone on the monophasic action potential duration in Langendorff-perfused female rabbit hearts. *Fundam Clin Pharmacol* 26: 219-226, 2012.

13. **Chugh SS, Havmoeller R, Narayanan K, Singh D, Rienstra M, Benjamin EJ, Gillum RF, Kim YH, McAnulty JH, Jr., Zheng ZJ, Forouzanfar MH, Naghavi M, Mensah GA, Ezzati M, and Murray CJ.** Worldwide epidemiology of atrial fibrillation: a Global Burden of Disease 2010 Study. *Circulation* 129: 837-847, 2014.

14. **Heijman J, Guichard J-B, Dobrev D, and Nattel S.** Translational Challenges in Atrial Fibrillation. *Circ Res* 122: 752-773, 2018.

15. **Heijman J, Voigt N, Nattel S, and Dobrev D.** Cellular and molecular electrophysiology of atrial fibrillation initiation, maintenance, and progression. *Circ Res* 114: 1483-1499, 2014.

16. **Holmes AP, Yu TY, Tull S, Syeda F, Kuhlmann SM, O'Brien S-M, Patel P, Brain KL, Pavlovic D, Brown NA, Fabritz L, and Kirchhof P.** A Regional Reduction in Ito and IKACh in the Murine Posterior Left Atrial Myocardium Is Associated with Action Potential Prolongation and Increased Ectopic Activity. *PLoS One* 11: e0154077, 2016.

17. **Huang H, Amin V, Gurin M, Wan E, Thorp E, Homma S, and Morrow JP.** Diet-induced obesity causes long QT and reduces transcription of voltage-gated potassium channels. *Journal of molecular and cellular cardiology* 59: 151-158, 2013.

18. **Kirchhof P, Benussi S, Kotecha D, Ahlsson A, Atar D, Casadei B, Castella M, Diener H-C, Heidbuchel H, Hendriks J, Hindricks G, Manolis AS, Oldgren J, Popescu BA, Schotten U, Van Putte B, Vardas P, and Group ESD.** 2016 ESC Guidelines for the management of atrial fibrillation developed in collaboration with EACTS. *Eur Heart J* 37: 2893-2962, 2016.

19. **Kurokawa J, Tamagawa M, Harada N, Honda S-I, Bai C-X, Nakaya H, and Furukawa T.** Acute effects of oestrogen on the guinea pig and human IKr channels and drug-induced prolongation of cardiac repolarization. *J Physiol* 586: 2961-2973, 2008.

20. **Lin YK, Chen YC, Chen JH, Chen SA, and Chen YJ.** Adipocytes modulate the electrophysiology of atrial myocytes: implications in obesity-induced atrial fibrillation. *Basic Res Cardiol* 107: 293, 2012.

21. **Linde C, Bongiorni MG, Birgersdotter-Green U, Curtis AB, Deisenhofer I, Furokawa T, Gillis AM, Haugaa KH, Lip GYH, Van Gelder I, Malik M, Poole J, Potpara T, Savelieva I, Sarkozy A, and Group ESD.** Sex differences in cardiac arrhythmia: a consensus document of the European Heart Rhythm Association, endorsed by the Heart Rhythm Society and Asia Pacific Heart Rhythm Society. *EP Europace* 20: 1565-1565ao, 2018.

22. **Meng T, Cheng G, Wei Y, Ma S, Jiang Y, Wu J, Zhou X, and Sun C.** Exposure to a chronic high-fat diet promotes atrial structure and gap junction remodeling in rats. *Int J Mol Med* 40: 217-225, 2017.

23. **Miyasaka Y, Barnes ME, Gersh BJ, Cha SS, Bailey KR, Abhayaratna WP, Seward JB, and Tsang TSM.** Secular Trends in Incidence of Atrial Fibrillation in Olmsted County,

Minnesota, 1980 to 2000, and Implications on the Projections for Future Prevalence. *Circulation* 114: 119-125, 2006.

24. **Nattel S, Xiong F, and Aguilar M.** Demystifying rotors and their place in clinical translation of atrial fibrillation mechanisms. *Nat Rev Cardiol* 14: 509-520, 2017.

25. **O'Shea C, Holmes AP, Yu TY, Winter J, Wells SP, Parker BA, Fobian D, Johnson DM, Correia J, Kirchhof P, Fabritz L, Rajpoot K, and Pavlovic D.** High-Throughput Analysis of Optical Mapping Data Using ElectroMap. *J Vis Exp*, 2019.

26. **O'Shea C, Holmes AP, Yu TY, Winter J, Wells SP, Correia J, Boukens BJ, De Groot JR, Chu GS, Li X, Ng GA, Kirchhof P, Fabritz L, Rajpoot K, and Pavlovic D.** ElectroMap: High-throughput open-source software for analysis and mapping of cardiac electrophysiology. *Scientific Reports* 9: 1389, 2019.

27. **Omran J, Bostick BP, Chan AK, and Alpert MA.** Obesity and Ventricular Repolarization: a Comprehensive Review. *Prog Cardiovasc Dis* 61: 124-135, 2018.

28. **Papaioannou A, Michaloudis D, Fraidakis O, Petrou A, Chaniotaki F, Kanoupakis E, Stamatiou G, Melissas J, and Askitopoulou H.** Effects of weight loss on QT interval in morbidly obese patients. *Obes Surg* 13: 869-873, 2003.

29. **Patel NJ, Deshmukh A, Pant S, Singh V, Patel N, Arora S, Shah N, Chothani A, Savani GT, Mehta K, Parikh V, Rathod A, Badheka AO, Lafferty J, Kowalski M, Mehta JL, Mitrani RD, Viles-Gonzalez JF, and Paydak H.** Contemporary Trends of Hospitalization for Atrial Fibrillation in the United States, 2000 Through 2010. *Circulation* 129: 2371-2379, 2014.

30. **Proietti R, Hadjis A, AlTurki A, Thanassoulis G, Roux J-F, Verma A, Healey JS, Bernier ML, Birnie D, Nattel S, and Essebag V.** A Systematic Review on the Progression of Paroxysmal to Persistent Atrial Fibrillation: Shedding New Light on the Effects of Catheter Ablation. *JACC: Clinical Electrophysiology* 1: 105-115, 2015.

31. **Sanders P, Berenfeld O, Hocini M, Jaïs P, Vaidyanathan R, Hsu L-F, Garrigue S, Takahashi Y, Rotter M, Sacher F, Scavée C, Ploutz-Snyder R, Jalife J, and Haïssaguerre M.** Spectral Analysis Identifies Sites of High-Frequency Activity Maintaining Atrial Fibrillation in Humans. *Circulation* 112: 789-797, 2005.

32. **Schnabel RB, Yin X, Gona P, Larson MG, Beiser AS, McManus DD, Newton-Cheh C, Lubitz SA, Magnani JW, Ellinor PT, Seshadri S, Wolf PA, Vasan RS, Benjamin EJ, and Levy D.** 50 year trends in atrial fibrillation prevalence, incidence, risk factors, and mortality in the Framingham Heart Study: a cohort study. *Lancet* 386: 154-162, 2015.

33. **Shattock MJ, Park KC, Yang H-Y, Lee AWC, Niederer S, MacLeod KT, and Winter J.** Restitution slope is principally determined by steady-state action potential duration. *Cardiovasc Res* 113: 817-828, 2017.

34. **Sonoda E, Aoki S, Uchihashi K, Soejima H, Kanaji S, Izuhara K, Satoh S, Fujitani N, Sugihara H, and Toda S.** A new organotypic culture of adipose tissue fragments maintains viable mature adipocytes for a long term, together with development of immature adipocytes and mesenchymal stem cell-like cells. *Endocrinology* 149: 4794-4798, 2008.

35. **Steinberg BA, Hellkamp AS, Lokhnygina Y, Patel MR, Breithardt G, Hankey GJ, Becker RC, Singer DE, Halperin JL, Hacke W, Nessel CC, Berkowitz SD, Mahaffey KW, Fox KAA, Califf RM, Piccini JP, Committee obotR-AS, and Investigators.** Higher risk of death and stroke in patients with persistent vs. paroxysmal atrial fibrillation: results from the ROCKET-AF Trial. *Eur Heart J* 36: 288-296, 2014.

36. **Takahashi K, Sasano T, Sugiyama K, Kurokawa J, Tamura N, Soejima Y, Sawabe M, Isobe M, and Furukawa T.** High-fat diet increases vulnerability to atrial arrhythmia by conduction disturbance via miR-27b. *J Mol Cell Cardiol* 90: 38-46, 2016.

37. **Thanassoulis G, Massaro JM, O'Donnell CJ, Hoffmann U, Levy D, Ellinor PT, Wang TJ, Schnabel RB, Vasan RS, Fox CS, and Benjamin EJ.** Pericardial fat is associated with prevalent atrial fibrillation: the Framingham Heart Study. *Circ Arrhythm Electrophysiol* 3: 345-350, 2010.

38. **Tisdale JE, Overholser BR, Wroblewski HA, and Sowinski KM.** The influence of progesterone alone and in combination with estradiol on ventricular action potential duration and triangulation in response to potassium channel inhibition. *J Cardiovasc Electrophysiol* 22: 325-331, 2011.

39. **Trépanier-Boulay V, Lupien M-A, St-Michel C, and Fiset C.** Postnatal development of atrial repolarization in the mouse. *Cardiovasc Res* 64: 84-93, 2004.

40. **Venteclef N, Guglielmi V, Balse E, Gaborit B, Cotillard A, Atassi F, Amour J, Leprince P, Dutour A, Clément K, and Hatem SN.** Human epicardial adipose tissue induces fibrosis of the atrial myocardium through the secretion of adipo-fibrokines. *Eur Heart J* 36: 795-805, 2015.

41. **Wang TJ, Parise H, Levy D, D'Agostino RB, Sr., Wolf PA, Vasan RS, and Benjamin EJ.** Obesity and the risk of new-onset atrial fibrillation. *JAMA* 292: 2471-2477, 2004.

42. **Weiss JN, Garfinkel A, Karagueuzian HS, Chen P-S, and Qu Z.** Early afterdepolarizations and cardiac arrhythmias. *Heart Rhythm* 7: 1891-1899, 2010.

43. **Wells SP, Waddell HM, Sim CB, Lim SY, Bernasochi GB, Pavlovic D, Kirchhof P, Porrello ER, Delbridge LMD, and Bell JR.** Cardiomyocyte functional screening: interrogating comparative electrophysiology of high-throughput model cell systems. *Am J Physiol Cell Physiol* 317: C1256-c1267, 2019.

44. **Wong CX, Abed HS, Molaee P, Nelson AJ, Brooks AG, Sharma G, Leong DP, Lau DH, Middeldorp ME, Roberts-Thomson KC, Wittert GA, Abhayaratna WP, Worthley SG, and Sanders P.** Pericardial fat is associated with atrial fibrillation severity and ablation outcome. *J Am Coll Cardiol* 57: 1745-1751, 2011.

45. **Wong CX, Brooks AG, Leong DP, Roberts-Thomson KC, and Sanders P.** The Increasing Burden of Atrial Fibrillation Compared With Heart Failure and Myocardial Infarction: A 15-Year Study of All Hospitalizations in Australia. *Arch Intern Med* 172: 739-741, 2012.

46. **Wong CX, Sullivan T, Sun MT, Mahajan R, Pathak RK, Middeldorp M, Twomey D, Ganesan AN, Rangnekar G, Roberts-Thomson KC, Lau DH, and Sanders P.** Obesity and the Risk of Incident, Post-Operative, and Post-Ablation Atrial Fibrillation: A Meta-

Analysis of 626,603 Individuals in 51 Studies. *JACC: Clinical Electrophysiology* 1: 139-152, 2015.

5.7 Figures

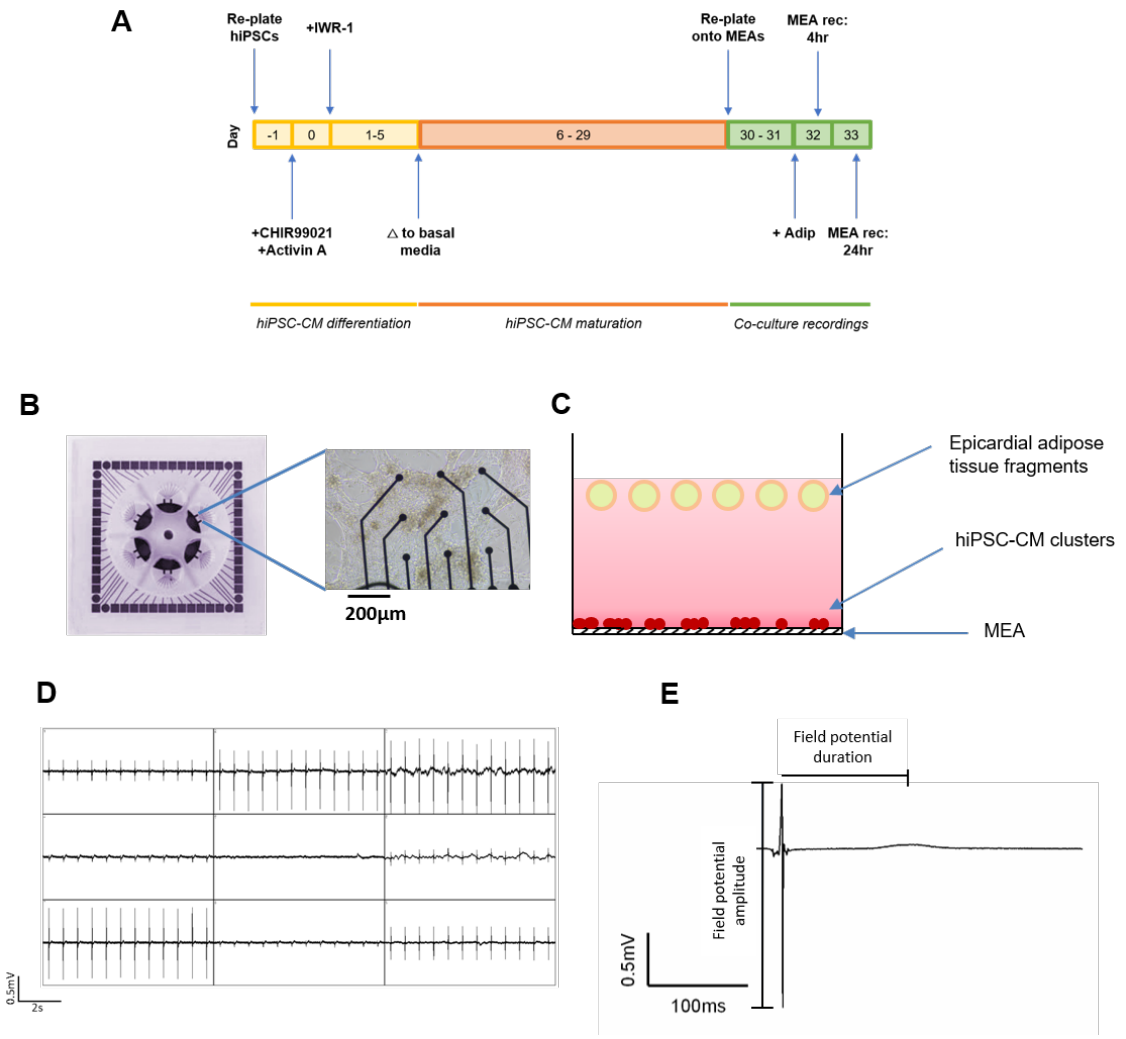

Figure 5.1 Visual overview of the co-culture-microelectrode array preparation. **(A)** hiPSC-CM differentiation, culture and recording timelines (+Adip, epicardial adipose tissue co-culture). **(B)** Exemplar images of a 6-well MEA (3x3 matrix, 200µm electrode spacing, 30µm electrode diameter) and hiPSC-CM clusters. **(C)** Schematic of epicardial adipose tissue fragment and hiPSC-CM co-culture on MEAs, with **(D)** multichannel recordings of spontaneous field potentials and **(E)** exemplar field potential trace.

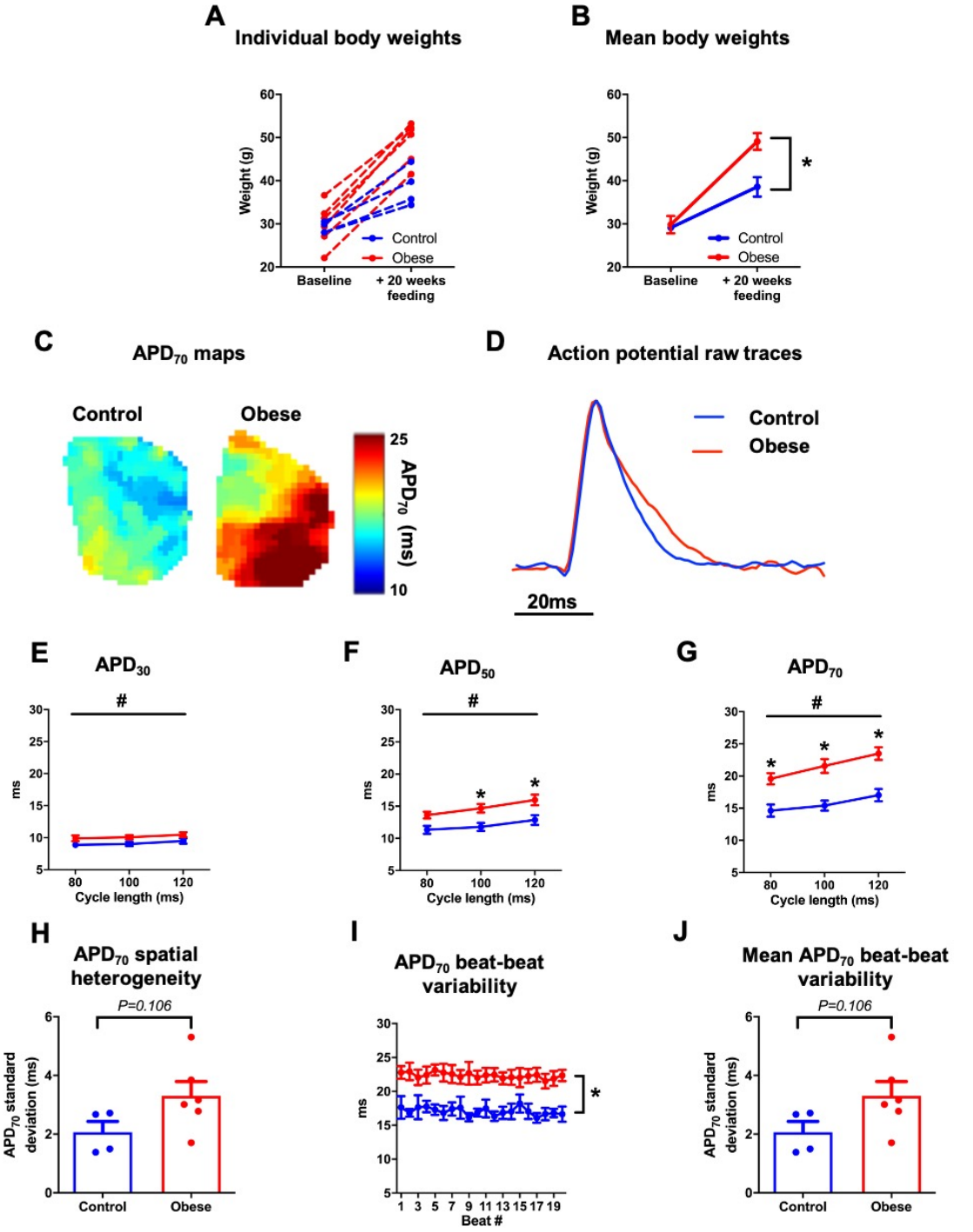

Figure 5.2 Effects of obesity on mouse left atrial action potential duration. Individual **(A)** and mean **(B)** animal body weights from control and obese mice fed for 20 weeks. **(C)** exemplar APD_{70} maps with raw action potential traces **(D).** Mean APD_{30}, APD_{50} and APD_{70} **(E-G)** across 80, 100 and 120ms paced cycle lengths. At 120ms cycle length: **(H)** APD_{70} spatial heterogeneity, **(I)** APD_{70} across 20 consecutive beats and **(J)** mean analysis of beat-beat variability of APD_{70}. Two-way repeated measures ANOVA with Sidak's post-hoc tests or unpaired *t*-tests; *n*=4-6 per group; $^{\#}$ and * indicate $P<0.05$ for cycle length and diet effect, respectively.

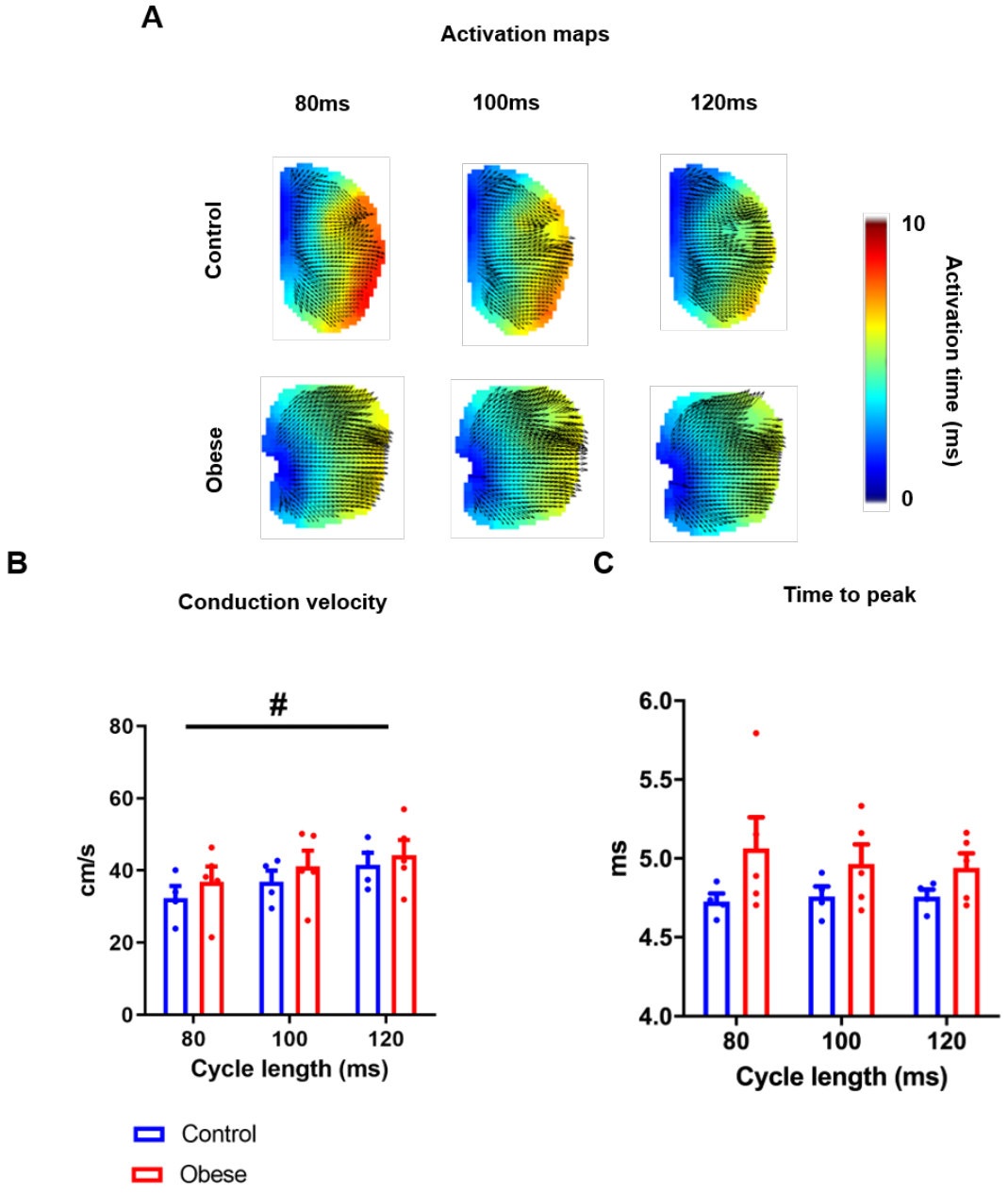

Figure 5.3 Effects of obesity on mouse left atrial conduction. **(A)** exemplar activation maps at 80, 100 and 120ms cycle lengths from control and obese mice. **(B)** mean conduction velocity and **(C)** time to action potential peak. Two-way repeated measures ANOVAs; *n*=4-6 per group; $^{\#}$ *P*<0.05 for cycle length effect.

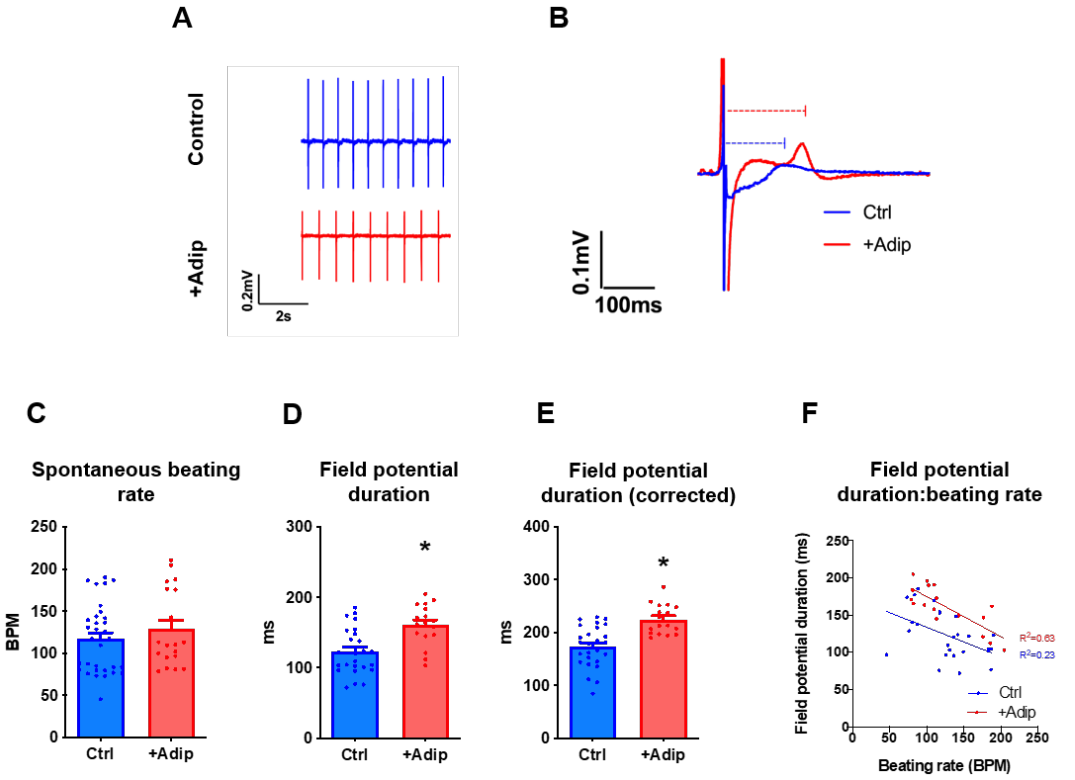

Figure 5.4 Effects 4hr epicardial adipose tissue co-culture on hiPSC-CM repolarisation. Exemplar hiPSC-CM spontaneous beating rate **(A)** and field potential duration measurements **(B)** - dashed lined indicate field potential duration. **(C)** mean spontaneous beating rate, **(D)** field potential duration, **(E)** rate-corrected field potential duration and **(F)** beating rate: field potential duration relationship. Unpaired t-tests or linear regression, $N_{cultures}$=7, n_{MEAs}=17-33, *P<0.05.

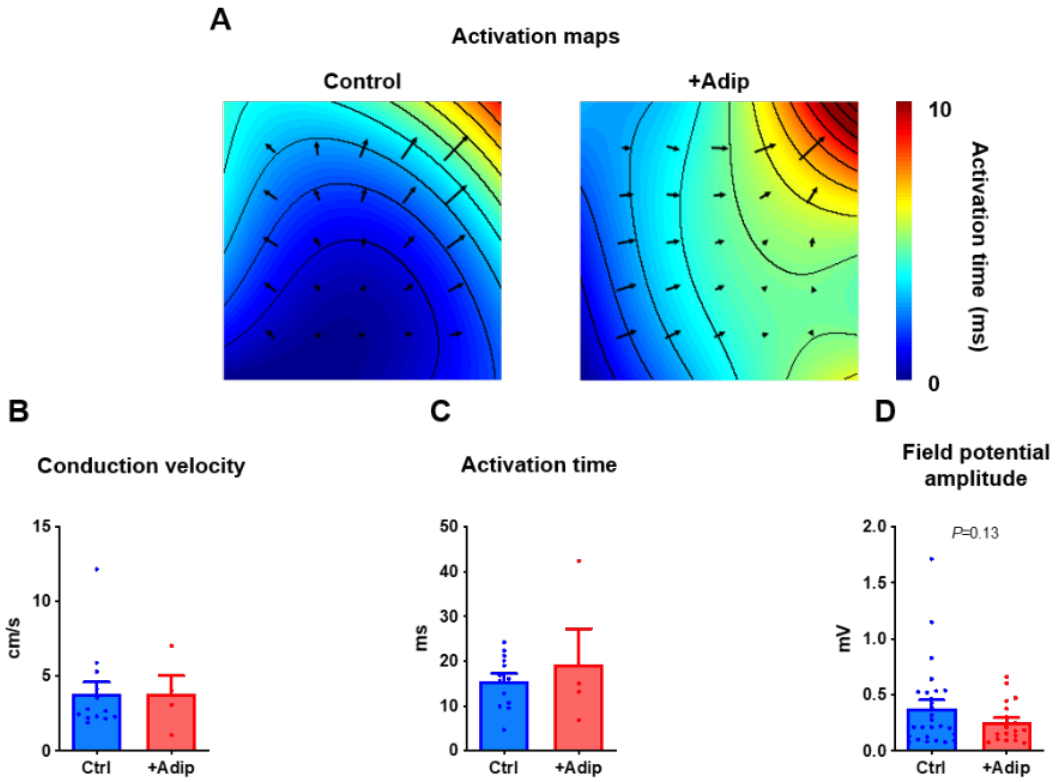

Figure 5.5 Effects 4hr epicardial adipose tissue co-culture on hiPSC-CM conduction. **(A)** Exemplar hiPSC-CM activation maps (isochrones, 1ms delay). **(B)** Mean conduction velocity, **(C)** activation time and **(D)** field potential amplitude. Unpaired t-tests, $N_{cultures}$=7, n_{MEAs}=4-33.

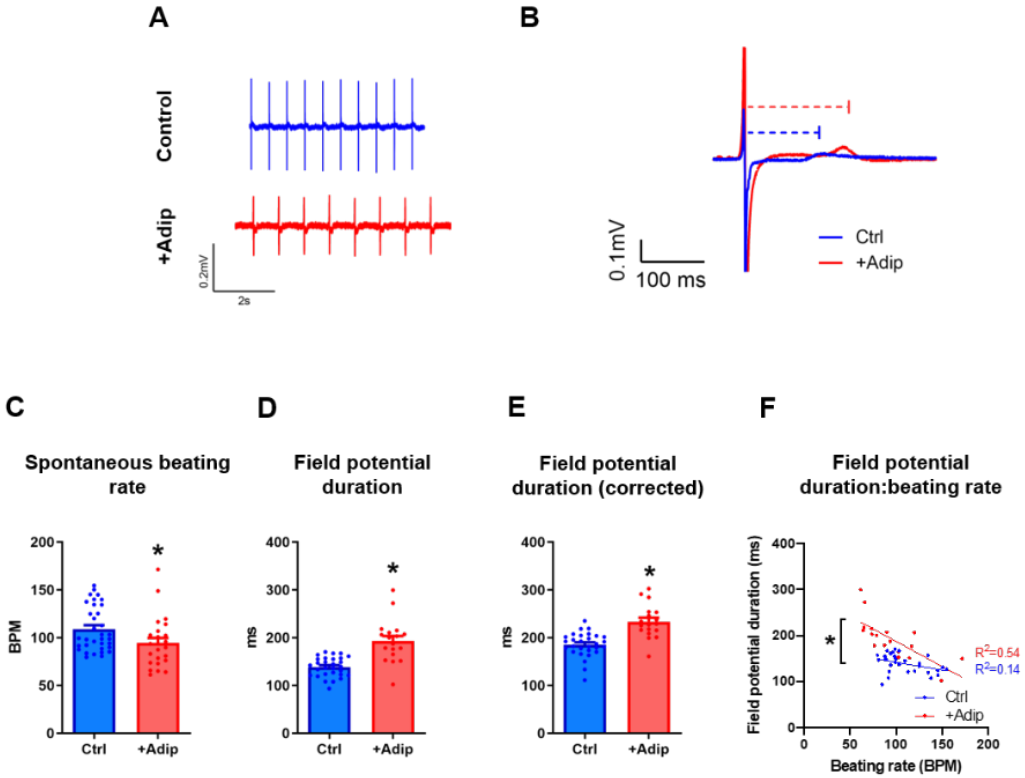

Figure 5.6 Effects 24hr epicardial adipose tissue co-culture on hiPSC-CM repolarisation. Exemplar hiPSC-CM spontaneous beating rate **(A)** and field potential duration measurements **(B)** - dashed lined indicate field potential duration. **(C)** mean spontaneous beating rate, **(D)** field potential duration, **(E)** rate-corrected field potential duration and **(F)** beating rate: field potential duration relationship. Unpaired t-tests or linear regression, $N_{cultures}$=7, n_{MEAs}=18-34, *P<0.05.

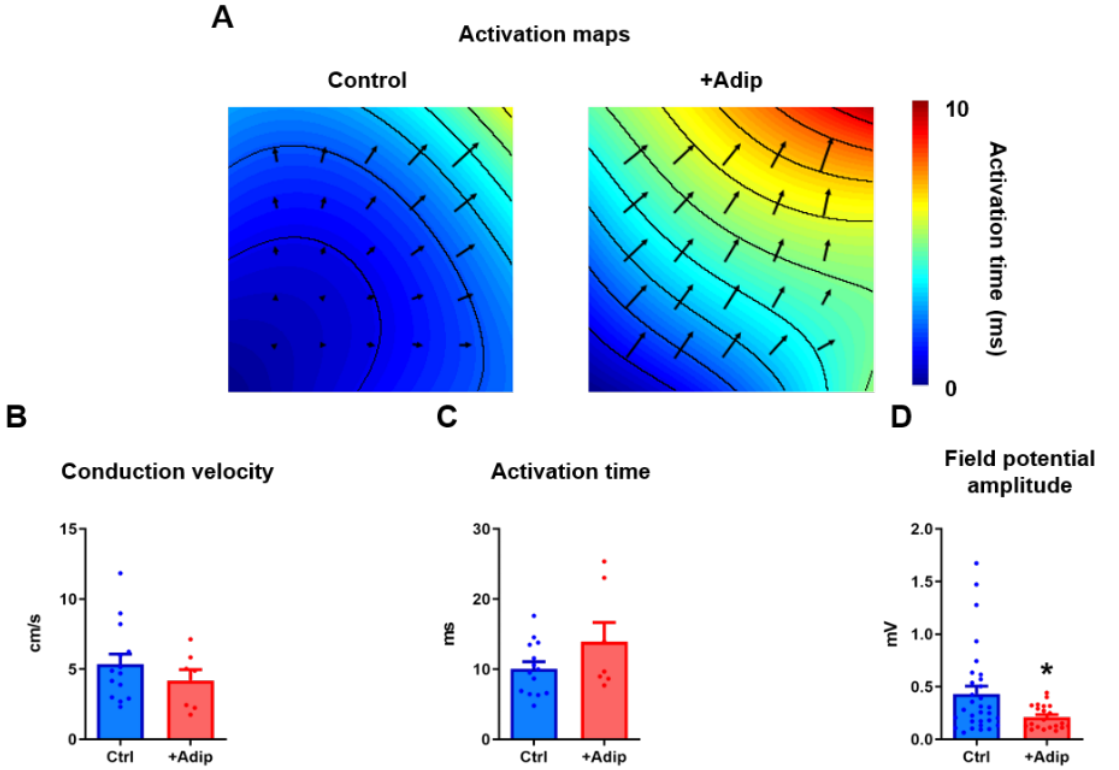

Figure 5.7 Effects 24hr epicardial adipose tissue co-culture on hiPSC-CM conduction. **(A)** Exemplar hiPSC-CM activation maps (isochrones, 1ms delay). **(B)** Mean conduction velocity, **(C)** activation time and **(D)** field potential amplitude. Unpaired t-tests, $N_{cultures}$=7, n_{MEAs}=7-31.

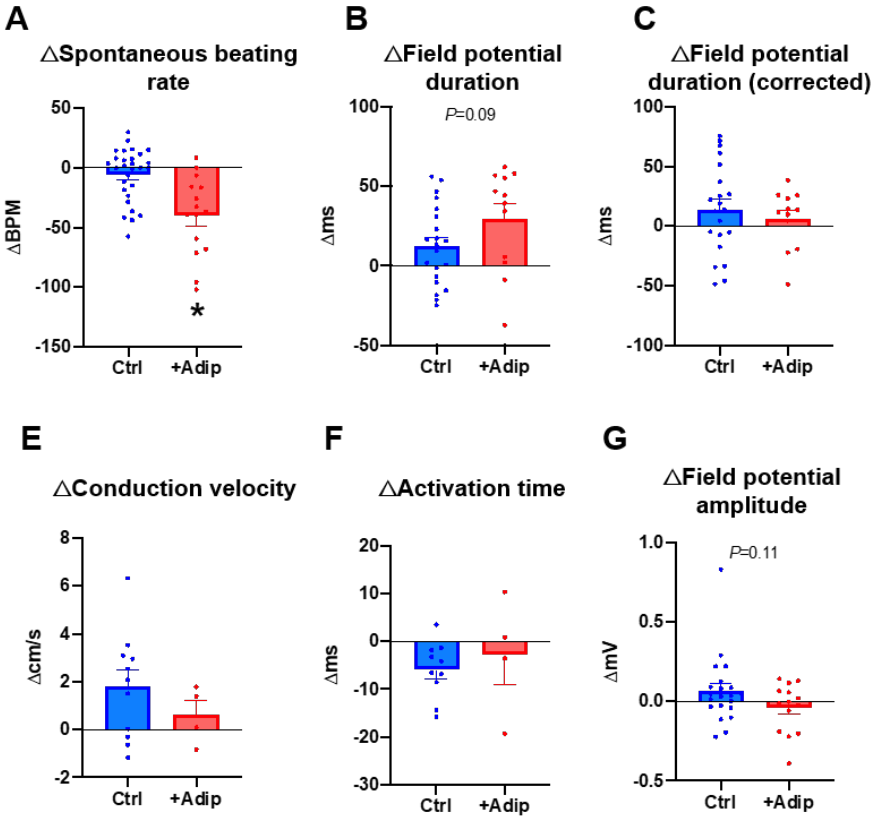

Figure 5.8 Change in hiPSC-CM electrophysiology between 4hr and 24hr co-culture with adipose tissue fragments. Mean change in: **(A)** spontaneous beating rate, **(B)** field potential duration and **(C)** rate-corrected field potential duration. **(D)** spontaneous beating rate:field potential duration relationship at 24hr. Mean change in **(E)** conduction velocity, **(F)** activation time and **(G)** field potential amplitude. Unpaired t-tests or linear regression, $N_{cultures}$=7, n_{MEAs}=4-33, *P<0.05.

5.8 Appendix

Published manuscript (contains data from Figures 5.6B-E)

Nalliah CJ[*], Bell JR[*], Raaijmakers AJA, Waddell HW, **Wells SP**, Bernasochi GB, Montgomery MK, Binny S, Watts TM, Joshi S, Lui E, Sim CB, Larobina M, O'Keefe M, Goldblatt J, Royse A, Lee G, Porrello ER, Watt MJ, Kistler PM, Sanders P, Delbridge LMD[#], Kalman JM[#]. Epicardial Adipose Tissue Accumulation Confers Atrial Conduction Abnormality *J Am Coll Cardiol*, 2020; 76: (10), 1197-1211

EPICARDIAL ADIPOSE TISSUE ACCUMULATION CONFERS CARDIAC CONDUCTION ABNORMALITY: A MULTIDIMENSIONAL STUDY IDENTIFYING NOVEL MECHANISTIC SUBSTRATES

Brief title: Epicardial adipose tissue accumulation confers cardiac conduction abnormality

Chrishan J. Nalliah, MBBS, PhD,[a,b,*] James R. Bell, PhD,[c,d,*] Antonia J.A. Raaijmakers, PhD,[d] Helen M. Waddell, BSc,[d] Simon P. Wells, MRes,[d,e] Gabriel B. Bernasochi, PhD,[d] Magdalene K. Montgomery, PhD,[d] Simon Binny, MBBS,[a] Troy Watts, BSc,[a] Subodh B. Joshi, MBBS,[a] Elaine Lui, MMed, MBBS,[f] Choon Boon Sim, PhD,[g] Marco Larobina, MBBS,[h] Michael O'Keefe, MBBS,[h] John Goldblatt, MBBS,[h] Alistair Royse, MBBS,[h] Geoffrey Lee, MBChB, PhD,[a,b] Enzo R. Porrello, PhD,[d,g] Matthew J. Watt, PhD,[d] Peter M. Kistler, MBBS, PhD,[i] Prashanthan Sanders, MBBS, PhD,[j] Lea M.D. Delbridge, PhD,[d,#] Jonathan M. Kalman, MBBS, PhD, [a,b,#]

*Drs. Nalliah and Bell and [#]Profs. Delbridge and Kalman contributed equally to this work.

Word Count: 4860 words

[a]Department of Cardiology, Royal Melbourne Hospital, Melbourne, Victoria, Australia
[b]Department of Medicine and Radiology, University of Melbourne, Melbourne, Victoria, Australia
[c]Department of Physiology, Anatomy and Microbiology, La Trobe University, Bundoora, Victoria, Australia
[d]Department of Physiology, University of Melbourne, Melbourne, Victoria, Australia
[e]Institute of Cardiovascular Sciences, College of Medical and Dental Sciences, University of Birmingham, United Kingdom
[f]Department of Radiology, Royal Melbourne Hospital, Melbourne, Victoria, Australia
[g]Murdoch Children's Research Institute, Royal Children's Hospital, Melbourne, Victoria, Australia
[h]Department of Cardiothoracic Surgery, Royal Melbourne Hospital, Melbourne, Victoria, Australia
[i]Department of Cardiology, The Alfred Hospital, Melbourne, Australia.
[j]Australia Centre for Heart Rhythm Disorders (CHRD), South Australian Health and Medical Research Institute (SAHMRI), University of Adelaide and Royal Adelaide Hospital, Adelaide, Australia

Funding: Research support provided through National Health and Medical Research Council project (#1099352 & #1125453 LMDD, JRB, JMK) and fellowship (#1093830 CJN; #1143224 MKM) grants.

Disclosures: Dr. Kalman has received research support from Biosense Webster, St. Jude Medical, and Medtronic. Dr. Sanders has served on the advisory board of Biosense Webster, Medtronic, St. Jude Medical, and Boston Scientific; has received lecture and/or consulting fees from Biosense Webster, Medtronic, St. Jude Medical, and Boston Scientific; and has received research funding from Medtronic, St. Jude Medical, Boston Scientific, Biotronik, and Sorin. All other authors have reported that they have no relationships relevant to the contents of this paper to disclose.

Address for correspondence:

Professor Jonathan M. Kalman
Department of Medicine
University of Melbourne
VIC Australia 3050
Ph: +61 3 9349 5400
Email: Jon.Kalman@mh.org.au

Professor Lea MD Delbridge
Department of Physiology
University of Melbourne
VIC Australia 3010
Ph: +61 3 8344 5853
Email: lmd@unimelb.edu.au

Tweet: Local epicardial adiposity increases atrial conduction abnormalities through release of paracrine factors that modulate cardiomyocyte electrophysiology

Acknowledgements: The authors acknowledge the Melbourne Histology Platform and Australian Phenomics Network for assistance with histological procedures, and to the Bio21 Mass Spectometry and Proteomics Facility for assistance with proteomics procedures.

ABSTRACT

BACKGROUND Clinical studies have reported epicardial adipose tissue (EAT) accumulation associates with progression of atrial fibrillation (AF) pathology and adversely impacts AF management. The role of local cardiac EAT deposition in disease progression is unclear and the electrophysiologic, cellular and molecular mechanisms involved remain poorly defined.

OBJECTIVES To identify the underlying mechanisms by which EAT influences the atrial substrate for AF.

METHODS Patients without AF undergoing coronary artery bypass surgery were recruited. Computed tomography and high density epicardial electrophysiologic mapping of the anterior right atrium (RA) were utilized to quantify EAT volumes and to assess association with the electrophysiologic substrate in situ. Excised RA appendages were analyzed histologically to characterize EAT infiltration, fibrosis and gap junction localization. Co-culture experiments were used to evaluate paracrine effects of EAT on cardiomyocyte electrophysiology. Proteomic analyses were applied to identify molecular mediators of cellular electrophysiologic disturbance.

RESULTS Higher local EAT volume clinically correlated with slowed conduction, greater electrogram fractionation, increased fibrosis and lateralization of cardiomyocyte connexin-40. In addition, atrial conduction heterogeneity was increased with more extensive myocardial EAT infiltration. Cardiomyocyte culture studies using multi-electrode arrays showed that cardiac adipose tissue secreted factors slowed conduction velocity, and contained proteins with capacity to disrupt intermyocyte electromechanical integrity.

CONCLUSIONS These findings indicate that atrial pathophysiology is critically dependent on local EAT accumulation and infiltration. In addition to myocardial architecture disruption, this effect can be attributed to an EAT-cardiomyocyte paracrine axis. The focal adhesion group proteins are identified as new disease candidates potentially contributing to arrhythmogenic atrial substrate.

KEY WORDS: epicardial adipose tissue, atrial fibrillation, electrophysiology, cardiomyocyte, proteomics

ABBREVIATIONS AND ACRONYMS:
AERP = atrial effective refractory period
AF = atrial fibrillation
BMI = body mass index
CT = computed tomography
Cx = connexin
EAT = epicardial adipose tissue
hiPSC-CMs = human induced pluripotent stem cell-derived cardiomyocytes
LVEF = left ventricular ejection fraction
RA = right atrium

INTRODUCTION

Epidemiologic, clinical and mechanistic data have linked the dual global epidemics of obesity and atrial fibrillation (AF) (1-3). Obesity associates with greater atrial conduction abnormalities and an increasingly remodeled atrial substrate that predisposes to AF (4,5). Among AF cohorts, clinical data have observed improved AF symptom scores, decreased AF burden, higher rates of AF ablation success and even regression of the atrial substrate in response to weight loss and risk factor management (6,7).

Epidemiological studies have observed an independent association between epicardial adipose tissue (EAT) and incident AF (8). Clinical data also suggest that EAT associates with progression of AF and adversely impacts AF management (9). The extent to which this pathology is dependent on local versus global cardiac adiposity is unclear, and the underlying cellular mechanisms are poorly defined. Multiple mechanistic possibilities have been invoked, and most recently EAT has emerged as a potentially important factor involved in atrial remodeling (5,10). While we have previously shown in an obese sheep model that infiltration of contiguous atrial myocardium with EAT may contribute to conduction abnormalities (5), the extent to which this occurs clinically has not been demonstrated.

Tissue culture studies indicate that EAT has capacity to release adipo-fibrokines, exacerbating the fibrotic atrial substrate that contributes to conduction abnormalities (11). However, little is known about the impact of cardiac adiposity on cardiomyocyte electrophysiology and connectivity in promoting AF vulnerability. In this study, we clinically evaluated the association of EAT localization with myocardial electrophysiologic, morphologic and molecular characteristics. Using a multidimensional approach, the relationship between atrial conduction abnormalities and the extent of local adipose tissue

deposition/infiltration was investigated. Cell culture multi-electrode array and proteomic studies were used to assess EAT paracrine influences on cardiomyocyte electrophysiology and to identify candidate proteins involved in local promotion of the AF substrate.

METHODS

Full methodological details are provided in the Online Appendix.

PATIENT RECRUITMENT. Nineteen consecutive patients having outpatient coronary artery bypass grafts for stable coronary artery disease were recruited at The Royal Melbourne Hospital. Written informed consent was acquired from all participants prior to study enrolment. This study was approved by the Melbourne Health Human Research Ethics Committee and complies with the Declaration of Helsinki.

EXCLUSION CRITERIA. History of AF was documented by clinical evaluation and medical record review. Pre-procedural transthoracic echocardiography according to standard American Society of Echocardiography guidelines (12) was performed on all participants. To determine the impact of EAT on the atrial substrate, patients with documented AF, congenital heart disease, left ventricular ejection fraction (LVEF) $\leq$ 55 %, significant valvular disease (greater than trivial regurgitation or any stenosis), prior cardiac catheter ablation or pulmonary hypertension (pulmonary artery systolic pressure $\geq$ 35 mmHg) were excluded from the study.

CARDIAC CT EAT QUANTIFICATION. Non-contrast computed tomography (CT) of the chest was performed (Figure 1A-C) using a dual source 128-slice scanner (SOMATOM Definition Flash, Siemens, Erlangen, Germany) a day before surgery. Images were acquired from the carina to below the cardiac apex to include all EAT. Non-overlapping slices were reconstructed every 2 mm in soft tissue (B26) kernels in an image matrix of 512 x 512. Data was exported onto OsiriX DICOM Viewer (version 6.0.2) and analyzed offline. Total cardiac EAT was quantified and segmented to determine bi-atrial EAT and anterior RA EAT volumes.

INTRAOPERATIVE ATRIAL EPICARDIUM SURFACE MAPPING. High density mapping of the anterior right atrium was performed utilizing a previously described triangular epicardium mapping plaque (6.75 cm^2) with 128 silver-plated copper electrodes creating 117 closed-spaced bi-poles (inter-electrode distance 2.5 mm) (13). The mapped area encompassed the right atrial appendage. Activation maps were acquired at paced rhythms of 600 ms and 300 ms. Pacing was performed from an electrode pair with stable capture located at one of the plaque vertices. Two isochronal maps were constructed (paced 600 ms, 300 ms), with 3 ms intervals in local activation time to assess conduction and activation patterns. Assessment of regional conduction slowing was performed by triangulating the plaque electrodes as previously described (14). The phase mapping method was used to determine conduction heterogeneity (15) and the proportion of complex electrograms determined for each map.

HISTOLOGIC ASSESSMENT. Prior to cardiopulmonary bypass, the right atrial appendage was surgically excised and fixed in 10% formalin for histologic analysis. Tissues were sectioned (10 μm) and stained with either oil-red-O (adiposity, hematoxylin counterstain) or picosirius red (fibrosis), or prepared for immunohistochemistry (gap junction visualization). Myocardial infiltration of EAT was quantified using a modified version of a previously described approach (5).

ANIMAL DETAILS. All experiments were approved by the Animal Ethics Committee of the University of Melbourne and performed in accordance with the guidelines of the National Health and Medical Research Council of Australia. Adult Merino ewe anesthesia was induced and maintained with 1.5%-2.0% isoflurane for the duration of the surgery (16). Male C57Bl/6 mice (Animal Resources Centre, WA, Australia) were fed a high-fat diet (SF04-001;

Specialty Feeds, WA, Australia) for 12 weeks and anesthetized with an intra-peritoneal injection of sodium pentobarbitone (70 mg/kg) and sodium heparin (200 IU/kg).

CELL CULTURE CARDIOMYOCYTE ELECTROPHYSIOLOGY. Human induced pluripotent stem cell-derived cardiomyocytes (hiPSC-CMs) were cultured and differentiated as previously described (17). Sheep EAT fragments were co-cultured with hiPSC-CMs on geltrex coated multi-electrode arrays (24 hrs). Murine adipose tissue fragments were incubated in a DMEM-based culture medium to harvest the secreted proteome – ie the 'secretome'. Cultured HL-1 atrial cardiomyocytes seeded on gelatin/fibronectin-coated multi-electrode arrays were incubated with the 'conditioned media' from mouse pericardial or inguinal subcutaneous adipose tissue fragments (24 hrs). Extracellular electrophysiological field potentials were recorded (Multichannel Systems, Germany) (18).

MOUSE ADIPOSE TISSUE CONDITIONED MEDIA PROTEOMICS. To compare abundance of proteins in conditioned media of different adipose types, murine adipose tissue fragments were incubated in a serum-free culture medium (6 hrs) and subjected to proteomic analysis by liquid chromatography-mass spectrometry/mass spectrometry (ie LC-MS/MS). Peptides were analyzed on an QExactive Hybrid Quadrupole-Orbitrap Mass Spectrometer coupled to a Vanquish UHPLC (Thermo Fisher Scientific; Scoresby, Australia). Protein identification and label free quantification were performed in MaxQuant (Max Planck Institute). The MS spectra were matched against UniProt mouse reference protein database using the MaxQuant search engine Andromeda. 'No number assigned' values were imputed to complete a normal distribution prior to t-tests and visualization in Perseus software (Max Planck Institute). Further characterization of the most abundant proteins released from pericardial adipose

tissue (relative to inguinal subcutaneous) was undertaken, performing Gene Ontology (GO) analysis (Enrichr) to identify cellular components implicated.

STATISTICAL ANALYSIS. For clinical data analaysis, normally distributed variables are presented as mean ± standard deviation unless otherwise stated, and non-normally distributed variables are presented as median (inter-quartile range). Normality was assessed using the Shapiro-Wilk test. Independent Student's t-test, one-way analysis of variance and Mann-Whitney U tests were used to compare variables between groups as appropriate. Proportions were compared using the chi-squared test. The relationship between continuous variables were evaluated using Spearman's correlation. A P-value < 0.05 was considered statistically significant. Tests were performed with SPSS (Version 23, NY, USA), GraphPad Prism (Version 8.0), Perseus (Version 1.6.0.7) or Enrichr where appropriate.

RESULTS

EAT VOLUME. Patient characteristics and the distribution of EAT are presented in Table 1. Mean patient BMI was 30 ± 7 kg/m^2 and median total cardiac EAT volume was 127.2 ml (range 104.0 – 168.3 ml). BMI correlated with both total cardiac EAT volume and bi-atrial EAT (Figure 1D; r = 0.71, p = 0.002) but not with anterior right atrial EAT (Figure 1E; r = 0.15, p = 0.54). Furthermore, anterior right atrial EAT volume did not correlate with total cardiac EAT or bi-atrial EAT volume (Figure 1F; r = 0.21, p = 0.43). These findings indicate that clinical measurement of obesity (ie BMI) provides an accurate indicator of global cardiac adiposity, but may not be representative of localized EAT depot volumes.

ELECTROPHYSIOLOGIC MAPPING. Incremental pacing at the anterior right atrium associated with prolonged plaque activation times (600 ms vs 300 ms pacing intervals: 61 ± 16 ms vs. 79 ± 33 ms, p < 0.001) and slowed mean conduction velocities (0.39 ± 0.14 m/s vs. 0.34 ± 0.13 m/s, p < 0.05). Right atrial electrophysiological characteristics at both pacing intervals also changed depending on regional cardiac adiposity (Table 2). Greater anterior right atrial EAT volume increased complexity of activation patterns and isochronal crowding (Figure 2A-B). Anterior right atrial EAT volume significantly correlated with prolonged right atrial plaque activation time, slowed conduction velocity, and increased complex points (Table 2 and Figure 2C). In contrast, these changes in right atrial electrophysiology did not correlate with bi-atrial EAT volume (Table 2 and Figure 2D), indicating a specific influence of local adiposity on right atrial conduction.

FIBROSIS. Fibrosis was assessed in right atrial appendage sections (Figure 3A), with mean fibrotic content of 16.9 ± 2.5% per sectional area. The extent of fibrosis strongly correlated

with anterior RA EAT volume (Figure 3B; $r = 0.78$, $p < 0.001$), with those patients with high anterior right atrial EAT volumes exhibiting the most extensive fibrosis.

CONNEXIN LOCALIZATION. The cardiomyocyte surface localization of the gap junction proteins (connexins) influences the properties of cell-to-cell electrical conduction and wavefront propogation. Sarcolemmal connexin-40 (Cx40) localization was assessed in excised right atrial appendage sections (Figure 3C). In patients with the lowest volumes of anterior right atrial EAT, Cx40 co-localized with the cell adhesion protein, cadherin, with primarily longitudinal cardiomyocyte loci. In contrast, patients with the highest volumes of anterior right atrial EAT exhibited significant lateral positioning of Cx40 proteins in the absence of cadherin co-localization (Figure 3C-D).

CARDIAC ADIPOSE TISSUE INFILTRATION. Right atrial appendage sections stained with oil-red-O showed the presence of cardiac adipose tissue on the epicardium, with an apparent fibrous cap on the external surface of the adipose tissue depot evident (Figure 4A). Higher magnification analysis revealed a heterogenous interface between the cardiac adipose tissue and the epicardium, with evidence of infiltration of the adipose tissue into the myocardium (Figure 4B). Adipose tissue infiltration patterns were irregular, ranging from extensive adipose tissue infiltration to regions of no infiltration. In patients with EAT infiltration (hybrid myocyte-adipocyte zone), the conduction heterogeneity increased (Figure 4C). This occured independent of the extent of fibrosis, as fibrosis content was similar in sections displaying either infiltrated or non-infiltrated adipose type (Figure 4D). The greater conduction heterogeneity in those tissues with adipose infiltration could therefore reflect the influence of a physical cellular barrier and/or a paracrine influence of the adipose.

CARDIAC ADIPOSE TISSUE PARACRINE INFLUENCE. In vitro studies were performed to evaluate the paracrine influence of cardiac adipose on conduction heterogeneity in the absence of the potential barrier effect of non-cardiomyocyte matrix components (fibrosis, fibrocytes and adipocytes). Sheep adipose tissue fragments or mouse adipose protein secretomes (harvested from adipose incubate) were applied to cardiomyocyte cultures (hiPSC-CMs and HL-1 cells respectively) prepared on multi-electrode array chips.

Co-culturing hiPSC-CMs with ovine EAT induced significant changes in cardiomyocyte electrophysiology (Figure 5A-B). hiPSC-CM spontaneous beating rate was slower (Figure 5C), and extracellular field potential duration significantly prolonged (Figure 5D) in the presence of EAT. A similar prolongation was evident in cardiomyocytes when field potential duration was matched for beating rate (Figure 5E). To assess influence of secretome on cardiomyocyte conduction, confluent mouse HL-1 atrial cardiomyocyte monolayers were incubated with conditioned media from mouse pericardial or inguinal subcutaneous adipose tissue (Figure 5F). Activation time was longer and conduction velocity slower in HL-1 monolayers incubated with pericardial, but not inguinal, adipose tissue conditioned media (Figure 5G-I). These findings demonstrate that adiposity-related electrophysiological changes are not only due to physical conduction block from infiltrating adipose (or fibrosis) but that a paracrine mediator effect is also implicated.

CARDIAC ADIPOSE TISSUE SECRETOME PROTEOMICS. Given that pericardial adipose tissue (and not inguinal subcutaneous) secretome selectively modulated cardiomyocyte function, proteomic analysis of the murine pericardial adipose tissue (vs inguinal subcutaneous) secretome was undertaken. Proteins secreted from pericardial and inguinal subcutaneous adipose tissues were visualised as a volcano plot (Figure 6A), showing pericardial adipose

secretome had 246 proteins of higher abundance (red) and 22 proteins of lower abundance (blue) compared with inguinal subcutaneous adipose secretome. These data were clustered on a heatmap to reveal hierarchical commonality in secretome protein abundance for samples within each adipose tissue type, yet differences in protein abundance when comparing secretome from pericardial and inguinal subcutaneous adipose tissues (Figure 6B). Proteins with the largest differential in abundance were listed in rank order (Figure 6C). The group of highest abundance in pericardial (vs inguinal subcutaneous) adipose tissue were proteins primarily involved in the regulation of cell metabolism. In contrast, the 10 least abundant proteins in pericardial adipose tissue conditioned media were more varied, including proteins involved with cytoskeleton scaffolding and proteins linked with anti-inflammatory activity.

Gene Ontology '*cellular component*' category ranking of the high abundance proteins released from pericardial adipose tissue (vs inguinal) was conducted (Figure 6D-G). Of particular novel importance, proteins linked with focal adhesion functionality (GO:0005925) were most represented – proteins known to regulate intermyocyte connectivity and gap junction structure (Figure 6D-E and Supplementary Table S1). In relation to GO analysis of '*biological processes*', proteins associated with cellular responses to interleukin-12 (IL-12; GO:0071349) were highly represented, indicating a novel role for this inflammatory pathway in the heart (Figure 6F-G and Supplementary Table S2).

DISCUSSION

MAJOR FINDINGS. This is the first clinical study to demonstrate the impact of EAT on the atrial substrate for AF, integrating findings generated in linked electrophysiologic, histologic and molecular domains. We show that local (rather than global) EAT content associates with conduction slowing and increased complexity of activation patterns, accompanied by increased cardiac fibrosis and sarcolemmal lateralization of Cx40 gap junction proteins. Furthermore, adipose tissue infiltration associates with conduction heterogeneity. Data generated from standardized cell culture settings demonstrate that EAT slows conduction and prolongs cardiomyocyte field potential duration. These changes associate with the release of a complement of proteins with capacity to disrupt intermyocyte adhesion, modulate cellular metabolism and increase inflammation. Together, these findings indicate that local epicardial adiposity influences adjacent myocardium and promotes functional heterogeneity which contributes to conduction abnormalities underlying the AF substrate.

LOCAL ADIPOSITY DISRUPTS REGIONAL ATRIAL CONDUCTION. Our findings provide novel demonstration that local adiposity may be critical in determining localized regions of atrial electrophysiologic dysfunction. Both BMI and weight gain correlate with EAT volume and AF risk (5,19,20). Existing data also associate areas of electrical remodeling with regions of high EAT (5,21). AF mapping studies co-localized regions of dominant frequency (22) and complex fractionated atrial electrograms (23) to areas of high EAT content, implicating local EAT depots in the mechanism for AF. In this study, conduction and EAT volume were both evaluated at the anterior right atrium. Within this region, conduction properties correlated only with anterior right atrial EAT but not bi-atrial EAT volumes. The implication of these findings is that BMI and more global evaluations of cardiac adiposity may not systematically

predict the vulnerability of localized myocardium to conduction changes that can contribute to the substrate for AF.

EAT REMODELS MYOCARDIAL TISSUE AND CARDIOMYOCYTE CONNECTIVITY. AF phenotype severity among cardiac surgery cohorts has previously been shown to associate with fibrotic remodeling of EAT (10). In that study, an inverse correlation between fibrotic remodelling and the amount of subepicardial adipose tissue suggested the progressive fibrosis of fatty infiltrates with permanent AF. In the present investigation, in patients without prior clinical documentation of AF, we observed a correlation between local EAT volume and the fibrosis content of underlying myocardium in right atrial appendages (Figure 3). Fibrosis was associated with more marked atrial conduction slowing providing a mechanism by which EAT may create regional substrate which promotes AF. Furthermore, our data also provide evidence to indicate that beyond fibrosis promotion, EAT exerts an influence on atrial electrophysiology via a more direct action on proximal cardiomyocyte populations (Figure 3). Cx40 gap junction proteins are critical mediators of intermyocyte conduction, and changes in human cardiomyocyte Cx40 expression/localization have been associated with AF (24). In our study, patients with the greatest volumes of anterior right atrial EAT exhibited more extensive lateralization of sarcolemmal Cx40. This re-distribution of connexin gap junction proteins from longitudinal to lateral positioning would diminish the directionality of electrical coupling from myocyte to myocyte contributing to an increase in atrial conduction heterogeneity, promoting re-entry pathways and forming potential substrate for AF.

ADIPOSE PARACRINE INFLUENCES ON CARDIOMYOCYTE FUNCTION. Infiltration of EAT into the myocardium exacerbated patient atrial conduction heterogeneity, independent of the extent of fibrosis (Figure 4). This suggests that EAT infiltration not only constitutes a

physical barrier to inter-myocyte conduction, but also exerts a paracrine influence on local electrophysiology. EAT is endocrinologically active, synthesizing and releasing factors with capacity to alter atrial gene expression (25), inflammatory mediators (11), oxidative stress (26) and arrhythmia vulnerability (27). Using two different cell culture systems (hiPSCs and HL-1 cells), here we show that incubating adipose tissue fragments or exposing cardiomyocytes to media conditioned by factors (protein secretome) released from cardiac adipose tissue modulates cardiomyocyte function - slowing conduction and prolonging field potential duration (Figure 5). Such effects would be predicted to increase vulnerability to re-entrant and triggered arrhythmias respectively. Together, these findings suggest that a paracrine influence of infiltrating EAT on the cardiomyocyte may contribute to the conduction heterogeneity that underlies AF, independent of direct adipose infiltration.

ADIPOSE-DERIVED PROTEINS WITH CAPACITY TO MODULATE CONDUCTION

Proteomic findings validated some previously reported findings and provided new insight, in particular to conduction related functional changes. Gelsolin has previously been identified to be down-regulated in the EAT secretome of patients with post-operative AF (28). In this study, gelsolin was shown to be amongst the least abundant proteins released from cardiac adipose tissue (vs inguinal; Figure 6C). Gelsolin is known to inactivate the L-type Ca channels (29). Thus the relatively low abundance of gelosin in the present study is consistent with cardiomyocyte action potential prolongation, as evidenced by increased field potential duration with EAT incubation (Figure 5D). Inflammation has previously been associated with adiposity and here we provide new evidence that the interleukin IL-12 may be of more importance than appreciated to date (Figure 6F-G). Implicated in the link between obesity, adiposity and insulin resistance (30), the role of IL-12 in the heart is poorly defined.

Of most importance, our proteomic analyses revealed that proteins linked with focal adhesion functionality were prominently represented in the cardiac adipose secretome, including increased abundance of talin-1, several heat shock proteins, plastin-2 (LCP1) and 14-3-3 family proteins (Figure 6E). Focal adhesion proteins are known to regulate inter-myocyte connectivity and gap junction structure. Talin-1 directly associates with connexins and regulates integrins mediating cell-cell adhesion (31), and hence may contribute to cardiomyocyte Cx40 lateralization and associated conduction heterogeneity observed here. Plastin-2 has been linked with regulation of adipocyte growth (32) and may have a complementary role in modulating cardiomyocyte morphology. These proteomic findings indicate that further studies are warranted to fully investigate the involvement of focal adhesion proteins in the cardiac adipose-cardiomyocyte paracrine axis.

STUDY LIMITATIONS. The clinical component of this study sampled tissue from the right atrium alone. Emerging data suggests regional variation of atrial microarchitecture and EAT may accordingly interact differently with atrial tissue depending on anatomic sub-location. However, as this was a study performed in situ without clinical indication for tissue removal, the right atrial appendage was considered safest for sampling. We also cannot exclude atrial remodeling caused by ischemic heart disease. We endeavored to exclude any clear structural abnormality or history of AF that might contribute to the atrial substrate. There were no differences in EAT volume (local or global), conduction characteristics, fibrosis content or molecular expression, when the cohort was evaluated based on number of stenosed vessels or ischemic arterial territory.

CONCLUSIONS

This is the first clinical study to show that regional EAT content impacts local myocardial electrophysiology by direct infiltration and inter-myocyte disruption, tissue fibrosis and gap junction remodeling. Novel cell culture findings show that cardiac adipose tissue modulates cardiomyocyte electrophysiology, at least partly through the release of distinct proteins with capacity to manifest proarrhythmic characteristics. These insights carry important implications for understanding the mechanisms linking EAT with AF and may lead to the development of potential therapies to attenuate their impact.

PERSPECTIVES.

COMPETENCY IN MEDICAL KNOWLEDGE:

Non-uniform infiltration of epicardial adipose into the myocardium is linked with localized regions of atrial conduction heterogeneity that may facilitate the incidence, maintenance and progression of atrial fibrillation. Specifically the anterior right atrial adipose volume is correlated with arrhythmia substrate. The profile of proteins released from the cardiac adipose tissue depot is distinctive and the adipose 'secretome' contains mediators which directly influence cardiomyocyte electrophysiology and cell-to-cell conduction.

TRANSLATIONAL OUTLOOK:

Further studies are required to identify interventions to limit progression of adiposity-associated atrial fibrillation vulnerability and to determine which cardiac adipose tissue-derived factors may be therapeutic targets to suppress development of atrial conduction abnormalities. In particular proteins involved in focal-adhesion signaling are implicated in disturbance of cardiomyocyte coupling.

REFERENCES:

1. Tedrow UB, Conen D, Ridker PM et al. The long- and short-term impact of elevated body mass index on the risk of new atrial fibrillation the WHS (women's health study). J Am Coll Cardiol 2010;55:2319-27.
2. Wang TJ, Parise H, Levy D et al. Obesity and the risk of new-onset atrial fibrillation. JAMA 2004;292:2471-7.
3. Andrade J, Khairy P, Dobrev D, Nattel S. The clinical profile and pathophysiology of atrial fibrillation: relationships among clinical features, epidemiology, and mechanisms. Circ Res 2014;114:1453-68.
4. Schram-Serban C, Heida A, Roos-Serote MC et al. Heterogeneity in Conduction Underlies Obesity Related Atrial Fibrillation Vulnerability. Circ Arrhythm Electrophysiol 2020; DOI:10.1161/circep.119.008161.
5. Mahajan R, Lau DH, Brooks AG et al. Electrophysiological, Electroanatomical, and Structural Remodeling of the Atria as Consequences of Sustained Obesity. J Am Coll Cardiol 2015;66:1-11.
6. Abed HS, Wittert GA, Leong DP et al. Effect of weight reduction and cardiometabolic risk factor management on symptom burden and severity in patients with atrial fibrillation: a randomized clinical trial. JAMA 2013;310:2050-60.
7. Pathak RK, Middeldorp ME, Lau DH et al. Aggressive risk factor reduction study for atrial fibrillation and implications for the outcome of ablation: the ARREST-AF cohort study. J Am Coll Cardiol 2014;64:2222-31.
8. Thanassoulis G, Massaro JM, O'Donnell CJ et al. Pericardial fat is associated with prevalent atrial fibrillation: the Framingham Heart Study. Circ Arrhythm Electrophysiol 2010;3:345-50.

9. Wong CX, Abed HS, Molaee P et al. Pericardial fat is associated with atrial fibrillation severity and ablation outcome. J Am Coll Cardiol 2011;57:1745-51.
10. Haemers P, Hamdi H, Guedj K et al. Atrial fibrillation is associated with the fibrotic remodelling of adipose tissue in the subepicardium of human and sheep atria. Eur Heart J 2017;38:53-61.
11. Venteclef N, Guglielmi V, Balse E et al. Human epicardial adipose tissue induces fibrosis of the atrial myocardium through the secretion of adipo-fibrokines. Eur Heart J 2015;36:795-805a.
12. Mitchell C, Rahko PS, Blauwet LA et al. Guidelines for Performing a Comprehensive Transthoracic Echocardiographic Examination in Adults: Recommendations from the American Society of Echocardiography. J Am Soc Echocardiogr 2019;32:1-64.
13. Walters TE, Lee G, Spence S et al. Acute atrial stretch results in conduction slowing and complex signals at the pulmonary vein to left atrial junction: insights into the mechanism of pulmonary vein arrhythmogenesis. Circ Arrhythm Electrophysiol 2014;7:1189-97.
14. Eijsbouts SC, Majidi M, van Zandvoort M, Allessie MA. Effects of acute atrial dilation on heterogeneity in conduction in the isolated rabbit heart. J Cardiovasc Electrophysiol 2003;14:269-78.
15. Lammers WJ, Schalij MJ, Kirchhof CJ, Allessie MA. Quantification of spatial inhomogeneity in conduction and initiation of reentrant atrial arrhythmias. Am J Physiol 1990;259:H1254-63.
16. Abukar Y, Ramchandra R, Hood SG et al. Increased cardiac sympathetic nerve activity in ovine heart failure is reduced by lesion of the area postrema, but not lamina terminalis. Basic Res Cardiol 2018;113:35.

17. Anderson DJ, Kaplan DI, Bell KM et al. NKX2-5 regulates human cardiomyogenesis via a HEY2 dependent transcriptional network. Nat Commun 2018;9:1373.

18. Wells SP, Waddell HM, Sim CB et al. Cardiomyocyte functional screening - interrogating comparative electrophysiology of high-throughput model cell systems. Am J Physiol Cell Physiol 2019;317:C1256-67.

19. Aitken-Buck HM, Moharram M, Babakr AA et al. Relationship between epicardial adipose tissue thickness and epicardial adipocyte size with increasing body mass index. Adipocyte 2019;8:412-420.

20. Nalliah CJ, Sanders P, Kottkamp H, Kalman JM. The role of obesity in atrial fibrillation. Eur Heart J 2016;37:1565-72.

21. Mahajan R, Nelson A, Pathak RK et al. Electroanatomical Remodeling of the Atria in Obesity: Impact of Adjacent Epicardial Fat. JACC Clin Electrophysiol 2018;4:1529-1540.

22. Nagashima K, Okumura Y, Watanabe I et al. Does location of epicardial adipose tissue correspond to endocardial high dominant frequency or complex fractionated atrial electrogram sites during atrial fibrillation? Circ Arrhythm Electrophysiol 2012;5:676-83.

23. Nakahara S, Hori Y, Kobayashi S et al. Epicardial adipose tissue-based defragmentation approach to persistent atrial fibrillation: its impact on complex fractionated electrograms and ablation outcome. Heart Rhythm 2014;11:1343-51.

24. Kanagaratnam P, Rothery S, Patel P, Severs NJ, Peters NS. Relative expression of immunolocalized connexins 40 and 43 correlates with human atrial conduction properties. J Am Coll Cardiol 2002;39:116-23.

25. Chilukoti RK, Giese A, Malenke W et al. Atrial fibrillation and rapid acute pacing regulate adipocyte/adipositas-related gene expression in the atria. Int J Cardiol 2015;187:604-13.

26. Salgado-Somoza A, Teijeira-Fernandez E, Fernandez AL, Gonzalez-Juanatey JR, Eiras S. Proteomic analysis of epicardial and subcutaneous adipose tissue reveals differences in proteins involved in oxidative stress. Am J Physiol Heart Circ Physiol 2010;299:H202-9.

27. Bernasochi GB, Boon WC, Curl CL et al. Pericardial adipose and aromatase: A new translational target for aging, obesity and arrhythmogenesis? J Mol Cell Cardiol 2017;111:96-101.

28. Viviano A, Yin X, Zampetaki A et al. Proteomics of the epicardial fat secretome and its role in post-operative atrial fibrillation. Europace : European pacing, arrhythmias, and cardiac electrophysiology : journal of the working groups on cardiac pacing, arrhythmias, and cardiac cellular electrophysiology of the European Society of Cardiology 2018;20:1201-1208.

29. Lader AS, Kwiatkowski DJ, Cantiello HF. Role of gelsolin in the actin filament regulation of cardiac L-type calcium channels. Am J Physiol 1999;277:C1277-83.

30. Nam H, Ferguson BS, Stephens JM, Morrison RF. Impact of obesity on IL-12 family gene expression in insulin responsive tissues. Biochim Biophys Acta 2013;1832:11-9.

31. Shimaoka M, Kawamoto E, Gaowa A, Okamoto T, Park EJ. Connexins and Integrins in Exosomes. Cancers (Basel) 2019;11.

32. Vogel MAA, Wang P, Bouwman FG et al. A comparison between the abdominal and femoral adipose tissue proteome of overweight and obese women. Sci Rep 2019;9:4202.

FIGURE LEGENDS:

Figure 1. Anterior right atrial EAT volume is independent of BMI and bi-atrial EAT volume. **(A)** Representative oblique-coronal slice of the cardiac computed tomography (RAA, right atrial appendage; RCA, right coronary artery; RVOT, right ventricular outflow tract), with **(B)** anterior RA EAT delineated (yellow). **(C)** Exemplar cardiac CT short axis slice summation of anterior right atrial EAT volume. **(D)** Body mass index significantly correlated with bi-atrial, **(E)** but not anterior right atrial EAT volume. **(F)** No correlation was evident between bi-atrial and anterior right atrial EAT volumes.

Figure 2. Right atrial conduction is selectively dependent on anterior right atrial adiposity. **(A)** Representative CT images of patients with low and high anterior right atrial EAT volumes. **(B)** Representative isochronal (3 ms steps) maps at 600 ms pacing rate from patients with either low or high anterior right atrial EAT volumes. White star: earliest plaque activation, yellow star: latest plaque activation. **(C)** Significant correlations existed between anterior right atrial EAT volume and plaque activation time, conduction velocity and number of complex points. **(D)** In contrast, these electrophysiological parameters did not correlate with the bi-atrial adipose tissue volume.

Figure 3. Anterior right atrial adiposity associated with fibrosis and Cx40 lateralization. **(A)** Exemplar picrosirius red stained right atrial appendage sections from patients with either low or high anterior right atrial EAT volumes. Sections were assessed for extent of fibrosis. **(B)** A significant correlation was evident between the extent of fibrosis and anterior right atrial EAT volume. **(C)** Right atrial appendage sections were assessed by immunohistochemistry for cardiomyocyte Cx40 localization (white arrows). **(D)** Lateralization of Cx40 was significantly greater in tissues from patients with the greatest (vs

lowest) anterior right atrial EAT volumes. Data are mean ± SEM, n=9-28 images/heart, N=3-4 hearts/group, *p < 0.05 using unpaired Student's t-test.

Figure 4. Myocardial EAT infiltration exacerbates conduction heterogeneity, but not fibrosis. (A) Exemplar right atrial appendage section stained with oil-red-O for assessing adiposity. **(B)** Higher magnification analysis revealed a non-uniform interface between the EAT (stained red) and myocardium (blue), with evidence of adipose tissue infiltrating into the epicardium. **(C)** EAT infiltration was associated with increased conduction heterogeneity, **(D)** but not the extent of fibrosis. Data are mean ± SEM, n=6-12/group, *p < 0.05 using unpaired Student's t-test.

Figure 5. Cardiac adipose tissue exerts paracrine influence on cardiomyocyte electrophysiology in vitro. (A) Sheep EAT fragments were co-cultured with hiPSC-CMs for 24 hrs on multielectrode arrays and **(B)** extracellular field potentials measured. **(C)** EAT co-culture significantly decreased spontaneous beating rate (vs non-adipose tissue co-cultured control) and **(D-E)** prolonged field potential duration. Data are mean ± SEM, n=24-34 arrays/group, N=7 cultures, *p < 0.05 using unpaired Students t-test. **(F)** HL-1 atrial cardiomyocytes were plated on multi-electrode arrays in the presence/absence of mouse pericardial or inguinal adipose tissue conditioned media for 24 hrs. **(G-I)** Incubation of HL-1 cells with pericardial, but not inguinal, adipose tissue conditioned media increased activation time and significantly reduced conduction velocity. Data are mean ± SEM, n=14-17/group, *p < 0.05 using one-way ANOVA with Fisher's LSD test.

Figure 6. Pericardial adipose tissue secretome exhibits a distinct proteomic profile. (A-B) Mouse pericardial and inguinal adipose tissue conditioned media were processed for data-

dependent acquisition proteomic analysis. The type and abundance of proteins differed in pericardial vs inguinal adipose tissue. **(C)** Overview of the highest/lowest abundant proteins released from pericardial vs inguinal adipose tissue. **(D)** Gene Ontology Cellular Component category ranking of the high abundance proteins released from pericardial adipose tissue (vs inguinal) **(E)** includes 'focal adhesion' (GO:0005925) proteins. **(F)** Gene Ontology Biological Processes category ranking of the high abundance proteins released from pericardial adipose tissue (vs inguinal) **(G)** shows a high abundance of proteins associated with the 'cellular response to interleukin-12' (GO:0071349).

26

Table 1. Patient characteristics and EAT distribution

	Recruited patients n = 19
Age (y)	64 ± 6
Male gender, % (n)	14 (78)
BMI (kg/m^2)	30 ± 7
Waist : Hip ratio	1.0 ± 0.1
Diabetes, % (n)	7 (39)
Hypertension, % (n)	17 (94)
Hyperlipidaemia, % (n)	11 (61)
Stroke/TIA, % (n)	3 (17)
2 vessel disease, % (n)	5 (28)
3 vessel disease, % (n)	13 (72)
Coronary stent/angioplasty, % (n)	7 (39)
Left atrial size (cm^2)	20 ± 5
Right atrial size (cm^2)	15 ± 4
LVEDV (mm)	45 ± 7
LVEF (%)	60 ± 4
Median EAT Volume (ml)	
Total cardiac EAT	127.2 (104.0-168.3)
Bi-atrial EAT	46.3 (34.9-62.7)
Left atrial EAT	26.6 (18.7-34.7)
Right atrial EAT	20.3 (16.3-29.6)
Anterior right atrial EAT	3.1 (2.5-5.8)

BMI, body mass index; TIA, transient ischemic attack; LVEDV, left ventricular end diastolic volume; LVEF, left ventricular ejection fraction; EAT, epicardial adipose tissue.

Table 2. Correlation of EAT volumes with atrial electrophysiologic parameters

Anterior right atrial EAT	**Paced 600ms**	**Paced 300ms**
Plaque activation times	r=0.64, p<0.005*	r=0.55, p<0.05*
Mean conduction velocity	r=-0.46, p<0.05*	r=-0.49, p<0.05*
Slowed conduction	r=0.36, p=0.14	r=0.58, p<0.05*
Complex points	r=0.69, p<0.001*	r=0.66, p<0.005*
Conduction heterogeneity	r=0.43, p=0.07	r=0.42, p=0.08
Bi-atrial EAT	**Paced 600ms**	**Paced 300ms**
Plaque activation times	r=-0.29, p=0.29	r=-0.42, p=0.11
Mean conduction velocity	r=0.24, p=0.37	r=0.10, p=0.72
Slowed conduction	r=-0.31, p=0.24	r=0.16, p=0.56
Complex points	r=-0.16, p=0.56	r=-0.16, p=0.56
Conduction heterogeneity	r=-0.34, p=0.19	r=-0.29, p=0.27

EAT, epicardial adipose tissue.

Epicardial adipose tissue accumulation confers cardiac conduction abnormality: a multidimensional study identifying novel mechanistic substrates

Chrishan J. Nalliah, MBBS, PhD,[a,b,*] James R. Bell, PhD,[c,d,*] Antonia J.A. Raaijmakers, PhD,[d] Helen W. Waddell, BSc,[d] Simon P. Wells, MRes,[d,e] Gabriel B. Bernasochi, PhD,[d] Magda K. Montgomery, PhD,[d] Simon Binny, MBBS,[a] Troy Watts, BSc,[a] Subodh B. Joshi, MBBS,[a] Elaine Lui,[f] Choon Boon Sim, PhD,[g] Marco Larobina, MBBS,[h] Michael O'Keefe, MBBS,[h] John Goldblatt, MBBS,[h] Alistair Royse, MBBS,[h] Geoffrey Lee, MBChB, PhD,[a,b] Enzo R. Porrello, PhD,[d,g] Matthew J. Watt, PhD,[d] Peter M. Kistler, MBBS, PhD,[i] Prashanthan Sanders, MBBS,[j] Lea M.D. Delbridge, PhD,[d,#] Jon M. Kalman, MBBS, PhD, [a,b,#]

ABSTRACT

BACKGROUND Clinical studies have reported epicardial adipose tissue (EAT) accumulation associates with progression of atrial fibrillation (AF) pathology and adversely impacts AF management. The role of local cardiac EAT deposition in disease progression is unclear and the electrophysiologic, cellular and molecular mechanisms involved remain poorly defined.

OBJECTIVES To identify the underlying mechanisms by which EAT influences the atrial substrate for AF.

METHODS Patients without AF undergoing coronary artery bypass surgery were recruited. Computed tomography and high density epicardial electrophysiologic mapping of the anterior right atrium (RA) were utilized to quantify EAT volumes and to assess association with the electrophysiologic substrate in situ. Excised RA appendages were analyzed histologically to characterize EAT infiltration, fibrosis and gap junction localization. Co-culture experiments were used to evaluate paracrine effects of EAT on cardiomyocyte electrophysiology. Proteomic analyses were applied to identify molecular mediators of cellular electrophysiologic disturbance.

RESULTS Higher local EAT volume clinically correlated with slowed conduction, greater electrogram fractionation, increased fibrosis and lateralization of cardiomyocyte connexin-40. In addition, atrial conduction heterogeneity was increased with more extensive myocardial EAT infiltration. Cardiomyocyte culture studies using multi-electrode arrays showed that cardiac adipose tissue secreted factors slowed conduction velocity, and contained proteins with capacity to disrupt intermyocyte electromechanical integrity.

CONCLUSIONS These findings indicate that atrial pathophysiology is critically dependent on local EAT accumulation and infiltration. In addition to myocardial architecture disruption, this effect can be attributed to an EAT-cardiomyocyte paracrine axis. The focal adhesion group proteins are identified as new disease candidates potentially contributing to arrhythmogenic atrial substrate.

From the [a]Department of Cardiology, Royal Melbourne Hospital, Melbourne, Victoria, Australia; [b]Department of Medicine and Radiology, University of Melbourne, Melbourne, Victoria, Australia; [c]Department of Physiology, Anatomy and Microbiology, La Trobe University, Bundoora, Victoria, Australia; [d]Department of Physiology, University of Melbourne, Melbourne, Victoria, Australia; [e]Institute of Cardiovascular Sciences, College of Medical and Dental Sciences, University of Birmingham, United Kingdom; [f]Department of Radiology, Royal Melbourne Hospital, Melbourne, Victoria, Australia; [g]Murdoch Children's Research Institute, Royal Children's Hospital, Melbourne, Victoria, Australia; [h]Department of Cardiothoracic Surgery, Royal Melbourne Hospital, Melbourne, Victoria, Australia; [i]Department of Cardiology, The Alfred Hospital, Melbourne, Australia; [j]Australia Centre for Heart Rhythm Disorders (CHRD), South Australian Health and Medical Research Institute (SAHMRI), University of Adelaide and Royal Adelaide Hospital, Adelaide, Australia.

*Drs. Nalliah and Bell and #Profs. Delbridge and Kalman contributed equally to this work.

FIGURE 1 **Anterior right atrial EAT volume is independent of BMI and bi-atrial EAT volume**

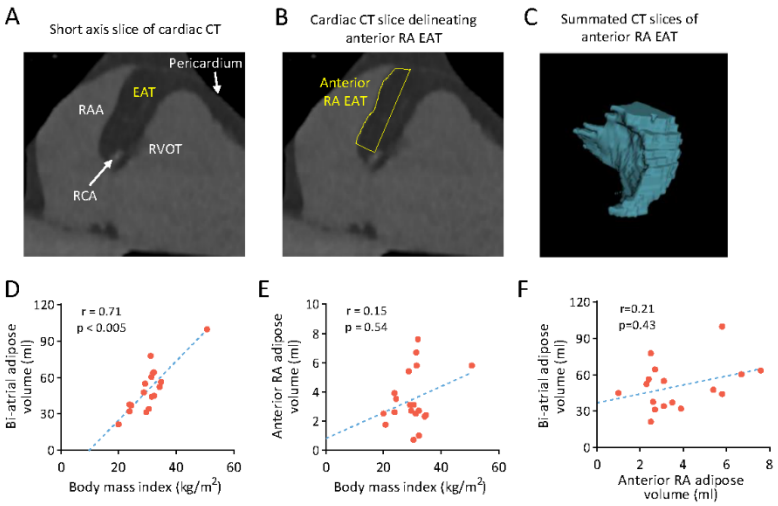

(A) Representative oblique-coronal slice of the cardiac computed tomography (RAA, right atrial appendage; RCA, right coronary artery; RVOT, right ventricular outflow tract), with **(B)** anterior right atrial EAT delineated (yellow). **(C)** Exemplar cardiac CT short axis slice summation of anterior right atrial EAT volume. **(D)** Body mass index significantly correlated with bi-atrial, **(E)** but not anterior right atrial EAT volume. **(F)** No correlation was evident between bi-atrial and anterior right atrial EAT volumes.

FIGURE 2 **Right atrial conduction is selectively dependent on anterior right atrial adiposity**

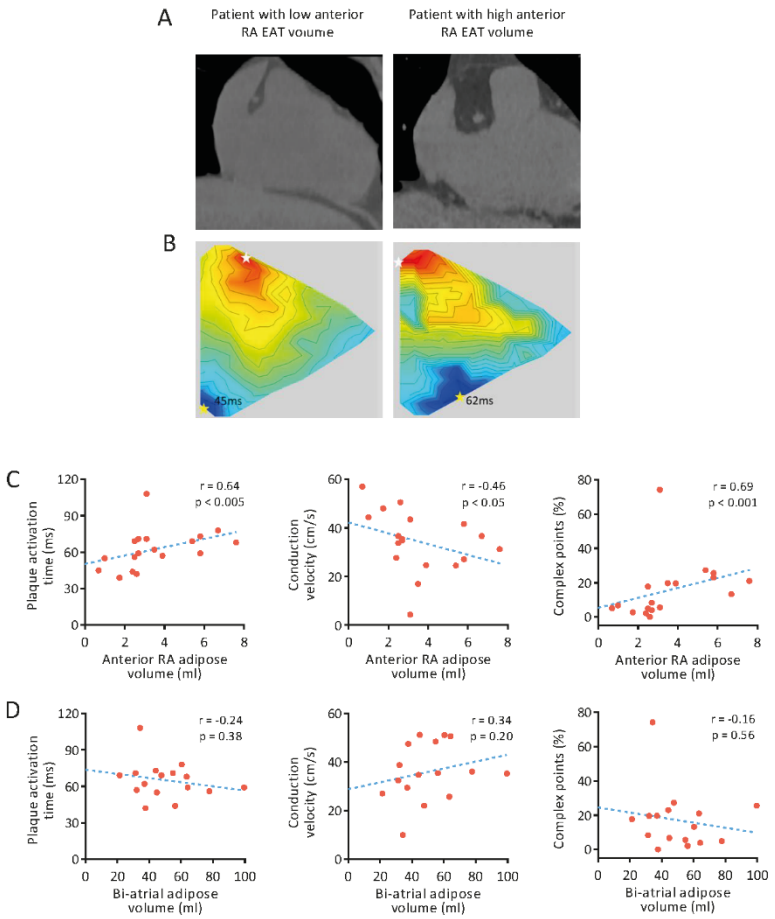

(A) Representative CT images of patients with low and high anterior right atrial EAT volumes. **(B)** Representative isochronal (3 ms steps) maps at 600 ms pacing rate from patients with either low or high anterior right atrial EAT volumes. White star: earliest plaque activation, yellow star: latest plaque activation. **(C)** Significant correlations existed between anterior right atrial EAT volume and plaque activation time, conduction velocity and number of complex points. **(D)** In contrast, these electrophysiological parameters did not correlate with the bi-atrial adipose tissue volume.

FIGURE 3 **Anterior right atrial adiposity associated with fibrosis and Cx40 lateralization**

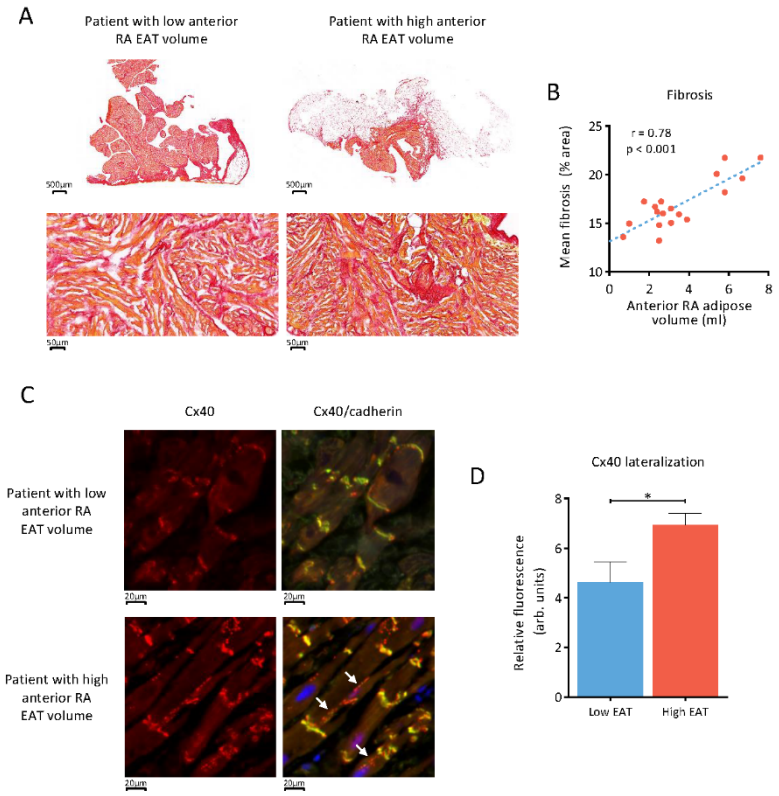

(A) Exemplar picrosirius red stained right atrial appendage sections from patients with either low or high anterior right atrial EAT volumes. Sections were assessed for extent of fibrosis. **(B)** A significant correlation was evident between the extent of fibrosis and anterior right atrial EAT volume. **(C)** Right atrial appendage sections were assessed by immunohistochemistry for cardiomyocyte Cx40 localization (white arrows). **(D)** Lateralization of Cx40 was significantly greater in tissues from patients with the greatest (vs lowest) anterior right atrial EAT volumes. Data are mean ± SEM, n=9-28 images/heart, N=3-4 hearts/group, *p < 0.05 using unpaired Student's t-test.

Figure 4 Myocardial EAT infiltration exacerbates conduction heterogeneity, but not fibrosis

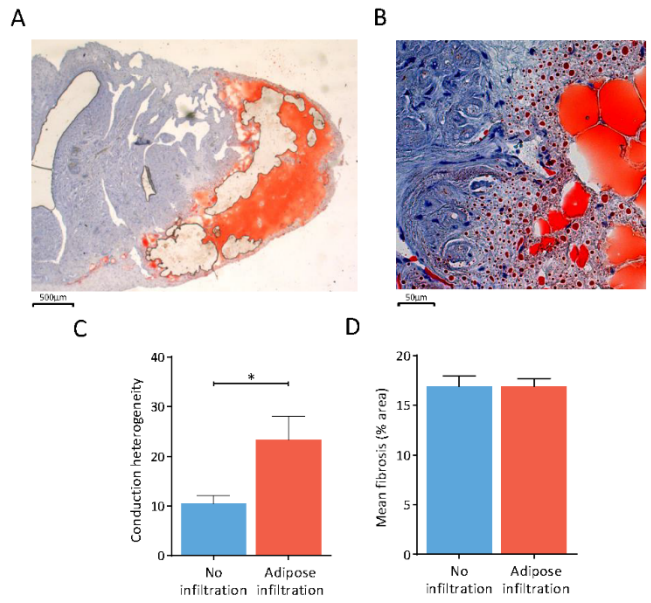

(A) Exemplar right atrial appendage section stained with oil-red-O for assessing adiposity. **(B)** Higher magnification analysis revealed a non-uniform interface between the EAT (stained red) and myocardium (blue), with evidence of adipose tissue infiltrating into the epicardium. **(C)** EAT infiltration was associated with increased conduction heterogeneity, **(D)** but not the extent of fibrosis. Data are mean ± SEM, n=6-12/group, *p < 0.05 using unpaired Student's t-test.

Figure 5 Cardiac adipose tissue exerts paracrine influence on cardiomyocyte electrophysiology in vitro

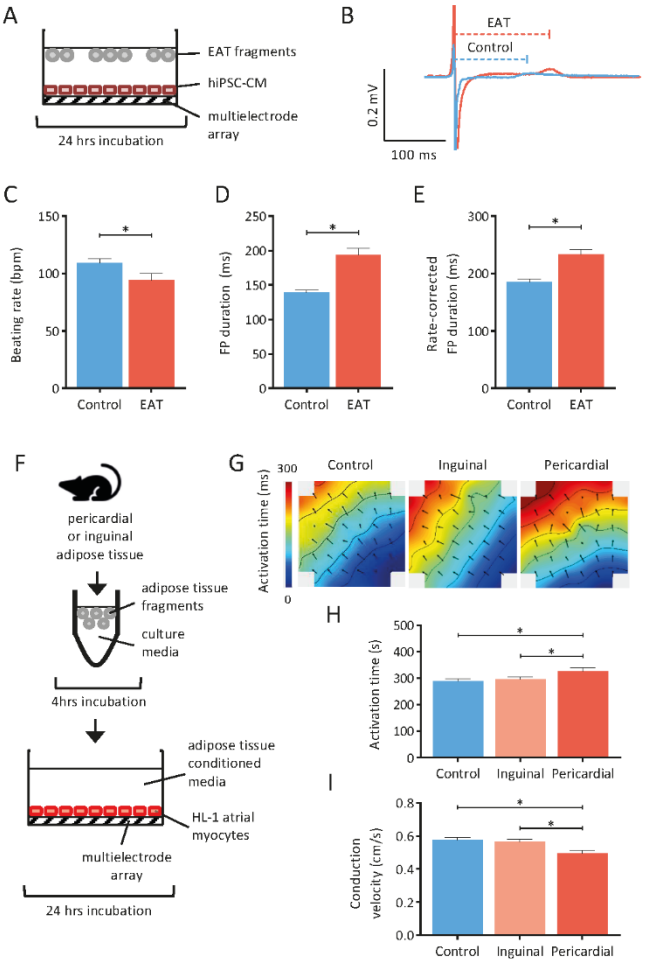

(A) Sheep EAT fragments were co-cultured with hiPSC-CMs for 24 hrs on multielectrode arrays and **(B)** extracellular field potentials measured. **(C)** EAT co-culture significantly decreased spontaneous beating rate (vs non-adipose tissue co-cultured control) and **(D-E)** prolonged field potential duration. Data are mean ± SEM, n=24-34 arrays/group, N=7 cultures, *p < 0.05 using unpaired Students t-test. **(F)** HL-1 atrial cardiomyocytes were plated on multi-electrode arrays in the presence/absence of mouse pericardial or inguinal adipose tissue conditioned media for 24 hrs. **(G-I)** Incubation of HL-1 cells with pericardial, but not inguinal, adipose tissue conditioned media increased activation time and significantly reduced conduction velocity. Data are mean ± SEM, n=14-17/group, *p < 0.05 using one-way ANOVA with Fisher's LSD test.

34

Figure 6 Pericardial adipose tissue secretome exhibits a distinct proteomic profile

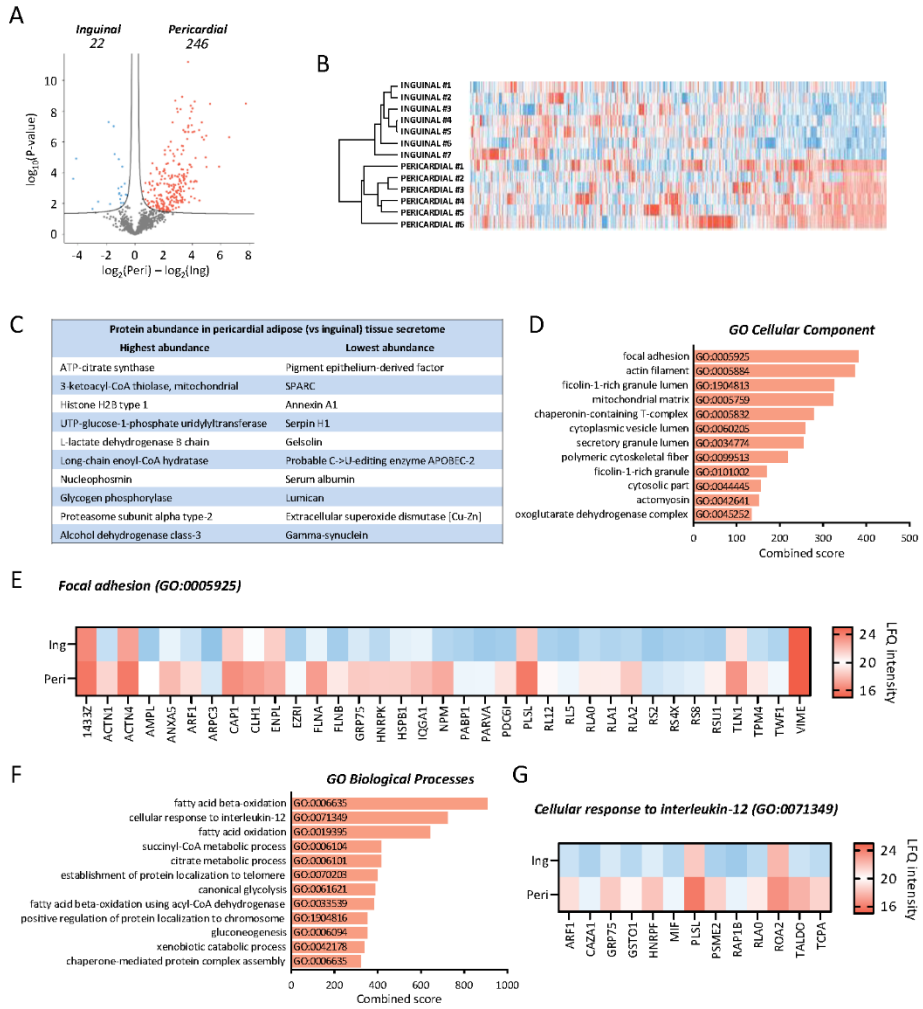

Protein abundance in pericardial adipose (vs inguinal) tissue secretome	
Highest abundance	**Lowest abundance**
ATP-citrate synthase	Pigment epithelium-derived factor
3-ketoacyl-CoA thiolase, mitochondrial	SPARC
Histone H2B type 1	Annexin A1
UTP-glucose-1-phosphate uridylyltransferase	Serpin H1
L-lactate dehydrogenase B chain	Gelsolin
Long-chain enoyl-CoA hydratase	Probable C->U-editing enzyme APOBEC-2
Nucleophosmin	Serum albumin
Glycogen phosphorylase	Lumican
Proteasome subunit alpha type-2	Extracellular superoxide dismutase [Cu-Zn]
Alcohol dehydrogenase class-3	Gamma-synuclein

(A-B) Mouse pericardial and inguinal adipose tissue conditioned media were processed for data-dependent acquisition proteomic analysis. The type and abundance of proteins differed in pericardial vs inguinal adipose tissue. **(C)** Overview of the highest/lowest abundant proteins released from pericardial vs inguinal adipose tissue. **(D)** Gene Ontology Cellular Component category ranking of the high abundance proteins released from pericardial adipose tissue (vs inguinal) **(E)** includes 'focal adhesion' (GO:0005925) proteins. **(F)** Gene Ontology Biological Processes category ranking of the high abundance proteins released from pericardial adipose tissue (vs inguinal) **(G)** shows a high abundance of proteins associated with the 'cellular response to interleukin-12' (GO:0071349).

CENTRAL ILLUSTRATION Local adipose tissue infiltration exerts paracrine influence on atrial conduction

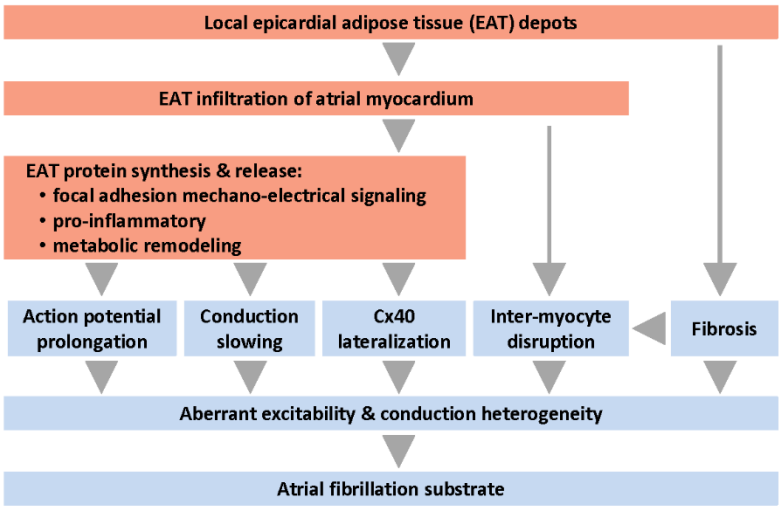

Proposed cellular mechanisms linking localized EAT accumulation with the substrate for atrial fibrillation. EAT – epicardial adipose tissue; Cx40 – connexin 40.

ONLINE APPENDIX

EPICARDIAL ADIPOSE TISSUE ACCUMULATION CONFERS CARDIAC CONDUCTION ABNORMALITY: A MULTIDIMENSIONAL STUDY IDENTIFYING NOVEL MECHANISTIC SUBSTRATES

Chrishan J. Nalliah, MBBS, PhD,[*] James R. Bell, PhD,[*] Antonia J.A. Raaijmakers, PhD, Helen M. Waddell, BSc, Simon P. Wells, MRes, Gabriel B. Bernasochi, PhD, Magdalene K. Montgomery, PhD, Simon Binny, MBBS, Troy Watts, BSc, Subodh B. Joshi, MBBS, Elaine Lui, MMed, MBBS, Choon Boon Sim, PhD, Marco Larobina, MBBS, Michael O'Keefe, MBBS, John Goldblatt, MBBS, Alistair Royse, MBBS, Geoffrey Lee, MBChB, PhD, Enzo R. Porrello, PhD, Matthew J. Watt, PhD, Peter M. Kistler, MBBS, PhD, Prashanthan Sanders, MBBS, PhD, Lea M.D. Delbridge, PhD,[#] Jonathan M. Kalman, MBBS, PhD,[#]

ONLINE APPENDIX - METHODS

PATIENT DETAILS.

PATIENT RECRUITMENT. Nineteen consecutive patients having outpatient coronary artery bypass grafts for stable coronary artery disease were recruited at The Royal Melbourne Hospital. Written informed consent was acquired from all participants prior to study enrolment. This study was approved by the Melbourne Health Human Research Ethics Committee and complies with the Declaration of Helsinki.

EXCLUSION CRITERIA. History of AF was documented by clinical evaluation and medical record review. Pre-procedural transthoracic echocardiography according to standard American Society of Echocardiography guidelines (1) was performed on all participants. To determine the impact of EAT on the atrial substrate, patients with documented AF, congenital heart disease, left ventricular ejection fraction (LVEF) $\leq$ 55%, significant valvular disease (greater than trivial regurgitation or any stenosis), prior cardiac catheter ablation or pulmonary hypertension (pulmonary artery systolic pressure $\geq$ 35mmHg) were excluded from the study.

CARDIAC CT EAT QUANTIFICATION. Non-contrast computed tomography (CT) of the chest was performed using a dual source 128-slice scanner (SOMATOM Definition Flash, Siemens, Erlangen, Germany). The scans were performed a day before surgery. The images were acquired from the carina to below the cardiac apex to include all EAT. Prospective ECG gating was used in a single systolic phase. Tube voltage varied between 100-120 kV depending on patient size. Non-overlapping 2 mm slices were reconstructed every 2 mm in soft tissue (B26) kernels in an image matrix of 512 x 512.

Data was exported onto OsiriX DICOM Viewer (version 6.0.2) and analyzed offline. Slices of the heart extending from the superior tip of the right atrial appendage to the diaphragm were analyzed. The pericardium (consisting of all adipose tissue within the pericardial sac) was identified by an image display threshold setting of -190 to -30 Houndsfield units and manually traced.

Left and right atrial EAT was defined as EAT above the plane of the mitral and tricuspid annulus respectively. Bi-atrial EAT was determined by summation of left atrial and right atrial EAT, with the inter-atrial septal adipose tissue counted once. We determined EAT volume at the site of electrophysiologic mapping and appendage excision (anterior right atrial EAT) to assess the impact of local versus bi-atrial EAT on the local atrial substrate. Anterior right atrial EAT was defined as adipose tissue within the pericardium surrounding the right atrial free wall 1 slice (2 mm) below the level of the right coronary artery ostium to 1 slice above the superior border of the right atrial appendage. The adipose tissue located between the anterior right atrial and right ventricular outflow tract was bisected in an axial plane, and the medial segment assigned to the anterior right atrium.

INTRAOPERATIVE ATRIAL EPICARDIUM SURFACE MAPPING. Anti-arrhythmic medications were ceased > 5 half-lives before surgery. High density mapping of the anterior right atrium was performed utilising a previously described triangular epicardium mapping plaque (6.75 cm^2) with 128 silver-plated copper electrodes creating 117 closed-spaced bi-poles (inter-electrode distance 2.5 mm). Following thoracotomy and pericardial sac division, and prior to cardiopulmonary bypass, the mapping plaque was positioned on the anterior right atrial surface. The mapped area comprised the right atrial appendage.

Activation maps were acquired at paced rhythms of 600 ms and 300 ms. Pacing was performed from an electrode pair with stable capture located at one of the plaque vertices. Two isochronal maps were constructed (paced 600 ms, 300 ms), with 3 ms intervals in local activation time to assess conduction and activation patterns. The total plaque activation time was defined as the time taken to activate the entire plaque from the earliest to latest point. Uniform plaque activation was defined by an even distribution of isochrones without slowed conduction or conduction block.

Assessment of regional conduction slowing was performed by triangulating the plaque electrodes as previously described (2,3). Local conduction velocity was calculated as the mean of 2 conduction vectors in a 2.5 x 2.5 mm area. Regional slowing or block was defined by the plaque proportion with conduction slowing (10 to 20 cm/s) or conduction block ($\leq$ 10 cm/s).

The phase mapping method was used to determine conduction heterogeneity (4). In brief, the greatest difference in activation times were calculated between 4 adjacent electrodes. Activation time differences are plotted on a histogram for the entire plaque and conduction heterogeneity calculated by subtracting the 5^{th} from the 95^{th} percentile. Electrograms > 50 ms duration and $\geq$ 3 deflections from baseline or double potentials separated by an isoelectric interval > 30 ms were defined as complex electrograms (5). The proportion of complex electrograms was determined for each map.

HISTOLOGIC ASSESSMENT. Prior to cardiopulmonary bypass, the right atrial appendage was surgically excised and fixed in 10% formalin for histological analysis. Tissues were sectioned (10 μm) and stained with either oil-red-O (adiposity, hematoxylin counterstain) or picosirius

red (fibrosis) or prepared for immunohistochemistry (gap junction visualization). For quantification of fibrosis and adipose infiltration, sections were scanned with a brightfield digital scanner using (Panoramic ScanII Scanner, 3D Histech) and images captured using CaseViewer version 2.2 acquisition software (3DHistech; 20x magnification). Image analysis was blinded and performed using ImageJ (V1.51, NIH). Briefly, images were converted to greyscale (255 pixel range) and a pixel intensity histogram was assessed to determine the non-biased threshold which was used to calculate the total area of fibrosis for each image (% area). For all images, a value of total fibrosis (% area) was determined and the mean value per patient was calculated. Regions with vascular fibrosis were excluded from the analysis. For quantification of myocardial infiltration of EAT, a modified version of a previously described approach was used (6). For immunohistochemistry, sections were incubated with primary antibodies against Cx40 (1:200 dilution; Alpha Diagnostics Cx40-A) and N-cadherin (1:800 dilution; Sigma C1821) overnight at 4°C. Sections were subsequently incubated with anti-rabbit Cy5 (1:500; Jackson ImmunoResearch) and anti-mouse FITC (1:250; Jackson ImmunoResearch) secondary antibodies and DAPI stain (300 nM; Invitrogen). Sections were imaged using the Zeiss AXIO Imager.m2 connected to an Axiocam 506 mono camera and ZEN blue software (V2.5, Zeiss). For quantification of Cx40 expression, Cx40 and background fluorescence was measured for each image (ImageJ V1.51, NIH) and the total corrected cellular fluorescence calculated (integrated density – (area of selected cell x mean fluorescence of background) (7).

ANIMAL & CELL RECORDING DETAILS.

ANIMAL ETHICS. All experiments were approved by the Animal Ethics Committee of the University of Melbourne and and performed in accordance with the guidelines of the National Health and Medical Research Council of Australia.

ADIPOSE TISSUE COLLECTION. Ovine EAT was harvested and fragmented for multielectrode array (MEA) co-incubation with human induced pluripotent stem cell-derived cardiomyocytes (hiPSC-CMs) to evaluate effects on field potential characteristics. Adult Merino ewe anaesthesia was induced and maintained with 1.5%-2.0% isoflurane for the duration of the surgery (8). Following thoracotomy and pericardial sac division, EAT was excised and processed for co-culture with hiPSC-CMs.

Murine adipose tissue conditioned media was generated to both evaluate the effects on field potential characteristics and identify the candidate proteins responsible. Male C57Bl/6 mice (Animal Resources Centre, WA, Australia) were fed a high-fat diet (SF04-001; Specialty Feeds, WA, Australia) for 12 weeks. Mice were anesthetized with an intra-peritoneal injection of sodium pentobarbitone (70 mg/kg) sodium heparin (200 IU/kg) prior to tissue harvest. Murine pericardial and inguinal subcutaneous adipose tissues were harvested, fragmented and incubated in a serum-free medium (EX-CELL 325 PF CHO Serum-Free Medium for CHO Cells; Sigma Aldrich) for 6 hrs to collect secreted/released proteins for preparation of 'conditioned' media for subsequent electrophysiological recordings (DMEM media) or mass spectroscopy analysis (protein free media).

CARDIOMYOCYTE CULTURE. The hiPSC-CMs were cultured and differentiated as previously described (9-11). Briefly, hiPSCs (line PB004.4 female; Murdoch Children's Research Institute) were cultured in a 75 cm^2 tissue culture flask with hiPSC media [DMEM-F-12 (11320033; Gibco), 20% (vol/vol) knockout serum replacement (10828028; Gibco), 1x nonessential amino acids (11140050; Gibco), 1x GlutaMAX (35050061; Gibco), penicillin/streptomycin (15140122; Gibco), 110 μM 2-mercaptoethanol (21985023; Gibco),

and 5 ng/mL recombinant human fibroblast growth factor (233-FB-025; R&D)] on irradiated mouse embryonic fibroblasts and passaged using TrypLE Express enzyme (12604013; ThermoFisher). One day before differentiation, 1.6 x 10^5 cells/cm^2 were seeded. To induce differentiation (day 0), cells were treated with basal differentiation media [RPMI (21870076; Sigma), B27 minus vitamin A (12587010; Gibco), and 50 µg/mL ascorbic acid (A8960; Sigma) supplemented with 10 µM CHIR-99021 (4423; Tocris Bioscience) and 80 ng/mL activin A (Peprotech)]. On days 1, 3, and 5, media were changed to basal differentiation media supplemented with 5 µM IWR-1 (I0161; Sigma). Cells were maintained in basal differentiation media from day 7 until used. For experiments, cells were dissociated with TrypLE Express, centrifuged (200 g, 4°C, 3 min), carefully resuspended in basal differentiation medium, and replated at 800,000 cells/mL as clusters across Geltrex-coated MEAs (Geltrex, 1:100, A1413202; Life Technologies). hiPSC-CMs were cultured with/without sheep epicardial adipose fragments (0.5 mm diameter) for 24 hrs and field potential characteristics recorded.

The immortalized atrial cardiomyocyte cell line, HL-1 (Merck, SCC065), was used to assess the electrophysiological effects of murine adipose tissue conditioned media. HL-1 cells were cultured and seeded on MEAs as previously described (12). Briefly, HL-1 cells were cultured in Claycomb media (51800C; Sigma) supplemented with 10% fetal bovine serum (A3160601; ThermoFisher), penicillin/streptomycin (100 U/mL/100 µg/mL, 15140122; Thermo- Fisher), norepinephrine (0.1 mM, A0937; Sigma), ascorbic acid (0.3 mM, A7631; Sigma), and L-glutamine (2 mM, 25030081; Thermo- Fisher) and were maintained as per the manufacturer's instructions. For MEA experiments, 70,000 cardiomyocytes were seeded as a droplet on gelatin- and/or fibronectin-coated MEAs [0.02% gelatin, G9391 (Sigma); 0.5 µg/mL fibronectin, F1141 (Sigma)]. After 48 hrs culture on MEAs, the HL-1 cell media was

replaced with murine pericardial and inguinal subcutaneous adipose tissue conditioned media [50% dilution in Dulbecco's Modified Eagle Medium + GlutaMAX (ThermoFisher, 10565-042), supplemented with: 10% fetal bovine serum (A3160601; ThermoFisher), pyruvic acid (3 mM, Sigma, P-8574), bovine serum albumin (2 g/L, Sigma, A-7030), ampicillin (100 µg/ml, Sigma, A-0166), insulin-transferrin-selenium 100x (ThermoFisher, 41400045), antibiotic/antimycotic (1%, ThermoFisher, 15240062), linoleic acid (5 µg/ml, Sigma, L5900) and ascorbic acid (100 µM, Sigma, A4544)] or adipose-free DMEM control. Cells were cultured on MEAs for a further 24 hours and field potential characteristics recorded. HL-1 cultures exhibiting spontaneous beating rates in excess of 200 beats per minute were excluded from analysis.

ELECTROPHYSIOLOGY RECORDINGS. Extracellular electrophysiological field potentials were recorded from spontaneously beating cardiomyocyte cultures using the MEA2100 system (Multichannel Systems, Reutlingen, Germany) maintained at 37°C. Field potential recordings were acquired using Cardio2D+ software (Multichannel Systems) sampling at 10 kHz (low pass filter: 3,500 Hz, high pass filter: 10 Hz), and electrophysiological parameters calculated as previously described (12). Briefly, 10 consecutive field potentials were ensemble averaged. Mean field potential duration for each MEA was calculated by averaging ensembled signals across 5-10 electrodes. Delay in activation between neighboring electrodes was computed using a multivector approach, and mean conduction velocity was calculated on a beat-beat basis. Conduction velocity was then averaged across 10 consecutive beats for each MEA. All analysis was performed using Cardio2D+, and arrhythmic cultures were excluded.

MOUSE ADIPOSE TISSUE CONDITIONED MEDIA PROTEOMICS. Conditioned media samples prepared in a protein-free media were subjected to proteomic analysis by liquid chromatography mass spectrometry/mass spectrometry (LC-MS/MS). Briefly, conditioned media were filtered in spin filters (Amicon Ultra-4; Sigma-Aldrich, Castle Hill, Australia) to remove cellular debris and non-protein material from samples prior to reduction with a solution of 10 mM tris(2-carboxyethyl)phosphine (Sigma-Aldrich, Castle Hill, Australia). Reduced samples underwent filter-aided sample preparation (FASP) and trypsin digestion (1 ug/100 ug protein). Following acidification with formic acid (pH 3.0), samples were simultaneously desalted, concentrated and purified using C18 Ziptips (Millipore; Sigma-Aldrich, Castle Hill, Australia). Samples were dried down with an Eppendorf Concentrator Plus (Macquarie Park, Australia), stored at -20°C and then reconstituted in 0.1% formic acid prior to mass spectrometric analysis. Peptides were analysed on an QExactive Hybrid Quadrupole-Orbitrap Mass Spectrometer coupled to a Vanquish UHPLC (Thermo Fisher Scientific; Scoresby, Australia). For both analyses at positive and negative ionization mode, each sample was injected into an Accucore C30 column (2.1 × 250 mm, 2.6 µm; Thermo Fisher Scientific).

For protein quantification, MS/MS spectra were matched against UniProt mouse reference protein database and calculated using the MaxQuant search engine Andromeda (13). Label free quantification (LFQ) was performed (13) and 'no number assigned' values were imputed to complete a normal distribution in Perseus prior to t-tests, false discovery rate exclusion and visualisation in Perseus software (Max Planck Institute).

Secreted proteins detected were visualised on a volcano plot and proteins exhibiting significant differences ($P < 0.05$) in abundance comparing tissue types represented.

Pericardial samples (compared with inguinal subcutaneous) had 246 proteins of higher abundance, and 22 proteins of lower abundance. These data were clustered on a heatmap to reveal depot-specific differences and sample-specific secretome profiles. Proteins with the largest differential in abundance were listed in rank order. The group of highest abundance in pericardial (vs inguinal subcutaneous) adipose tissue were primarily metabolic proteins (and lowest were more varied), suggesting pericardial adipose tissue has more mobile metabolically active proteins.

Further characterization of the more abundant proteins released from pericardial adipose tissue was undertaken (vs inguinal, $P < 0.05$), performing Gene Ontology (GO) analysis (Enrichr) to identify cellular components most implicated (14,15). Of particular novel importance, proteins linked with focal adhesion functionality (GO:0005925) were most represented – proteins known to regulate intermyocyte connectivity and gap junction structure. In relation to GO analysis of biological processes, proteins associated with cellular responses to interleukin-12 (IL-12; GO:0071349) were highly represented, indicating a novel role for this inflammatory pathway in the heart.

STATISTICAL ANALYSES. For clinical data analysis, normally distributed variables are presented as mean ± standard deviation, and non-normally distributed variables are presented as median (inter-quartile range). Normality was assessed using the Shapiro-Wilk test. Independent Student's t-test, one-way analysis of variance and Mann-Whitney U tests were used to compare variables between groups as appropriate. The paired Student's t-test was used to compare within patient changes across mapped rhythms (600 ms/300 ms) of plaque activation times and conduction heterogeneity. Proportions were compared using the chi-squared test. The relationship between continuous variables were evaluated using Spearman's

correlation. Cell culture experiments were analysed using unpaired t Student's t-test or one-way ANOVA with post hoc Fisher's LSD tests, where appropriate. A P-value < 0.05 was considered statistically significant. Tests were performed with SPSS (Version 23, NY, USA), GraphPad Prism (Version 8.0), Perseus (Version 1.6.0.7) or Enrichr where appropriate.

REFERENCES

1. Mitchell C, Rahko PS, Blauwet LA et al. Guidelines for Performing a Comprehensive Transthoracic Echocardiographic Examination in Adults: Recommendations from the American Society of Echocardiography. J Am Soc Echocardiogr 2018.
2. Eijsbouts SC, Houben RP, Blaauw Y, Schotten U, Allessie MA. Synergistic action of atrial dilation and sodium channel blockade on conduction in rabbit atria. J Cardiovasc Electrophysiol 2004;15:1453-61.
3. Eijsbouts SC, Majidi M, van Zandvoort M, Allessie MA. Effects of acute atrial dilation on heterogeneity in conduction in the isolated rabbit heart. J Cardiovasc Electrophysiol 2003;14:269-78.
4. Lammers WJ, Schalij MJ, Kirchhof CJ, Allessie MA. Quantification of spatial inhomogeneity in conduction and initiation of reentrant atrial arrhythmias. Am J Physiol 1990;259:H1254-63.
5. Rostock T, Rotter M, Sanders P et al. High-density activation mapping of fractionated electrograms in the atria of patients with paroxysmal atrial fibrillation. Heart Rhythm 2006;3:27-34.
6. Mahajan R, Lau DH, Brooks AG et al. Electrophysiological, Electroanatomical, and Structural Remodeling of the Atria as Consequences of Sustained Obesity. J Am Coll Cardiol 2015;66:1-11.
7. McCloy RA, Rogers S, Caldon CE, Lorca T, Castro A, Burgess A. Partial inhibition of Cdk1 in G 2 phase overrides the SAC and decouples mitotic events. Cell Cycle 2014;13:1400-12.
8. Abukar Y, Ramchandra R, Hood SG et al. Increased cardiac sympathetic nerve activity in ovine heart failure is reduced by lesion of the area postrema, but not lamina terminalis. Basic Res Cardiol 2018;113:35.

9. Anderson DJ, Kaplan DI, Bell KM et al. NKX2-5 regulates human cardiomyogenesis via a HEY2 dependent transcriptional network. Nat Commun 2018;9:1373.
10. Costa M, Dottori M, Sourris K et al. A method for genetic modification of human embryonic stem cells using electroporation. Nat Protoc 2007;2:792-6.
11. Elliott DA, Braam SR, Koutsis K et al. NKX2-5(eGFP/w) hESCs for isolation of human cardiac progenitors and cardiomyocytes. Nat Methods 2011;8:1037-40.
12. Wells SP, Waddell HM, Sim CB et al. Cardiomyocyte functional screening: interrogating comparative electrophysiology of high-throughput model cell systems. Am J Physiol Cell Physiol 2019;317:C1256-C1267.
13. Cox J, Mann M. MaxQuant enables high peptide identification rates, individualized p.p.b.-range mass accuracies and proteome-wide protein quantification. Nat Biotechnol 2008;26:1367-72.
14. Chen EY, Tan CM, Kou Y et al. Enrichr: interactive and collaborative HTML5 gene list enrichment analysis tool. BMC Bioinformatics 2013;14:128.
15. Kuleshov MV, Jones MR, Rouillard AD et al. Enrichr: a comprehensive gene set enrichment analysis web server 2016 update. Nucleic Acids Res 2016;44:W90-7.

ONLINE APPENDIX – SUPPPLEMENTARY RESULTS

Supplementary Table 1. High abundance proteins relating to '*focal adhesion*' (GO:0005925) released from pericardial adipose tissue (vs inguinal)

Abbreviation	Protein name	Difference	P-value
1433Z	14-3-3 protein zeta/delta	0.57	1.57E-03
ACTN1	Alpha-actinin-1	3.11	2.79E-05
ACTN4	Alpha-actinin-4	1.23	3.52E-04
AMPL	Cytosol aminopeptidase	2.94	2.00E-03
ANXA5	Annexin A5	2.86	1.94E-02
ARF1	ADP-ribosylation factor 1	2.67	1.36E-03
ARPC3	Actin-related protein 2/3 complex subunit 3	2.05	5.00E-04
CAP1	Adenylyl cyclase-associated protein 1	1.99	2.21E-02
CLH1	Clathrin heavy chain 1	3.23	1.60E-03
ENPL	Endoplasmin	1.07	1.69E-02
EZRI	Ezrin	2.34	2.09E-03
FLNA	Filamin-A	3.77	1.01E-03
FLNB	Filamin-B	3.52	4.67E-04
GRP75	Stress-70 protein, mitochondrial	2.89	3.99E-03
HNRPK	Heterogeneous nuclear ribonucleoprotein K	3.67	1.01E-04
HSPB1	Heat shock protein beta-1	2.41	1.20E-02
IQGA1	Ras GTPase-activating-like protein IQGAP1	2.75	2.74E-03
NPM	Nucleophosmin	4.93	1.02E-05
PABP1	Polyadenylate-binding protein 1	1.99	7.07E-03
PARVA	Alpha-parvin	2.47	7.62E-03
PDC6I	Programmed cell death 6-interacting protein	3.73	8.79E-08
PLSL	Plastin-2 (LCP1)	2.46	1.73E-03
RL5	60S ribosomal protein L5	2.30	2.47E-05
RL12	60S ribosomal protein L12	2.81	1.55E-04
RLA0	60S acidic ribosomal protein P0	2.66	6.00E-06
RLA1	60S acidic ribosomal protein P1	3.00	8.64E-03
RLA2	60S acidic ribosomal protein P2	3.90	3.53E-04
RS2	40S ribosomal protein S2	1.51	6.76E-03
RS4X	40S ribosomal protein S4	1.55	8.52E-03
RS8	40S ribosomal protein S8	1.70	2.02E-02
RSU1	Ras suppressor protein 1	3.27	6.03E-05
TLN1	Talin-1	2.46	3.68E-06
TPM4	Tropomyosin alpha-4 chain	2.61	1.15E-03
TWF1	Twinfilin-1	1.96	2.69E-02
VIME	Vimentin	1.10	1.10E-04

Supplementary Table 2. High abundance proteins relating to '*cellular response to interleukin-12*' (GO:0071349) released from pericardial adipose tissue (vs inguinal)

Abbreviation	Protein name	Difference	P-value
ARF1	ADP-ribosylation factor 1	2.67	1.36E-03
CAZA1	F-actin-capping protein subunit alpha-1	1.84	2.19E-02
GRP75	Stress-70 protein, mitochondrial	2.89	3.99E-03
GSTO1	Glutathione S-transferase omega-1	2.50	4.09E-03
HNRPF	Heterogeneous nuclear ribonucleoprotein F	2.87	8.38E-03
MIF	Macrophage migration inhibitory factor	1.71	1.18E-04
PLSL	Plastin-2 (LCP-1)	2.46	1.73E-03
PSME2	Proteasome activator complex subunit 2	4.02	6.44E-09
RAP1B	Ras-related protein Rap-1A	2.33	2.01E-02
RLA0	60S acidic ribosomal protein P0	2.66	6.00E-06
ROA2	Heterogeneous nuclear ribonucleoproteins A2/B1	1.22	2.46E-05
TALDO	Transaldolase	3.94	4.19E-05
TCPA	T-complex protein 1 subunit alpha	3.39	1.69E-07

Chapter 6

Male and female atria exhibit distinct acute electrophysiological responses to sex steroids

Manuscripts generated from this chapter:

Wells SP, O'Shea C, …, Kirchhof P, Pavlovic D, Delbridge LMD and Bell JR. Male and female atria exhibit distinct acute electrophysiological responses to sex steroids. **In preparation**.

Research article

Male and female atria exhibit distinct acute electrophysiological responses to sex steroids

Wells SP[1,2]; O'Shea C[2]; …; Kirchhof P[2,3]; Pavlovic D[2]; Delbridge LMD[1,*,#]; Bell JR[1,4,*,#]

[1]Department of Physiology, University of Melbourne, Parkville, Victoria, Australia, 3010

[2]Institute of Cardiovascular Sciences, University of Birmingham, Birmingham, United Kingdom, B15 2TT

[3]Department of Cardiology, University Heart and Vascular Center UKE Hamburg, Hamburg, Germany, 20251

[4]Department of Physiology, Anatomy & Microbiology, La Trobe University, Bundoora, Victoria, Australia, 3086

[*]LMD and JRB contributed equally to this work

[#]Correspondence: Cardiac Phenomics Laboratory, School of Biomedical Sciences

University of Melbourne, Victoria, Australia, 3010

Email address: [redacted] (L.M.D. Delbridge)

[redacted] (J.R. Bell)

Abstract

Background

Sex differences in ventricular electrophysiology are recognised clinically with experimental evidence implicating sex steroids as mediators. There is limited data exploring electrophysiological sexual dimorphism and sex steroid responsiveness in the atrium. The aim of this investigation was to determine electrophysiological differences in male and female left atria at baseline and in response to acute sex steroid exposure.

Methods

Left atria were isolated from male and female C57BL/6 age-matched mice and loaded with Di-4-ANEPPS. Optical mapping was used to assess action potential duration at 70% repolarisation (APD_{70}) and conduction velocity in atria acutely treated with: 0nM, 1nM and 100nM 17β-oestradiol or testosterone.

Results

Male and female left atria demonstrated similar baseline conduction velocity (male *vs* female: 53.8±4.8cm/s *vs* 45.7±3.0cm/s, *P*=ns) and APD_{70} (16.1±0.8ms *vs* 17.0±0.7ms, *P*=ns) – although APD_{70} spatial heterogeneity was significantly greater in females (2.1±0.2ms *vs* 3.1±0.3ms, *P*<0.05). Oestradiol prolonged APD_{70} in males (0nM *vs* 1nM: 14.7±0.9ms *vs* 16.6±1.1ms, *P*<0.05) and females (15.5±0.9ms *vs* 18.8±1.1ms, *P*<0.05). The extent of this was greater in females (ΔAPD_{70}, male *vs* female: 3.8±0.7 *vs* 6.0±0.7ms, *P*<0.05). 100nM oestradiol also slowed conduction velocity in both males (58.8±8.3cm/s *vs* 44.0±6.9cm/s, *P*<0.05) and females (45.0±2.5 *vs* 41.9±2.3, *P*<0.05), although the extent of this was greater in males (Δconduction velocity: -14.8±4.5cm/s *vs* -

4.3±1.5cm/s, $P<0.05$). Testosterone prolonged APD_{70} in males only (0nM *vs* 1nM *vs* 100nM: 17.4±1.4ms *vs* 22.1±1.3ms *vs* 24.9±1.4ms, $P<0.05$) and did not modulate conduction velocity (P=ns).

Conclusion

This is the first study to show that acute administration of oestrogen/testosterone rapidly modulates left atrial electrophysiology in a sexually dimorphic manner. These data are important, indicating that changes in systemic/intracardiac sex steroid synthesis/balance can cause sudden changes in atrial electrophysiology. Disruption of sex steroid balance might lead to pathological modulation of atrial electrophysiology (i.e. conduction slowing/repolarisation prolongation) to increase arrhythmia risk.

Keywords

Action potential duration ▪ Androgens ▪ Atrial electrophysiology ▪ Conduction velocity ▪ Oestrogen ▪ Oestradiol ▪ Sex steroids ▪ Testosterone

Abbreviations

APD, Action potential duration ▪ APD_{70}, Action potential duration at 70% repolarisation ▪ I_K, delayed rectifier currents ▪ I_{Kr}, rapid delayed rectifier current ▪ I_{Ks}, slow delayed rectifier current ▪ I_{to}, transient outward currents ▪ I_{Kur}, ultra-rapid delayed rectifier current

6.1 Background

Sex differences in cardiac electrophysiology are recognised clinically, with women demonstrating faster heart rates, longer rate-corrected Q-T intervals and steeper electrical restitution than men [1, 2]. These differences are, at least in part, mediated through acute/genomic actions of sex steroids on their respective receptors expressed throughout the myocardium [3]. Myocardial sex steroid receptor expression is comparable between sexes; however, males have approximately 10-fold higher circulating androgens and 10-fold lower circulating oestrogens than females – indicating sex steroid balance is an important factor mediating myocardial sex differences [4-6].

The lower incidence of cardiovascular disease in age-matched premenopausal women compared to men has led to the classical contention that oestrogens are cardioprotective. This is supported by the substantial increase in cardiovascular disease risk/severity post-menopause – a timepoint where systemic oestrogens decline [7, 8]. Contrarily, the Women's Health Initiative trial demonstrated oestradiol hormone replacement therapy increased atrial fibrillation risk in postmenopausal women, indicating the effects of sex steroids on the heart are not fully understood [9].

The cellular electrophysiological mechanisms underpinning atrial fibrillation involve heterogeneic prolongation/shortening of the cardiac action potential duration (APD) and/or conduction velocity slowing [10]. Pre-clinical data examining the effects of sex and sex steroids on atrial electrophysiology are distinctly lacking and ventricular data has failed to yield consensus, with various preparations/species showing similar and

different repolarisation times between sexes [11-16]. Greater insight into atrial electrophysiological sexual dimorphism and sex steroid responsiveness is needed.

We have recently reported pericardial adipose tissue expresses aromatase, indicating capacity to synthesise oestrogens from androgens to modulate sex steroids locally around the myocardium [17]. Clinically, pericardial adipose tissue accumulation is linked with increased atrial fibrillation risk [18, 19]. Evidence suggests release of factors from the adipose tissue exert paracrine influence on the surrounding myocardium that may increase vulnerability to atrial arrhythmias. We previously reported that increased pericardial adipose tissue aromatase expression was associated with greater arrhythmia vulnerability in isolated male mouse hearts. Also, isolated mouse hearts perfused with exogenous oestradiol exhibited increased atrial arrhythmia incidence [17]. This suggests that infiltration of pericardial adipose tissue into the atrial epicardium may lead to localised regions of oestrogenic influence, modulating atrial electrophysiology to increase atrial fibrillation vulnerability.

The aim of this investigation was to assess the actions of acute sex steroid treatment on male and female mouse left atrial electrophysiology.

6.2 Methods

Animal details

Mouse experiments were conducted under the Animals (Scientific Procedures) Act 1986 and approved by the Home Office and the institutional review board at the University of Birmingham. C57BL/6 male and female mice (details in **Supplementary table S6.1**) were housed in individually ventilated cages, under 12hr light/dark cycles (22^{o}C, 55% humidity). Chow and drinking water were available *ad libitum*.

Isolated left atrial optical mapping

Optical mapping experiments were performed as previously reported [20, 21] and a visual overview of the preparation and output measures are depicted in **Fig 6.1**. Hearts were rapidly excised from mice under deep anaesthesia (4% isoflurane in O_2, 3L/min) and retrogradely perfused on a Langendorff apparatus (4ml/min) with 37^{o}C Krebs-Henseleit buffer (in mM: NaCl, 118.0; KCl, 3.52; $MgSO_4 7H_2O$, 0.83; KH_2PO_4, 1.18; $NaHCO_3$, 24.90; glucose, 11.0; $CaCl_2$, 1.80; 95% O_2/5% CO_2). Hearts were loaded with Di-4-ANEPPS (5µM; Cambridge Biosciences, Cambridge, UK) via bolus injection into the perfusate over 5min. The left atrium was then resected, pinned flat onto the silicone base of an organ bath and continuously superfused with Krebs-Henseleit buffer + blebbistatin (60µM; 37^{o}C; 95% O_2/5% CO_2) to reduce motion artefacts.

Left atria were paced from the posterior wall using a 2ms bipolar pulse via platinum electrodes at twice the capture threshold. Di-4-ANEPPS was excited at 530nm by two twin LEDs (Cairn Research, Kent, UK). Emitted fluorescence (630nm) was captured at 1KHz using a high spatial resolution ORCA flash 4.0 camera (Hamamatsu Photonics,

Japan). Wide field macroscopic images of tissue sequentially paced at 120ms, 100ms and 80ms cycle lengths (100 pulses/cycle length) were acquired using WinFluor V3.4.9 at various recording timepoints.

After 10min of equilibration, a baseline recording was made at all cycle lengths, then 1nM 17β-oestradiol, testosterone, or vehicle (0.0001% ethanol) introduced into the superfusate. After 10min, a second recording was made, then the superfusate changed to buffer containing either 100nM oestradiol, testosterone, or vehicle (0.01% ethanol). A final recording at all cycle lengths was made 10min thereafter.

Optical mapping analysis

Optical mapping data were analysed using ElectroMap [20, 22]. Ensemble averaging of the last 10 beats of each cycle length was used to assess conduction velocity and APD at 70% repolarisation (APD_{70}) across the whole left atrium. Images at these specific beats were spatially and temporally filtered with a 4x4 Gaussian filter and a 3rd order Savitzky-Golay filter, respectively. Non-physiological baseline deviations were corrected for using a Top-Hat filter (100ms). APD_{70} spatial heterogeneity was defined as the standard deviation of the mean APD_{70} measure across a whole left atrium.

Statistical analysis

All data are presented as mean ± standard error and were analysed blinded. Statistical analyses were performed in GraphPad Prism 8.4 and are indicated in the Figure legends throughout. $P<0.05$ was deemed significant and *n* denotes the number of mice. In Figures, #, * and † indicate $P<0.05$ cycle length effect, treatment effect (0nM *vs* 1nM or 100nM, at all cycle lengths) and sex difference, respectively.

6.3 Results

Male and female left atria have similar basal electrophysiology

Male mice were significantly heavier than age-matched females (36.6±1.0g *vs* 29.0±0.9g, *P*<0.05; **Supplementary Table S6.1**). Males also had larger hearts (153.4±11.3mg *vs* 111.8±3.3mg, *P*<0.05), a trend for larger left atria (3.8±0.4mg *vs* 3.0±0.2mg, *P*=0.09) and comparable heart weight:body weight (*P*=ns). Neither body weight or left atrial weight correlated with basal APD_{70} or conduction velocity (**Supplementary Fig S6.1**).

Although all hearts were loaded with the same volume and concentration of Di-4-ANEPPS, we noticed some hearts were more receptive than others, emitting a greater level of baseline fluorescence. Di-4-ANEPPS can slow conduction velocity [23], so we wanted to ensure that dye uptake was equal between sexes. Baseline emitted fluorescence (used here as a surrogate measure of dye uptake) was similar in male and female atria (**Supplementary Fig S6.2A**). APD_{70} was unaffected by variations in dye uptake; however, conduction velocity negatively correlated with Di-4-ANEPPS uptake (**Supplementary Fig S6.2B & C**).

Mean whole left atrial APD_{70} was not significantly different between males and females (100ms cycle length, male *vs* female: 16.1±0.8ms *vs* 17.0±0.7ms, *P*=ns; **Fig 6.2A-C**) and both sexes exhibited APD_{70}-rate dependency (**Fig 6.2C**). Females demonstrated more variability in APD_{70} across the left atrium than males (2.1±0.2ms *vs* 3.1±0.3ms, *P*<0.05; **Fig 6.2B & D**). Conduction velocity was consistent between sexes (53.8±4.8cm/s *vs* 45.7±3.0cm/s, *P*=ns; **Fig 6.2E & F**).

Acute oestradiol prolongs repolarisation and slows conduction in a sexually dimorphic manner

To examine the acute electrophysiological responsiveness of the left atrium to sex steroids, subsets of atria were acutely exposed to 1nM (physiological range) or 100nM of either 17β-oestradiol, testosterone, or vehicle (ethanol; 0.0001% or 0.01%). Vehicle did not modulate left atrial APD_{70} or conduction velocity (**Supplementary Fig S5.3A-D**). Both 1nM and 100nM oestradiol prolonged male and female left atrial APD_{70} across all paced cycle lengths (100ms cycle length, 0nM *vs* 1nM, male: 14.7±0.9ms *vs* 16.6±1.1ms; female: 15.5±0.9ms *vs* 18.8±1.1ms; $P<0.05$; **Fig 6.3A-D**). This effect was of similar magnitude between sexes treated with 1nM oestradiol, but significantly greater in females than males treated with 100nM (ΔAPD_{70}: 3.8±0.7 *vs* 6.0±0.7ms, $P<0.05$; **Fig 6.3E**). Male APD_{70} spatial heterogeneity was unaffected by oestradiol treatment (**Fig 6.3F**); however, female left atrial spatial heterogeneity was significantly increased at 1nM and 100nM (0nM *vs* 1nM *vs* 100nM: 2.2±0.4ms *vs* 3.2±0.5ms *vs* 3.7±0.5ms, $P<0.05$; **Fig 6.3G**).

1nM oestradiol did not significantly change male or female left atrial conduction velocity (**Fig 6.4A-C**); however, 100nM oestradiol slowed conduction velocity in both sexes (0nM *vs* 100nM, male: 58.8±8.3cm/s *vs* 44.0±6.9cm/s; female: 45.0±2.5 *vs* 41.9±2.3, $P<0.05$; **Fig 6.4A-C**). This slowing in conduction was greater in male than female left atria treated with 100nM oestradiol (Δconduction velocity male *vs* female: -14.8±4.5cm/s *vs* -4.3±1.5cm/s, $P<0.05$; **Fig 6.4D**).

Acute testosterone modulates male, but not female left atrial electrophysiology

Acute exposure to 1nM and 100nM testosterone prolonged male APD_{70} at all paced cycle lengths (100ms cycle length, 0nM *vs* 1nM *vs* 100nM: 17.4±1.4ms *vs* 22.1±1.3ms *vs* 24.9±1.4ms, $P<0.05$; **Fig 6.5A-C**), but females were unresponsive (P=ns; **Fig 6.5A, B & D**). Testosterone did not modulate male or female APD_{70} spatial heterogeneity (P=ns; **Fig 6.5E & F**). Conduction velocity in both sexes was also unaffected by acute testosterone treatment (P=ns, **Fig 6.6A-C**).

6.4 Discussion

This is the first study to demonstrate that sex steroids can rapidly modulate left atrial conduction and repolarisation in a sexually dimorphic manner (see **Table 5.1** for summary). No differences were detected in basal left atrial conduction and APD_{70} between males and females (**Fig 6.2C & F**), though greater female repolarisation heterogeneity (*vs* males) was evident (**Fig 6.2D**). Oestradiol prolongs atrial repolarisation to a greater extent in females but slows conduction velocity more in males. Testosterone prolongs male repolarisation but does not modulate female left atrial electrophysiology. These data indicate that changes in sex steroid concentration can rapidly modulate atrial electrophysiology through a non-transcriptional mechanism.

Male and female left atria demonstrate similar basal electrophysiology

There is a distinct lack of literature assessing atrial electrophysiological sexual dimorphism. Wen-Chin *et al*. demonstrated no sex difference in APD between male and female isolated rabbit left atrial cardiomyocytes paced at long cycle lengths [24]; however, pacing intact left atria at physiological rates revealed a male APD longer than female [25]. Our data demonstrate male and female mouse left atria exhibit similar repolarisation times at physiological pacing frequencies (**Fig 6.2A-C**). There are several potential explanations as to why no APD sex difference was seen in our investigation. Wen-Chin *et al*. used traditional microelectrode methodology for their experiments, recording from a single site across the large rabbit atrium [25]. Optical mapping approaches used here revealed that APD varies significantly across the small female mouse left atrium (**Fig 6.2B & D**), indicating the latter finding of Wen-Chin *et al*. might be an artefact of microelectrode positioning. Species differences in electrophysiological

repolarisation reserve might also explain the discrepancy between investigations. Mouse atrial action potentials have little-to-no repolarisation plateau phase due to a greater contribution of the transient outward currents (I_{to}), and lesser contribution of the delayed rectifier currents (I_K) compared to rabbits and larger mammals [26, 27].

The novel finding that female left atrial epicardial repolarisation is more variable than male is interesting. The underlying cellular mechanisms and physiological relevance of this are not clear. Although there is no data for the mouse atria, in the ventricle, $I_{to,}$ and the ultra-rapid component of the delayed rectifier current (I_{Kur}) is uniform between sexes [28, 29]. It could be that distribution of these channels is not uniform across the atrial epicardium. Indeed, greater transmural heterogeneities in repolarisation times and L-type Ca^{2+} currents have been demonstrated in female ventricles compared to the male [16, 30].

Oestradiol prolongs repolarisation in the male and female left atrium

Low and high dose oestradiol prolonged APD in both sexes, although prolongation was significantly more pronounced in females (**Fig 6.3A-E**). There is limited literature examining the effects of oestradiol on atrial electrophysiology and conflicting results in ventricular tissue with data demonstrating oestradiol-induced APD shortening [31, 32], prolongation [32-34] or no effect [35]. In part, this may be a result of a biphasic concentration-dependent effect [32], but also inconsistencies between studies, with varying treatment durations/concentrations, paced cycle lengths, and historical poor reporting on sex. Supraphysiological concentrations of oestradiol (1-30μM) prolong APD in male mouse ventricular cardiomyocytes through reducing I_{to} and L-type Ca^{+} currents [34]. Data from ovariectomised mice indicate that oestrogens negatively regulate

ventricular I_{to} via oestrogen receptor α [36]. Together, these ventricular studies indicate that the atrial APD prolongation we demonstrate might be mediated through inhibition of I_{to}, via oestradiol interactions with oestrogen receptor α.

Kurokawa *et al.* have shown that 1nM oestradiol prolongs male and female guinea pig ventricular APD through direct inhibition of $K_V11.1$ (carries the rapid delayed rectifier current, I_{Kr}) [32]. I_{Kr} contributes only a small amount to mouse atrial repolarisation, so this direct oestradiol-$K_V11.1$ interaction likely plays a smaller role than that of I_{to} in the atrial data we present [26, 27]. Contrasting with Kurokawa *et al.*, higher concentrations of oestradiol in the present study did not shorten APD. 100-300nM oestradiol induced APD shortening through enhancing the slow delayed rectifier current (I_{Ks}) and suppressing L-type Ca^{2+} currents [32]. Besides potential chamber-specific responses to oestradiol, this discrepancy may be because the mouse exhibits almost negligible I_{Ks} and substantially smaller L-type Ca^{2+} currents than larger species [26, 27]. Also, oestradiol increased female atrial APD heterogeneity (**Fig 6.3G**). This means various populations of cardiomyocytes possibly exhibited APD: shortening, no change or prolongation, masking effects of specific cardiomyocyte populations.

It is interesting that females, who typically have 10-fold higher circulating oestrogens (*vs* males), had greater basal APD heterogeneity (**Fig 6.2D**) and this was further increased by exogenous oestradiol (**Fig 6.3G**). This potentially indicates non-uniform I_{to}, I_{Kr} and oestrogen receptor α expression in the female atrial epicardium, although the physiological relevance is not clear [32, 34, 36].

Oestradiol slows conduction velocity in the male and female left atrium

There is limited evidence comparing male and female atrial conduction velocity. Here, we demonstrate for the first time that it is similar between sexes (**Fig 6.2E & F**), indicating the electrophysiological factors which dictate conduction (gap junction coupling and $Na_V1.5$ function) are similar between sexes. 100nM oestradiol slowed conduction velocity in both sexes, but the effect was significantly more pronounced in males (**Fig 6.4**). Conduction slowing has been seen in right atrial electrograms of (post-)menopausal women acutely receiving oestradiol, but the cellular interactions between oestradiol and the conduction system have not been extensively investigated. Acute oestradiol (3.3nM) does not influence maximal action potential amplitude (a conduction velocity determinant) in rabbit ventricular tissue [35]. This is consistent with our absence of an effect on conduction with 1nM oestradiol.

Oestradiol-induced conduction slowing, and repolarisation prolongation are both potentially pro-arrhythmic, increasing the risk of reentrant and triggered arrhythmias, respectively. This finding has important implications for those taking oestradiol in transgender or post-menopause hormone replacement therapy, particularly where evidence already indicates increased risk of atrial fibrillation and associated stroke [9, 37]. This might also provide further mechanistic link between the established association of augmented pericardial adiposity and elevated atrial fibrillation risk [18, 19]. Pericardial adipose tissue has capacity to synthesise oestrogens which may be released locally to exert paracrine effects on the atrial myocardium [17]. In mice, pericardial adipose tissue aromatase content associates with the degree of arrhythmia vulnerability and acute oestradiol increases arrhythmia incidence [17]. In areas of fibro-

fatty infiltration into the atrial epicardium, we hypothesise that there are micro-regions of highly concentrated oestradiol (100nM). It is therefore feasible that pericardial adipose-derived oestrogens exert a paracrine effect on localised regions of the atria, causing a non-uniform slowing of conduction/repolarisation prolongation that could lead to the re-entrant pathways that culminate in atrial fibrillation.

Testosterone prolongs male left atrial repolarisation, but does not modulate female electrophysiology

The acute effects of testosterone on atrial electrophysiology have not been previously investigated. We report that females do not exhibit an acute electrophysiological response to testosterone, whilst males demonstrate pronounced APD prolongation. Evidence from guinea pig cardiomyocytes and SH-SY5Y cells identifies that testosterone inhibits I_{Kr} through androgen receptor-mediated phosphoinositide 3-kinases signalling and this may similarly prolong APD [32, 38]. Whilst males and females express comparable levels of the androgen receptor in the atrium [5], evidence suggests greater receptor activity in the male heart [39]. Testosterone supplementation post-castration can prolong ventricular APD [40]. Others have shown ventricular cardiomyocyte APD shortening in response to acute testosterone - an effect driven through androgen receptor-regulated I_{Ks} enhancement and L-type Ca^{2+} current inhibition in the guinea pig [41]. The discrepancy between our findings and this report could be due to several factors, including pacing frequency, species differences, but also the limited contribution of I_{Ks} to atrial *vs* ventricular repolarisation [42].

It is interesting that females do not possess a rapid electrophysiological response to testosterone. Taking this together with the potentially pro-arrhythmic effects of oestradiol, indicates that inhibition of oestradiol synthesis (i.e. aromatase inhibition) may be beneficial in females with atrial fibrillation, as there are no detrimental consequences of the inevitable testosterone build up. In breast cancer patients, aromatase inhibitors associate with reduced torsade de pointes incidence than patients receiving oestrogen receptor blockade [43] – likely because oestradiol can modulate repolarisation independent of oestrogen receptors [32]. In males, the situation is more complex and use of aromatase inhibitors may not be so beneficial.

Perspectives and significance

In summary, this is the first evidence that sex steroids can rapidly modulate atrial electrophysiology. Although male and female basal atrial electrophysiology is similar, acute responsiveness to sex steroids is sexually dimorphic. Data here indicate changes in sex steroid concentration/balance may be pro-arrhythmic, prolonging atrial repolarisation and slowing conduction. This is an important consideration for scenarios where steroid levels are altered (e.g. with age, menopause, medications). The absence of a testosterone response in females indicates value in exploring the antiarrhythmic potential of oestrogen synthesis inhibition in female atrial fibrillation patients. Future investigations should explore the signalling mechanisms mediating these rapid electrophysiological responses to sex steroids in the atrium.

6.5 Conclusions

We conclude that male and female left atrial electrophysiology can be rapidly modulated by sex steroids through a non-transcriptional mechanism. The effects of sex steroids are sexually dimorphic with female atria lacking responsiveness to testosterone but showing greater repolarisation prolongation in response to oestradiol (*vs* males). Males show greater oestradiol-induced conduction slowing than females. These data are important, indicating that changes in systemic/intracardiac sex steroid concentration/balance can cause sudden changes in atrial electrophysiology. Disruption of sex steroid balance (i.e. through alterations in systemic or intracardiac synthesis) might lead to pathological modulation of atrial electrophysiology to increase atrial fibrillation risk.

6.6 Declarations

Ethics approval and consent to participate

Mouse experiments were conducted under the Animals (Scientific Procedures) Act 1986 and approved by the Home Office and the institutional review board at the University of Birmingham.

Consent for publication

All authors provide consent for publication.

Availability of data and materials

The datasets used and/or analysed during the current study are available from the corresponding author on reasonable request.

Competing interests

PK receives research support from several drug and device companies active in atrial fibrillation and has received honoraria from several such companies. PK is also listed as an inventor on two patents held by University of Birmingham (Atrial Fibrillation Therapy WO 2015140571, Markers for Atrial Fibrillation WO 2016012783). All other authors declare no potential conflict of interest.

Funding

This research was supported by the National Health and Medical Research Council (nos. 1099352 and 1125453; L.M.D. Delbridge, J.R. Bell), the Australian Research Council (no. DP160102404; L.M.D. Delbridge), Wellcome Trust Seed Award Grant (109604/Z/15/Z, to DP) and British Heart Foundation Grants (PG/17/55/33087, RG/17/15/33106, to DP).

Authors' contributions

SPW, JRB, LMD, DP and PK conceived and designed the research. SPW performed the experiments with assistance from COS. Analysis was performed by SPW and COS, with interpretation by SPW and JRB. SPW prepared the Figures and drafted the manuscript. SPW, COS, PK, DP, LMD and JRB reviewed and approved the final manuscript version.

Acknowledgements

Assistance with animal cohort management and experimental blinding from Clara Apicella and Syeeda Nashitha Kabir is gratefully acknowledged.

6.7 References

1. Rautaharju PM, Zhou SH, Wong S, Calhoun HP, Berenson GS, Prineas R, et al. Sex differences in the evolution of the electrocardiographic QT interval with age. Canadian Journal of Cardiology. 1992;8:7:690-5.

2. Malik M, Hnatkova K, Kowalski D, Keirns JJ, van Gelderen EM. QT/RR curvatures in healthy subjects: sex differences and covariates. Am J Physiol Heart Circ Physiol. 2013;305:12:H1798-806; doi:10.1152/ajpheart.00577.2013.

3. Menazza S, Murphy E. The Expanding Complexity of Estrogen Receptor Signaling in the Cardiovascular System. Circ Res. 2016;118:6:994-1007; doi:10.1161/circresaha.115.305376.

4. Carmina E, Lobo RA. Evaluation of Hormonal Status. In: Strauss JF, Barbieri RL, editors. Yen & Jaffe's Reproductive Endocrinology (Sixth Edition). Philadelphia: W.B. Saunders; 2009. p. 801-23. doi:10.1016/B978-1-4160-4907-4.00032-2.

5. Lizotte E, Grandy SA, Tremblay A, Allen BG, Fiset C. Expression, distribution and regulation of sex steroid hormone receptors in mouse heart. Cell Physiol Biochem. 2009;23:1-3:75-86; doi:10.1159/000204096.

6. Bell JR, Bernasochi GB, Varma U, Raaijmakers AJ, Delbridge LM. Sex and sex hormones in cardiac stress--mechanistic insights. J Steroid Biochem Mol Biol. 2013;137:124-35; doi:10.1016/j.jsbmb.2013.05.015.

7. Go AS, Hylek EM, Phillips KA, Chang Y, Henault LE, Selby JV, et al. Prevalence of Diagnosed Atrial Fibrillation in AdultsNational Implications for Rhythm Management and Stroke Prevention: the AnTicoagulation and Risk Factors In Atrial Fibrillation (ATRIA) Study. JAMA. 2001;285:18:2370-5; doi:10.1001/jama.285.18.2370.

8. Iorga A, Cunningham CM, Moazeni S, Ruffenach G, Umar S, Eghbali M. The protective role of estrogen and estrogen receptors in cardiovascular disease and the controversial use of estrogen therapy. Biol Sex Differ. 2017;8:1:33-; doi:10.1186/s13293-017-0152-8.

9. Perez MV, Wang PJ, Larson JC, Virnig BA, Cochrane B, Curb JD, et al. Effects of postmenopausal hormone therapy on incident atrial fibrillation: the Women's Health Initiative randomized controlled trials. Circ Arrhythm Electrophysiol. 2012;5:6:1108-16; doi:10.1161/circep.112.972224.

10. Heijman J, Guichard J-B, Dobrev D, Nattel S. Translational Challenges in Atrial Fibrillation. Circ Res. 2018;122:5:752-73; doi:10.1161/circresaha.117.311081.

11. Linde C, Bongiorni MG, Birgersdotter-Green U, Curtis AB, Deisenhofer I, Furokawa T, et al. Sex differences in cardiac arrhythmia: a consensus document of the European Heart Rhythm Association, endorsed by the Heart Rhythm Society and Asia Pacific Heart Rhythm Society. EP Europace. 2018;20:10:1565-ao; doi:10.1093/europace/euy067.

12. Wells SP, Waddell HM, Sim CB, Lim SY, Bernasochi GB, Pavlovic D, et al. Cardiomyocyte functional screening: interrogating comparative electrophysiology of high-throughput model cell systems. Am J Physiol Cell Physiol. 2019;317:6:C1256-c67; doi:10.1152/ajpcell.00306.2019.

13. Zhu Y, Ai X, Oster RA, Bers DM, Pogwizd SM. Sex differences in repolarization and slow delayed rectifier potassium current and their regulation by sympathetic stimulation in rabbits. Pflugers Arch. 2013;465:6:805-18; doi:10.1007/s00424-012-1193-9.

14. Trépanier-Boulay V, St-Michel C, Tremblay A, Fiset C. Gender-based differences in cardiac repolarization in mouse ventricle. Circ Res. 2001;89:437-44; doi:10.1161/hh1701.095644.

15. Wu Y, Anderson ME. Reduced repolarization reserve in ventricular myocytes from female mice. Cardiovasc Res. 2002;53:3:763-9; doi:10.1016/s0008-6363(01)00387-x.

16. Xiao L, Zhang L, Han W, Wang Z, Nattel S. Sex-based transmural differences in cardiac repolarization and ionic-current properties in canine left ventricles. Am J Physiol Heart Circ Physiol. 2006;291:2:H570-H80; doi:10.1152/ajpheart.01288.2005.

17. Bernasochi GB, Boon WC, Curl CL, Varma U, Pepe S, Tare M, et al. Pericardial adipose and aromatase: A new translational target for aging, obesity and arrhythmogenesis? J Mol Cell Cardiol. 2017;111:96-101; doi:10.1016/j.yjmcc.2017.08.006.

18. Wong CX, Abed HS, Molaee P, Nelson AJ, Brooks AG, Sharma G, et al. Pericardial fat is associated with atrial fibrillation severity and ablation outcome. J Am Coll Cardiol. 2011;57:17:1745-51; doi:10.1016/j.jacc.2010.11.045.

19. Thanassoulis G, Massaro JM, O'Donnell CJ, Hoffmann U, Levy D, Ellinor PT, et al. Pericardial fat is associated with prevalent atrial fibrillation: the Framingham Heart Study. Circ Arrhythm Electrophysiol. 2010;3:4:345-50; doi:10.1161/circep.109.912055.

20. Holmes AP, Yu TY, Tull S, Syeda F, Kuhlmann SM, O'Brien S-M, et al. A Regional Reduction in Ito and IKACh in the Murine Posterior Left Atrial Myocardium Is Associated with Action Potential Prolongation and Increased Ectopic Activity. PLOS ONE. 2016;11:5:e0154077; doi:10.1371/journal.pone.0154077.

21. O'Shea C, Holmes AP, Yu TY, Winter J, Wells SP, Correia J, et al. ElectroMap: High-throughput open-source software for analysis and mapping of cardiac electrophysiology. Sci Rep. 2019;9:1:1389; doi:10.1038/s41598-018-38263-2.

22. O'Shea C, Holmes AP, Yu TY, Winter J, Wells SP, Parker BA, et al. High-Throughput Analysis of Optical Mapping Data Using ElectroMap. J Vis Exp. 2019:148; doi:10.3791/59663.

23. Larsen AP, Sciuto KJ, Moreno AP, Poelzing S. The voltage-sensitive dye di-4-ANEPPS slows conduction velocity in isolated guinea pig hearts. Heart Rhythm. 2012;9:9:1493-500; doi:10.1016/j.hrthm.2012.04.034.

24. Tsai W-C, Chen Y-C, Lin Y-K, Chen S-A, Chen Y-J. Sex Differences in the Electrophysiological Characteristics of Pulmonary Veins and Left Atrium and Their Clinical Implication in Atrial Fibrillation. Circ Arrhythm Electrophysiol. 2011;4:4:550-9; doi:doi:10.1161/CIRCEP.111.961995.

25. Tsai W-C, Chen Y-C, Kao Y-H, Lu Y-Y, Chen S-A, Chen Y-J. Distinctive sodium and calcium regulation associated with sex differences in atrial electrophysiology of rabbits. Int J Cardiol. 2013;168:5:4658-66; doi:10.1016/j.ijcard.2013.07.183.

26. Cordeiro JM, Spitzer KW, Giles WR. Repolarizing K+ currents in rabbit heart Purkinje cells. J Physiol. 1998;508 (Pt 3):Pt 3:811-23; doi:10.1111/j.1469-7793.1998.811bp.x.

27. Babij P, Askew GR, Nieuwenhuijsen B, Su CM, Bridal TR, Jow B, et al. Inhibition of cardiac delayed rectifier K+ current by overexpression of the long-QT syndrome HERG G628S mutation in transgenic mice. Circ Res. 1998;83:6:668-78; doi:10.1161/01.res.83.6.668.

28. Brouillette J, Rivard K, Lizotte E, Fiset C. Sex and strain differences in adult mouse cardiac repolarization: importance of androgens. Cardiovasc Res. 2005;65:1:148-57; doi:10.1016/j.cardiores.2004.09.012.

29. Brunet S, Aimond F, Li H, Guo W, Eldstrom J, Fedida D, et al. Heterogeneous expression of repolarizing, voltage-gated K+ currents in adult mouse ventricles. J Physiol. 2004;559:Pt 1:103-20; doi:10.1113/jphysiol.2004.063347.

30. Pham TV, Robinson RB, Danilo P, Jr., Rosen MR. Effects of gonadal steroids on gender-related differences in transmural dispersion of L-type calcium current. Cardiovasc Res. 2002;53:3:752-62; doi:10.1016/s0008-6363(01)00449-7.

31. Jiang C, Poole-Wilson PA, Sarrel PM, Mochizuki S, Collins P, MacLeod KT. Effect of 17 beta-oestradiol on contraction, Ca2+ current and intracellular free Ca2+ in guinea-pig isolated cardiac myocytes. Br J Pharmacol. 1992;106:3:739-45; doi:10.1111/j.1476-5381.1992.tb14403.x.

32. Kurokawa J, Tamagawa M, Harada N, Honda S, Bai CX, Nakaya H, et al. Acute effects of oestrogen on the guinea pig and human IKr channels and drug-induced prolongation of cardiac repolarization. J Physiol. 2008;586:12:2961-73; doi:10.1113/jphysiol.2007.150367.

33. Zhang Y, Hao YC, Song LL, Guo SM, Gu SZ, Lu SG. Effects of sex hormones on action potential and contraction of guinea pig papillary muscle. Zhongguo Yao Li Xue Bao. 1998;19:3:248-50.

34. Berger F, Borchard U, Hafner D, Pütz I, Weis TM. Effects of 17beta-estradiol on action potentials and ionic currents in male rat ventricular myocytes. Naunyn Schmiedebergs Arch Pharmacol. 1997;356:6:788-96; doi:10.1007/pl00005119.

35. Moller RA, Datta S, Strichartz GR. Beta-estradiol acutely potentiates the depression of cardiac excitability by lidocaine and bupivacaine. J Cardiovasc Pharmacol. 1999;34:5:718-27; doi:10.1097/00005344-199911000-00014.

36. El Gebeily G, El Khoury N, Mathieu S, Brouillette J, Fiset C. Estrogen regulation of the transient outward K+ current involves estrogen receptor α in mouse heart. J Mol Cell Cardiol. 2015;86:85-94; doi:10.1016/j.yjmcc.2015.07.013.

37. Nota NM, Wiepjes CM, Blok CJMd, Gooren LJG, Kreukels BPC, Heijer Md. Occurrence of Acute Cardiovascular Events in Transgender Individuals Receiving Hormone Therapy. Circulation. 2019;139:11:1461-2; doi:doi:10.1161/CIRCULATIONAHA.118.038584.

38. Ridley JM, Shuba YM, James AF, Hancox JC. Modulation by testosterone of an endogenous hERG potassium channel current. J Physiol Pharmacol. 2008;59:3:395-407.

39. Dart DA, Waxman J, Aboagye EO, Bevan CL. Visualising androgen receptor activity in male and female mice. PLOS ONE. 2013;8:8:e71694-e; doi:10.1371/journal.pone.0071694.

40. D'Antona G, Gualea MR, Ceriani T. Effects of Gonadectomy, Testosterone Replacement and Supplementation on Cardiac Action Potentials in the Rat. Basic Appl Myol. 2001;11:1:23-9.

41. Bai CX, Kurokawa J, Tamagawa M, Nakaya H, Furukawa T. Nontranscriptional regulation of cardiac repolarization currents by testosterone. Circulation. 2005;112:12:1701-10; doi:10.1161/circulationaha.104.523217.

42. Jost N. Transmembrane ionic currents underlying cardiac action potential in mammalian hearts. 2009. p. 1-45.

43. Barber M, Nguyen LS, Wassermann J, Spano JP, Funck-Brentano C, Salem JE. Cardiac arrhythmia considerations of hormone cancer therapies. Cardiovasc Res. 2019;115:5:878-94; doi:10.1093/cvr/cvz020.

6.8 Tables

Table 6.1 Summary of male and female left atrial electrophysiology at baseline and in response to sex steroids. ↑, ↓ and – indicate increase, decrease or no difference respectively between sexes or in response to sex steroid treatment.

	APD_{70}		APD_{70} heterogeneity		Conduction velocity	
	Male	Female	Male	Female	Male	Female
Basal	–	–	–	↑	–	–
Oestradiol	↑	↑↑	–	↑	↓↓	↓
Testosterone	↑	–	–	–	–	–

6.9 Figures

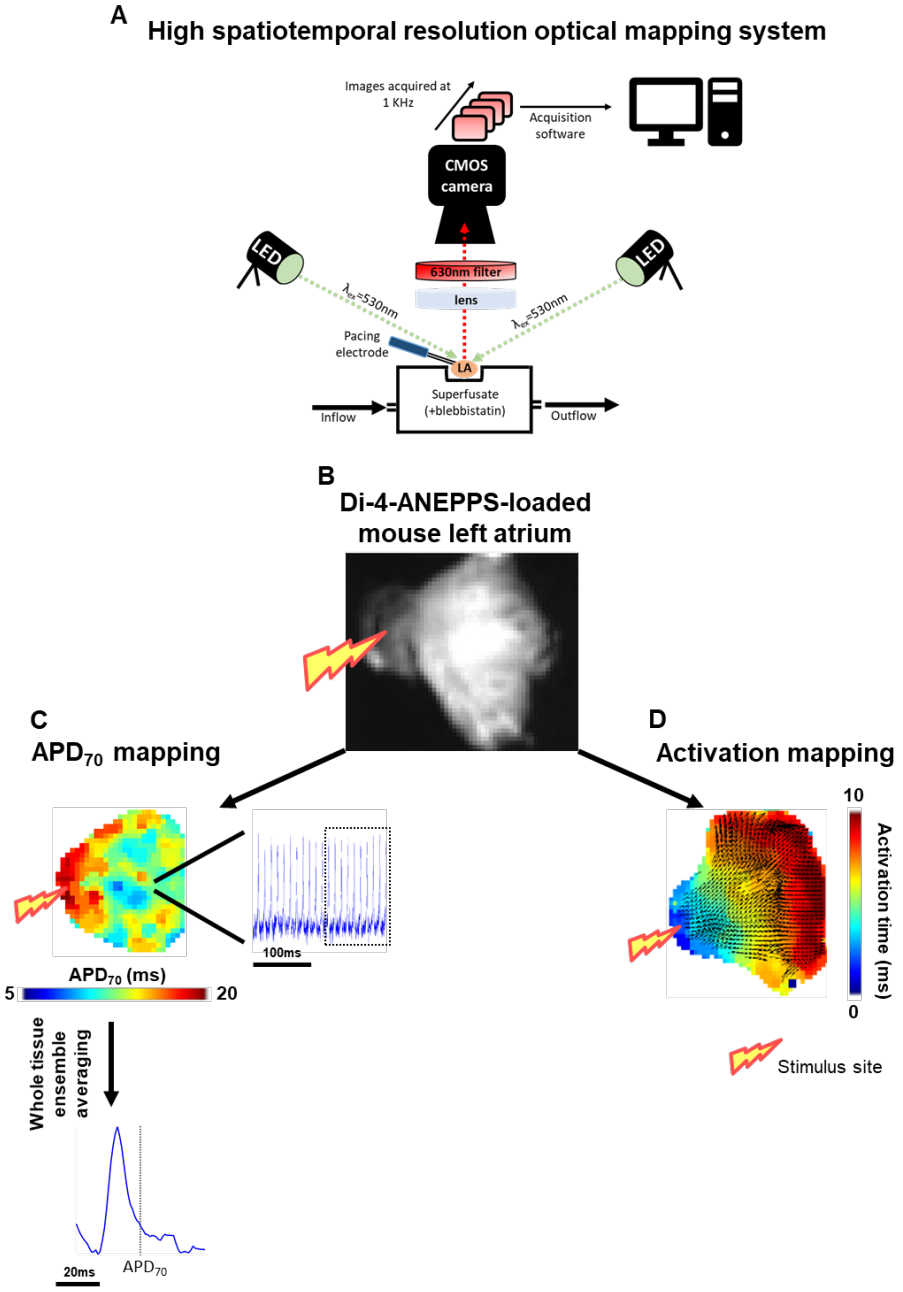

Fig 6.1 High spatiotemporal resolution optical mapping of the isolated mouse left atrium. **(A)** schematic of the isolated mouse left atrium optical mapping rig. **(B)** image of a Di-4-ANEPPS-loaded left atrium excited by 530nm LEDs. **(C)** APD_{70} mapping across the isolated left atrium. Pixel colour indicates APD_{70} at a specific location. Zooming in on a single pixel (right), reveals optical action potentials, of which the last 10 in a stimulus train were ensemble averaged for data analysis (dotted box). Ensemble averaging of these 10 beats from all pixels across a whole atrium (bottom) allows generation of a single action potential and calculation of mean tissue APD_{70}. **(D)** activation maps indicate propagation pathway from the stimulus site (posterior wall) across the appendage. Colours indicate time of depolarisation, allowing for mean whole left atrial conduction velocity to be calculated.

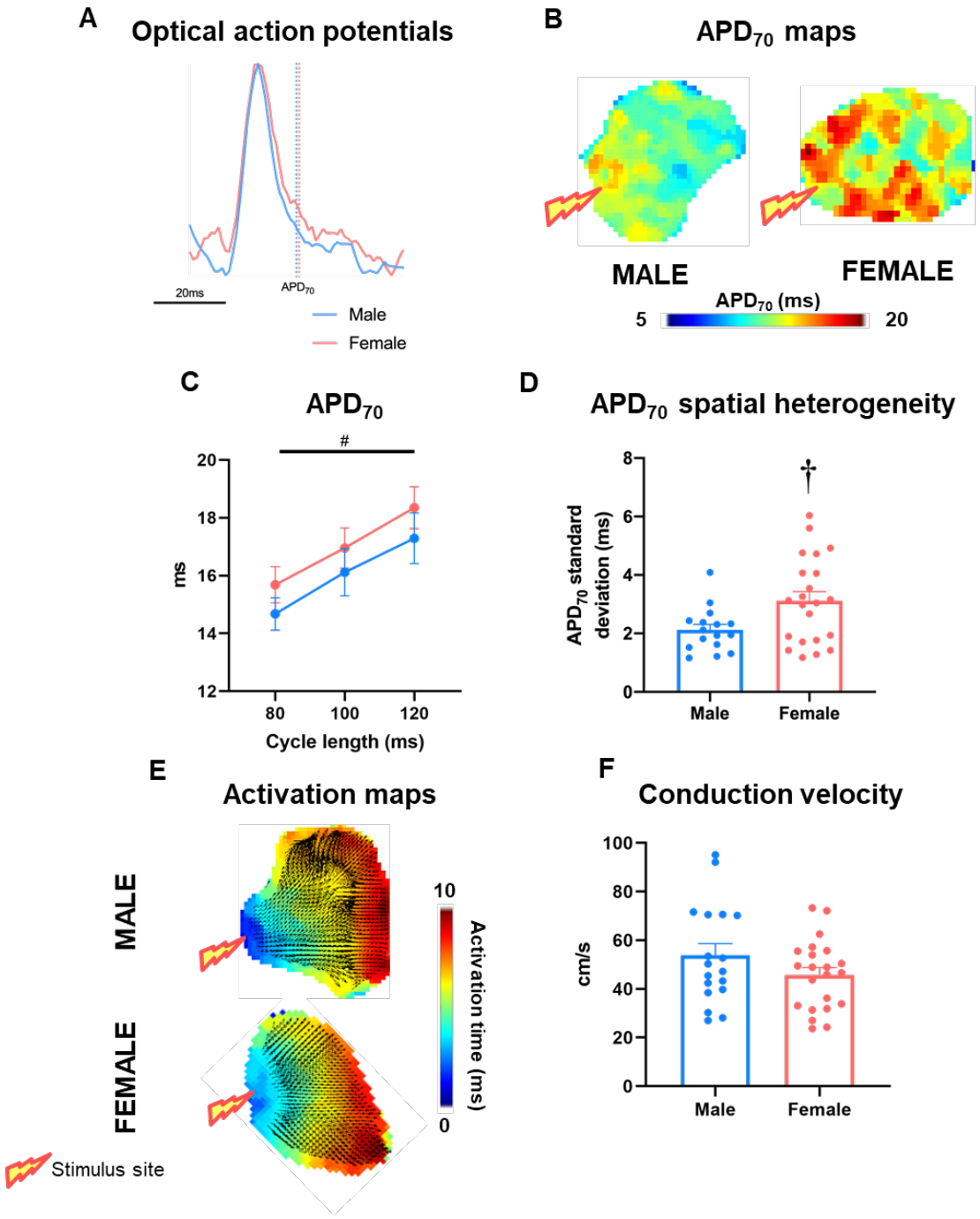

Fig 6.2 Basal electrophysiology in male and female mouse left atria. **(A)** exemplar ensemble averaged optical action potential traces, indicating APD_{70} measurement point in male and female left atria and **(B)** APD_{70} maps of tissue paced at 100ms cycle length. **(C)** Mean APD_{70} across 80, 100 and 120ms paced cycle lengths and **(D)** APD_{70} spatial heterogeneity at 100ms cycle length. **(E)** exemplar activation maps from male and female left atria at 100ms cycle length and **(F)** mean conduction velocity. Two-way repeated measures ANOVA **(C)** and unpaired t-tests **(D & F).** †P<0.05 between sexes and $^{\#}P$<0.05 indicates cycle length effect; n=18 and n=20 for male and female, respectively.

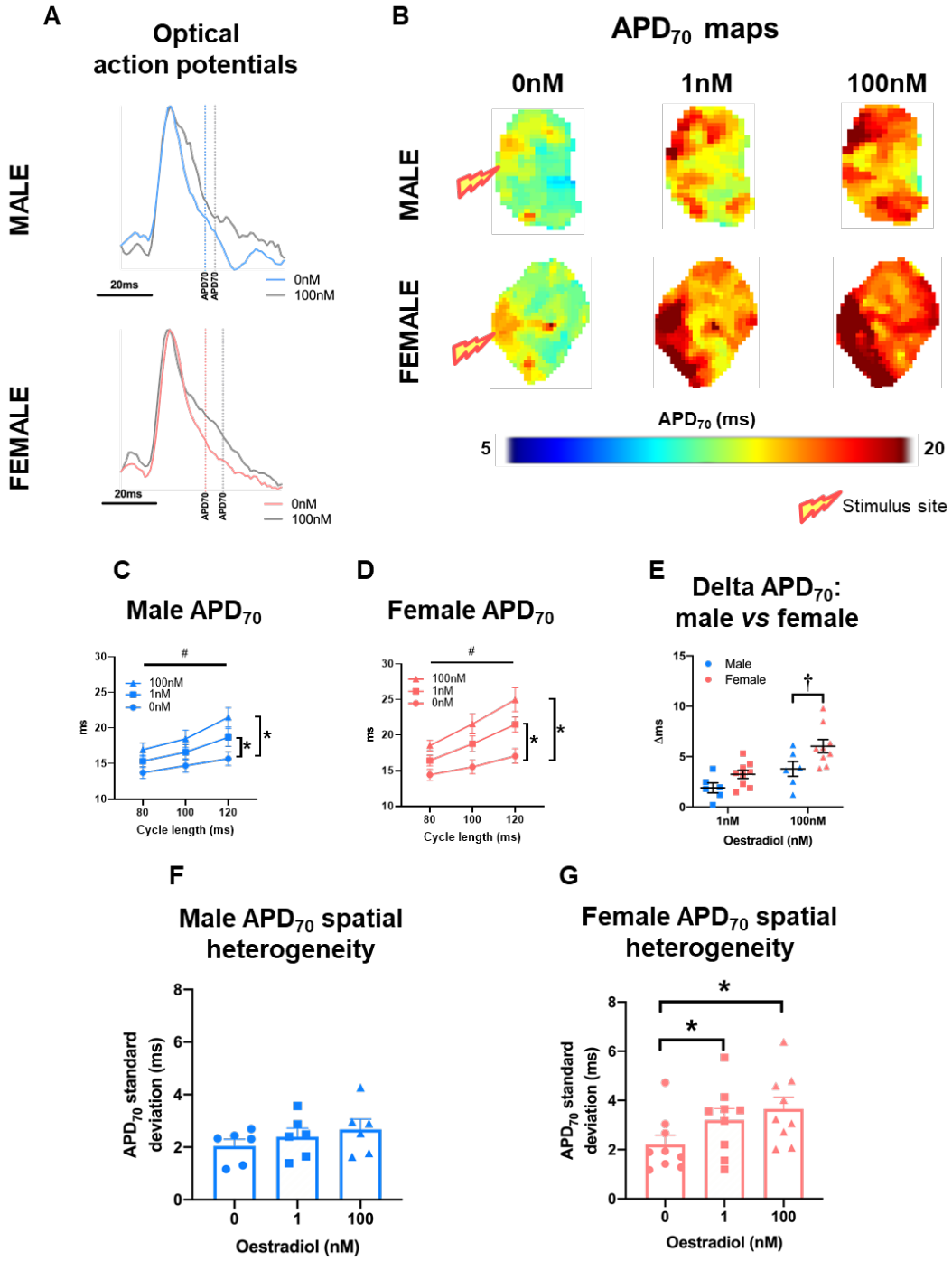

Fig 6.3 Oestradiol prolongs left atrial repolarisation to a greater extent in females than males. **(A)** exemplar male and female ensemble averaged left atrial optical action potentials treated with 0nM or 100nM oestradiol and **(B)** APD_{70} maps (100ms cycle length). Male **(C)** and female **(D)** mean whole left atrial APD_{70} with 0nM, 1nM and 100nM oestradiol treatment at 80ms, 100ms and 120ms cycle lengths. **(E)** oestradiol-induced change in APD_{70} in male *vs* female left atria. Male **(F)** and female **(G)** APD_{70} spatial heterogeneity with increasing oestradiol concentration (100ms cycle length). Two-way **(C-E)** or one-way **(F & G)** repeated measures ANOVA with Sidak's multiple comparison tests. #, * and † indicate $P<0.05$ cycle length effect, treatment effect (*vs* 0nM at all cycle lengths) and sex difference, respectively; n=6-9.

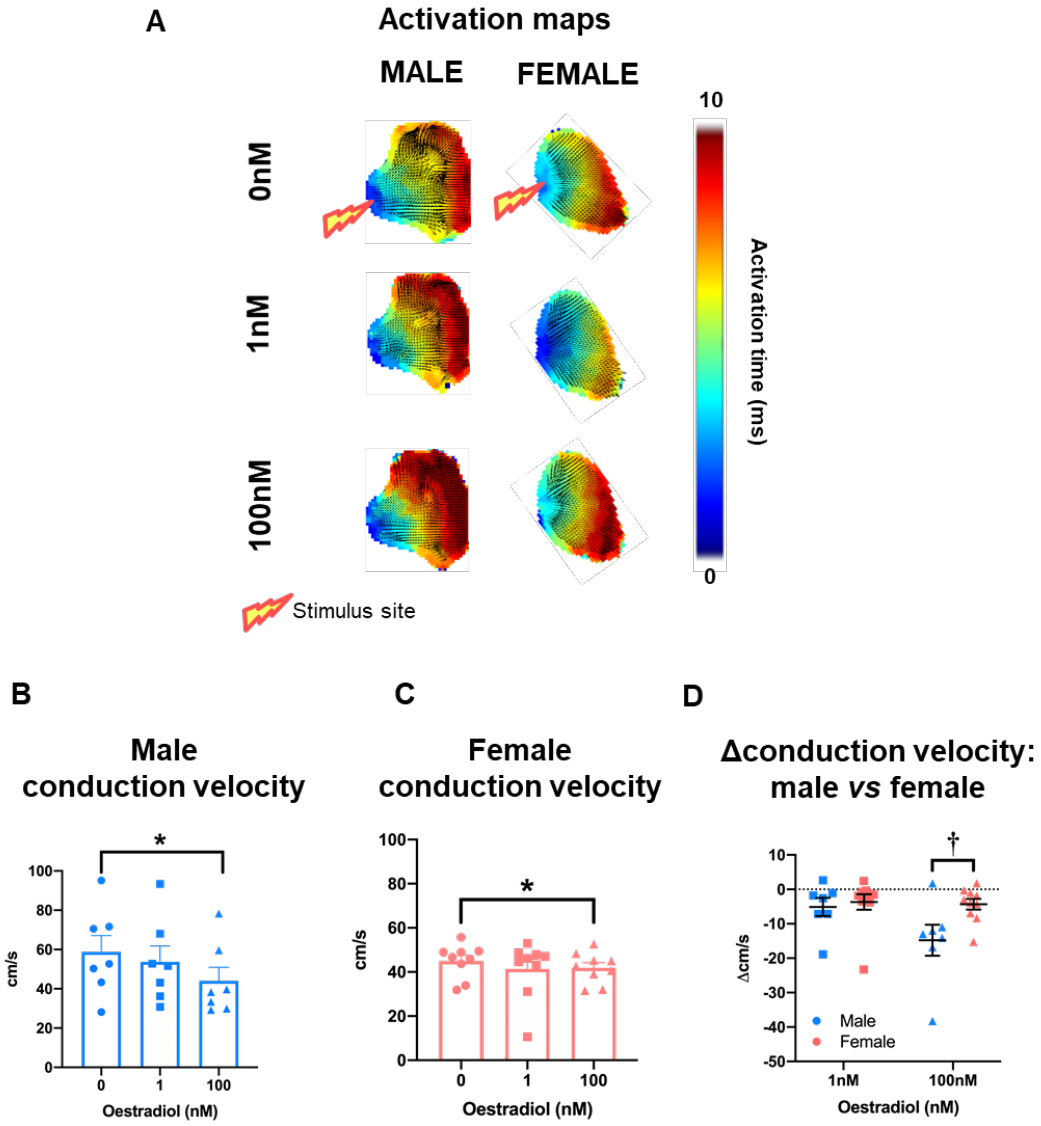

Fig 6.4 Oestradiol slows left atrial conduction velocity to a greater extent in males than females. **(A)** exemplar male and female left atrial activation maps treated with 0nM, 1nM or 100nM oestradiol. Male **(B)** and female **(C)** mean conduction velocity with 0nM, 1nM and 100nM oestradiol treatment. **(D)** oestradiol-induced change in conduction velocity in male *vs* female left atria. One-way **(B & C)** or two-way **(D)** repeated measures ANOVA with Sidak's multiple comparisons. * and † indicate $P<0.05$, treatment effect and sex difference, respectively; n=7-9.

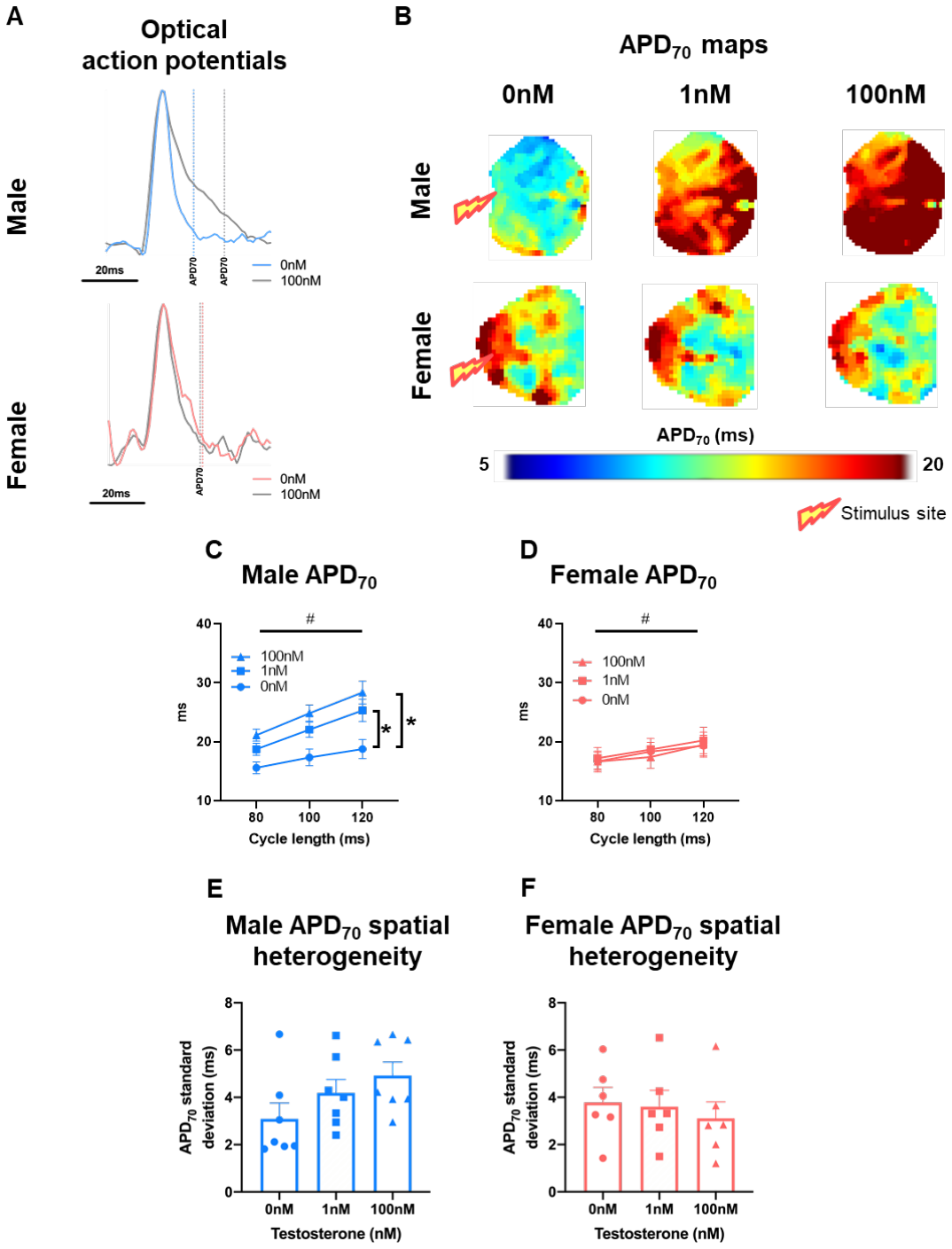

Fig 6.5 Testosterone prolongs male, but not female left atrial repolarisation. **(A)** exemplar male and female ensemble averaged left atrial optical action potentials treated with 0nM or 100nM testosterone and **(B)** APD_{70} maps(100ms cycle length). Male **(C)** and female **(D)** mean whole left atrial APD_{70} with 0nM, 1nM and 100nM testosterone treatment at 80ms, 100ms and 120ms cycle lengths. Male **(E)** and female **(F)** APD_{70} spatial heterogeneity with increasing testosterone concentration (100ms cycle length). Two-way **(C & D)** or one-way **(E & F)** repeated measures ANOVA with Sidak's multiple comparison tests. # and * indicate $P<0.05$ cycle length effect and treatment effect (*vs* 0nM at all cycle lengths), respectively; n=6-7.

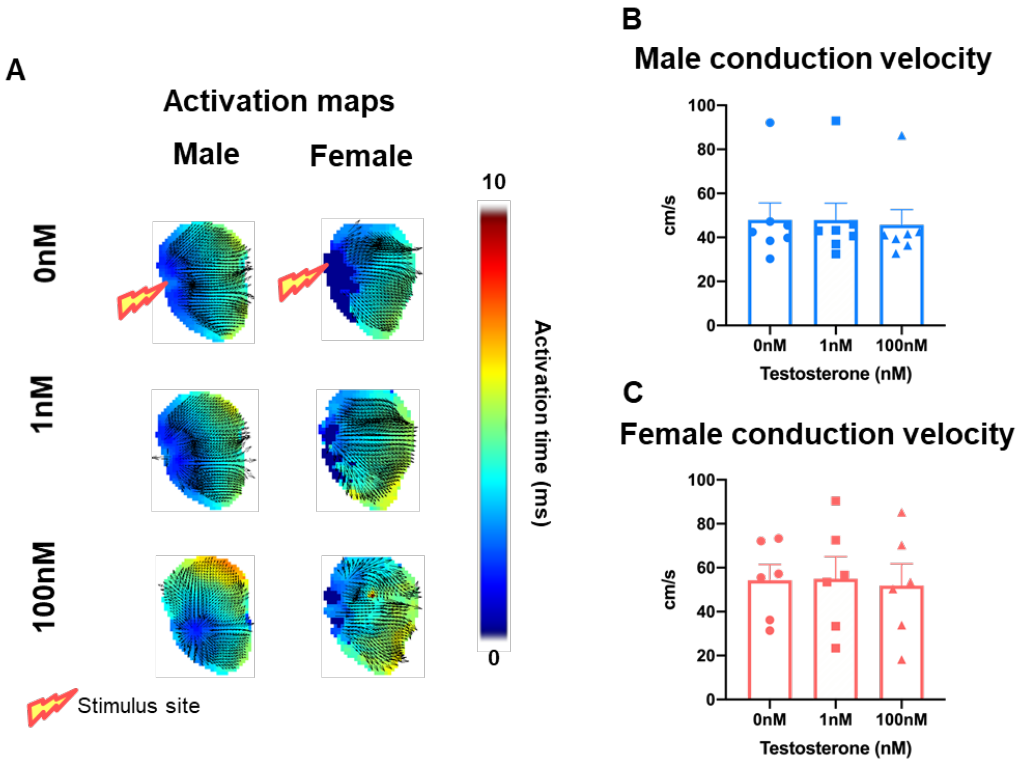

Fig 6.6 Testosterone does not modulate left atrial conduction velocity. **(A)** exemplar male and female left atrial activation maps treated with 0nM, 1nM or 100nM testosterone. Male **(B)** and female **(C)** mean conduction velocity with 0nM, 1nM and 100nM testosterone treatment. Repeated measures one-way ANOVA' P>0.05 in all cases; n=6-7.

6.10 Supplementary Tables

Supplementary Table S6.1 Male and female mouse body characteristics. Age, body weight, left atrial weight whole heart weight and heart:body weight ratio in male and female C57BL/6 mice. Unpaired *t-tests,* †*P*<0.05; *n*=18-20.

	Male	Female	*P-value*
Age (weeks)	28.4±0.7	27.7±0.6	>0.05
Body weight (g)	36.6±1.0	29.0±0.9	<0.05 (†)
Left atrial weight (mg)	3.8±0.4	3.0±0.2	0.09
Whole heart weight (mg)	153.4±11.3	111.8±3.3	<0.05 (†)
Heart weight: body weight (mg/g)	4.5±0.4	4.5±0.2	>0.05

6.11 Supplementary Figures

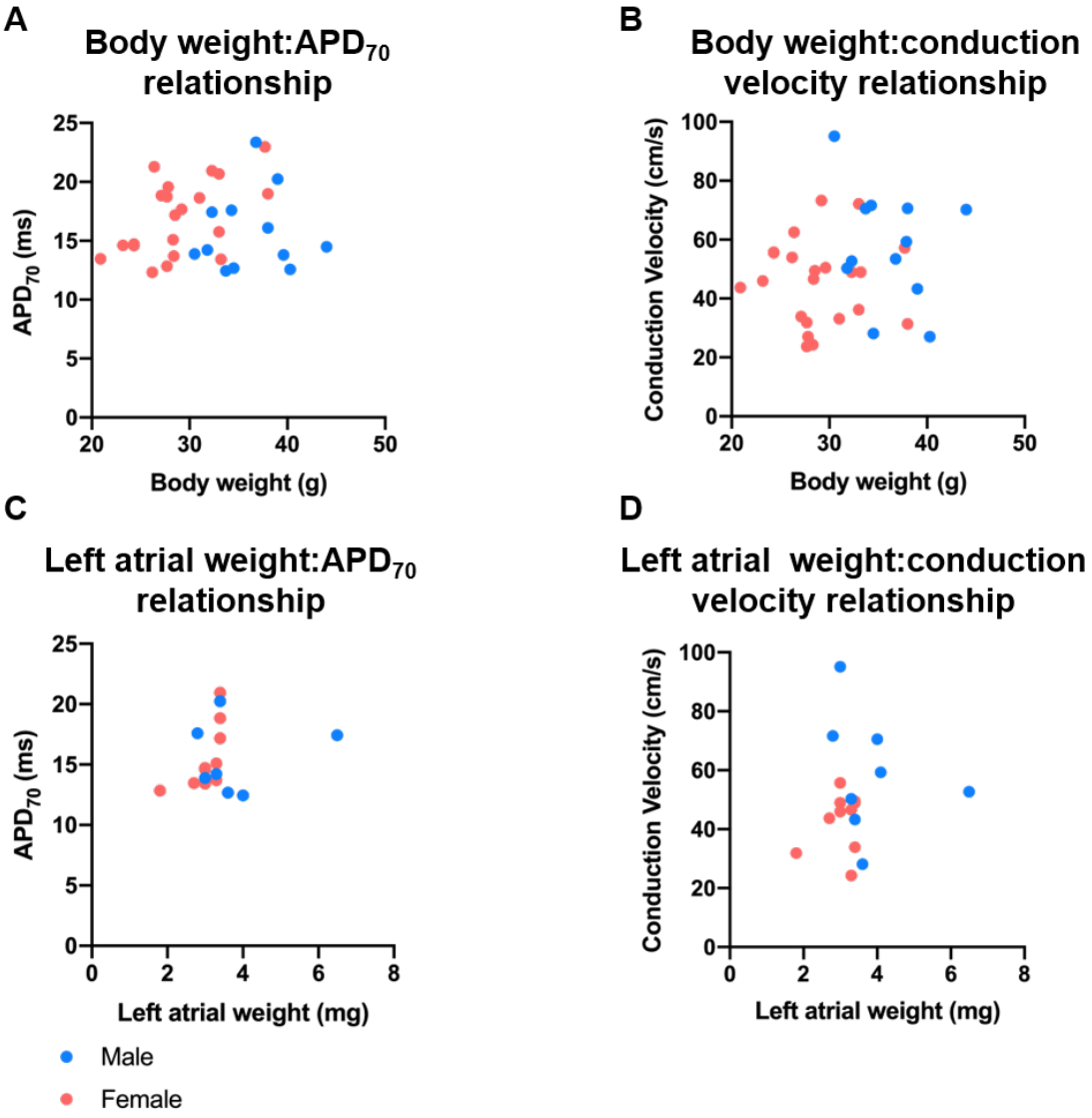

Supp Fig S6.1 Body weight and left atrial weight do not associate with basal electrophysiology. Body weight *vs* APD_{70} **(A)** and conduction velocity **(B)**. Left atrial weight *vs* APD_{70} **(C)** and conduction velocity **(D)**. Linear regression, $P>0.05$ in all cases; n=16-20.

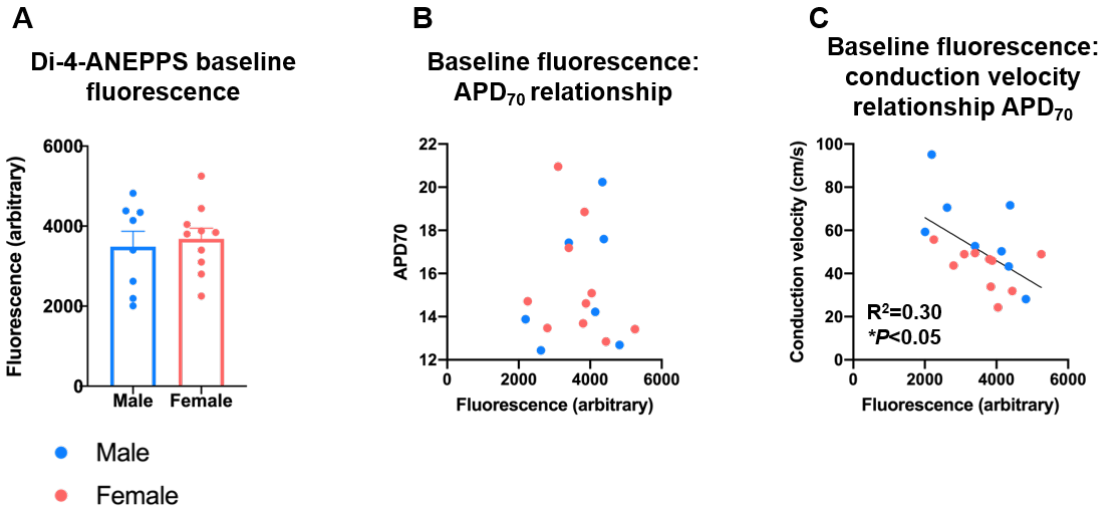

Supp Fig S6.2 Di-4-ANEPPS loading is uniform between sexes. **(A)** baseline fluorescence between males and female left atria loaded with DI-4-ANEPPS. Baseline Di-4-ANEPPS-loaded atrial fluorescence *vs* APD_{70} **(B)** and conduction velocity **(C)**. Unpaired *t*-test **(A)** and linear regression **(B & C)**, **P*<0.05 (significant correlation); *n*=7-10.

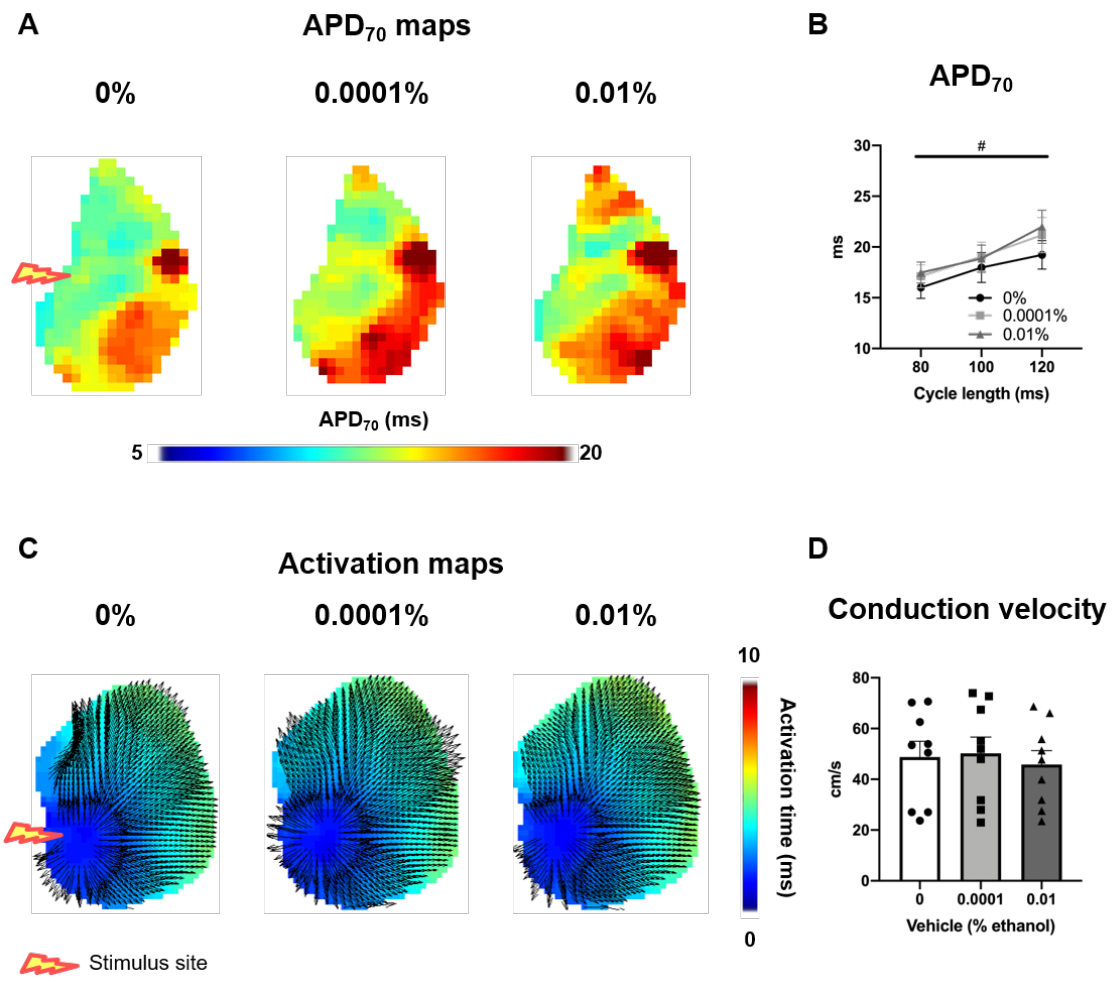

Supplementary Fig S6.3 Vehicle does not affect left atrial electrophysiology. Left atria were treated with increasing concentrations vehicle corresponding to the amount present in either 0nM (0%), 1nM (0.0001%) or 100nM (0.01%) of sex steroid. **(A)** exemplar APD_{70} maps from left atria at 100ms cycle length and **(B)** mean APD_{70} across 80ms, 100ms and 120ms paced cycle lengths. **(C)** exemplar activation maps and **(D)** mean conduction velocity. Two-way **(B)** or one-way **(D)** repeated measures ANOVA, $^{\#}P<0.05$ cycle length effect; n=7-9.

Chapter 7

General discussion

7.1 Summary of key findings

Cardiac arrhythmias pose a significant risk to life and healthcare burden. Atrial fibrillation is the most common arrhythmia, impeding life quality and posing significant risk of stroke and heart failure (1). Ventricular fibrillation associates with abrupt onset, resulting in sudden cardiac death without immediate cardiopulmonary resuscitation and defibrillation (2-4). Current therapeutic options aim to target the electrophysiological defects with limited success and do not address the processes that generate an arrhythmic substrate (5-8). Recent evidence implicates pericardial adipose tissue accumulation as an independent risk factor for fibrillation in both heart chambers (9-22). Evidence for the mechanisms underlying these associations is limited. Studies so far have focussed on pericardial adipose tissue release of pro-inflammatory mediators and their paracrine actions promoting epicardial fibrosis (23-29), with virtually no understanding of how cardiac adiposity affects cardiomyocyte electrophysiology and inter-myocyte conduction. Recently the presence of a local androgen-oestrogen system in/around the heart has been detected which may be involved in arrhythmia vulnerability (30,31).

Experiments in this thesis addressed the cardiac electrophysiological implications of augmented pericardial adiposity to define the mechanisms by which arrhythmia risk is elevated in this context.

Four major aims were addressed in this thesis:

1. Establish whether transmural electrophysiology is modulated in the context of elevated cardiac adiposity.

2. Compare electrophysiology of cardiomyocyte cultures from different origins as prelude to examining the paracrine influences of pericardial adipose tissue.

3. Ascertain whether obesity and epicardial adiposity associate with cardiac electrophysiological remodelling which may increase arrhythmia vulnerability.

4. Examine whether sex steroids can modulate atrial electrophysiology, indicating their potential as paracrine regulators of arrhythmia vulnerability.

The major findings from these investigations were:

1. The ventricular myocardium exhibits a transmural conduction velocity gradient, consistent with the activation sequence. High fat feeding causes epicardial conduction slowing, hence loss of the transmural gradient, increasing vulnerability to transmural/intramural reentry. Augmented pericardial adiposity and epicardial fibrosis evident with high fat feeding implicates them as potential mediators.

2. hiPSC-CM and NRVM cultures display similar electrophysiology and exhibit good capacity to detect changes in repolarisation via experimental intervention.

3. Obesity associates with prolonged left atrial repolarisation and epicardial adipose tissue exerts a paracrine effect to similarly modulate hiPSC-CM electrophysiology. Prolonged repolarisation predisposes to triggered arrhythmia – a key feature of

atrial fibrillation onset, indicating a potential paracrine role for epicardial adipose tissue in the initial formation of an unstable electrical substrate.

4. Oestrogen and testosterone prolong repolarisation and slow conduction in the left atrium, indicating their potential as paracrine regulators of arrhythmia vulnerability.

7.2 Pericardial adipose tissue and arrhythmia vulnerability: new electrophysiological insights

7.2.1 Pericardial adiposity and atrial electrophysiology

Obesity associates with increased atrial fibrillation risk, but the cellular electrophysiological mechanisms are poorly understood (32). Atrial fibrillation onset is progressive, with paroxysmal symptoms typically underpinned by triggered arrhythmia processes, and permanent/persistent disease states a result of structural/electrical remodelling predisposing to reentry. To investigate the electrophysiological remodelling that occurs with obesity, mice were fed a high fat diet and left atrial electrophysiology assessed. Repolarisation was prolonged and conduction velocity unaffected in obese mice, indicating their increased vulnerability to triggered arrhythmias which underpin paroxysmal atrial fibrillation.

Pericardial adipose tissue accumulates with obesity (31,33,34). The last decade has seen numerous studies establishing pericardial adiposity as an independent risk factor for atrial fibrillation risk, severity, and post-ablation outcomes (9-11,14). It is well understood that certain cellular electrophysiological changes must occur for atrial fibrillation to precipitate; however, there is virtually no understanding of how cardiac

adiposity affects cardiomyocyte electrophysiology. Co-culturing human induced pluripotent stem cell-derived cardiomyocytes (hiPSC-CMs) with epicardial adipose tissue fragments prolonged repolarisation. This is consistent with epicardial adipocyte-induced action potential duration prolongation demonstrated in rabbit atrial cardiomyocytes (30). Further, these data are consistent with the prolonged repolarisation in the obese mouse left atrium. Although this thesis did not assess pericardial adiposity in these mice, various clinical and preclinical studies indicate pericardial adipose tissue accumulates with obesity/high fat feeding (31,33,34). Together these data indicate pericardial adipose tissue exerts a paracrine effect to rapidly induce electrophysiological remodelling in a manner conducive with increased triggered arrhythmia vulnerability, classically implicated in atrial fibrillation onset.

Introduction of epicardial adipose tissue fragments into hiPSC-CM culture medium increases bioavailability of free fatty acids. An important hallmark of cardiomyocyte maturation from a neonatal to adult state is the switch of metabolic substrate from glucose to fatty acids (35-37). Maturation of cardiomyocytes from a neonatal/immature state to adult involves prolongation of repolarisation and so potentially the electrophysiological response detected in hiPSC-CM-epicardial adipose tissue co-culture are a result of an altered metabolic profile, rather than pathological (38). Nevertheless, switching metabolic substrate from glucose to free fatty acids in hiPSC-CM cultures does not affect repolarisation time, supporting the contention that the effect demonstrated in this thesis is proarrhythmogenic and likely not mediated by free fatty acids (39,40). Furthermore, this thesis also demonstrates an important thirty-day timeframe for maturation of hiPSC-CM electrophysiology. As such, experiments in this thesis only used

cultures which showed stable electrophysiology from 30 days post differentiation induction for epicardial adipose tissue co-culture experiments. Similarly, hiPSC-CM electrophysiology was compared to NRVM as prelude to epicardial adipose tissue co-culture investigations to benchmark the characteristics of the locally produced hiPSC-CMs against more classically used NRVMs. These data revealed similar repolarisation times and β-adrenergic responsiveness between hiPSC-CM and NRVM, validating the use of these locally produced hiPSC-CMs in electrophysiological investigations.

Together these data support the use of pericardial adipose tissue accumulation as a potential early marker for atrial fibrillation vulnerability. This thesis speculates that obese patients with paroxysmal symptoms may be most responsive to weight loss and Class IV antiarrhythmic drugs which shorten repolarisation. Concurrently, Class III antiarrhythmic drugs which prolong repolarisation, may exacerbate arrhythmia vulnerability in these patients. Class III antiarrhythmic agents are the most commonly prescribed drug among atrial fibrillation patients and so perhaps stratifying patients who are obese with paroxysmal symptoms into initial treatment with Class IV antiarrhythmics may be beneficial (41,42). Further studies are warranted to identify the signalling molecules facilitating the paracrine actions of pericardial adipose tissue on the atrial myocardium which may identify novel therapeutic targets of the processes which drive the disease, not just the symptoms.

7.2.2 Pericardial adiposity and ventricular electrophysiology

The sudden onset of ventricular fibrillation makes diagnosis and identification of at-risk patients difficult. Recent data indicate pericardial adipose tissue accumulation as a risk

factor for ventricular fibrillation vulnerability, but the cellular mechanisms are unknown (15-19,21,22). This thesis demonstrates a transmural conduction velocity gradient in the rat ventricle, whereby epicardial conduction velocity is faster than endocardial. This gradient is abolished in the setting of high cardiac adiposity. A conduction velocity gradient has not been previously probed for in the ventricle although numerous studies, including this thesis, demonstrate a clear action potential duration gradient (43-49). Further studies are required to examine the functional relevance of this gradient, which we hypothesise helps maintain normal endocardial-epicardial activation sequence.

Loss of this conduction gradient in the setting of augmented pericardial adiposity is interesting – especially because this is driven by a slowing in the myocardial region nearest the overlaying fat depots. Augmented fibrosis in the epicardium is likely a driver of slowed conduction. This thesis does not provide empirical evidence for the stimulus of fibrosis but notes the association between pericardial adiposity and extent of epicardial fibrosis. Others have demonstrated pericardial adipose tissue has capacity to release factors, such as activin A, to promote atrial fibrosis (23). This thesis hypothesises occurrence of similar mechanisms within the ventricular epicardium.

It is interesting that without obesity, relatively short-term high fat diet intake is sufficient to induce pathological structural and electrical remodelling of the ventricular myocardium. This contrasts the classic consensus that general adiposity and subsequent systemic delivery of adipose released factors are driving disease. These data support the emerging viewpoint that local adiposity is clearly implicated, and likely releasing factors with a substantially greater local concentration than those of systemic origin. Establishing whether a conduction velocity gradient is present in the human ventricle is

important to further understand the mechanisms leading to ventricular fibrillation. Data in this thesis indicate that inhibition of fibrosis deposition may be beneficial.

7.2.3 Integrated cardiac response to pericardial adipose tissue

This thesis highlights that the atria and ventricles respond differently to augmented pericardial adiposity. Atrial repolarisation is prolonged, whilst ventricular repolarisation is unaffected. Conversely, atrial conduction velocity is unaffected, whilst ventricular conduction is slowed. At least in part, these effects are mediated through paracrine effects of pericardial adipose tissue on the myocardium. It is possible this discrepancy is not due to differences in chamber *per se*, but differences in chamber proximity to different components of pericardial adipose tissue depots in rodents. Rodents have minimal pericardial adipose tissue compared to humans, especially epicardial depots. The small amount of epicardial adipose tissue in rodents is situated near the atria/atrioventricular groove and outflow tracts (50). The majority of rodent cardiac adipose is paracardial adipose, which surrounds the heart and has and can access the myocardium through pores in the pericardial sac (50,51). It could be that these two different constituents of pericardial adipose tissue synthesise and release different factors to modulate myocardial function. Indeed, they are of distinct embryonic origin and supplied by different vasculature (52). Epicardial adipose tissue may release factors which facilitate repolarisation prolongation, whilst paracardial adipose releases factors which promote fibrosis formation and conduction slowing. Consistent with this, hiPSC-CMs (primarily of ventricular phenotype) exhibited prolonged repolarisation in co-culture with epicardial adipose tissue fragments – indicating the effects are not chamber specific, but likely pericardial adipose tissue depot-mediated. Although Venteclef *et al.,*

(2015) have demonstrated atrial fibrosis in culture with epicardial adipose tissue, this context in not consistent with the volume of epicardial adipose tissue present in rodents, so perhaps explains the absence of a conduction slowing in the obese mouse atrium presented in this thesis (23).

It is interesting that C57BL/6J mice fed a high fat became obese, but Sprague Dawley rats fed a high fat diet did not. The additional supplementation of sucrose water in the mouse diet is unlikely to be responsible for this difference, since mice fed the same high fat diet as rats used in this study demonstrate significant weight gain (31). Existing literature indicates high fat feeding of Sprague Dawley rats has mixed effects, sometimes leading to significant weight gain over controls and sometimes not (53-56). This perhaps just reflects natural biological variation that is a result of using outbred animals. Systemic obesity may potentially play a role in modulating cardiac electrophysiology, potentially offering an alternative explanation for differences between mouse and rat studies in this thesis. Further the absence of any significant weight gain in rats, highlights they may serve as a better model for cardiac adiposity studies than mice.

The overall combined response of both chambers to pericardial adipose tissue elevation is complex, mediated through a variety of factors and the remodelling is likely species specific and age dependent. Nevertheless, evidence in this thesis indicates that in the setting of obesity and elevated pericardial adiposity, electrical remodelling of both heart chambers can occur to predispose to arrhythmia. This is the first direct evidence of the capacity of pericardial adipose tissue to modulate electrophysiology of both heart chambers.

7.3 Sex and sex steroids as modulators of cardiac electrophysiology

Pericardial adipose tissue has capacity to synthesise and release oestrogens, implicating sex steroids as potential paracrine modulators of atrial electrophysiology (31). Experimentally, oestradiol can acutely increase atrial arrhythmia inducibility in mouse hearts (31). This thesis provides the first evidence that sex steroids can modulate atrial electrophysiology through an acute, non-transcriptional-based mechanism. Oestradiol prolongs repolarisation and slows conduction in both sexes, albeit to differing extents. This response may be proarrhythmic, predisposing to early afterdepolarisations and reentry, respectively. Repolarisation prolongation is consistent with data in this thesis examining the electrophysiology of obese mouse left atria and hiPSC-CMs co-cultured with epicardial adipose tissue fragments. Testosterone was also able to rapidly prolong repolarisation in the male left atrium. Together, this indicates the possibility that pericardial adipose tissue-derived sex steroids may similarly modulate atrial electrophysiology in a paracrine fashion to predispose to arrhythmia. The relative balance of local oestrogen/testosterone may be critical in mediating rapid electrophysiological changes in the atrium. Further studies are required to confirm that pericardial adipose-derived sex steroids are directly involved in regulating atrial electrophysiology and arrhythmia vulnerability.

7.4 Study limitations

This thesis employed two different electrophysiological mapping techniques to elucidate the cellular myocardial changes that occur in the presence of elevated pericardial adipose tissue. Combined use of two different mapping approaches for electrophysiological investigations is rare, with laboratories typically selecting either microelectrode array or optical mapping methodology through cost-benefit evaluation. The use of both approaches in combination here strengthens the validity of these findings; however, the drawbacks of these methodologies should be noted. Both approaches only allow two-dimensional mapping, meaning data of a 3-dimensional heart surface is somewhat interpolated. For optical mapping this is particularly important as the setup used assumes equal pixel size across an entire image, which is not true for three-dimensional heart tissue. Nevertheless, the isolated atrial preparation is pinned relatively flat, so this limitation is not so problematic as it would be for whole heart preparations which were not used here.

The use of excitation-contraction uncouplers and voltage-sensitive dyes also limits the physiological relevance of optical mapping as a technique. Uncoupling contraction reduces tissue metabolic demand and limits the contribution of strain/stress to electrophysiological changes – features which are important in arrhythmia pathology (57). Contraction uncouplers and voltage sensitive dyes can be toxic and themselves modulate electrophysiology (58-60). Nevertheless, these experiments were performed over a short timeframe where consistent tissue viability was demonstrated.

Whilst microelectrode array experiments were not performed in the presence of toxic dyes or excitation-contraction uncouplers, 2,3-Butanedione monoxime was present during tissue slice generation to prevent contraction and minimise cutting damage. Evidence indicates 2,3-Butanedione monoxime rapidly washes out of myocardium (<5min for complete return of contraction), and so a minimum period of 5 min washout was included before commencement of mapping experiments (61). Others cardiac slice mapping protocols employ longer 2,3-Butanedione monoxime washout periods and gradual temperature increases from 4^{o}C (during slicing and in the holding chamber) to 37^{o}C (during recordings)(49,62). Observationally, contraction was restored rapidly (<30sec) and electrophysiological parameters consistent with published literature, indicating the protocol employed was appropriate.

Tissue weights were required to maintain cardiac slice contact with recording electrodes. Such additional stress on the tissue may itself affect stress/strain-induced electrophysiological parameters. Tangential cardiac slices themselves were generated from endocardium to epicardium, meaning the epicardial surface was adhered to the vibratome specimen holder, potentially limiting oxygen/solution supply during the slicing process. Hypoxic myocardium demonstrates shortened action potential duration and slowed conduction velocity (63-66). Although we did not assess for hypoxia-reoxygenation markers, electrophysiological evidence indicated good viability, with conduction velocity fastest in the epicardium and velocities consistent with other literature (62,67,68). The epicardium demonstrated shorter field potential durations than the endocardium; however, numerous studies indicate this transmural repolarisation duration gradient is physiologically intrinsic to the myocardium (43-49).

Rodent tissue was primarily used throughout investigations presented here. Whilst some investigations used human stem cell-derived cardiomyocytes and recapitulated rodent findings, it should be noted that there are several electrophysiological differences between rodent and human tissue. Importantly, rodent myocardium exhibits a reduced repolarisation reserve, more dependent on the transient outward currents and ultra-rapid delayed rectifier current than the human myocardium (69,70). This results in rapid repolarisation with minimal plateau phase in rodent tissue which conferred experimental difficulty in the microelectrode array-cardiac slice preparation which has also be noted by others (71).

hiPSC-CM cultures used in this thesis re-plated onto microelectrode arrays as clusters, limiting the scope to analyse conduction velocity. In Chapter 3 where the hiPSC-CM-microelectrode array mapping procedures were being optimised, cells were re-seeded onto 8x8 microelectrode arrays, which limited the capacity to reliably assess conduction velocity, hence this parameter was not reported. In Chapter 5 this optimised methodology was refined further, whereby cells were reseeded onto 3x3 microelectrode arrays and strict inclusion criteria were employed to define cultures where conduction could be mapped (i.e. those cultures with synchronised intercellular connectivity). This improved mapping capacity; however, it is important to acknowledge conduction velocity in these instances is not directly comparable to monolayers or intact myocardium.

7.5 Conclusions and future directions

There is a clinical association between pericardial adipose tissue accumulation and atrial/ventricular arrhythmia vulnerability. Through experimental electrophysiological mapping and histological methodology, this thesis demonstrates the electrophysiological remodelling that occurs to potentially predispose to arrhythmia in the setting of augmented pericardial adiposity. This is the first direct evidence that atrial and ventricular electrophysiology is modulated in the setting of augmented pericardial adiposity, and at least a component of this is mediated through paracrine interactions between pericardial adipose tissue and the atrial/ventricular epicardium. Future studies should investigate the paracrine factors involved in the structural and electrical remodelling process. This thesis also indicates the potential for sex steroids to rapidly modulate atrial electrophysiology. With the established presence of an intra-cardiac androgen-oestrogen system in the myocardium and surrounding pericardial adipose tissue, future studies should examine the contribution of pericardial adipose tissue-derived sex steroids as paracrine modulators of electrophysiology, and their potential contribution to arrhythmia vulnerability. Investigations into the downstream cardiomyocyte signalling mechanisms affected by pericardial adipose tissue-derived paracrine mediators should also be examined.

Future investigations should aim to identify novel pericardial adipose tissue-derived signalling molecules which might yield better therapeutic options, offering a more targeted antiarrhythmia treatment strategy to limit off-target effects prevalent with current treatment options.

7.6 References

1. Chugh SS, Havmoeller R, Narayanan K et al. Worldwide epidemiology of atrial fibrillation: a Global Burden of Disease 2010 Study. Circulation 2014;129:837-47.

2. Gillum RF. Geographic variation in sudden coronary death. Am Heart J 1990;119:380-389.

3. Hayashi M, Shimizu W, Albert CM. The Spectrum of Epidemiology Underlying Sudden Cardiac Death. Circ Res 2015;116:1887-1906.

4. Myerburg R, Castellanos A. Cardiac electrophysiology: from cell to bedside, vol. 1. Philadelphia: Saunders Elsevier, 2009.

5. Valembois L, Audureau E, Takeda A, Jarzebowski W, Belmin J, Lafuente-Lafuente C. Antiarrhythmics for maintaining sinus rhythm after cardioversion of atrial fibrillation. Cochrane Database Syst Rev 2019.

6. Capucci A, Cipolletta L, Guerra F, Giannini I. Emerging pharmacotherapies for the treatment of atrial fibrillation. Expert Opin Emerg Drugs 2018;23:25-36.

7. Kirchhof P, Calkins H. Catheter ablation in patients with persistent atrial fibrillation. Eur Heart J 2017;38:20-26.

8. Al-Khatib SM, Stevenson WG, Ackerman MJ et al. 2017 AHA/ACC/HRS Guideline for Management of Patients With Ventricular Arrhythmias and the Prevention of Sudden Cardiac Death. Circulation 2018;138:e272-e391.

9. Al Chekakie MO, Welles CC, Metoyer R et al. Pericardial fat is independently associated with human atrial fibrillation. J Am Coll Cardiol 2010;56:784-8.

10. Thanassoulis G, Massaro JM, O'Donnell CJ et al. Pericardial fat is associated with prevalent atrial fibrillation: the Framingham Heart Study. Circ Arrhythm Electrophysiol 2010;3:345-50.

11. Batal O, Schoenhagen P, Shao M et al. Left atrial epicardial adiposity and atrial fibrillation. Circ Arrhythm Electrophysiol 2010;3:230-6.

12. Nakatani Y, Kumagai K, Minami K, Nakano M, Inoue H, Oshima S. Location of epicardial adipose tissue affects the efficacy of a combined dominant frequency and complex fractionated atrial electrogram ablation of atrial fibrillation. Heart Rhythm 2015;12:257-65.

13. Kusayama T, Furusho H, Kashiwagi H et al. Inflammation of left atrial epicardial adipose tissue is associated with paroxysmal atrial fibrillation. J Cardiol 2016;68:406-411.

14. Wong CX, Abed HS, Molaee P et al. Pericardial fat is associated with atrial fibrillation severity and ablation outcome. J Am Coll Cardiol 2011;57:1745-51.

15. Nerlekar N, Muthalaly RG, Wong N et al. Association of Volumetric Epicardial Adipose Tissue Quantification and Cardiac Structure and Function. J Am Heart Assoc 2018;7:e009975.

16. Vural M, Talu A, Sahin D et al. Evaluation of the relationship between epicardial fat volume and left ventricular diastolic dysfunction. Jap J Radiol 2014;32:331-339.

17. Konishi M, Sugiyama S, Sugamura K et al. Accumulation of pericardial fat correlates with left ventricular diastolic dysfunction in patients with normal ejection fraction. J Cardiol 2012;59:344-51.

18. Fontes-Carvalho R, Fontes-Oliveira M, Sampaio F et al. Influence of epicardial and visceral fat on left ventricular diastolic and systolic functions in patients after myocardial infarction. Am J Cardiol 2014;114:1663-9.

19. Lai Y-H, Hou CJ-Y, Yun C-H et al. The association among MDCT-derived three-dimensional visceral adiposities on cardiac diastology and dyssynchrony in asymptomatic population. BMC Cardiovascular Disorders 2015;15:142.

20. Lee DS, Gona P, Albano I et al. A systematic assessment of causes of death after heart failure onset in the community: impact of age at death, time period, and left ventricular systolic dysfunction. Circ Heart Fail 2011;4:36-43.

21. Wu CK, Tsai HY, Su MY et al. Pericardial fat is associated with ventricular tachyarrhythmia and mortality in patients with systolic heart failure. Atherosclerosis 2015;241:607-14.

22. Sepehri Shamloo A, Schoene K, Stauber A et al. Epicardial adipose tissue thickness as an independent predictor of ventricular tachycardia recurrence following ablation. Heart Rhythm 2019;16:1492-1498.

23. Venteclef N, Guglielmi V, Balse E et al. Human epicardial adipose tissue induces fibrosis of the atrial myocardium through the secretion of adipo-fibrokines. Eur Heart J 2015;36:795-805.

24. Miksztowicz V, Morales C, Barchuk M et al. Metalloproteinase 2 and 9 Activity Increase in Epicardial Adipose Tissue of Patients with Coronary Artery Disease. Curr Vasc Pharmacol 2017;15:135-143.

25. Zeller J, Kruger C, Lamounier-Zepter V et al. The adipo-fibrokine activin A is associated with metabolic abnormalities and left ventricular diastolic dysfunction in obese patients. ESC Heart Fail 2019;6:362-370.

26. Wang Q, Xi W, Yin L et al. Human Epicardial Adipose Tissue cTGF Expression is an Independent Risk Factor for Atrial Fibrillation and Highly Associated with Atrial Fibrosis. Sci Rep 2018;8:3585.

27. Li SJ, Wu TW, Chien MJ, Mersmann HJ, Chen CY. Involvement of pericardial adipose tissue in cardiac fibrosis of dietary-induced obese minipigs- Role of mitochondrial function. Biochimica et biophysica acta Molecular and cell biology of lipids 2019;1864:957-965.

28. Horckmans M, Bianchini M, Santovito D et al. Pericardial Adipose Tissue Regulates Granulopoiesis, Fibrosis, and Cardiac Function After Myocardial Infarction. Circulation 2018;137:948-960.

29. Mazurek T, Zhang L, Zalewski A et al. Human epicardial adipose tissue is a source of inflammatory mediators. Circulation 2003;108:2460-6.

30. Lin YK, Chen YC, Chen JH, Chen SA, Chen YJ. Adipocytes modulate the electrophysiology of atrial myocytes: implications in obesity-induced atrial fibrillation. Basic Res Cardiol 2012;107:293.

31. Bernasochi GB, Boon WC, Curl CL et al. Pericardial adipose and aromatase: A new translational target for aging, obesity and arrhythmogenesis? J Mol Cell Cardiol 2017;111:96-101.

32. Wang TJ, Parise H, Levy D et al. Obesity and the risk of new-onset atrial fibrillation. Jama 2004;292:2471-7.

33. Iacobellis G, Ribaudo MC, Assael F et al. Echocardiographic epicardial adipose tissue is related to anthropometric and clinical parameters of metabolic syndrome: a new indicator of cardiovascular risk. J Clin Endocrinol Metab 2003;88:5163-8.

34. Willens HJ, Byers P, Chirinos JA, Labrador E, Hare JM, de Marchena E. Effects of weight loss after bariatric surgery on epicardial fat measured using echocardiography. Am J Cardiol 2007;99:1242-5.

35. Ascuitto RJ, Ross-Ascuitto NT. Substrate metabolism in the developing heart. Semin Perinatol 1996;20:542-63.

36. Bartelds B, Knoester H, Smid GB et al. Perinatal changes in myocardial metabolism in lambs. Circulation 2000;102:926-31.

37. Lopaschuk GD, Jaswal JS. Energy metabolic phenotype of the cardiomyocyte during development, differentiation, and postnatal maturation. J Cardiovasc Pharmacol 2010;56:130-40.

38. Kato Y, Masumiya H, Agata N, Tanaka H, Shigenobu K. Developmental Changes in Action Potential and Membrane Currents in Fetal, Neonatal and Adult Guinea-pig Ventricular Myocytes. J Mol Cell Cardiol 1996;28:1515-1522.

39. Mills RJ, Titmarsh DM, Koenig X et al. Functional screening in human cardiac organoids reveals a metabolic mechanism for cardiomyocyte cell cycle arrest. Proc Natl Acad Sci USA 2017;114:E8372-E8381.

40. Yang X, Rodriguez ML, Leonard A et al. Fatty Acids Enhance the Maturation of Cardiomyocytes Derived from Human Pluripotent Stem Cells. Stem Cell Rep 2019;13:657-668.

41. Nabar A, Rodriguez LM, Timmermans C, van Mechelen R, Wellens HJJ. Class IC antiarrhythmic drug induced atrial flutter: electrocardiographic and electrophysiological findings and their importance for long term outcome after right atrial isthmus ablation. Heart 2001;85:424-429.

42. Zimetbaum P. Antiarrhythmic Drug Therapy for Atrial Fibrillation. Circulation 2012;125:381-389.

43. Bányász T, Fülöp L, Magyar J, Szentandrássy N, Varró A, Nánási PP. Endocardial versus epicardial differences in L-type calcium current in canine ventricular myocytes studied by action potential voltage clamp. Cardiovasc Res 2003;58:66-75.

44. Boukens BJ, Sulkin MS, Gloschat CR, Ng FS, Vigmond EJ, Efimov IR. Transmural APD gradient synchronizes repolarization in the human left ventricular wall. Cardiovasc Res 2015;108:188-96.

45. Brunet S, Aimond F, Li H et al. Heterogeneous expression of repolarizing, voltage-gated K+ currents in adult mouse ventricles. J Physiol 2004;559:103-120.

46. Glukhov AV, Fedorov VV, Lou Q et al. Transmural dispersion of repolarization in failing and nonfailing human ventricle. Circ Res 2010;106:981-991.

47. Sicouri S, Antzelevitch C. A subpopulation of cells with unique electrophysiological properties in the deep subepicardium of the canine ventricle. The M cell. Circ Res 1991;68:1729-41.

48. Volk T, Nguyen TH, Schultz JH, Ehmke H. Relationship between transient outward K+ current and Ca2+ influx in rat cardiac myocytes of endo- and epicardial origin. J Physiol 1999;519 Pt 3:841-850.

49. Wen Q, Gandhi K, Capel RA et al. Transverse cardiac slicing and optical imaging for analysis of transmural gradients in membrane potential and Ca(2+) transients in murine heart. J Physiol 2018;596:3951-3965.

50. Yamaguchi Y, Cavallero S, Patterson M et al. Adipogenesis and epicardial adipose tissue: a novel fate of the epicardium induced by mesenchymal transformation and PPARγ activation. Proc Natl Acad Sci USA 2015;112:2070-5.

51. Nakatani T, Shinohara H, Fukuo Y, Morisawa S, Matsuda T. Pericardium of rodents: pores connect the pericardial and pleural cavities. Anat Rec 1988;220:132-7.

52. Iacobellis G. Epicardial and pericardial fat: close, but very different. Obesity (Silver Spring) 2009;17:625; author reply 626-7.

53. Meng T, Cheng G, Wei Y et al. Exposure to a chronic high-fat diet promotes atrial structure and gap junction remodeling in rats. Int J Mol Med 2017;40:217-225.

54. Marques C, Meireles M, Norberto S et al. High-fat diet-induced obesity Rat model: a comparison between Wistar and Sprague-Dawley Rat. Adipocyte 2015;5:11-21.

55. Aubin M-C, Cardin S, Comtois P et al. A high-fat diet increases risk of ventricular arrhythmia in female rats: Enhanced arrhythmic risk in the absence of obesity or hyperlipidemia. J Appl Physiol 2010;108:933-40.

56. Reig J, Domingo E, Segura R, Tovar JL, Viñallonga M, Borrell M. Rat myocardial tissue lipids and their effect on ventricular electrical activity: influence on dietary lipids. Cardiovasc Res 1993;27:364-370.

57. Johnson DM, Antoons G. Arrhythmogenic Mechanisms in Heart Failure: Linking β-Adrenergic Stimulation, Stretch, and Calcium. Front Physiol 2018;9:1453.

58. Winter J, O'Shea C, Pavlovic D, Fabritz L, Kirchhof P. 151 Direct evidence that sympathetic nervous activation accelerates ventricular conduction velocity, but inhibition of responses by DI-8-ANEPPS. Heart 2018;104:A107-A108.

59. Larsen AP, Sciuto KJ, Moreno AP, Poelzing S. The voltage-sensitive dye di-4-ANEPPS slows conduction velocity in isolated guinea pig hearts. Heart Rhythm 2012;9:1493-500.

60. Brack KE, Narang R, Winter J, Ng GA. The mechanical uncoupler blebbistatin is associated with significant electrophysiological effects in the isolated rabbit heart. Exp Physiol 2013;98:1009-1027.

61. Biermann M, Rubart M, Moreno A, Wu J, Josiah-Durant A, Zipes DP. Differential Effects of Cytochalasin D and 2, 3 Butanedione Monoxime on Isometric Twitch Force and Transmembrane Action Potential in Isolated Ventricular Muscle: Implications for Optical Measurements of Cardiac Repolarization. J Cardiovasc Electrophys 1998;9:1348-1377.

62. Lane JD, Montaigne D, Tinker A. Tissue-Level Cardiac Electrophysiology Studied in Murine Myocardium Using a Microelectrode Array: Autonomic and Thermal Modulation. J Membr Biol 2017;250:471-481.

63. Asano T, Shigenobu K, Kasuya Y. TEA prevents the decline of the duration of the action potential in hypoxic cardiac muscle. Jpn J Pharmacol 1985;38:65-72.

64. Koyano T, Kakei M, Nakashima H, Yoshinaga M, Matsuoka T, Tanaka H. ATP-regulated K+ channels are modulated by intracellular H+ in guinea-pig ventricular cells. J Physiol 1993;463:747-766.

65. Kodama I, Wilde A, Janse MJ, Durrer D, Yamada K. Combined effects of hypoxia, hyperkalemia and acidosis on membrane action potential and excitability of guinea-pig ventricular muscle. J Mol Cell Cardiol 1984;16:247-259.

66. Furuta T, Kodama I, Shimizu T, Toyama J, Yamada K. Effects of hypoxia on conduction velocity of ventricular muscle. Jpn Heart J 1983;24:417-25.

67. O'Shea C, Pavlovic D, Rajpoot K, Winter J. Examination of the Effects of Conduction Slowing on the Upstroke of Optically Recorded Action Potentials. Front Physiol 2019;10:1295-1295.

68. Takanari H, Bourgonje VJA, Fontes MSC et al. Calmodulin/CaMKII inhibition improves intercellular communication and impulse propagation in the heart and is antiarrhythmic under conditions when fibrosis is absent. Cardiovasc Res 2016;111:410-421.

69. Cordeiro JM, Spitzer KW, Giles WR. Repolarizing K+ currents in rabbit heart Purkinje cells. J Physiol 1998;508 (Pt 3):811-823.

70. Babij P, Askew GR, Nieuwenhuijsen B et al. Inhibition of cardiac delayed rectifier K+ current by overexpression of the long-QT syndrome HERG G628S mutation in transgenic mice. Circ Res 1998;83:668-78.

71. Bussek A, Wettwer E, Christ T, Lohmann H, Camelliti P, Ravens U. Tissue slices from adult mammalian hearts as a model for pharmacological drug testing. Cell Physiol Biochem 2009;24:527-36.

Appendix

Additional manuscripts published

during PhD candidature

Manuscript references:

O'Shea C, Holmes AP, Yu TY, Winter J, **Wells SP**, *et al*., ElectroMap: High-throughput open-source software for analysis and mapping of cardiac electrophysiology. *Sci Rep*, 9: (1), 1389. Creative Commons license: https://creativecommons.org/licenses/by/4.0/

O'Shea C, Holmes AP, Yu TY, Winter J, **Wells SP**, *et al.,* High-Throughput Analysis of Optical Mapping Data Using ElectroMap. *J Vis Exp*, 4: (148), DOI: 10.3791/59663

www.nature.com/scientificreports

OPEN

ElectroMap: High-throughput open-source software for analysis and mapping of cardiac electrophysiology

Received: 6 September 2018
Accepted: 21 December 2018
Published online: 04 February 2019

Christopher O'Shea[1,2,3], Andrew P. Holmes[1,4], Ting Y. Yu[1], James Winter[1], Simon P. Wells[1,11], Joao Correia[5], Bastiaan J. Boukens[6], Joris R. De Groot[7], Gavin S. Chu[8,9], Xin Li[8], G. Andre Ng[8,9], Paulus Kirchhof[1,10], Larissa Fabritz[1,10], Kashif Rajpoot[3] & Davor Pavlovic[1]

The ability to record and analyse electrical behaviour across the heart using optical and electrode mapping has revolutionised cardiac research. However, wider uptake of these technologies is constrained by the lack of multi-functional and robustly characterised analysis and mapping software. We present ElectroMap, an adaptable, high-throughput, open-source software for processing, analysis and mapping of complex electrophysiology datasets from diverse experimental models and acquisition modalities. Key innovation is development of standalone module for quantification of conduction velocity, employing multiple methodologies, currently not widely available to researchers. ElectroMap has also been designed to support multiple methodologies for accurate calculation of activation, repolarisation, arrhythmia detection, calcium handling and beat-to-beat heterogeneity. ElectroMap implements automated signal segmentation, ensemble averaging and integrates optogenetic approaches. Here we employ ElectroMap for analysis, mapping and detection of pro-arrhythmic phenomena in silico, in cellulo, animal model and *in vivo* patient datasets. We anticipate that ElectroMap will accelerate innovative cardiac research and enhance the uptake, application and interpretation of mapping technologies leading to novel approaches for arrhythmia prevention.

The incidence and prevalence of cardiac diseases continues to increase every year[1,2]. Adequate prevention and treatment requires a better understanding of the mechanistic drivers[3]. Detailed understanding of spatial and temporal electrical behaviour and ionic handling across the heart is integral to this.

Ability to measure field potentials and conduction from multiple sites can be achieved by contact/non-contact electrodes arrays. More recently, optical mapping has allowed measurement and mapping of action potential and calcium transient morphology and conduction, leading to a broader utilisation of mapping technologies in the cardiovascular sphere. Increasingly, electrode array mapping has made its way from pre-clinical to clinical arena whilst the use of optical mapping continues to expand in experimental research. Optically imaging intact tissue using voltage or calcium sensitive fluorescent dyes has advantages over surface electrodes but the requirement for contraction uncouplers and inability to perform *in vivo* experiments limits clinical utility of optical mapping[4]. Nevertheless, insights from optical mapping experiments have informed our understanding of complex arrhythmias and electrophysiological remodelling in heart disease[5–8]. Electrode mapping has equally provided

[1]Institute of Cardiovascular Sciences, University of Birmingham, Birmingham, UK. [2]EPSRC Centre for Doctoral Training in Physical Sciences for Health, School of Chemistry, University of Birmingham, Birmingham, UK. [3]School of Computer Science, University of Birmingham, Birmingham, UK. [4]Institute of Clinical Sciences, University of Birmingham, Birmingham, UK. [5]Institute of Microbiology and Infection, School of Biosciences, University of Birmingham, Birmingham, UK. [6]Amsterdam UMC, University of Amsterdam, Department of Anatomy and Physiology, Amsterdam, The Netherlands. [7]Amsterdam UMC, University of Amsterdam, Heart Center, Department of Cardiology, Amsterdam, The Netherlands. [8]Department of Cardiovascular Sciences, University of Leicester, Leicester, UK. [9]NIHR Leicester Biomedical Research Centre, Glenfield Hospital, Leicester, UK. [10]Department of Cardiology, UHB NHS Trust, Birmingham, UK. [11]Department of Physiology, University of Melbourne, Melbourne, Australia. Kashif Rajpoot and Davor Pavlovic jointly supervised this work. Correspondence and requests for materials should be addressed to K.R. (email: k.m.rajpoot@bham.ac.uk or d.pavlovic@bham.ac.uk)

vital knowledge[9,10], demonstrating that re-entry drives ventricular tachycardia[11], actively guiding current clinical ablation strategies. Some arrhythmogenic principles, for example in atrial fibrillation (AF), remain poorly understood from a mechanistic standpoint[12,13] and thus require further experimentation.

Increased availability of optical mapping hardware in the laboratory has led to expansion of this technology. Further uptake and wider application is hindered by limitations with respect to data processing and analysis. This challenge is intensified as developing camera technology provides ever-increasing spatio-temporal resolution. Furthermore, multiple processing algorithms are employed before the underlying data can be interpreted[14,15]. These algorithms require computational expertise to implement and are commonly developed and used within individual research groups, utilising techniques specific to camera resolution, file type and animal species. Whilst some software solutions are accessible, even straightforward calculation of conduction velocity (CV) across the heart is currently unavailable, but to a few specialist groups. There is an unmet need for a robustly tested mapping software that allows high-throughput data processing, analysis, and mapping of electrophysiology from different acquisition modalities and diverse datasets with distinct electrophysiological (EP) properties (for example: animal, human tissue and cell monolayers). Therefore, we present novel and robust open-source software, ElectroMap, for analysis of voltage and calcium optical mapping data. This work builds upon our previously published algorithms[15–17] while integrating analytic approaches developed and validated by others[6,14,18,19]. ElectroMap provides analysis of key EP parameters including action potential and calcium transient morphology, calcium decay constant (τ), activation and repolarisation times, diastolic interval (DI), time-to-peak, phase mapping and dominant frequency (DF). A key innovation is the introduction of a comprehensive CV module for robust investigation of CV changes. This module integrates established single vector[18] and multi vector[20] techniques for CV measurement as well as a novel "activation constant" analysis. Furthermore, semi-automated alternans analysis is enabled through development of a comprehensive alternans detection and quantification module. ElectroMap integrates automated pacing frequency recognition, ensemble (i.e. multi-beat) averaging and beat-to-beat analysis options. Here we employ ElectroMap for analysis, mapping and detection of pro-arrhythmic phenomena in silico, in cellulo, animal model and *in vivo* patient datasets, and thus demonstrate its utility for cardiac research.

Methods

Expanded details about methods are provided in the Supplementary Material. All animal procedures were undertaken in accordance with ethical guidelines set out by the UK Animals (Scientific Procedures) Act 1986 and Directive 2010/63/EU of the European Parliament on the protection of animals used for scientific purposes. Studies conformed to the Guide for the Care and Use of Laboratory Animals published by the U.S. National Institutes of Health under assurance number A5634-01. Experiments were approved by the home office (mouse: PPL 30/2967 and PFDAAF77F, guinea pig: PPL PF75E5F7F) and the institutional review boards at University of Birmingham (murine) and King's College London (guinea pig). For optical mapping of human tissue, left atrial appendages were obtained from patients with atrial fibrillation (AF) during thoracoscopic surgery, as described before[21]. The study was in accordance with the declaration of Helsinki and approved by the Review Board of the Academic Medical Center, Amsterdam. *In vivo* intracardiac data were obtained in a clinical study approved by local ethics committee for patients undergoing AF ablation at the University Hospitals of Leicester NHS Trust as previously described[22]. All patients gave written informed consent.

Optical Mapping. Both mouse and guinea pig optical mapping experiments were conducted as previously reported. For experiments in mouse[7,15,17] fluorescent dye (Voltage: DI-4-ANEPPS, Calcium: Rhod-2AM) was loaded into Langendorff perfused whole hearts. Left atria were isolated, with the posterior atrial surface exposed. Atria were superfused under normoxic (95%O_2/5%CO_2) or hypoxic (95%N_2/5%CO_2) conditions. Pacing was performed via bipolar platinum electrode, and fluorescence captured using ORCA flash 4.0 camera (1 kHz sampling rate, maximum field of view: 200 × 2048 pixels, 71 µm/pixel, Hamamatsu Electronics, Japan). Isolated guinea pig hearts[8] were loaded with voltage dye Di-8-ANEPPS, paced via silver bipolar electrodes and imaged using Evolve Delta 512 × 512 pixel EMCCD cameras (500 Hz sampling rate, 64 × 64 pixels, 320 µm/pixel, Photometrics, USA) mounted on a Olympus MVX10 stereomicroscope.

Human left atrial appendages[21] were removed using an endoscopic stapling device (Endo Gia stapler, Tyco Healthcare Group) and transported to the optical mapping setup in 100 mL cooled superfusion fluid. Atrial preparation was submerged in a recording chamber, loaded with Di-4-ANEPPS and paced using an epicardial electrode. MiCAM Ultima camera (2 kHz sampling rate, 100 × 100pixels, 100 µm/pixel SciMedia, USA) was used to record epicardial images.

***In-vivo* Human Mapping.** A high-density non-contact multi-electrode array catheter (Ensite Array, St. Jude Medical, USA) was positioned in the right atrium. Virtual unipolar electrograms were bandpass filtered from 1–100 Hz with additional noise filtering, then exported from a 2048 node geometry as previously described[22].

ElectroMap Design and Development. All data processing and analysis was performed using ElectroMap, Fig. 1a. ElectroMap is developed to run on multiple platforms. It can run either within MATLAB or as a standalone executable (.exe for Windows and.dmg for macOS) with download of the freely available MATLAB runtime (see Supplementary Material). Processing parameters and additional modules are adjustable using custom made graphical user interfaces. Software is designed to handle the widely used TIFF and MAT formats. Custom input of sampling frequency and pixel size makes it compatible with various cameras and acquisition systems. ElectroMap allows automatic or adjusted region selection (Fig. 1b) and multiple filtering options (see Supplementary Material for full details of filtering options). Unless stated otherwise, all the signals in Figs 1–8 underwent spatial (4 × 4 pixel Gaussian, sigma = 1.5) and temporal (3rd order Savitzky-Golay) filtering to allow

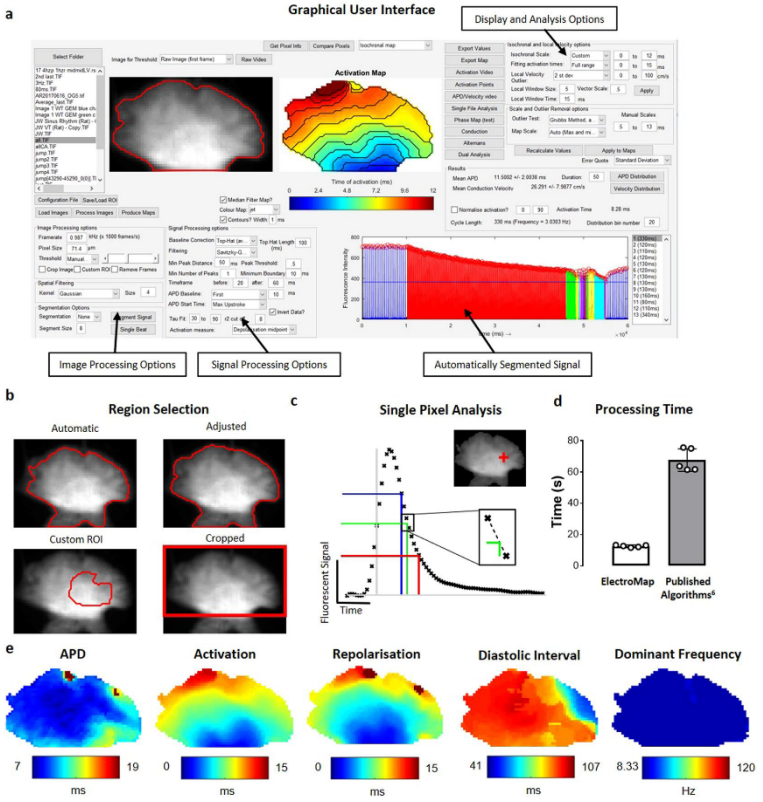

Figure 1. ElectroMap interface and function. (**a**) ElectroMap Graphical User Interface with automatic signal segmentation, image processing, signal processing, display and analysis options highlighted. (**b**) Illustration of 4 different region selection methods available in ElectroMap. (**c**) Example of analysis from one pixel (top inset) within murine atrial images. Action potential duration (APD) 30 (blue), 50 (green) and 70 (red) are calculated from time of maximum upstroke velocity (vertical grey line) to 30%, 50%, 70% repolarisation respectively. Time of repolarisation calculated by linear interpolation (dotted line) between sampling points, as shown for 50% repolarisation in lower inset. (**d**) Time taken to process and analyse 5 image stacks of murine left atria from raw images to conduction velocity calculation, comparison of ElectroMap and our previously published algorithms. (**e**) Selection of pseudo-colour maps denoting some of the electrophysiological parameters measurable using ElectroMap.

effective EP parameter quantification from single image pixels (Fig. 1c). The ElectroMap user interface permits signal inversion via a simple checkbox option. User-defined settings can be stored and recalled for future analysis.

Integration of automated pacing frequency recognition and numerous user-defined segmentation options (Supplementary Fig. I) enables simple and intuitive application of powerful analysis strategies including beat-to-beat analysis of long experimental files and multi-beat (ensemble) averaging to improve signal-to-noise ratio (SNR). Code optimization resulted in increased processing speed of up to five-times, compared to our previously published algorithms[15] (Fig. 1d).

ElectroMap incorporates several definitions for activation (Start – d^2F/dt^2_{max}, Upstroke – dF/dt_{max}, Depolarisation Midpoint, Peak) and repolarisation (Downstroke – dF/dt_{min}, Repolarization Percentage, End – d^2F/dt^2_{max}), Supplementary Fig. II. Repolarisation percentage can be set to any custom value between 0 and 100% repolarisation/decay from peak for both repolarization and duration mapping (Supplementary Fig. III). Unless stated otherwise, depolarization midpoint was used to create activation maps, action potential duration (APD) was defined from upstroke to 50% repolarization and calcium transient duration (CaT) was defined from upstroke

to 50% repolarization/decay. For calcium transient analysis, τ was calculated by fitting a mono-exponential model to a user defined region of decay from peak cytosolic calcium. Cardiac alternans were measured as change in duration or peak amplitude from one calcium transient to the previous. Additionally, effects of cytosolic calcium load were investigated by comparing 'load' and 'release' alternans amplitude, as in Wang *et al.*[23]. Analysis results can be exported from ElectroMap's interface as TIFF files for individual maps, AVI/GIF files for multi-image analyses such as beat-to-beat (see Supplementary Video I), and comma separated value (.csv) files for parameter distribution and beat-to-beat analysis.

Statistical analysis. Data are presented as mean ± standard error. Differences between group means were examined using two-tailed, paired Student's t-test or using One Way Analysis of Variance (ANOVA) with Bonferroni test, and were accepted as significant when $P < 0.05$.

Results

We have developed a novel, user-adaptable, semi-automated, robust, open-source software ElectroMap using MATLAB, see Fig. 1a for graphical user interface. The software is freely downloadable from https://github.com/CXO531/ElectroMap, and is available as a standalone executable file or as source code which can be run and edited in MATLAB. Algorithms implemented within ElectroMap have previously been validated against monophasic and transmembrane potentials in murine atria[15]. Here, we present the application and further validation of ElectroMap for the analysis and mapping of basic and complex cardiac electrophysiology from optical mapping datasets (Figs 1–8) and endocardial electrograms (Fig. 8).

Conduction Velocity Module. Analysis of the spread of electrical activation in cardiac tissue at high spatiotemporal resolution is one of the most powerful applications of optical mapping. We have developed a comprehensive CV analysis module within ElectroMap (Supplementary Fig. IV), to overcome a multitude of complexities and potential user-bias associated with CV calculations[18,24]. The module incorporates two established methods that rely on superimposing a vector field upon the activation map: (i) multi-vector and (ii) single vector method (see Fig. 2a,b). Additionally, we have developed a novel method that quantifies time taken to activate a percentage of the tissue. This approach allows calculation of 'activation constant' (see Fig. 2c,d), thereby providing a measure of activation spread across the whole tissue.

To validate the three CV calculation methods, we generated computationally simulated model data (Fig. 3a and Supplementary Fig. V; for algorithms, see Supplementary Material). All three methods accurately measured conduction velocities ranging from 10 to 100 cm/s in isotropic model data (Fig. 3a(i)). As shown in Fig. 3b,c, single vector and multi-vector methods demonstrate a linear increase in CV with faster model conduction speed. Activation curve method accurately detected a change in CV (Fig. 3d), increase in model CV led to a reduction in the time taken to activate 50% (act_{50}) of the tissue. We also validated CV analysis methods using models of anisotropic activation (Fig. 3aii) and regional conduction block (Fig. 3aiii). Single vector analysis correctly detected slower CV along the transverse ($180^0/360^0$) compared to longitudinal ($0^0/270^0$) direction in anisotropic waves, and conduction slowing adjacent to the region of conduction block (Fig. 3e). Similarly, multi-vector method successfully identified regions of reduced CV in anisotropic waves and severe conduction slowing around the area of conduction block (Fig. 3f). Activation curve analysis was able to detect the slowing of conduction in the anisotropic wave, as evident by a prolongation of the activation curve, and a delay in activation caused by conduction block (Fig. 3g). Additionally, Gaussian noise with incrementally increasing standard deviation (defined as percentage of action potential amplitude, Supplementary Fig. VII) was introduced to isotropic simulated data with CV of 50 cm/s, Fig. 3h. As expected, increased noise in single beat data decreases the ability to accurately calculate CV, with noise levels above 20% resulting in erroneous CV measurements (Fig. 3i). However, SNR can be improved using temporal and spatial filtering or multi-beat ensemble avenging within ElectroMap. Temporal filtering (Savitzky-Goaly filter) did not improve CV measurement, whereas both spatial filtering (3×3 Gaussian filter) and ensemble averaging of 10 beats substantially improved CV measurement accuracy.

Further validation was performed using experimental datasets acquired from murine left atrial tissue. We focused on two physiologically relevant stimuli known to reduce CV: an increase in pacing frequency[25] and acute hypoxia[26] (Fig. 4a). Indeed, significant slowing of CV, due to increased pacing frequency, was detected by multi-vector method (Fig. 4b, $P = 0.0335$) and activation curve method, as shown by an increase in the act_{50} (Fig. 4c and D, $P = 0.0119$). Both methods also accurately detected a more severe slowing of CV caused by exposure to acute hypoxia (Fig. 4e–g, $P < 0.0001$ and $P = 0.0051$ respectively).

High-Throughput Beat-to-Beat Analysis. Studies of beat-to-beat variation can provide important information about short periods of regional or whole tissue electrical instability, e.g. in response to pacing frequency change, pharmacological agents or disease states. Therefore, we developed and tested algorithms to allow high-throughput analysis of beat-to-beat alterations in long experimental files. Guinea pig hearts were paced over 70 seconds with a 5-8-5 Hz pacing protocol[27] and beat-to-beat changes in APD50 examined (Fig. 5a and Supplementary Videos I and II). Increasing the pacing frequency (from 5 Hz to 8 Hz) induced reversible shortening of mean ventricular APD (Fig. 5b). Furthermore, significant APD heterogeneity was detected in the first 4 beats, immediately after transition from 5 Hz to 8 Hz (Fig. 5b,c). Switching back from 8 Hz to 5 Hz (at 40 s) also induced some APD heterogeneity while highlighting a slow return to the steady state APD (Fig. 5b,d).

Calcium Decay Mapping. Optical mapping is increasingly utilised to study calcium release patterns across myocardial tissue or cellular monolayers, in response to disease, genetic factors or drug administration[19]. The estimation of calcium decay constant (τ) is common in single cell studies. However, τ is not commonly mapped

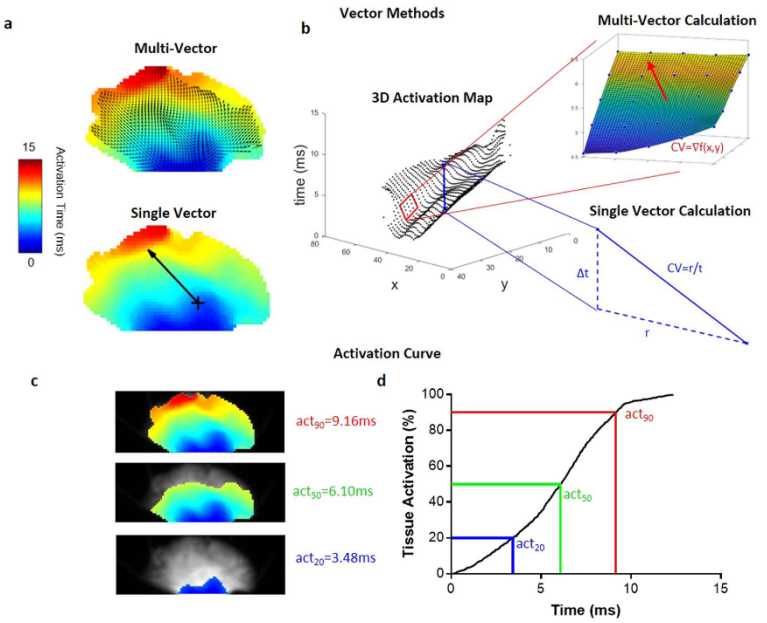

Figure 2. ElectroMap conduction velocity module quantification methods. (**a**) Vector methods applied to murine atria. Top panel: multi-vector method, with local conduction vectors (arrows) calculated across the tissue. Lower panel: single velocity method, where conduction speed is measured along the vector (arrow) connecting two points. (**b**) Activation map represented in 3D with x,y pixel positions and activation time on z-axis. Upper inset demonstrates calculation of one local vector from a 5×5 pixel region by fitting of a polynomial surface (f(x,y)) to measured activation times (t(x,y)). Lower inset shows calculation of single vector velocity from activation time difference (Δt) and distance (**r**) between two selected points. (**c**) Activation of the murine atria at 20% (act_{20}), 50% (act_{50}), and 90% (act_{90}), total activation. (**d**) The associated activation curve, with act_{20}, act_{50} and act_{90} highlighted.

across multicellular preparations[28], likely due to lack of support for this function in available software platforms. We developed algorithms for calculation of CaT and τ maps, as shown in Fig. 6a,b. Importantly, CaT can be measured from various 'activation times' during upstroke (Supplementary Figs II and VI), allowing for assessment of both calcium release and uptake (Fig. 6a inset). Moreover, τ can be fitted from any user-defined value (Fig. 6b inset). To test and validate algorithms developed for calculation of τ, mouse atria were loaded with Rhod-2AM and paced at incremental frequencies (3-8.33-10-12.5 Hz). Software accurately calculated progressively shorter τ values at higher pacing frequencies (Fig. 6c,d, $P < 0.0001$ for all pacing frequencies compared to 3 Hz). Interestingly, higher pacing frequencies were associated with a reduction in τ heterogeneity (Fig. 6c, $P = 0.0286$ and $P = 0.0168$ for 10 Hz and 12.5 Hz pacing respectively).

Alternans Analysis Module. Alternans are beat-to-beat 2-period oscillations in ion handling, electrical activity and hence mechanical contraction of the myocardium that can act as a precursor to conduction block and lethal arrhythmias[29,30]. We have developed a module within ElectroMap to detect and quantify alternans across tissue and cellular monolayers. Alternans module is capable of quantifying peak, duration, and release or load alternans (see Supplementary Fig. VIII for alternans definitions).

In Fig. 7 we demonstrate utility of the alternans module in detection and quantification of calcium alternans in a murine left atrium loaded with Rhod-2AM. The atrium was subjected to high frequency pacing of 12.5 Hz, initially leading to moderate alternans (Fig. 7a, blue CaTs) and then transitioning to more pronounced alternans (Fig. 7a, red CaTs). ElectroMap was used to generate maps allowing visualization and alternans quantification across the atrium (Fig. 7b,c). Alternans displayed clear spatial heterogeneity (Fig. 7b,c) with increased 'CaT Peak Alternans' correlating with changes in diastolic calcium load ('Load Alternans'), see Fig. 7c.

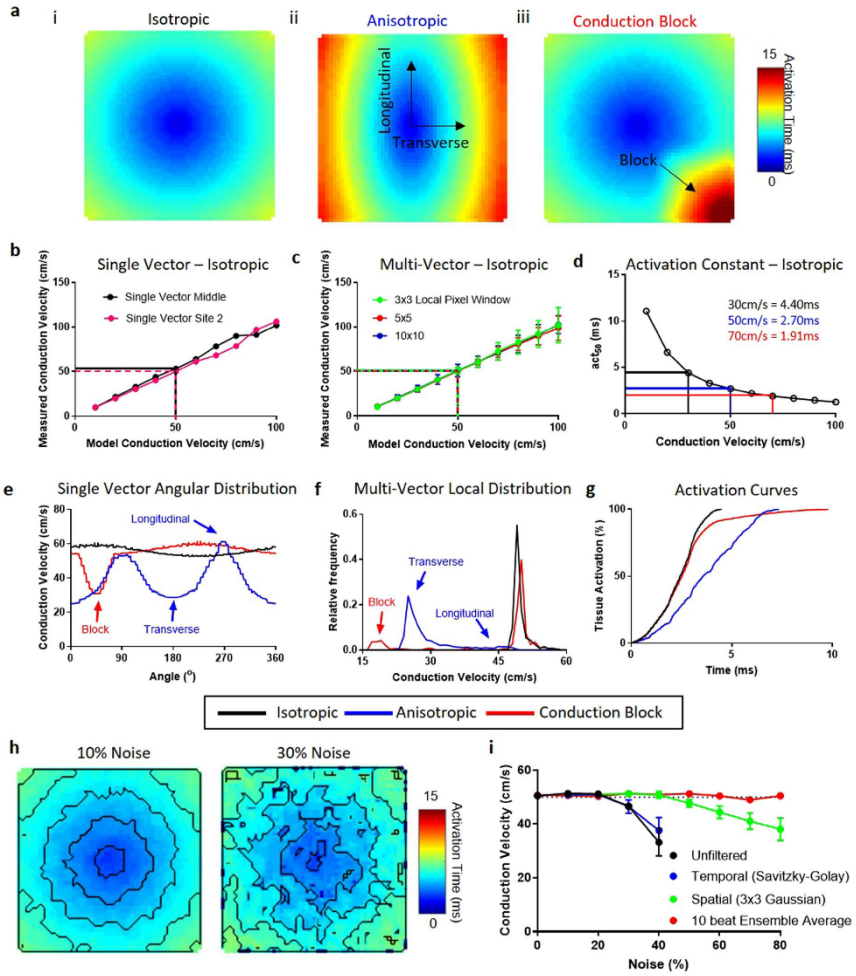

Figure 3. Validation of conduction velocity quantification methods using model datasets. (**a**) Model conduction datasets exhibiting isotropic conduction (i), anisotropic conduction (ii) and isotropic conduction with a 2:1 conduction block in lower right region (iii). (**b–d**) Measured conduction velocities (CV) from isotropic conduction model datasets spanning 10 to 100 cm/s using ElectroMap. (**b**) CV is measured using a single vector from centre of sample (black) and from edge of sample (pink). (**c**) multi-vector method is used with windows sizes of 3×3 (green), 5×5 (red) and 10×10 (blue) pixels. CV is then measured as mean of the magnitude of all local vectors calculated, with error bars representing the standard deviation of the mean. (**d**) Activation curve method with act_{50} (time to 50% activation) used to quantify conduction. (**e–g**) Three CV quantification methods applied to model datasets with isotropic, anisotropic and conduction block present conduction. In all three cases, fastest model conduction was 50 cm/s. (**e**) Change in measured CV as a function of angle using single vector method from centre of tissue. (**f**) Distribution of local vector magnitude measured by multi-vector method (5×5 pixel window) in the three model datasets. (**g**) Activation curves from the model datasets. (**h**) Example activation maps from unfiltered model datasets with isotropic conduction of 50 cm/s, but with 10% and 30% signal noise. (**i**) Measured CV using multi-vector method (5×5 pixel window) from unfiltered (Black), temporally filtered (Savitzky-Golay, Blue), Spatially filtered (3×3 Gaussian, Green) and 10 beat ensemble averaged (Red) model datasets at increasing noise levels, n = 5 at each noise level.

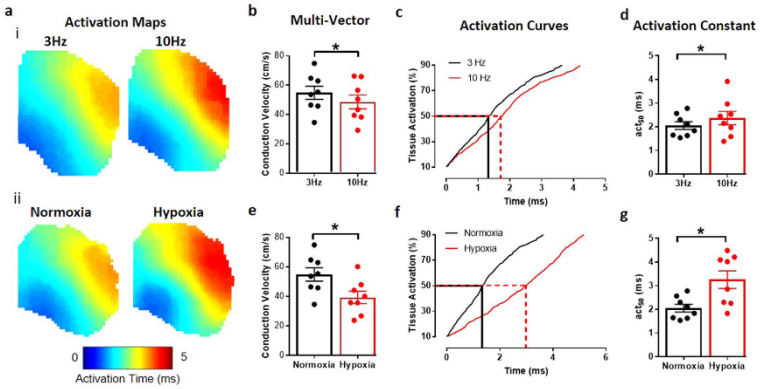

Figure 4. Validation of conduction velocity quantification methods in murine atria. (**a**) Activation maps from murine atria at 3 Hz and 10 Hz pacing (i), and during normoxia and hypoxia (ii). (**b**) Pacing at 10 Hz slows CV, measured using multi-vector method. (**c**) Representative activation curve showing prolongation of activation at 10 Hz vs 3 Hz pacing. (**d**) Pacing at 10 Hz slows CV, measured by time to 50% activation (act_{50}). (**e**) CV slowing induced by hypoxia, measured using multi-vector method. (**f**) Representative activation curve showing prolongation of activation curve by hypoxia. (**g**) Hypoxia slows CV, measured by time to 50% activation (act_{50}). Grouped data displayed as mean ± standard error, n = 8, *P < 0.05 by paired t-test.

Human Optical Mapping and Electrogram Recordings. ElectroMap's utility extends to human tissue, see Fig. 8a for optical mapping of human atrial appendages. We also looked to test whether ElectroMap can be applied to analysis of clinically relevant mapping technologies. Right atrial virtual electrograms from a patient during sinus rhythm and AF were recorded and analysed after QRST subtraction[22]. During sinus rhythm, the spread of activation was calculated from the timing of dV/dt_{min} in each electrogram, generating an activation map (Fig. 8b). ElectroMap clearly identified higher DF components (Fig. 8c) during AF in the physiological range of 4–10 Hz (DF range can be set within ElectroMap's interface). Additionally, marked phase discontinuities (Fig. 8d and Supplementary Video III) are observed in the electrogram recordings during AF. These findings are confirmed using previously published algorithms[22] with similar areas of high dominant frequency and discontinuous phase behaviour identified (Fig. 8e,f).

Additional Features. ElectroMap analysis options further extend to measure diastolic interval (DI) and time to peak. DI is measured from APD90 to the following activation time, which can be difficult to quantify in low SNR samples on a single beat. To validate the DI function, guinea pig hearts were loaded with Di-8-ANEPPS and pacing cycle length was decreased in 10 ms intervals from 170 ms to 110 ms. Ensemble averaging of 10 beat segments was used to produce an 'average beat diastolic interval', with improved SNR, and DI mapping function was validated by plotting DI-APD restitution curves (Supplementary Fig. VIII). Both APD50 and DI decrease more rapidly at higher pacing frequencies as previously demonstrated[31].

Optogenetic excitation and pacing via light pulses in cardiac tissue expressing light sensitive ion channels is a novel research tool[32,33] and may even be used for cardiac pacing in patients[34]. However, introduction of large amplitude light pulses will distort optical mapping images and thus preclude processing and analysis of such data. To this end, ElectroMap integrates a pacing artefact removal algorithm (Supplementary Fig. IX), which can identify and correct for light-pacing peaks, thereby allowing processing and analysis of previously obscured data.

Discussion

This work presents the development and validation of a novel open-source software for analysing and mapping optical and electrical signals. We demonstrate the compatibility of ElectroMap with a variety of camera types, species and experimental models. Key features include comprehensive measurement, analysis and mapping of global and regional conduction, versatile signal segmentation and semi-automated high-throughput analysis of action potential and its spatial and temporal (beat-to-beat) variations, calcium transients, and cardiac alternans. Using model and real data, we demonstrate the application of ElectroMap for analysis, measurement and mapping of basic and complex electrophysiology and its utility in dissecting pro-arrhythmic mechanisms *in vitro* and *in vivo*.

ElectroMap is built on years of international research and development in optical mapping processing and analysis, described in many excellent papers and reviews[6,14,15,18,35,36]. Algorithms that ElectroMap relies on have previously been validated against monophasic and transmembrane potentials in murine atria[15]. Further validation performed against established open-source (Rhythm[14]) and commercially available software (Optiq, Cairn Research, UK) yielded similar APD values and activation maps (Supplementary Fig. X). To the best of our knowledge, this is the first such comparison of commonly used analysis algorithms, which should help instil confidence

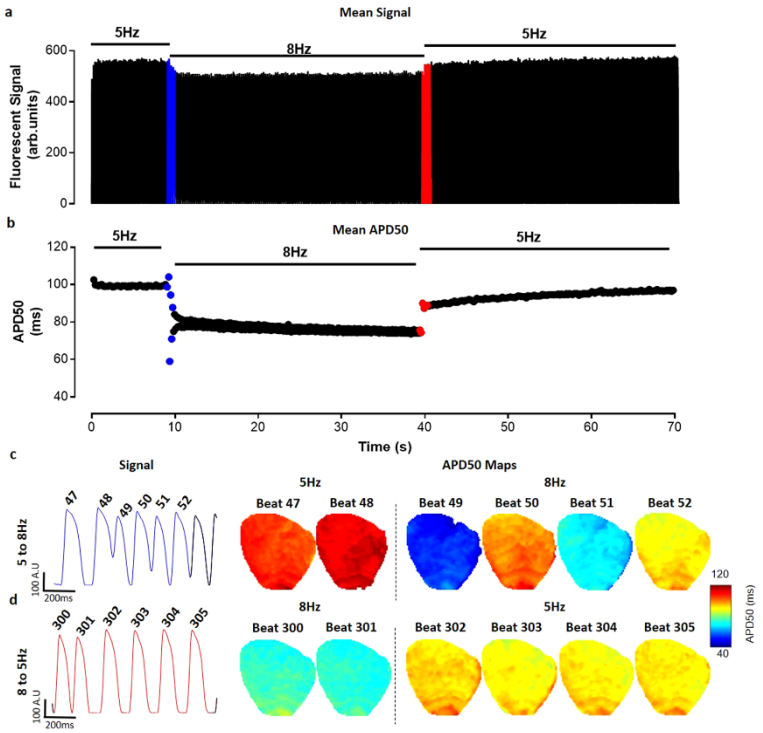

Figure 5. Beat to beat analysis of whole guinea pig heart. (**a**) Tissue averaged fluorescent signal from voltage dye loaded guinea pig heart across 70 s experiment. (**b**) Graph of whole heart beat-to-beat changes in mean APD50. (**c**) Raw trace and whole heart APD50 maps prior to (beats 47 & 48) and immediately after (beats 49–52) pacing frequency increase from 5 Hz to 8 Hz (blue in A and B). (**d**) Raw trace and whole heart APD50 maps prior to (beats 300 & 301) and immediately after (beats 302–305) pacing frequency return to 5 Hz.

in interpretation of data generated thus far. Importantly, ElectroMap provides further functionalities and outputs, not widely available currently, including ensemble averaging, multiple CV methodologies, automatic frequency detection, signal segmentation, alternans analysis and decay constant mapping. The use of ElectroMap extends beyond optical mapping, allowing for its application in clinical settings with electrogram array data.

Robust validation studies performed using both model and experimental data demonstrate ElectroMap's utility for accurately quantifying key parameters of electrical function and calcium release across cardiac tissue. CV quantification in model data with noise verified that processing using ElectroMap allows accurate parameter quantification. In this case, ensemble averaging proved the most effective processing strategy due to the randomness of the noise and the underlying identical morphology of all simulated action potentials. In other circumstances, (e.g. beat-to-beat variations) ensemble averaging of signals should be avoided, necessitating distinct processing strategies such as spatial filtering, temporal filtering and baseline correction which are all employable using ElectroMap.

Additionally, we demonstrate that improved processing speeds with automatic or user defined signal segmentation enable more complex and computationally challenging analyses; e.g. beat-to-beat variations in APD or regional differences in calcium decay. Indeed, we demonstrate that using ElectroMap, rapid and straightforward analysis of long experimental datasets can reveal acute periods of pro-arrhythmic EP behaviour throughout the entire guinea pig myocardium (Fig. 5). Such analysis would otherwise be missed by ensemble averaging of multiple beats or analysis of a single beat. ElectroMap, in contrast, provides rapid analysis of these complex EP parameters and exports to video and spreadsheet formats that facilitate interpretation of the observed patterns. This may be of particular importance when examining the pathophysiological effects of rapid changes in heart rate and/or immediate and prolonged responses to stimuli such as adrenaline or acute ischaemia. With improving SNR through better cameras and dyes, there is an increasing demand for beat-to-beat analysis of mapping data[37,38]. We

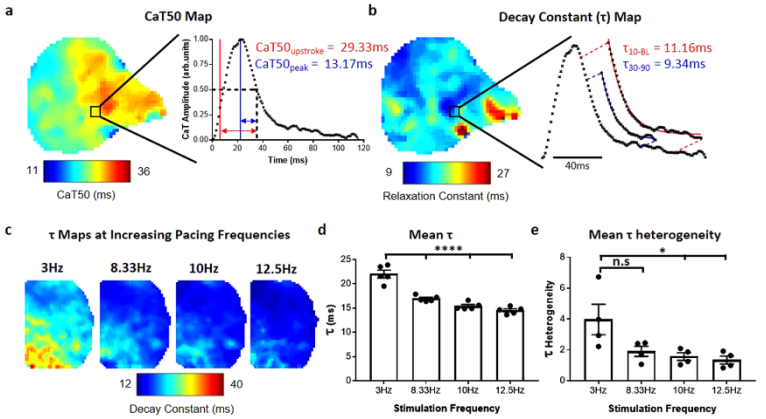

Figure 6. Calcium analysis and decay constant validation. (**a**) CaT50 map from murine atrium as measured from time of maximum upstroke velocity to 50% decay, illustrated in red in region of interest signal ($CaT50_{upstroke}$). Also shown is the measurement of CaT50 from peak amplitude in region of interest (blue, $CaT50_{peak}$ map in Supplementary Fig. VA). (**b**) Map of decay constant, τ, from the same atrium. Map shows calculation of τ by fitting of exponential decay points between 30% and 90% decay from peak ($\tau_{30\ 90}$), illustrated for the regional signal in blue. Also shown is calculation of τ between 10% decay and baseline (red, $\tau_{10\text{-}BL}$ map in Supplementary Fig. VD). (**c**) Representative τ maps ($\tau_{30\text{-}90}$) from murine left atria as pacing frequency is increased. (**d**) Data showing shortening of mean τ across the atria with increased pacing frequency. (**e**) Data showing decrease of τ heterogeneity (measured as standard deviation of mean τ across individual atria) across the atria with increased pacing frequency. Data displayed as mean + standard error, n = 5. $P < 0.05$, One-Way ANOVA followed by Bonferroni multiple comparison test against 3 Hz pacing.

anticipate that ElectroMap's ability to achieve such analysis in a high-throughput semi-automated manner will prove valuable for preclinical and clinical researchers.

The ability to simultaneously use three CV quantification methods is a key feature of ElectroMap. This is essential due to inherent limitations of each individual methodology for analysis of cardiac CV[18,24]. Here, we demonstrate that single vector method can suffer from significant user-generated overestimation of CV (see Supplementary Fig. IVA). More automated approaches have been proposed, such as that of Doshi *et al.*[39] whereby single vector quantification is limited to areas where activation time linearly increases. Within ElectroMap's conduction module, we have looked to overcome and highlight difficulties with the single vector method via an automatic angular sweep of measured CV from a user chosen point, as in Fig. 3e and Supplementary Fig. IVA. This approach reveals inherent variability that stems from user-defined propagation direction. ElectroMap automatically identifies the slowest conduction direction, which, in normal circumstances, will be parallel to wavefront propagation. The angular sweep additionally allows straightforward identification of longitudinal and transverse CVs[40,41].

Application of multi-vector method reduces the likelihood of user-introduced errors but does not eliminate them completely. Simulation studies by Linnenbank *et al.*[18] for instance demonstrate that despite increased automation, multi-vector methods can introduce systematic errors in CV quantification. The successful use of the method requires minimum criteria to be met in terms of grid size, local region size and angular binning for identification of propagation directions. Another problem can stem from inability to fit local vectors to some areas of the tissue. For example, activation definitions that are intrinsically limited to sampling rate (such as upstroke) can result in local regions where measured activation time is the same throughout. In such circumstances, meaningful surface fit (e.g. Fig. 2b) or other methods for describing local activation such as finite difference analysis[42], are not achievable[24]. This can be particularly problematic in small tissue samples, like isolated murine left atria, or in tissues exhibiting fast conduction and/or wavebreak. Viable solutions to this issue include interpolation of data between sampling points or use of alternative activation definitions such as depolarisation midpoint (see Supplementary Fig. II and IV). However, this relies on accurate signal interpolation, not always achievable in practice[43]. Epicardial conduction velocity quantification can also be complicated by multiple breakthroughs in the endocardium leading to inaccurate CV estimation during complex arrhythmias[44] or in the absence of epicardial pacing. In conclusion, there is no universally applicable activation measure suited for every optical mapping experiment, further validating the need for integration of multiple activation and CV quantification methodologies within ElectroMap.

ElectroMap incorporates a novel activation curve method of conduction analysis. This method allows users to quantify the time taken to activate a defined tissue percentage or study the whole activation curve. The

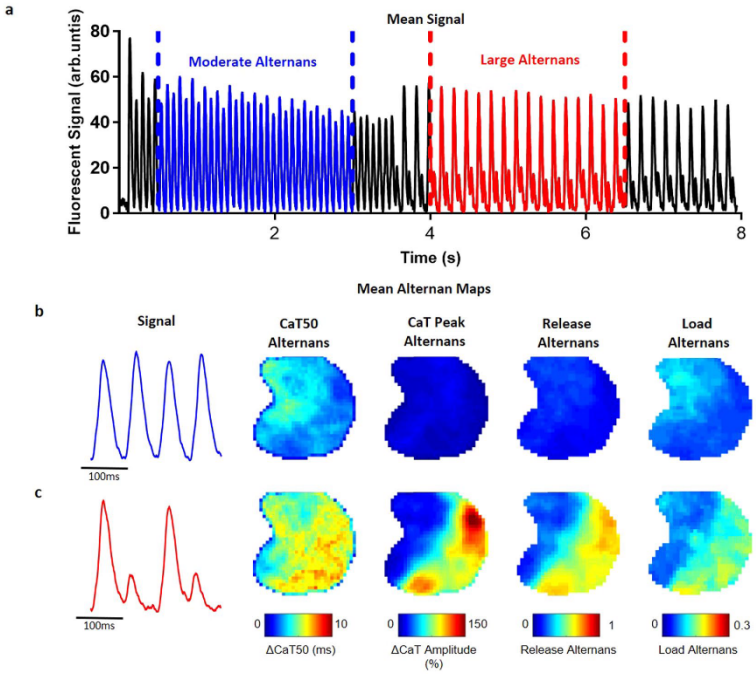

Figure 7. Alternans module. (**a**) Tissue averaged fluorescent signal from calcium dye loaded mouse atrium paced at 12.5 Hz, showing distinct alternans behaviour at 0.5–3 s (blue, moderate alternans), and 4–6.5 s (red, large alternans). (**b**) Representative signals and time averaged alternans maps from tissue during moderate alternans behaviour. Four maps shown correspond to the four measures of alternans available in ElectroMap (see methods and Supplementary Fig. VI). (**c**) Maps during period of large alternans (4–6.5 s) show increase in alternans amplitude, and clear spatial discordance.

methodology is less susceptible to user bias or to sparsity of local vectors in areas of rapid conduction as it does not rely on user input or vector calculation. Furthermore, activation time can be normalized to tissue size, yielding an activation constant in units such as ms/mm^2. This extends the use of the activation constant to studies where tissue morphology may be altered, such as in hypertrophy or genotype dependent differences in cardiac structure. However, activation constant only provides a summarised measure of activation, thus a combination of analysis methods may be required for robust interrogation of cardiac conduction. Additionally, despite the various CV methods within ElectroMap, conduction analysis can remain challenging if the underlying activation pattern is heterogeneous, often observed in arrhythmic tissue and cultured cardiac monolayers[45]. The 'Ccoffinn' method of Tomek *et al.*[24] combines sophisticated image processing techniques with novel wavefront tracking algorithms and can potentially overcome heterogeneity issues[24].

Defining activation times for APD and CaT duration mapping is an important but complex and often poorly understood analysis option. Different studies utilize distinct features of the upstroke to define activation, including dF/dt_{max} (upstroke)[44], d^2F/dt^2_{max} (start)[46], depolarization midpoint[47] and peak[8]. Similarly, time of repolarisation/decay can be measured at a defined repolarisation percentage[15,48], dF/dt_{min} (downstroke) or d^2F/dt^2_{max}[36]. The parameters best suited for duration measurement will depend on experimental model, signal quality and experimental question. We have integrated all of these user-selectable definitions within ElectroMap for both APD (Supplementary Fig. II) and CaT mapping (Fig. 6a and Supplementary Fig. VI).

Similarly, τ calculations can be customised in ElectroMap's interface to calculate decay constant for any user-defined segment of the calcium reuptake. This permits analysis of cytosolic or SR[23] calcium handling kinetics in different animal species and cells. For example, note the regional discrepancy between CaT50 and τ atrial maps in Fig. 6a,b. This contrast results from the definition in CaT50 used, i.e. time from upstroke to 50% decay ($CaT50_{upstroke}$). $CaT50_{upstroke}$ is a measure of both the release and reuptake of the cytosolic calcium. In contrast, τ depends only on reuptake kinetics, and so is unaffected by the changes in calcium release. By measuring CaT

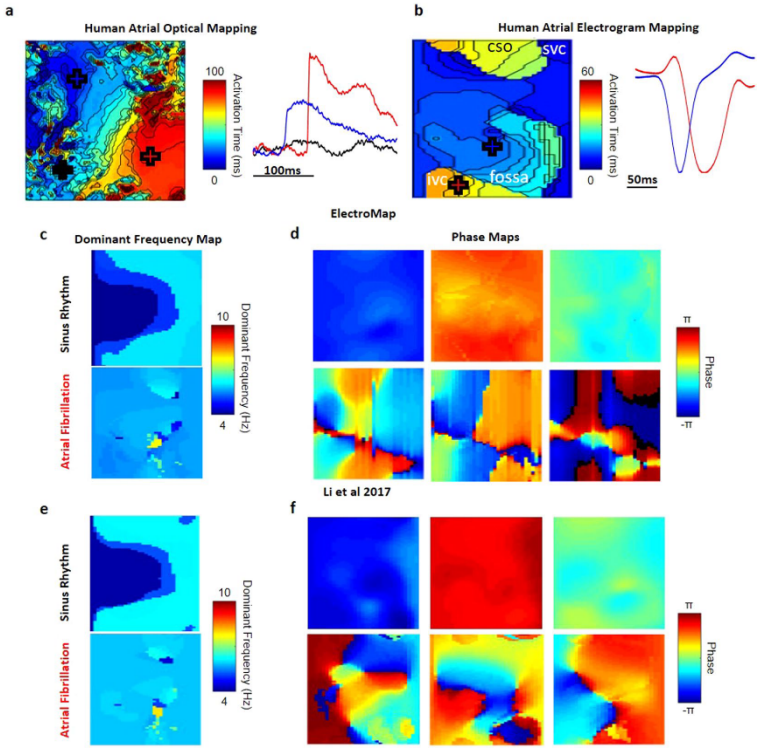

Figure 8. Human atrial optical and electrogram mapping analysis. (**a**) Activation map and example signals generated from human left atrial appendage stained with voltage sensitive dye. (**b**) Activation map and example signals generated from human right atrial *in vivo* electrogram array recordings. Labels refer to closest anatomical structure on 2D map - IVC and SVC: Inferior and Superior Vena Cava, CSO – Coronary Sinus Ostium, Fossa - Fossa Ovalis. (**c**) Dominant Frequency analysis between 4 and 10 Hz, showing localized area of increased frequency during AF. (**d**) Phase maps at 3 time points during sinus rhythm and AF. Synchronised phase behaviour during sinus rhythm is not replicated during AF. The displayed frames are taken from phase mapping over 30 s, Supplementary Video II. (**e**) Dominant Frequency analysis and (**f**) Phase maps at 3 time points during sinus rhythm and AF performed using previously published algorithms of similar datasets[22].

from peak ($CaT50_{peak}$), the CaT50 and τ values become more similar across the atria (Supplementary Fig. VI). Deciphering pathophysiological relevance of these observations is not within the remit of this manuscript. However, we predict the user-defined tools for comprehensive measurement of vital duration and relaxation parameters that ElectroMap provides will aid understanding of cardiac pathophysiology.

The utility of processing and analysis algorithms in ElectroMap can extend beyond optical mapping. Here, we show analysis of *in vivo* virtual unipolar electrogram recordings from human right atrium (Fig. 8b–d). Despite the contrasting waveforms compared to optical mapping, by analysing the timing of dV/dt_{min} in electrogram recordings, ElectroMap is able to accurately calculate local activation times. Beyond its clinical utility, access to analyses such as dominant frequency and phase mapping, allowing mapping the site of triggered activity during arrhythmia (Fig. 8c,d), can aid the translation of experimental data[10,49]. These capabilities of ElectroMap require further systematic validation against a range of clinically used platforms, however current outputs are comparable to previous published analysis of similar datasets[22], see Fig. 8c–f. Implementation of other analysis options available within ElectroMap such as beat-to-beat segmentation, CV quantification and alternans detection and quantification hold immense potential for the analysis of electrogram data.

ElectroMap provides a robustly validated open-source flexible tool for processing and analysis of optical mapping data. We anticipate ElectroMap to facilitate increased uptake of optical mapping in cardiac electrophysiology. Furthermore, application of novel data analysis strategies developed here will further our understanding of

the mechanisms underpinning lethal arrhythmia. The application of ElectroMap extends beyond optical mapping. Here, we have demonstrated that ElectroMap can also be used in the analysis of clinical electrogram-based mapping data. Moreover, application of high-throughput CV quantification methodologies can be applied to drug-screening pipelines for cardiotoxic effects in cell monolayers. There is scope to broaden the existing functions of ElectroMap, for example, by introducing dual-analysis of simultaneous voltage and calcium recordings and implementing computational approaches to overcome motion artefacts[50]. Furthermore, increases in computational efficiency through more sophisticated computational techniques, such as parallel processing, would allow for faster data processing and could eventually facilitate in-acquisition analysis.

References

1. Mozaffarian, D. *et al.* Heart disease and stroke statistics-2016 update a report from the American Heart Association. *Circulation* **133** (2016).
2. Kirchhof, P. *et al.* The continuum of personalized cardiovascular medicine: A position paper of the European Society of Cardiology. *Eur. Heart J.* **35**, 3250–3257 (2014).
3. Atienza, F., Martins, R. P. & Jalife, J. Translational research in atrial fibrillation: A quest for mechanistically based diagnosis and therapy. *Circ. Arrhythmia Electrophysiol.* **5**, 1207–1215 (2012).
4. Herron, T. J., Lee, P. & Jalife, J. Optical imaging of voltage and calcium in cardiac cells & tissues. *Circ. Res.* **110**, 609–623 (2012).
5. Jalife, J. Rotors and spiral waves in atrial fibrillation. *J. Cardiovasc. Electrophysiol.* **14**, 776–780 (2003).
6. Myles, R. C., Wang, L., Kang, C., Bers, D. M. & Ripplinger, C. M. Local β-adrenergic stimulation overcomes source-sink mismatch to generate focal arrhythmia. *Circ. Res.* **110**, 1454–1464 (2012).
7. Syeda, F. *et al.* PITX2 Modulates Atrial Membrane Potential and the Antiarrhythmic Effects of Sodium-Channel Blockers (2016).
8. Winter, J. *et al.* Sympathetic nervous regulation of cardiac alternans in the intact heart. *Front. Physiol.* **9**, 1–12 (2018).
9. Desk, R., Williams, L. & Health, W. K. Total Excitation of the Isolated Human Heart Total Excitation of the Isolated Human Heart. *Circulation* **41**, 899–912 (1970).
10. de Groot, N. M. S. *et al.* Electropathological Substrate of Longstanding Persistent Atrial Fibrillation in Patients With Structural Heart Disease. *Circulation* **122**, 1674–1682 (2010).
11. Allessie, M. A., Bonke, F. I. M. & Schopman, F. J. G. Circus movement in rabbit atrial muscle as a mechanism of tachycardia. III. The 'leading circle' concept: a new model of circus movement in cardiac tissue without the involvement of an anatomical obstacle. *Circ. Res.* **41**, 9–18 (1977).
12. Schotten, U., Verheule, S., Kirchhof, P. & Goette, A. Pathophysiological Mechanisms of Atrial Fibrillation: A Translational Appraisal. *Physiol. Rev.* **91**, 265–325 (2011).
13. Heijman, J., Guichard, J.-B., Dobrev, D. & Nattel, S. Translational Challenges in Atrial Fibrillation. *Circ. Res.* **122**, 752–773 (2018).
14. Laughner, J. I., Ng, F. S., Sulkin, M. S., Arthur, R. M. & Efimov, I. R. Processing and analysis of cardiac optical mapping data obtained with potentiometric dyes. *AJP Hear. Circ. Physiol.* **303**, H753–H765 (2012).
15. Yu, T. Y. *et al.* An automated system using spatial oversampling for optical mapping in murine atria. Development and validation with monophasic and transmembrane action potentials. *Prog. Biophys. Mol. Biol.* **115**, 340–348 (2014).
16. Yu, T. Y. *et al.* Optical mapping design for murine atrial electrophysiology. *Comput. Methods Biomech. Biomed. Eng. Imaging Vis.* **5**, 368–378 (2017).
17. Holmes, A. P. *et al.* A Regional Reduction in Ito and IKACh in the Murine Posterior Left Atrial Myocardium Is Associated with Action Potential Prolongation and Increased Ectopic Activity. *PLoS One* **11**, e0154077 (2016).
18. Linnenbank, A. C., de Bakker, J. M. T. & Coronel, R. How to measure propagation velocity in cardiac tissue: A simulation study. *Front. Physiol.* 5(JUL), 1–7 (2014).
19. Jaimes, R. 3rd. *et al.* A Technical Review of Optical Mapping of Intracellular Calcium within Myocardial Tissue. *Am. J. Physiol. Heart Circ. Physiol.* 2015 (2016).
20. Bayly, P. V. *et al.* Estimation of Conduction Velocity Vector Fields from Epicardial Mapping. *Data.* **45**, 563–571 (1998).
21. Krul, S. P. J. *et al.* Treatment of Atrial and Ventricular Arrhythmias Through Autonomic Modulation. *JACC Clin. Electrophysiol.* **1**, 496–508 (2015).
22. Li, X. *et al.* An interactive platform to guide catheter ablation in human persistent atrial fibrillation using dominant frequency, organization and phase mapping. *Comput. Methods Programs Biomed.* **141**, 83–92 (2017).
23. Wang, L. *et al.* Optical mapping of sarcoplasmic reticulum Ca2+ in the intact heart: Ryanodine receptor refractoriness during alternans and fibrillation. *Circ. Res.* **114**, 1410–1421 (2014).
24. Tomek, J., Burton, R. A. B. & Bub, G. Ccoffinn: Automated Wave Tracking in Cultured Cardiac Monolayers. *Biophys. J.* **111**, 1595–1599 (2016).
25. Weber, F. M. *et al.* Conduction velocity restitution of the human atriuman-An efficient measurement protocol for clinical electrophysiological studies. *IEEE Trans. Biomed. Eng.* **58**, 2648–2655 (2011).
26. Zeevi-Levin, N. *et al.* Gap junctional remodeling by hypoxia in cultured neonatal rat ventricular myocytes. *Cardiovasc. Res.* **66**, 64–73 (2005).
27. Fabritz, L. *et al.* Effect of pacing and mexiletine on dispersion of repolarisation and arrhythmias in ΔKPQ SCN5A (long QT3) mice. *Cardiovasc. Res.* **57**, 1085–1093 (2003).
28. Cheng, Y.-J. *et al.* Focal but reversible diastolic sheet dysfunction reflects regional calcium mishandling in dystrophic mdx mouse hearts. *AJP Hear. Circ. Physiol.* **303**, H559–H568 (2012).
29. Ng, G. A. Feasibility of selection of antiarrhythmic drug treatment on the basis of arrhythmogenic mechanism — Relevance of electrical restitution, wavebreak and rotors. *Pharmacol. Ther.* **176**, 1–12 (2017).
30. Weiss, J. N., Nivala, M., Garfinkel, A. & Qu, Z. Alternans and arrhythmias: From cell to heart. *Circ. Res.* **108**, 98–112 (2011).
31. Clayton, R. H. *et al.* Models of cardiac tissue electrophysiology: Progress, challenges and open questions. *Prog. Biophys. Mol. Biol.* **104**, 22–48 (2011).
32. Entcheva, E. & Bub, G. All-optical control of cardiac excitation: Combined high-resolution optogenetic actuation and optical mapping. *J. Physiol.* **9**, 2503–2510 (2016).
33. Feola, I. *et al.* Localized Optogenetic Targeting of Rotors in Atrial Cardiomyocyte Monolayers. *Circ. Arrhythmia Electrophysiol.* **10** (2017).
34. Nussinovitch, U. & Gepstein, L. Optogenetics for *in vivo* cardiac pacing and resynchronization therapies. *Nat. Biotechnol.* **33**, 750–754 (2015).
35. Jaimes, R. *et al.* A technical review of optical mapping of intracellular calcium within myocardial tissue. *Am. J. Physiol. - Hear. Circ. Physiol.* **310**, H1388–H1401 (2016).
36. Efimov, I. R., Huang, D. T., Rendt, J. M. & Salama, G. Optical mapping of repolarization and refractoriness from intact hearts. *Circulation* **90**, 1469–1480 (1994).
37. Kelly, A. *et al.* Normal interventricular differences in tissue architecture underlie right ventricular susceptibility to conduction abnormalities in a mouse model of Brugada syndrome. *Cardiovasc. Res.* 790–799 (2017).

38. Roney, C. H. *et al.* Rotor Tracking Using Phase of Electrograms Recorded During Atrial Fibrillation. *Ann. Biomed. Eng.* **45**, 910–923 (2017).
39. Doshi, A. N. *et al.* Feasibility of a semi-automated method for cardiac conduction velocity analysis of high-resolution activation maps. *Comput. Biol. Med.* **65**, 177–183 (2015).
40. Thompson, S. A. *et al.* Acute slowing of cardiac conduction in response to myofibroblast coupling to cardiomyocytes through N-cadherin. *J. Mol. Cell. Cardiol.* **68**, 29–37 (2014).
41. Egorov, Y. V., Glukhov, A. V., Efimov, I. R. & Rosenshtraukh, L. V. Hypothermia-induced spatially discordant action potential duration alternans and arrhythmogenesis in nonhibernating versus hibernating mammals. *Am J Physiol Hear. Circ Physiol* **303**, H1035–H1046 (2012).
42. Salama, G., Kanai, A. & Efimov, I. R. Subthreshold stimulation of Purkinje fibers interrupts ventricular tachycardia in intact hearts: Experimental study with voltage-sensitive dyes and imaging techniques. *Circ. Res.* **74**, 604–619 (1994).
43. Walton, R. D. *et al.* Extracting surface activation time from the optically recorded action potential in three-dimensional myocardium. *Biophys. J.* **102**, 30–38 (2012).
44. Glukhov, A. V. *et al.* Transmural dispersion of repolarization in failing and nonfailing human ventricle. *Circ. Res.* **106**, 981–991 (2010).
45. Tung, L. & Zhang, Y. Optical imaging of arrhythmias in tissue culture. *J. Electrocardiol.* **39**, 2–6 (2006).
46. Jaimes, R. *et al.* Functional response of the isolated, perfused normoxic heart to pyruvate dehydrogenase activation by dichloroacetate and pyruvate. *Pflugers Arch.* **468**, 131–142 (2016).
47. Kong, W., Ideker, R. E. & Fast, V. G. Transmural optical measurements of Vm dynamics during long-duration ventricular fibrillation in canine hearts. *Hear. Rhythm* **6**, 796–802 (2009).
48. Wang, K. *et al.* Cardiac tissue slices: preparation, handling, and successful optical mapping. *Am. J. Physiol. Heart Circ. Physiol.* **308**, H1112–25 (2015).
49. Salinet, J. *et al.* Propagation of meandering rotors surrounded by areas of high dominant frequency in persistent atrial fibrillation. *Hear. Rhythm* **14**, 1269–1278 (2017).
50. Christoph, J., Schröder-Schetelig, J. & Luther, S. Electromechanical optical mapping. *Prog. Biophys. Mol. Biol.* **130**, 150–169 (2017).

Acknowledgements

This work was funded by the EPSRC studentship (Sci-Phy-4-Health Centre for Doctoral Training L016346) to D.P., K.R. and L.F., Wellcome Trust Seed Award Grant (109604/Z/15/Z) to D.P., British Heart Foundation Grants (PG/17/55/33087, RG/17/15/33106) to D.P., European Union (grant agreement No 633196 [CATCH ME] to P.K. and L.F.), British Heart Foundation (FS/13/43/30324 to P.K. and L.F.; PG/17/30/32961 to P.K. and A.H.), and Leducq Foundation to P.K. J.W. is supported by the British Heart Foundation (FS/16/35/31952).

Author Contributions

C.O., A.H., T.Y., J.W., J.C., P.K., L.F., K.R. and D.P., designed the research. C.O., A.H., T.Y., J.W., S.W., B.B., J.d.G., G.C., X.L., G.N. and D.P., designed and conducted the experiments. C.O. and T.Y., designed and wrote the software. C.O. analysed the data. C.O., A.H., J.W., P.K., L.F., K.R., and D.P., wrote the paper.

Additional Information

Supplementary information accompanies this paper at https://doi.org/10.1038/s41598-018-38263-2.

Competing Interests: PK receives research support from several drug and device companies active in atrial fibrillation and has received honoraria from several such companies. LF has received institutional research grants from EU, BHF, MRC, DFG and Gilead. PK and LF are listed as inventors on two patents held by University of Birmingham (Atrial Fibrillation Therapy WO 2015140571, Markers for Atrial Fibrillation WO 2016012783). All other authors declare no potential conflict of interest.

Publisher's note: Springer Nature remains neutral with regard to jurisdictional claims in published maps and institutional affiliations.

Fwd: JoVE Reprint Permissions: Article 59663

nam.nguyen@jove.com
Yesterday, 14:01
Simon Wells (MDS/Univ Melb Joint PhD 3.5Yr)

Reply all

Inbox

Action Items

Hi Simon,

Thanks for reaching out.

Please consider this explicit permission to reuse the JoVE article in your thesis. Please ensure that JoVE is cited properly throughout.

If you have any further questions, please do not hesitate to contact me.

Best,

Nam Nguyen, Ph.D.
Manager of Review
JoVE
617.674.1888
Follow us: Facebook | Twitter | LinkedIn
About JoVE

---------- Forwarded message ---------
From: **JoVE** <no-reply@jove.com>
Date: Fri, Jun 12, 2020 at 12:34 AM
Subject: JoVE Reprint Permissions: Article 59663
To: <nam.nguyen@jove.com>
Cc: <editorial_office@jove.com>

jove

I am Simon Wells, an author of the JoVE article 59663. I want to use the following material from my article for the following purpose:

I would like to insert the entire article (text and Figures of the PDF published by JOVE) into a section of my PhD thesis. Can you please confirm whether this is possible and what permissions are required?

Best wishes,
Simon.

I can be reached at sxw113@student.bham.ac.uk

This message was sent to you by JoVE, the Journal of Visualized Experiments.
JoVE, One Alewife Center, Suite 200, Cambridge, MA 02140 | tel: 617.945.9051 | fax: 866.381.2236

jove Journal of Visualized Experiments www.jove.com

Video Article

High-Throughput Analysis of Optical Mapping Data Using ElectroMap

Christopher O'Shea[1,2,3], Andrew P. Holmes[1,4], Ting Y. Yu[1], James Winter[1], Simon P. Wells[1], Beth A. Parker[1], Dannie Fobian[1], Daniel M. Johnson[1], Joao Correia[5], Paulus Kirchhof[1], Larissa Fabritz[1], Kashif Rajpoot[3], Davor Pavlovic[1]

[1]Institute of Cardiovascular Sciences, University of Birmingham

[2]EPSRC Centre for Doctoral Training in Physical Sciences for Health, School of Chemistry, University of Birmingham

[3]School of Computer Science, University of Birmingham

[4]Institute of Clinical Sciences, University of Birmingham

[5]Institute of Microbiology and Infection, School of Biosciences, University of Birmingham

Correspondence to: Kashif Rajpoot at k.m.rajpoot@bham.ac.uk, Davor Pavlovic at D.Pavlovic@bham.ac.uk

URL: https://www.jove.com/video/59663
DOI: doi:10.3791/59663

Keywords: Medicine, Issue 148, cardiac optical mapping, software, electrophysiology, arrythmia, fluorescent sensors, action potential, calcium

Date Published: 6/4/2019

Citation: O'Shea, C., Holmes, A.P., Yu, T.Y., Winter, J., Wells, S.P., Parker, B.A., Fobian, D., Johnson, D.M., Correia, J., Kirchhof, P., Fabritz, L., Rajpoot, K., Pavlovic, D. High-Throughput Analysis of Optical Mapping Data Using ElectroMap. *J. Vis. Exp.* (148), e59663, doi:10.3791/59663 (2019).

Abstract

Optical mapping is an established technique for high spatio-temporal resolution study of cardiac electrophysiology in multi-cellular preparations. Here we present, in a step-by-step guide, the use of ElectroMap for analysis, quantification, and mapping of high-resolution voltage and calcium datasets acquired by optical mapping. ElectroMap analysis options cover a wide variety of key electrophysiological parameters, and the graphical user interface allows straightforward modification of pre-processing and parameter definitions, making ElectroMap applicable to a wide range of experimental models. We show how built-in pacing frequency detection and signal segmentation allows high-throughput analysis of entire experimental recordings, acute responses, and single beat-to-beat variability. Additionally, ElectroMap incorporates automated multi-beat averaging to improve signal quality of noisy datasets, and here we demonstrate how this feature can help elucidate electrophysiological changes that might otherwise go undetected when using single beat analysis. Custom modules are included within the software for detailed investigation of conduction, single file analysis, and alternans, as demonstrated here. This software platform can be used to enable and accelerate the processing, analysis, and mapping of complex cardiac electrophysiology.

Video Link

The video component of this article can be found at https://www.jove.com/video/59663/

Introduction

Optical mapping utilizes fluorescent reporters of voltage and/or calcium concentration to interrogate cardiac electrophysiology (EP) and calcium handling in multicellular preparations, with greater spatial resolution than achievable with traditional techniques[1,2,3]. Therefore, optical mapping has emerged as an important and ever increasingly utilized technique, providing key insights into physiological and pathophysiological electrical behavior in the heart[3,4,5,6,7,8]. Effective processing and analysis of data obtained from optical mapping experiments is complicated by several factors. The high spatiotemporal resolution nature of optical mapping datasets results in raw videos files composed of thousands of image frames, each made up of a number of individual pixels, giving rise to large data files that necessitate high-throughput and automated processing[9]. Small pixel sizes, poor and uneven dye loading and small fractional changes in fluorescence result in optical signals with low signal to noise ratio (SNR), requiring pre-processing before effective analysis is achievable[10]. Processing and analysis can be further complicated by the use of optogenetic pacing protocols which utilize light to initiate activation, potentially distorting the recorded signal from the fluorescent sensors[11,12]. Furthermore, once data has been processed, several non-consistent techniques and definitions can be applied to measure parameters of interest, with the most applicable techniques varying depending on experimental setup, model and question[2,10,13]. These limitations prevent further uptake of the technology and hinder truly objective analysis.

To overcome these limitations, several research groups have designed custom processing pipelines tailored towards their experimental model, question and hardware[7,14,15,16]. Others utilize commercial proprietary software where the underlying algorithms may be difficult to access[4,17]. As a result, there is a clear need for a freely available open-source software platform for processing and analysis of optical mapping data. It is important that this software is open-source, easy to use, flexible to parameter adjustment, applicable to a range of experimental models with distinct EP properties and crucially allows straightforward and tunable quantification of the range of cardiac parameters that can be studied using optical mapping.

We have recently published and released a comprehensive software platform, ElectroMap, for high-throughout, semi-automated processing, analysis and mapping of cardiac optical mapping datasets[13]. Here, we present a video manual for the utilization of ElectroMap and demonstrate

how it can be used to process, analyze and map several optical mapping datasets. We focus on the use of ElectroMap to quantify standard EP and calcium handling variables and demonstrate the use of standalone conduction velocity, single file analysis and alternans modules.

Protocol

1. Optical mapping data collection

1. Perform cardiac optical mapping using one of a wide range of experimental models including intact and isolated whole hearts[6,18], isolated atria[14,19], ventricular wedges[20], cardiac slices[21,22], and cellular monolayers[23]. See associated references for experimental designs to collect raw optical mapping data from these preparations. Provided that data obtained can be converted to a tiff stack or saved in a .MAT file, it should be analyzable using ElectroMap. This includes data of varying dimensions (square/rectangular) and resolutions (maximum tested currently 2048 pixels x 2048 pixels).

2. Software installation and start-up

NOTE: Below are detailed the two methods for installing and running ElectroMap – either within MATLAB run from the source (.m) code or as a standalone executable file (.exe for windows). The final software and its functionality are invariant between the two setup options (other than a few differences in directory navigation). Therefore, the main considerations for choosing version to install are access to MATLAB and required toolboxes and whether access to source code is desired. Where possible, it is recommended to use the MATLAB version for faster start up times, shorter processing times, and easier error reporting.

1. **Setup 1: Running electromap within MATLAB**
    1. Install MATLAB. ElectroMap was designed in MATLAB 2017a, however, software has been tested for use in all subsequent releases of MATLAB (up to 2018b at time of writing). The following toolboxes are required: Image Processing, Signal Processing, Statistics and Machine Learning, and Curve Fitting.
    2. Download/clone **all** files from the latest 'source code' release of ElectroMap from the GitHub repository (https://github.com/CXO531/ElectroMap). Unzip the downloaded contents to a desired location.
    3. Open MATLAB and navigate to the folder location hosting the ElectroMap source code. Then, open the file **ElectroMap.m** and press run in the editor, or alternatively type **ElectroMap** in the command window and press **RETURN**. This will start the ElectroMap user interface, **Figure 1A**.

2. **Setup 2: Standalone .exe file**
    1. Download the installer file: https://drive.google.com/open?id=1nJyl07w9Wlt5zWcit0aEylbtg31tANxI.
    2. Follow the instructions in the installer, which will download required the MATLAB runtime from the web alongside ElectroMap software.
    3. Run **ElectroMap.exe**.
    NOTE: Start up time for the standalone version can be several minutes.

3. Image loading and pre-processing

1. Press **Select Folder** and navigate to the location of the data file(s) to be analyzed. This will populate the left-hand listbox with all files within that directory that are of the correct file type (.tif or .MAT). .MAT files must only contain the image stack variable.
NOTE: Only folders and not individual files will appear as you navigate through the directory selector.
2. Select file to be loaded from within the interface and press **Load Images**.
    1. Once loaded, the first frame will appear, and the red outline will indicate automatic thresholding of the image. If needed, reload previously used ROIs by selecting **Save/Load ROI**. In this case, skip step 3.3.
    2. As default, thresholding is based on the pixel intensities in the first frame. If desired, modify this to a threshold based to the signal time course amplitude by changing the option in the **Image for threshold** dropdown menu. Please note that once the thresholding is selected, it is then applied for the whole image stack.

3. If desired, change the threshold option to **manual**, which will activate the slider to manually adjust the image threshold. Additionally, crop images (**Crop Image**) and/or draw a custom region of interest (**Custom ROI**) for analysis by selecting the appropriate tick box(es) below threshold options. Note that advanced options for region of interest selection such as number of areas are available from **ROI Selection** from the top menu.
4. Once an appropriate threshold has been applied, press **Process Images** to apply processing. Settings for processing are detailed below (step 3.4.1-3.4.5). At this point, ensure that the correct camera settings have been entered. These are **Pixel Size** in µm (IMPORTANT: this is the image pixel size, and not the size of the pixels that make up the chip or equivalent hardware in the imaging device) and **Framerate** in kHz.
    1. For signal inversion, tick the **Invert Data** checkbox to enable. If reported fluorescent signal is inversely proportional to parameter of interest (as with commonly used potentiometric dyes) the signal can be inverted.
    2. For spatial filtering, select **Gaussian** or **Average** from the kernel menu. The size of the spatially averaged area is controlled by the **Size** input adjacent to the **Kernel** dropdown menu (i.e. 3 results in 3 pixel x 3 pixel filter kernel). When applying a Gaussian filter, the standard deviation can also be set from the **Sigma** input.
    3. For baseline correction, select Top-hat[24] or polynomial (4^{th} or 11^{th} degree) correction[25] from the **Baseline** menu. Correction can be applied to each pixel individually (long processing time) or as an average of the entire image (quicker but assumes homogenous baseline alterations). Top-hat correction can also be modified by setting the **Top-Hat Length** in milliseconds, adjacent to the baseline selection dropdown menu. The length of the Top-Hat kernel should be greater than the timescale of the individual action potentials/ calcium transients.

4. For temporal filtering, select Savitzky-Goaly or infinite impulse (IIR) filtering from the **Filtering** menu.
   NOTE: Other than for the tissue averaged signal that appears in the bottom left, temporal filtering is applied to each pixel individually at time of parameter quantification from ensemble averaged image ranges. This has been implemented to reduce processing time by filtering small sections of data when required rather than entire files.
5. For frame removal, note that if the **Remove Frames** option is selected, large peaks with amplitude greater than the signal of interest can be removed from the image set. This may be useful in optically paced datasets such as optogenetic pacing where depolarization is initiated by optical activation of opsins such as channelrhodopsin 2[11,12].
   NOTE: As frame removal will potentially introduce unphysiological step changes into the image signals, temporal filtering may introduce artifacts to the data and so is not recommended here.

5. Note that signal will be segmented once **Process Images** has been selected according to the options under **Segmentation options**, however this can quickly be changed without reprocessing the entire dataset (see section 4).

4. Data segmentation and ensemble averaging

NOTE: Once the file has been processed, peaks in the tissue averaged signal (bottom right trace, **Figure 1A**) will have been detected and labelled by red circles. Only peaks above a set threshold (blue line on trace that is set by **Peak Threshold**) are counted. Additionally, peaks are only counted if they are sufficiently delayed compared to the previous peaks, set by the **Min Peak Distance** input. Signal is then segmented based on the detected peaks. First, the effective cycle length (CL) of each peak is calculated by measuring the time between it and the next peak. If a number of peaks (set by **Min Number of Peaks** input) have similar CLs (threshold for which is set by **Minimum Boundary** input) then they are grouped and the average CL for those peaks calculated.

1. For further segmentation of the data, press **Segment Signal**. Sub-segmentation options are: **None** – all peaks with same CL grouped together; **All** – Segments of n_{peaks} within the constant CL times (n_{peaks} is set by the **Segment size** input) are identified; **Last** – Final n_{peaks} before a CL change are identified and grouped, and all others are not analyzed; and **Single Beat** – This is equivalent to applying the **All** segmentation with n_{peaks} = 1, and so no grouping or ensemble averaging (see 4.5) are applied. This can be applied by selecting the **Single Beat** button.
   1. Apply custom segmentation of the signal by zooming in on a time of interest and selecting **Segment Signal**. This will add an additional option entitled **Zoomed Section** to the section list box, corresponding to the time points selected.

2. The results of the segmentation will appear in the list-box adjacent to the tissue averaged signal, and will show section number and the estimated CL. All segmented time sections are denoted by different colors. Select a segment from the list-box to highlight that section in red. This will also automatically trigger analyses of this section, as if the **Produce Maps** button was selected (see section 5).
3. Analyses of grouped peaks will be performed on the 'ensemble averaged' data. This involves averaging the peaks in a segment together, with the reference times being the peaks identified in step 4.2. Update the time window to average by modifying the **before** and **after** inputs and pressing **Segment Signal**.

5. Action potential/calcium transient duration and conduction velocity analysis

1. Once images have been processed, the **Produce Maps** button will become active. Press **Produce Maps** to apply action potential duration (APD), activation time, conduction velocity and SNR analysis. By default, the analysis will be applied to the first signal segment. Select other segments from the list-box will apply analysis to chosen segment.
   NOTE: Results of analysis are displayed in results table, including mean, standard deviation, standard error, variance and 5th to 95th percentile analysis. Duration maps are termed 'APD' maps however, calcium signals processed using the same settings will measure calcium transient duration.
2. Select **Get Pixel Info** to see a detailed display of the signal from any pixel within the image, and **Compare Pixels** to simultaneously plot signals from up to 6 locations.
   1. Use the **Signal Processing** panel to adjust settings for duration analysis. These are: **Duration** – Time of percentage repolarisation/ decay to measure from peak; **'APD' Baseline** – Time period of signal that is defined as reference baseline for amplitude measurements; and **'APD' Start time** – Start time for duration measurements. These are the same options for deciding the activation time for isochronal maps (discussed below) and are termed: Start (d^2F/dt^2_{max}), Upstroke (dF/dt_{max}), Depolarisation midpoint (time of 50% amplitude), Peak (time of maximum amplitude). These definitions applied to mouse and guinea pig action potentials are shown in **Figure 2A**.
      NOTE: Changing any of these options will automatically update the duration map and the results table. Map scale and outlier removal options are also available.

3. Conduction velocity is also measured automatically within the main software interface. This is achieved using the multi-vector method of Bayly et al[26] from the isochronal map defined by the chosen activation measure (discussed in step 5.4). Press **Activation Points** to render a 3D representation of the activation map.
4. The multi-vector conduction velocity measurement method spatially segments the isochronal map into regions of *n* x *n* pixels. Set the value of *n* using the **Local Window Size** input, and set the range of activation times to apply analysis to using the **Fitting activation times** inputs.
   NOTE: For each local region, a polynomial surface, *f*, is fitted that best describes the relationship between activation time and spatial position, (*x*,*y*). The gradient vector, CV_{local}, of this surface is then calculated as:
   $$CV_{local} = \nabla f(x,y) \quad (1)$$
   where ∇ denotes the two-dimensional cartesian spatial differential operator[26].
5. For each pixel in the isochronal map, a local vector representing speed and direction of conduction is calculated. Select **Isochronal Map with vectors** from the display dropdown menu to view this analysis.

6. SNR is calculated as the ratio of the maximum amplitude compared to the standard deviation of the signal at baseline. This analysis is performed post all processing steps. Press **SNR calculation** in the top menu to edit settings for the period of the signal defined as baseline.

6. Conduction analysis module

1. Press **Conduction** to access more detailed analysis of conduction velocity. This opens a separate module where conduction can be quantified using the Bayly multi-vector method as in the main interface, single vector methods, and as an activation curve.
2. Press **Single Vector** to analyze conduction using the single vector method, where CV is calculated from the delay in activation time between two points. This can be done using **Automatic** or **Manual** methods, selectable below the **Single Vector** button.
    1. For automatic single vector method, select a distance and start point from which to measure conduction. The software will then perform a 360-degree sweep from the selected point, measuring the time delay and calculating the associated conduction velocity along all directions in 1-degree increments. The results of this analysis are displayed in the graph adjacent to the map, and the direction of slowest conduction is shown in red.
    2. For manual single vector method, choose both a start and end point from the isochronal map to calculate conduction velocity. To select a new start point, press **Clear Start Point**.
3. Press **Local Vector** to apply the multi vector method, with the settings matching those from the main interface. Within the conduction module, the distribution of conduction speeds, as well as the angular distribution of calculated vectors and angular dependence of conduction speed can be displayed.
4. Press activation curve to plot the percentage of tissue activated as a function of time. Time to 100% activation is automatically displayed, while custom values for minimum (blue) and maximum (red) activation percentages between which to measure can also be selected.

7. Additional analyses and modules

1. Aside from automatically performed duration and conduction velocity analyses, several other parameters can be quantified using ElectroMap. These analyses are selectable from the dropdown menu above the display map. Select one of these options to perform the analysis, and the results will appear in the 4th row of the results table: 1) **Diastolic Interval** – Time from 90% repolarization to activation time of the next action potential; 2) **Dominant Frequency** – Frequency spectrum of each pixel is calculated using the fast Fourier Transform, and the frequency with the most power is defined as the dominant frequency. Advanced range and window settings for dominant frequency analysis are available by selecting **Frequency Mapping**; 3) **Time to peak** – The rise time between two user selected percentages (default 10 to 90%) of the depolarization phase of the action potential or the release of calcium. Percentage values can be changed by selecting **TTP Settings**; and 4) **Relaxation constant** (τ) – Relaxation constant is calculated by fitting a mono-exponential decay of the form of the form:
   $F(t) = F_0 e^{-t/\tau} + C$ (2)
   where the fluorescence level at time *t* depends on the peak fluorescence, F_0, and the subsequent decay (*C* is a constant)[27]. The value between which to fit equation 2 are selectable within the main ElectroMap user interfaces, as well as a goodness of fit exclusion criteria based on the r^2 value.
2. Press **Single File Analysis** to open a dedicated module for high-throughput duration and conduction analysis of each identified segment in a file. Analysis can be performed on either the whole image (duration, conduction and activation time) or on selected regions or points of interest (currently duration only). Results are outputted to a .csv file.
   NOTE: For APD values from the whole image, the first column in the .csv file is the mean, while the second column is the standard deviation.
3. Press **Alternans** to initiate a standalone module for dedicated analysis and mapping of beat-to-beat variability. See O'Shea et al. 2019[13] for details on alternans processing and analysis options. Specifically, this module is designed to identify two period oscillations, known as alternans. Both duration and amplitude alternans are calculated and outputted.
   NOTE: Duration alternans are measured by comparing the duration measurement from one peak to the next; i.e. if peak one and two and APD_1 and APD_2 respectively, then the duration alternan (ΔAPD) is calculated as
   $\Delta APD = |APD_1 - APD_2|$ (3)
   The duration measurement is performed using the settings in the main interface. Meanwhile, amplitude alternans can be quantified and mapped across multi-cellular preparations as absolute change (defined as a percentage where 0% = same amplitude between one beat and the next). Furthermore, the effects of phenomena such as calcium load can be further investigated by measuring and comparing **Load** and **Release** alternans, as has been previously reported[28]. If *L* is defined as the peak amplitude of the large beats (i.e. where the amplitude is greater than the previous beat), *S* the amplitude of the small beats, and *D* the diastolic load of the small beats, the release alternans ($ALT_{release}$) are defined as:
   $ALT_{release} = 1 - (S/L)$ (4)
   Conversely, load alternans (ALT_{load}) are defined as:
   $ALT_{load} = D/L$ (5)
   Alternans measurements can be made across the whole tissue, and the results of the analysis are displayed in the bottom right of the module. When first using the module, the analysis is performed across the entire experimental file, and the results displayed are an average beat-beat difference across the whole file. However, analysis can be restricted to specific times in the file by de-selecting **Hold Zoom**, zooming in on a specific time period, and selecting **Analyse Zoomed Section**. This will update the results panel to show analysis from the selected time period.
    1. Select play to show a beat-to-beat video of the alternans analysis. Additionally, select **Create Mean Map** to export a map of the alternans behavior averaged from the selecting time points, which are set in the pop-up menu when using this feature.
4. Press **Phase Map** to initiate the phase mapping module. A Hilbert transform is performed to calculate the instantaneous phase (between -π and +π) of the signals at each timepoint. Press play or drag slider to visualize phase behavior over time and click on a pixel to render a phase diagram.

8. Exporting data

1. Data is exported from ElectroMap in a variety of forms. Press **Export Values** to save the values of the currently displayed map in the main used interface. Measured values can be saved as either a map (preserving pixel locations) or condensed into a single list, and can be saved as .csv,.txt or .MAT files.
2. Press **Export Map** to bring up a pop-up containing the currently displayed map, which can then be saved in a variety of image formats. Display options for the map are controlled by selecting **Map Settings** but can also be edited once **Export Map** has been selected. For example, a color bar can be added by selecting this icon from the top menu, and the scale can be set by selecting **Edit** > **Colormap**.
3. Press **Activation Video** to render an animation of the activation sequence, which can be saved as an animated .gif file.
4. Press **Segment Video** to save a .avi video file of the currently displayed parameter of each identified segment.

Representative Results

All work performed as part of this study was undertaken in accordance with ethical guidelines set out by the UK Animals (Scientific Procedures) Act 1986 and Directive 2010/63/EU of the European Parliament on the protection of animals used for scientific purposes. Experiments were approved by the home office (mouse: PPL 30/2967 and PFDAAF77F, guinea pig: PPL PF75E5F7F) and the institutional review boards at University of Birmingham (mouse) and King's College London (guinea pig). Detailed methods for collection of the raw data that has been analyzed here can be found in our previous publications[5,6,14,19].

The main interface from which ElectroMap is controlled is shown in **Figure 1A**. The necessary steps to analyze a dataset are controlled primarily by the **Load Images**, **Process Images**, and **Produce Maps** buttons, and are shown highlighted in green, blue, and red, respectively in **Figure 1A**. **Figure 1B-D** shows the operations that occur on selection of each of these buttons. **Load Images** applies the image thresholding options as selected by the user (**Figure 1B**), while **Process Images** (**Figure 1C**) applies filtering and baseline correction. Finally, **Produce Maps** will first average data according to the time window and segmentation settings (unless single beat segmentation is chosen) and then perform analyses described above.

A key aspect of ElectroMap is its flexibility with respect to camera type and experimental model. This is crucial for the utility of an optical mapping software due to the distinct cardiac EP and anatomical characteristics that exist between widely used models. **Figure 2A** for example shows the action potential morphology of the murine atria when compared to the guinea pig ventricle, recorded using voltage sensitive dyes as previously reported[6,14]. Despite the distinct shape of the action potential, and the use of two separate optical mapping cameras with different framerates and pixel sizes, ElectroMap can be utilized to successfully analyze both datasets. However, this requires modification of some parameters within the user interface (**Figure 2B**). Note that the prolonged guinea pig action potential necessitates a larger time window. Additionally, to prevent top-hat baseline correction unphysiologically modifying the optically recorded signals, its time length must be increased so that it is greater than the time course of the action potential.

ElectroMap offers a multitude of processing options to help improve the SNR of optically recorded signals which may be required to effectively recover EP parameters. An example is automated ensemble averaging of peaks following data segmentation. **Figure 3A-C** demonstrates how the application of ensemble averaging, in lieu of other methods, can improve SNR from isolated murine left atria (n = 13). This reduces measurement heterogeneity and likelihood of analysis failure (**Figure 3D**). For example, a change of pacing frequency from 3 Hz to 10 Hz did not alter APD_{50}, when no ensemble averaging is undertaken, yet an expected[29] decrease in APD_{50} at 10 Hz pacing was observed when measured from ensemble averaged data (**Figure 3E**).

Figure 4 demonstrates the efficacy and utility of automated pacing frequency detection and segmentation offered by ElectroMap. Here, mouse left atria (n = 5) were paced at a 120 ms cycle length and cycle length was incrementally shortened by 10 ms until it reached 50 ms. ElectroMap automatically identified the pacing cycle length and grouped tissue averaged peaks accordingly (**Figure 4A**). This was achieved with high accuracy in all datasets (**Figure 4B**). Automated segmentation of the data allowed straightforward and high throughput analysis of the slowing of conduction velocity with increased pacing frequency/shortened cycle length (**Figure 4C,D**). Concurrently, APD_{50} (**Figure 4E**) and diastolic interval (**Figure 4F**) shortened. Amplitude of the optically measured peaks decreased, while time to peak increased **(Figure 4G,H**). These are again the expected restitution responses in cardiac tissue[29,30] and use of ElectroMap can help therefore elucidate changes in response to pacing frequency in presence of pharmacological agents, genetic modification, or disease states.

An important consideration in the use of a software such as ElectroMap is the presence of artifacts in the underlying data. **Figure 5**, for example demonstrates that motion artifacts (the distortion of the optically recorded signal by tissue movement) can preclude accurate measurements of activation and especially repolarization within ElectroMap. See Discussion for further considerations.

jove Journal of Visualized Experiments www.jove.com

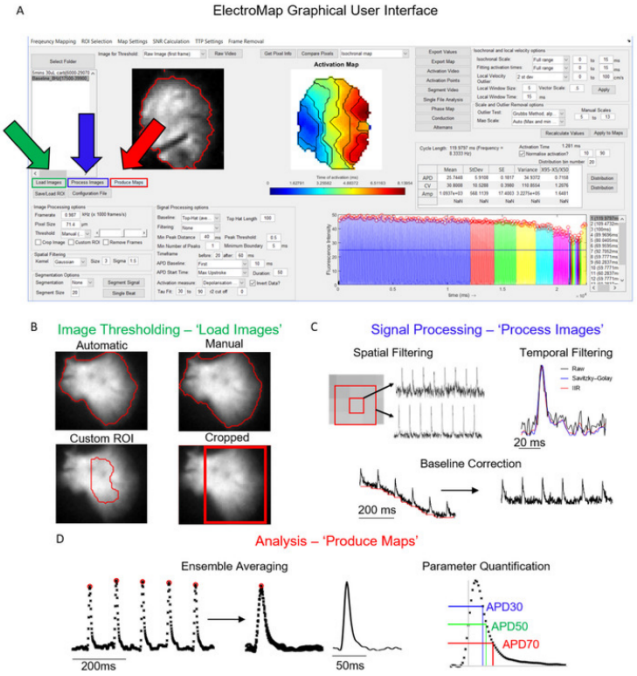

Figure 1: ElectroMap main processing steps. (**A**) Graphical user interface of ElectroMap, with the **Load Images** (green), **Process Images** (blue), and **Produce Maps** (red) buttons highlighted. (**B**) Image thresholding options that can be applied on selecting **Load Images**. (**C**) Signal processing options available to the user include spatial and temporal filtering and baseline correction and can be applied to the image stack by pressing **Process Images**. (**D**) Ensemble averaging and parameter quantification (shown APD measurement) that is activated by selecting **Produce Maps**. Figure adapted from O'Shea et al., 2019[13]. Please click here to view a larger version of this figure.

jove Journal of Visualized Experiments www.jove.com

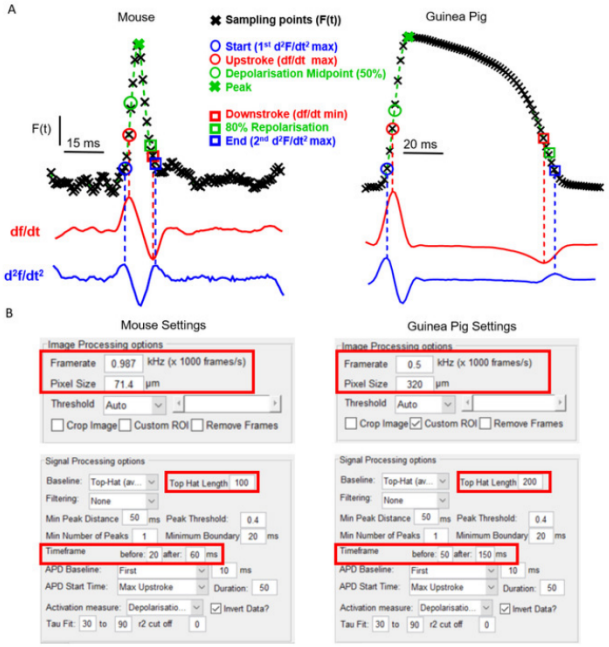

Figure 2: Analysis of mouse and guinea pig data using ElectroMap. (**A**) Optically recorded action potential from mouse atria and guinea pig ventricles, along with both the first (df/dt) and second (d^2f/dt^2) derivate of these signals. The various definitions for activation and repolarization times employable within ElectroMap are highlighted. (**B**) Screenshots of Image and signal processing settings utilized in ElectroMaps interface. Red boxes highlight settings that required modification between analyses of mouse and guinea pig data. Figure adapted from O'Shea et al., 2019[13]. Please click here to view a larger version of this figure.

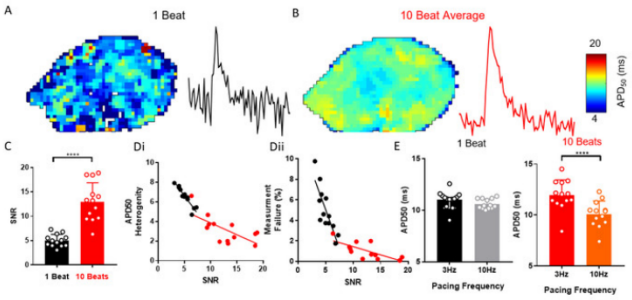

Figure 3: Ensemble averaging to resolve APD changes. (**A**) APD_{50} map and example single pixel signal from single beat optical action potentials. (**B**) APD_{50} map and example single pixel signal from optical action potentials generated by ensemble averaging of 10 successive beats (peak method). (**C**) SNR of single beat compared to 10 beat averaged signals. (**D**) APD_{50} heterogeneity (i) and number of measurement failures (ii) as a function of SNR for single beat and 10 beat averaged APD_{50} maps. (**E**) APD_{50} at 3 and 10 Hz pacing frequency, as measured from single beat and 10 beat maps. (Data shown as mean ± standard error, n = 13 left atria, ****p < 0.001 by student's paired t-test). Please click here to view a larger version of this figure.

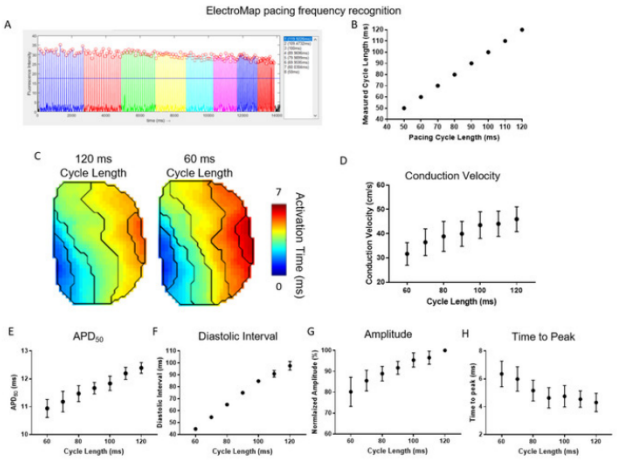

Figure 4: Use of ElectroMap to study pacing frequency responses in cardiac tissue. (**A**) Example ElectroMap screenshot of pacing frequency recognition and segmentation. (**B**) Comparison of known and ElectroMap measured pacing cycle lengths. (**C**) Activation maps at 120 ms and 60 ms pacing cycle lengths. (**D-H**) Grouped data of conduction velocity (**D**), APD_{50} (**E**), diastolic interval (**F**), amplitude (**G**), and time to peak (**H**) as a function of pacing cycle length decreasing from 120 ms to 60 ms in 10 ms increments. (Data shown as mean ± standard error, *n* = 5 left atria) Please click here to view a larger version of this figure.

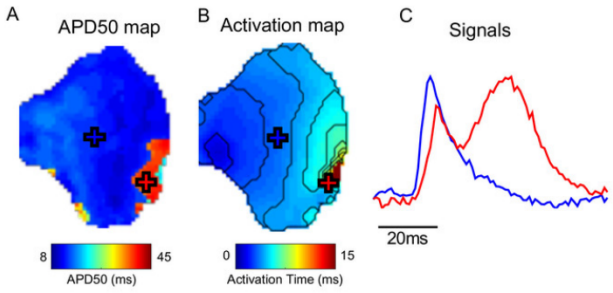

Figure 5: Effect of motion artifacts. (**A**) APD_{50} map. (**B**) Activation map. (**C**) Example signals from locations marked (crosses) on APD and activation maps. In the area of the tissue marked with the red cross, contraction has not been successfully uncoupled, distorting the measured optical signal. Please click here to view a larger version of this figure.

Discussion

Here, we present a step-by-step guide for the utilization of open-source software ElectroMap for flexible and multi variable analysis of cardiac optical mapping datasets. For successful use of ElectroMap, imaging data is required to be in .tif or .MAT formats. ElectroMap incorporates several modifiable user settings. As demonstrated in **Figure 2A**, this is necessary due to the wide heterogeneity that exists between experimental models and imaging hardware. This means however that default settings within the software will not always be optimal, so a critical step in using the software is for the user to tune settings for their particular experimental setup. These include camera settings and timescales, as shown in **Figure 2B**. Once optimal settings have been found, these can be saved and reloaded at later times by selecting **Configuration File**.

Incorporation of automated CL measurement and signal segmentation are key advantages of the software. These features allow analysis of acute responses in experimental recordings and widen analysis from focusing on isolated single beats. Once desired segmentation has been achieved, the **Single File Analysis** module allows automated analysis of each individual segment (including single beats), realizing high-throughput analysis of multiple variables across the recording outputted in a single .csv file. In conjunction, ensemble averaging of grouped

peaks is an effective method to improve quality of noisy signals that is automatically performed in ElectroMap. However, ensemble averaging is not ubiquitously beneficial, for example in studies of beat-to-beat variability. Therefore, ElectroMap integrates single beat segmentation to avoid ensemble averaging, alternative processing options to improve SNR (spatial and temporal filtering) and includes the **Alternans** analysis module to further investigate and map beat-to-beat variability.

Optical Mapping datasets often exhibit artifacts such as baseline drift and motion artifacts. Equally, the signals generated can be low quality due to small pixel sizes, short exposure times and low fractional fluorescent changes[2]. These factors prevent effective and accurate analysis of the underlying EP behavior. As outlined, ElectroMap has several processing strategies to overcome these issues. However, application of these algorithms to fundamentally poor quality/distorted data will still prevent effective analysis. SNR is therefore one of the parameters that is measured and displayed in ElectroMap. Equally, the user can select and compare the signals from specific regions from the sample using the **Pixel Info** and **Compare** modules, allowing identification of phenomena such as motion artifacts shown in **Figure 5**, and appropriate exclusion of data.

At present, ElectroMap does not support removal of motion artifacts from raw data in the same manner as baseline correction. Therefore, a possible future development of the software is inclusion of motion artefact removal by computational methods as has been reported[31,32]. Furthermore, ElectroMap is currently limited to study of one optical signal. However, for ratiometric dyes and simultaneous use of voltage and calcium dyes[27], concurrent processing of two wavelength channels is required. The integration of dual signal analysis is therefore an important future addition to the software. Extension of analysis options applicable to arrhythmic datasets, such as phase singularity tracking, would equally broaden the scope of the software[33,34]. Finally, several of the analysis options described can also be useful in analysis of the electrode mapping data. Indeed, ElectroMap has been used to analyze electrode mapping data despite the contrasting electrogram waveform[20,35], and further optimization will expand its use for this modality.

Disclosures

P.K. receives research support from several drug and device companies active in atrial fibrillation and has received honoraria from several such companies. L.F. has received institutional research grants EU, BHF, MRC, DFG and Gilead. P.K. and L.F. are listed as inventors on two patents held by University of Birmingham (Atrial Fibrillation Therapy WO 2015140571, Markers for Atrial Fibrillation WO 2016012783).

All other authors declare no potential conflict of interest.

Acknowledgments

This work was funded by the EPSRC studentship (Sci-Phy-4-Health Centre for Doctoral Training L016346) to D.P., K.R. and L.F., Wellcome Trust Seed Award Grant (109604/Z/15/Z) to D.P., British Heart Foundation Grants (PG/17/55/33087, RG/17/15/33106) to D.P., European Union (grant agreement No 633196 [CATCH ME] to P.K. and L.F.), British Heart Foundation (FS/13/43/30324 to P.K. and L.F.; PG/17/30/32961 to P.K. and A.H.), and Leducq Foundation to P.K.. J.W. is supported by the British Heart Foundation (FS/16/35/31952).

References

1. Efimov, I. R., Nikolski, V. P., Salama, G. Optical Imaging of the Heart. *Circulation Research*. **94**, 21-33 (2004).
2. Herron, T. J., Lee, P., Jalife, J. Optical imaging of voltage and calcium in cardiac cells & tissues. *Circulation Research*. **110**, 609-623 (2012).
3. Boukens, B. J., Efimov, I. R. A century of optocardiography. *IEEE Reviews in Biomedical Engineering*. **7**, 115-125 (2014).
4. Myles, R. C., Wang, L., Kang, C., Bers, D. M., Ripplinger, C. M. Local β-adrenergic stimulation overcomes source-sink mismatch to generate focal arrhythmia. *Circulation Research*. **110**, 1454-1464 (2012).
5. Syeda, F. et al. PITX2 Modulates Atrial Membrane Potential and the Antiarrhythmic Effects of Sodium-Channel Blockers. *Journal of the American College of Cardiology*. **68**, 1881-1894 (2016).
6. Winter, J. et al. Sympathetic nervous regulation of cardiac alternans in the intact heart. *Frontiers in Physiology*. **9**, 1-12 (2018).
7. Faggioni, M. et al. Suppression of spontaneous ca elevations prevents atrial fibrillation in calsequestrin 2-null hearts. *Circulation: Arrhythmia and Electrophysiology*. **7**, 313-320 (2014).
8. Sato, P. Y. et al. Loss of Plakophilin-2 Expression Leads to Decreased Sodium Current and Slower Conduction Velocity in Cultured Cardiac Myocytes. *Circulation Research*. **105**, 523-526 (2009).
9. Yu, T. Y. et al. Optical mapping design for murine atrial electrophysiology. *Computer Methods in Biomechanics and Biomedical Engineering: Imaging & Visualization*. **5**, 368-378 (2017).
10. Laughner, J. I., Ng, F. S., Sulkin, M. S., Arthur, R. M., Efimov, I. R. Processing and analysis of cardiac optical mapping data obtained with potentiometric dyes. *American Journal of Physiology. Heart and Circulatory Physiology*. **303**, H753-65 (2012).
11. Crocini, C., Ferrantini, C., Pavone, F. S., Sacconi, L. Optogenetics gets to the heart: A guiding light beyond defibrillation. *Progress in Biophysics and Molecular Biology*. **130**, 132-139 (2017).
12. Entcheva, E., Bub, G. All-optical control of cardiac excitation: Combined high-resolution optogenetic actuation and optical mapping. *The Journal of Physiology*. **9**, 2503-2510 (2016).
13. O'Shea, C. et al. ElectroMap: High-throughput open-source software for analysis and mapping of cardiac electrophysiology. *Scientific Reports*. **9**, 1-13 (2019).
14. Yu, T. Y. et al. An automated system using spatial oversampling for optical mapping in murine atria. Development and validation with monophasic and transmembrane action potentials. *Progress in Biophysics and Molecular Biology*. **115**, 340-348 (2014).
15. Jaimes, R. et al. Functional response of the isolated, perfused normoxic heart to pyruvate dehydrogenase activation by dichloroacetate and pyruvate. *Pflugers Archiv*. **468**, 131-142 (2016).
16. Wang, K. et al. Cardiac tissue slices: preparation, handling, and successful optical mapping. *American Journal of Physiology. Heart and Circulatory Physiology*. **308**, H1112-25 (2015).

17. Parrish, D. C. et al. Transient denervation of viable myocardium after myocardial infarction does not alter arrhythmia susceptibility. *American Journal of Physiology. Heart and Circulatory Physiology.* (2017).
18. Ihara, K. et al. Electrophysiological Assessment of Murine Atria with High-Resolution Optical Mapping. *Journal of Visualized Experiments.* **132**, e56478 (2018).
19. Holmes, A. P. et al. A Regional Reduction in Ito and IKACh in the Murine Posterior Left Atrial Myocardium Is Associated with Action Potential Prolongation and Increased Ectopic Activity. *Plos One.* **11**, e0154077 (2016).
20. Lang, D. et al. Arrhythmogenic remodeling of β<inf>2</inf> versus β<inf>1</inf> adrenergic signaling in the human failing heart. *Circulation: Arrhythmia and Electrophysiology.* **8**, 409-419 (2015).
21. Kang, C. et al. Human Organotypic Cultured Cardiac Slices: New Platform For High Throughput Preclinical Human Trials. *Scientific Reports.* **6**, 1-13 (2016).
22. Wen, Q. et al. Transverse cardiac slicing and optical imaging for analysis of transmural gradients in membrane potential and Ca2+ transients in murine heart. *The Journal of Physiology.* **596**, 3951-3965 (2018).
23. Houston, C. et al. Characterisation of re-entrant circuit (or rotational activity) in vitro using the HL1-6 myocyte cell line. *Journal of Molecular and Cellular Cardiology.* **119**, 155-164 (2018).
24. Yu, T. Y. et al. Optical mapping design for murine atrial electrophysiology. *Computer Methods in Biomechanics and Biomedical Engineering: Imaging and Visualization.* **5**, 368-376 (2017).
25. Laughner, J. I., Ng, F. S., Sulkin, M. S., Arthur, R. M., Efimov, I. R. Processing and analysis of cardiac optical mapping data obtained with potentiometric dyes. *AJP: Heart and Circulatory Physiology.* **303**, H753-H765 (2012).
26. Bayly, P. V et al. Estimation of Conduction Velocity Vector Fields from Epicardial Mapping Data. *IEEE Transactions on Bio-Medical Engineering.* **45**, 563-571 (1998).
27. Jaimes, R. et al. A technical review of optical mapping of intracellular calcium within myocardial tissue. *American Journal of Physiology. Heart and Circulatory Physiology.* **310**, H1388-H1401 (2016).
28. Wang, L. et al. Optical mapping of sarcoplasmic reticulum Ca2+ in the intact heart: Ryanodine receptor refractoriness during alternans and fibrillation. *Circulation Research.* **114**, 1410-1421 (2014).
29. Winter, J., Shattock, M. J. Geometrical considerations in cardiac electrophysiology and arrhythmogenesis. *Europace.* (2016).
30. Mironov, S., Jalife, J., Tolkacheva, E. G. Role of conduction velocity restitution and short-term memory in the development of action potential duration alternans in isolated rabbit hearts. *Circulation.* **118**, 17-25 (2008).
31. Khwaounjoo, P. et al. Image-Based Motion Correction for Optical Mapping of Cardiac Electrical Activity. *Annals of Biomedical Engineering.* **43**, 1235-1246 (2014).
32. Christoph, J., Luther, S. Marker-Free Tracking for Motion Artifact Compensation and Deformation Measurements in Optical Mapping Videos of Contracting Hearts. *Frontiers in Physiology.* **9**, (2018).
33. Umapathy, K. et al. Phase Mapping of Cardiac Fibrillation. *Circulation: Arrhythmia and Electrophysiology.* **3**, 105-114 (2010).
34. Tomii, N. et al. Detection Algorithm of Phase Singularity Using Phase Variance Analysis for Epicardial Optical Mapping Data. *IEEE Transactions on Biomedical Engineering.* **63**, 1795-1803 (2016).
35. Cantwell, C. D. et al. Techniques for automated local activation time annotation. and conduction velocity estimation in cardiac mapping. *Computers in Biology and Medicine.* **65**, (2015).

